

The volume-limited A-star survey

Exploring the multiplicity of intermediate-mass stars

Mr Robert John De Rosa

Submitted by Mr Robert John De Rosa to the University of Exeter as a thesis for the degree of Doctor of Philosophy in Physics, January, 2012.

This thesis is available for Library use on the understanding that it is copyright material and that no quotation from the thesis may be published without proper acknowledgement.

I certify that all material in this thesis which is not my own work has been identified and that no material has previously been submitted and approved for the award of a degree by this or any other University.

Signed:

Mr Robert John De Rosa

Date:

I present the results of the first volume-limited adaptive optics multiplicity survey of A-type stars. Using high-resolution observations obtained using adaptive optics instruments at five observatories, I have estimated the frequency of binary companions to a sample of 233 A-type stars within 60 parsecs. The survey is complete within a projected separation range of $56 < a[\text{AU}] \leq 891$, and a companion mass ratio range of $0.05 \leq q \leq 1.00$, corresponding to the bottom of the Main Sequence for companions to A-type stars. The multiplicity fraction of the sample, when corrected for completeness, is measured to be $24.2\% \pm 3.5\%$, continuing the trend of increasing multiplicity as a function of increasing primary mass reported in previous volume-limited surveys of Solar-type and M-dwarf primaries. A companion mass ratio and separation distribution are constructed over the restricted separation range, and are compared with previous observations of lower-mass primaries and theoretical predictions. The mass ratio distribution is strongly skewed towards lower-mass companions, consistent with the formation of binary companions within large circumstellar disks, while the shape of the separation distribution is not fully resolved due to the incompleteness of the survey. Over the separation range to which the observations are sensitive, a significant separation dependence on the mass ratio is observed, with a greater frequency of lower-mass companions measured at wider separations.

Using this large dataset of adaptive optics observations, I have also explored the unexplained X-ray detection of a subset of A-type stars, whose interior structures theoretically preclude the generation of X-rays. By constructing two similarly sensitive samples of X-ray and non X-ray detected early-type stars, I have tested the hypothesis that an unresolved, lower-mass companion is responsible for the emission. A comparison of the fraction of targets with resolved binary companions within both samples reveals a significantly higher multiplicity fraction for the X-ray detected sample of A-type stars, consistent with the prediction of this companion hypothesis. I have also studied the orbital motions of thirteen A-type stars, and determined the dynamical mass of each system. These dynamical mass estimates are compared with theoretical values from stellar evolutionary models, with discrepancies between these values within several systems used as evidence of unresolved companions, providing potential targets for future interferometric and spectroscopic observations.

Abstract	2
List of Figures	10
List of Tables	11
Declaration	11
Acknowledgements	12
Definitions	13
1 Introduction	16
1.1 Binary star formation theories	18
1.1.1 Fragmentation	18
1.1.2 Disk fragmentation	20
1.1.3 Capture	21
1.1.4 Simultaneous ejection	22
1.1.5 Fission	23
1.2 Multiplicity and A-type stars	23
1.3 Adaptive optics	27
1.3.1 Atmospheric turbulence	27
1.3.2 Wavefront detection	29
1.3.3 Wavefront correction	31
2 The VAST sample	33
2.1 Sample completeness	33
2.2 Sample properties	35
2.2.1 Distance and absolute photometry estimates	35
2.2.2 Metallicity estimates	35
2.2.3 Age and mass estimates	36

2.2.4	Spectral type distribution	38
2.2.5	Spatial distribution	38
3	Primary comparison samples	49
3.1	Volume-limited surveys	49
3.1.1	Solar-type primaries	49
3.1.2	M-dwarf primaries	52
3.1.3	Brown dwarfs primaries	54
3.2	Environment-specific surveys	55
3.3	Other surveys	57
3.3.1	Southern early-type stars	57
3.3.2	Herbig AeBe stars	57
4	Observations and data reduction	58
4.1	Dedicated observations	60
4.1.1	CFHT - PUEO/AOB + KIR	60
4.1.2	Gemini North - ALTAIR + NIRI	60
4.1.3	Lick Observatory (Shane Telescope) - IRCAL	61
4.1.4	Palomar Observatory (Hale Telescope) - PHARO	62
4.2	Archival data	63
4.3	Data reduction pipeline	65
4.3.1	Image processing	65
4.3.2	Image registration	70
4.4	Astrometric calibration	71
4.4.1	Trapezium observations	71
4.4.2	Calibration binary observations	71
4.5	Candidate identification	73
4.5.1	Separation and position angle estimates	73
4.5.2	Photometry estimates	75
4.5.3	Mass-magnitude relations	77
4.5.4	Background probability	77
4.6	Detection limits	79
5	Statistical results	81
5.1	Survey completeness	81
5.2	Correction for incompleteness	87
5.3	Identified companion candidates	87
5.4	Mass ratio distribution	93
5.5	Separation distribution	93

6	Comparison with previous observations and theoretical predictions	95
6.1	Multiplicity as a function of primary mass	95
6.2	Comparison of mass ratio distributions	98
6.3	Comparison of separation distributions	103
6.4	Summary	105
7	Companions and the unexplained X-ray detection of B6 – A7 stars	107
7.1	X-ray emission of Main Sequence stars	107
7.2	Previous observations	108
7.2.1	X-ray detection of B6-A7 stars	108
7.2.2	High-resolution imaging companion searches	109
7.3	Sample	117
7.4	Observations	122
7.5	Data analysis	122
7.6	Results	123
7.6.1	Detections	127
7.6.2	Detection limits	127
7.6.3	Probability of chance superpositions	127
7.7	Discussion	129
7.7.1	Multiplicity comparison	129
7.7.2	<i>ROSAT</i> positional uncertainty	130
7.7.3	Comparison of measured and expected X-ray luminosities	131
7.8	Summary	134
8	Orbital motion monitoring of A-type star multiples	136
8.1	Introduction	136
8.2	Sample	137
8.3	Observations	138
8.4	Data analysis	143
8.4.1	AO image processing	143
8.4.2	Orbital determination	143
8.4.3	Theoretical mass-magnitude relations	145
8.5	Results	156
8.5.1	Astrometric results	156
8.5.2	Orbital elements and dynamical masses	156
8.6	Discussion	158
8.6.1	Comparison to theoretical models	162
8.6.2	Higher-order multiplicity	169
8.6.3	Continued monitoring targets	172
8.7	Summary	174

9	Future prospects for research	177
9.1	Continued study of A-type binaries	177
9.2	Future research areas	178

LIST OF FIGURES

1.1	Binary formation phase space schematic	18
1.2	Formation of a multiple system through fragmentation	19
1.3	Mass dependence of the formation of binaries through disk fragmentation	20
1.4	Velocity distribution of a stellar cluster N-body simulation demonstrating simultaneous ejection	22
1.5	A simulation of the development of a protostellar disk around a rapidly rotating protostar	24
1.6	The ζ Ursae Majoris system	25
1.7	Planets resolved around HR 8799 and β Pictoris	26
1.8	Image angular resolution as a function of telescope aperture	28
1.9	Schematic of a perfect plane wave incident on a Shack-Hartmann wavefront sensor	29
1.10	Schematic of a distorted plane wave incident on a Shack-Hartmann wavefront sensor	29
1.11	Schematic of an individual element of a Shack-Hartmann wavefront sensor	30
1.12	Schematic of a wavefront curvature sensor	30
1.13	Schematic of the corrective action of a deformable mirror	31
1.14	An example of a seeing-limited and diffraction-limited observation.	32
2.1	A colour-magnitude diagram of the VAST sample	34
2.2	The completeness of the survey, as a function of the distance and $B_T - V_T$ cut-off	34
2.3	Metallicity estimates for 96 members of the VAST sample	36
2.4	Age estimates based on position on a colour-magnitude diagram	37
2.5	Age and mass distributions of the VAST sample	37
2.6	Spectral type distribution of the VAST sample targets	39
2.7	The VAST sample as a function of right ascension and declination	39
2.8	The spatial density of A-type stars within 100pc	40
3.1	Multiplicity as a function of primary mass	50
3.2	Separation and mass ratio distributions of the Raghavan et al. (2010) survey	51

3.3	Separation and mass ratio distributions of the Fischer & Marcy (1992) survey . . .	52
3.4	Separation and mass ratio distributions of the Reid et al. (2008) survey	54
3.5	Mass ratio distribution of the Kouwenhoven et al. (2005) Sco OB2 survey	56
4.1	Colour-magnitude diagram of <i>Hipparcos</i> stars within 75pc, demonstrating the rationale of the observational strategy	59
4.2	The CFHT observatory, with example narrow-band and wide-band images . . .	59
4.3	The Gemini observatory, with example narrow-band and wide-band images . .	60
4.4	The Lick observatory, with example narrow-band images	62
4.5	The Palomar observatory, with example narrow-band images	62
4.6	The VLT observatory, with an example narrow-band image	63
4.7	Example dark frame obtained at the CFHT, and corresponding pixel value histogram	66
4.8	Example flat field obtained at the CFHT, and corresponding pixel value histogram	67
4.9	Histogram of pixel values within the example flat field frame obtained at CFHT	68
4.10	Example of the sky background estimation procedure	69
4.11	An observation of the Trapezium cluster is used to calibrate the plate scale and orientation of the KIR detector	72
4.12	The distribution of plate scale and true North angle estimates obtained from an observation of the Trapezium cluster	73
4.13	Magnitude difference between a target star and a resolved companion candidate, estimated using aperture photometry	75
4.14	The transmission of the narrow- and wide-band filters at the CFHT	76
4.15	The mass-magnitude relations used to estimate the mass of each resolved companion candidate	78
4.16	<i>2MASS</i> point source density used to estimate the background probability for each companion candidate	78
4.17	Detection limits estimated for HIP 44127, and corresponding radial profile . . .	79
5.1	Detection limits for an observation of HIP 44127	82
5.2	Completeness of an observation of HIP 44127 as a function of separation and magnitude difference	83
5.3	Survey completeness as a function of separation and magnitude difference . . .	84
5.4	Survey completeness as a function of separation and companion mass	85
5.5	Survey completeness as a function of separation and mass ratio	86
5.6	Region of phase space used to construct binary statistics based on the level of survey completeness	88
5.7	Coarse resolution completeness distribution	88
5.8	The resolved companion candidates plotted as a function of projected separation and mass ratio	89
5.9	The measured mass ratio distribution of the resolved companions	94
5.10	The measured projected separation distribution of the resolved companions . .	94

6.1	The observed companion star fraction between 56 and 891 AU as a function of primary mass	96
6.2	Multiplicity fraction of four stellar cluster simulations as a function of primary mass	97
6.3	Comparison with the Raghavan et al. (2010) Solar-type mass ratio distribution .	98
6.4	Comparison with the Fischer & Marcy (1992) M-dwarf mass ratio distribution .	99
6.5	Comparison with the Kouwenhoven et al. (2005) Sco OB2 mass ratio distribution	100
6.6	Mass ratio distribution compared with random pairing from the IMF	102
6.7	Variation in the cumulative mass ratio distribution as a function of separation .	103
6.8	Comparison with the Raghavan et al. (2010) Solar-type separation distribution .	104
6.9	Location of peak of the separation distribution as a function of primary mass .	105
7.1	Spectral type distribution of the sample	117
7.2	Colour-magnitude diagram of the sample	118
7.3	<i>RASS</i> X-ray luminosity detection limits	118
7.4	<i>RASS</i> spectral type sensitivity limits	119
7.5	Distribution of <i>Hipparcos</i> and <i>ROSAT</i> offsets	119
7.6	Magnitude difference versus separation for the resolved companion candidates .	128
7.7	<i>2MASS</i> source count as a function of magnitude within the vicinity of HIP 57646	128
7.8	A colour-magnitude diagram of three resolved companions	131
7.9	A sub-arcsecond companion candidate resolved in the vicinity of HIP 17608 . .	132
7.10	Estimated X-ray to bolometric luminosity ratio of the resolved candidates . . .	133
8.1	Colour-magnitude diagram of the sample	139
8.2	Magnitude difference as a function of separation for the complete sample	140
8.3	Mass-magnitude relations derived from four theoretical evolutionary models . .	146
8.4	System age estimate based on colour-magnitude diagram position	147
8.5	Example mass-magnitude relation for a hypothetical binary system	148
8.6	Estimated orbital fit for the first six binary systems	159
8.7	Estimated orbital fit for the remaining six binary systems	160
8.8	Comparison of the photometric and dynamical system masses	163
8.9	Photometric system mass as a function of age for systems with no indication of additional unresolved components	164
8.10	The dependence on metallicity of the dynamical mass estimate	165
8.11	The HIP 44127 hierarchical system	167
8.12	The theoretical system mass as a function of age for the HIP 82321 BC system .	168
8.13	Schematic of the seven hierarchical systems within the sample	169
8.14	The mass-age relation for six systems with known or suspected spectroscopic components	170
8.15	Twelve of the thirteen systems suggested as future orbital monitoring targets . .	173
8.16	The final system suggested as a future orbital monitoring target	174
8.17	Historical observations of the HIP 77660 binary system	175

LIST OF TABLES

2.1	Metallicity subsamples	35
2.2	VAST sample table	41
3.1	Primary comparison samples	50
4.1	List of instruments used to obtain observations	58
4.2	Source of archival observations	64
4.3	Photometric filter transmission estimates	75
5.1	List of companion candidates resolved within the survey observations	90
7.1	X-Ray Detected Sample	110
7.2	Control sample	113
7.3	Instruments used to obtain observations	121
7.4	Candidate binary systems within control sample	123
7.5	Candidate binary systems within X-ray detected sample	125
7.6	Multiplicity fraction within both samples	127
8.1	Basic properties of sample members	137
8.2	Observing run details with calculated astrometric calibration values	141
8.3	Summary of theoretical model grids	145
8.4	Measured binary position angle and separation for previously resolved systems	150
8.5	Measured binary position angle and separation for potential orbital monitoring targets	152
8.6	Derived parameters of individual components	153
8.7	Visual magnitude differences for a subset of the sample	156
8.8	Estimated orbital parameters and corresponding 1σ uncertainties	157
8.9	Previous and revised dynamical system masses	158
8.10	Comparison of dynamical and photometric system masses for each system within the orbit subsample	161

DECLARATION

I hereby declare the my thesis entitled *The volume-limited A-star survey: Exploring the multiplicity of intermediate-mass stars* is not substantively similar to any thesis, or dissertation, submitted pursuant to the conferment of a degree, or diploma, or other academic qualification, at any other university, or institution, by myself or any third party. I also declare that no part of this thesis, or any derivative work, forms the basis of, or any substantive part of, the thesis, or dissertation, of any third party. I note that Chapter 1 and Chapter 3 contain no original research, and are intended as a literature review of the scientific background. I also note that the parts of the thesis which are based on papers that are published, or accepted for publication, are as follows:

- The work contained in Chapter 7 is wholly based on the paper **De Rosa, R. J.**, Bulger, J., Patience, J., Leland, B., Macintosh, B., Schneider, A., Song, I., Marois, C., Graham, J. R., Bessel, M., Doyon, R. (2011) ‘The Volume-limited A-Star (VAST) survey - I. Companions and the unexpected X-ray detection of B6-A7 stars’, published in the *Monthly Notices of the Royal Astronomical Society* **415** 854–866, of which I was the principal author.
- The work contained in Chapter 8 is wholly based on the paper **De Rosa, R. J.**, Patience, J., Vigan, A., Wilson, P. A., Schneider, A., McConnell, N. J., Wiktorowicz, S. J., Marois, C., Song, I., Macintosh, B., Graham, J. R., Bessel, M., Doyon, R., Lai, O., (2012) ‘The VAST Survey - II. Orbital motion monitoring of A-type star multiples’, accepted for publication in the *Monthly Notices of the Royal Astronomical Society*, of which I was the principal author.

Robert John De Rosa

ACKNOWLEDGEMENTS

I wish to first express my gratitude to my thesis advisor, Jennifer Patience, for her continuing support and encouragement through the previous four years, and providing me with numerous opportunities, both observing at the beautiful observatories in Hawai'i and La Palma, and attending both scientific conferences and collaborative meetings to further my training and education as a young astronomer. I also wish to give a big shout-out to Lee Summers, who started his PhD programme at the same time as me, and who shared my office for the majority of our respective programmes; long will I miss our much venerated trips to the shop! Also, a big thanks to all my friends both within, and outside of, Exeter, who have filled the last seven-and-a-half years with fond memories. Finally, I would like to express my warmest thanks to my family, who have been a constant support to me throughout the years.

Robert John De Rosa
Exeter, U.K., January 2012

DEFINITIONS

Symbol	Unit	Description
A, B, F, G	-	Thiele-Innes elements
A	count	Peak flux of primary
a	AU	Projected separation between primary and companion candidate
a	arc-second	Orbital semi-major axis (Chapter 7)
α	degree	Right ascension (RA)
B_T	magnitude	Apparent <i>Tycho2</i> visual magnitude (360 – 480 nm)
$B_T - V_T$	-	Ratio of <i>Tycho2</i> B_T and <i>Tycho2</i> V_T magnitudes
β	radian	Estimated detector true north correction
C	-	Completeness of survey
c	-	Completeness of individual observation
D	parsec	Distance
$D(t_{\text{exp}})$	-	Average dark frame of exposure time t_{exp}
$d_n(t_{\text{exp}})$	-	Individual dark frame of exposure time t_{exp}
δ	degree	Declination
$\Delta\alpha$	arc-second	RA displacement of companion within observed plane
$\Delta\delta$	arc-second	Declination displacement of companion within observed plane
ΔK	magnitude	Magnitude difference within <i>2MASS</i> K -band
Δm	magnitude	Magnitude difference
Δx	pixel	Horizontal position of companion candidate relative to primary
Δy	pixel	Vertical position of companion candidate relative to primary
D_{tel}	metre	Telescope diameter
E	radian	Eccentric anomaly
e	-	Orbital eccentricity
F_a	count	Flux of primary
F_b	count	Flux of companion candidate
[Fe/H]	-	Iron to Hydrogen ratio, relative to Solar
F_n	count	Flux of primary in narrow-band image
F_w	count	Estimated flux of primary in wide-band image
Γ	-	Relative transmission between narrow-band and wide-band filters
H	magnitude	Apparent <i>2MASS</i> near-infrared magnitude (1.50 – 1.80 μm)
\bar{h}	metre	Average characteristic turbulence altitude
HgCdTe	-	Mercury cadmium telluride
i	radian	Orbital inclination
$I(t_{\text{exp}})$	-	Science image of exposure time t_{exp}

Symbol	Unit	Description
I_0	count	Curvature sensor intensity
I_1	count	Curvature sensor intensity
I_2	count	Curvature sensor intensity
InSb	-	Indium antimonide
J	magnitude	Apparent <i>2MASS</i> near-infrared magnitude (1.10 - 1.35 μm)
K_S	magnitude	Apparent <i>2MASS</i> near-infrared magnitude (1.95 - 2.35 μm)
λ	micron	Wavelength
M	magnitude	Absolute magnitude
m	magnitude	Apparent magnitude
M_1	solar mass	Primary mass
M_2	solar mass	Companion candidate mass
M_a	magnitude	Absolute magnitude of primary
M_b	magnitude	Absolute magnitude of companion candidate
M_\odot	Solar mass	Solar mass (1.98892×10^{30} kg)
M_K	magnitude	Absolute <i>2MASS</i> near-infrared magnitude (1.95 - 2.35 μm)
μ	-	Distance modulus
M_V	magnitude	Absolute <i>Tycho2</i> visual magnitude (450 - 600 nm)
n_{lenslet}	-	Number of lenslets
ω	radian	Longitude of periastron
Ω	radian	Longitude of the ascending node
P	year	Orbital period
p	arc-second/pixel	Estimated detector plate scale
P_d	day	Orbital period
ϕ	radian	Position angle of companion candidate on detector
π	milli-arcsecond	<i>Hipparcos</i> parallax
q	-	Mass ratio (M_1/M_2)
r	pixel	Separation between primary and companion candidate
r_0	metre	Atmospheric coherence length
RA	-	Right ascension
ρ	arc-second	Angular separation between primary and companion candidate
σ_x	-	Estimated uncertainty on the parameter x
$\log t$	year	Estimated stellar age
T_0	year	Epoch of periastron passage
t_i	year	Epoch of observation
τ_0	second	Turbulence time constant
t_{exp}	second	Exposure time
θ	radian	Position angle of companion relative to celestial north
θ_0	radian	Isoplanatic angle
t_n	second	Exposure time of narrow-band image
T_n	-	Transmission of narrow-band filter
t_w	second	Exposure time of wide-band image
T_w	-	Transmission of wide-band filter
V_T	magnitude	Apparent <i>Tycho2</i> visual magnitude (450 - 600 nm)
$V - K$	-	Ratio of <i>Tycho2</i> V_T and <i>2MASS</i> K_S magnitudes
\bar{V}	m s^{-1}	Average wind velocity
$v \sin i$	km s^{-1}	Stellar rotational velocity
x_i	arc-second	RA displacement of companion within observed plane at t_i
x'_i	arc-second	RA displacement position of companion within orbital plane at t_i
x_a	pixel	Horizontal position of primary on detector
x_b	pixel	Horizontal position of companion candidate on detector

Symbol	Unit	Description
y_i	arc-second	Declination displacement of companion within observed plane at t_i
y'_i	arc-second	Declination displacement position of companion within orbital plane at t_i
y_a	pixel	Vertical position of primary on detector
y_b	pixel	Vertical position of companion candidate on detector
Z	-	Fraction by mass of metallic elements



My thesis, entitled *The volume-limited A-star survey: Exploring the multiplicity of intermediate-mass stars* (VAST survey), constitutes a significant portion of the work I have undertaken as a part of my graduate training. The thesis is divided into nine chapters, two of which are derived from first-author published articles:

- Chapter 1 – *Introduction* - I briefly discuss various binary formation models, A-type stars, and provide background on adaptive optics instrumentation.
- Chapter 2 – *The VAST sample* - The volume-limited sample of A-type stars is constructed, and its completeness in terms of the overall population of A-type stars is discussed. Various sample member properties are estimated, such as the mass and age, and corresponding sample distributions are calculated.
- Chapter 3 – *Primary comparison samples* - Presents previous multiplicity surveys of both lower-mass primaries within the Solar neighbourhood, and early-type stars within the nearby young stellar association Scorpius OB 2. The separation and mass ratio distribution of each survey are detailed, in preparation for a subsequent comparison with the results of this study.
- Chapter 4 – *Observations and data reduction* - Describes the observations I obtained as a part of this research, and details the data reduction process. The identification and characterisation of companion candidates within the observations is discussed, and the corresponding detection limits of the data.
- Chapter 5 – *Statistical results* - Presents the primary statistical results of the survey, namely the fraction of multiple stars within the sample, and the mass ratio and separation distributions.
- Chapter 6 – *Comparison with previous observations and theoretical predictions* - The statistical results are compared to the results of previous surveys of lower-mass stars, and to

theoretical predictions. The implications of the results are discussed in the context of the theories of binary formation.

- Chapter 7 - *Companions and the unexplained X-ray detection of B6 - A7 stars* - The unexplained X-ray detection of a subset of early-type stars is described. Using the large dataset obtained as a part of this study, I explore the hypothesis that states lower-mass companions to these bright stars are responsible for the X-ray detections.
- Chapter 8 - *Orbital motion monitoring of A-type star multiples* - The orbital motion of 13 A-type stars is determined, using a combination of the data from this study, and historical measurements. A dynamical mass is determined for each system, and compared with predictions from theoretical models.
- Chapter 9 - *Future prospects for research* - I conclude with a brief discussion of the future avenues of research I intend to explore to expand the scientific returns from the VAST survey.

1.1 Binary star formation theories

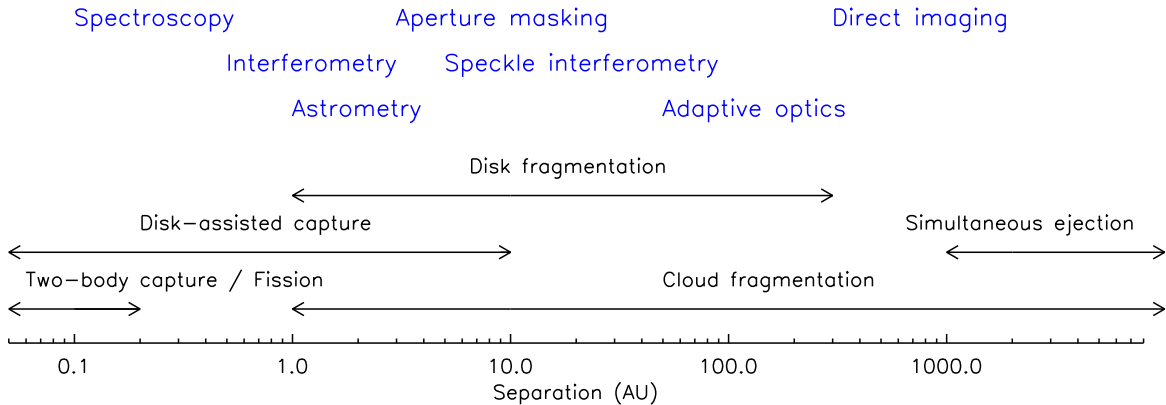


Figure 1.1: A schematic representation of the separation range over which the various binary formation mechanisms are thought to operate. Various binary detection techniques have also been indicated. The separation ranges indicated are not the exact delineation between the various mechanisms, and are intended only as a guide.

Numerous theories exist within the literature regarding the formation of binary and multiple stars (e.g. Tohline 2002), which can be divided into two broad groupings; fragmentation, either of cores, disks, or protostars themselves; and dynamical interaction, either through two- or three-body capture, or simultaneous ejection from a stellar cluster. A sketch of the separation range over which each formation mechanism operates is shown in Figure 1.1, although subsequent dynamical processing within the formation environment may cause significant orbital migration of any binary system formed through these processes (Bate et al. 2002).

1.1.1 Fragmentation

Fragmentation, encompassing both fragmentation of collapsing cores and disk fragmentation, is regarded as the primary mechanism for the formation of most binary stars (Boss 1986; Bonnell 2001). The fragmentation of cores, caused by the localised satisfaction of the Jeans criterion due to turbulent fluctuations within the gravitationally bound core (Offner et al. 2010), is predicted to be an efficient method of binary formation (e.g. Fisher 2004; Goodwin et al. 2004a). Multiple density enhancements can be created within a single collapsing core, leading to the formation of a bound binary or multiple system (Figure 1.2, Offner et al. 2010). Simulations of large stellar clusters have shown that the majority of binaries are formed due to fragmentation (e.g. Bate et al. 2003), and it is thought to be the dominant mode of binary formation for low mass stars (Offner et al. 2010). Fragmentation can lead to the formation of binary systems with separations between 10^1 and 10^4 AU (Bate et al. 1995), limited by the size of the collapsing star forming core (e.g. Ward-Thompson et al. 2007). Although fragmentation cannot directly form binary companions within 10 AU, of which a substantial population are observed to exist (e.g. Raghavan et al. 2010), subsequent dynamical interaction and accretion of surrounding material can cause the inward migration of a wide binary to separations of < 10 AU (Bate et al. 2002).

Image Copyrighted
Figure can be found in Bonnell
& Bastien 1992 (Figure 8, p 665)

Figure 1.2: A simulation of the formation of a hierarchical multiple system through fragmentation of a $4 M_{\odot}$ cloud (Bonnell & Bastien 1992). The subsequent formation and fragmentation of protostellar disks around each object may lead to the production of additional companions. Each panel shows the central 10^4 AU of the simulation, with times of (a) $1.1481t_{\text{ff}}$, (b) $1.1849t_{\text{ff}}$, (c) $1.2090t_{\text{ff}}$, (d) $1.2296t_{\text{ff}}$, (e) $1.2365t_{\text{ff}}$, (f) $1.2499t_{\text{ff}}$, (g) $1.2618t_{\text{ff}}$, (h) $1.2737t_{\text{ff}}$, where t_{ff} is the free-fall time of 8.6414×10^{12} seconds (2.74×10^5 years).

Image Copyrighted
Figure can be found in Kratter 2011
(Figure 1, p 5)

Figure 1.3: Hydrodynamical simulations of the fragmentation of a protostellar disk as a function of two dimensionless parameters, the normalised accretion rate and the normalised rotation period (Kratter 2011; Kratter et al. 2010a). The various realisations are divided into two mass regimes, with those on the left resembling disks of low mass stars, and those on the right resembling disks of high mass stars (Kratter 2011). Within these simulations, fragmentation becomes more pronounced with increasing stellar mass.

Fragmentation is predicted to produce companions of a wide range of mass ratios, with models predicting either little or no correlation between primary mass and the companion mass ratio distribution (Clarke 1996), or a general trend of decreasing mass ratios as a function of increasing initial density (Bonnell & Bastien 1992). The mass ratios of close binary systems are thought to equalise due to the preferential accretion of material onto the secondary (Bate 2000), consistent with observations of Solar-type primaries (Mazeh et al. 1992; Raghavan et al. 2010). Close binaries are not always equalised (e.g. Mazeh et al. 2003), either due to the cessation of accretion, or inward orbital migration. Wide binary companions, formed through fragmentation, are not necessarily coplanar with the rotation axis of the protostellar disk of the primary. In this situation, the orbit of any additional companion formed through subsequent disk fragmentation would not be coplanar with the wide companion (Bonnell 1994b). This combination of formation processes will lead to an observational signature, with a number of hierarchical systems not lying within the same orbital plane, consistent with observations (Fekel 1981; Sterzik & Tokovinin 2002; Bate 2009).

1.1.2 Disk fragmentation

The conservation of angular momentum during the collapse of a cloud leads to the formation of a large protostellar disk, with such structures being ubiquitous within observed star forming regions (e.g. Andrews & Williams 2007; Hernandez et al. 2007). The rapid rotation of a central protostar can also lead to the formation of a protostellar disk (Bonnell 1994a). If these

massive disks are able to become unstable, and cool efficiently, fragmentation can occur due to gravitational instabilities within the disk (Adams et al. 1989; Bonnell & Bate 1994; Boss 2001). Disk fragmentation is often cited as a potential formation scenario for giant planets at wide separations (e.g. Meru & Bate 2010), as have been observed around stars which may have previously harboured massive protostellar disks (Marois et al. 2008; Kalas et al. 2008). Simulations have shown that through the continued accretion of material onto the outer edge of a protostellar disk, the mass of any formed companion can grow substantially (Stamatellos & Whitworth 2009; Kratter et al. 2010a), suggesting disk fragmentation can form binary systems with a wide range of mass ratios (Kratter 2011). The maximum separation of binary systems formed through this process would be strongly dependent on the size of the protostellar disk, with the more massive stars typically having more extended disks (e.g. Dent et al. 2006; Hamidouche et al. 2006; Fukagawa et al. 2010).

Within hydrodynamical simulations of protostellar disks, the occurrence of fragmentation appears strongly correlated with the mass of the disk (Figure 1.3), with the most massive disks forming either a binary companion, or numerous fragments (Kratter & Matzner 2006; Kratter et al. 2010a). Lower-mass disks are predicted to be preferentially stable against fragmentation via gravitational instability (e.g. Matzner & Levin 2005; Offner et al. 2010), and thus unable to form stellar and substellar companions through this route. Observations of low-mass stars within young star forming regions, however, suggest that disk fragmentation may play a role in the formation of binary companions within 200 AU (Kraus et al. 2011). The observed flat mass ratio distribution is consistent with the theoretical prediction that companions formed via disk fragmentation will have a wide range of mass ratios. Due to the apparent correlation between fragmentation and disk mass, A-type stars may exhibit a significant population of companions formed through the fragmentation of a massive protostellar disk.

1.1.3 Capture

There are three distinct types of capture scenarios which lead to the formation of a binary system; simple two-body tidal capture (Fabian et al. 1975), where two stars pass each other sufficiently close to become tidally bound; three-body capture (Hills 1976), where the kinetic energy of the impactor is transferred to a third star which is ejected from the system; and disk-assisted capture (Clarke & Pringle 1991), where the kinetic energy of the impactor is dissipated within the disk. Two-body tidal capture requires a high stellar number density for the frequency of such events to become significant (Bonnell 2001), and is thought to be most effective within globular clusters (Krolik 1983). The orbit of any binary formed through a two-body tidal capture will rapidly become circularised (Zahn 1977), and the separation of the binary system will typically be on the order of a few stellar radii, thus providing an observational signature for this formation scenario. For the most massive stars, two-body tidal capture may be responsible for a portion of the close binaries resolved, due to the enhanced stellar number density within the dense core of the star forming region (Bonnell et al. 1998). Simulations of dynamical interactions between three stars have also been shown to produce binary systems (Agekyan et al. 1969; Aarseth & Heggie 1976). Within the three-body scenario, the excess kinetic energy

Image Copyrighted
Figure can be found in
Kouwenhoven et al. 2010
(Figure 3, p 1838)

Figure 1.4: The velocity distribution of a $N = 1000$ stellar cluster simulated using an N-body code (Kouwenhoven et al. 2010). The encircled pair of cluster members represents a possible wide binary system in the process of being ejected from the cluster.

of the new companion is removed from the system through the ejection of a third star (Bonnell 2001). The ejection of this excess energy allows for the formation of wider systems than is possible with two-body tidal capture, with the lowest mass object of the three-body encounter being preferentially ejected (Valtonen 1988).

As with two and three-body capture scenarios, disk-assisted capture requires a significant stellar number density to efficiently produce binary systems (Bonnell 2001). Although the capture cross section within this scenario is significantly larger, the size of the disk as opposed to the star, the rates of star-disk interaction within simulations of representative stellar clusters are very small, on the order of 0.1 events per 10^6 years for Solar-mass stars (Clarke & Pringle 1991). Simulations have shown a mass dependence on the disk-assisted capture rate (Moeckel & Bally 2007), and are consistent with the high multiplicity fraction observed for the high-mass members of the Orion Nebula Cluster. The significant disruption of the disk caused by the impactor may prevent the remnant disk from fragmenting due to the strong tidal heating induced by the companion, and prevent the subsequent formation of low-mass companions within the disk (see §1.1.2; Lodato et al. 2007).

1.1.4 Simultaneous ejection

The observed binary population (e.g. Fischer & Marcy 1992; Raghavan et al. 2010) is the likely result of an initial binary population processed in a number of different dynamical environments (Goodwin 2010). This processing acts to preferentially reduce the frequency of wide,

less-bound binary companions (Heggie 1975; Hills 1975). However, a number of extremely wide binaries are known with separations $\gg 10^3$ AU (e.g. Chaname & Gould 2004; Makarov et al. 2008), comparable to the size of known star forming cores (Ward-Thompson et al. 2007). The formation, outside of the nascent environment, of wide binary systems by dynamical interactions is thought to be rare. This is thought to be primarily due to the very low stellar density in the field (Goodman & Hut 1993). An alternative mechanism for the formation of these wide systems is the simultaneous ejection of two cluster members during the cluster dissolution phase (Figure 1.4; Kouwenhoven et al. 2010). In this formation scenario, two stars with sufficiently small separations and velocity differences may become gravitationally bound as the cluster dissolves (Moeckel & Bate 2010), due to the decreasing gravitational influence of the other cluster members. This newly formed binary will be very susceptible to future dynamical interaction, either within the cluster or in the field (Kouwenhoven et al. 2010), and as such likely formed at the extremities of the cluster (Moeckel & Bate 2010).

1.1.5 Fission

The fission of a rapidly rotating protostar is one of the earliest theories of binary star formation (Jeans 1919). The rapid rotation of the protostar, spun up due to both the conservation of angular momentum of the infalling material and the contraction of the protostar, will cause it to become unstable to non-axisymmetric perturbations (Bonnell 2001), and become deformed into an oblate spheroid. It was theorised that this object would, due to the increasing intensity of the perturbation, become split into two distinct objects of roughly equal mass (Roxburgh 1966). This formation mechanism would preferentially produce equal-mass binaries at very close separations (Bonnell 2001). Subsequent hydrodynamical simulations of this formation process have shown that fission does not occur for compressible fluids such as stars (Durisen et al. 1986). Instead, the protostar, significantly deformed due to rapid rotation, would develop spiral arms, which would efficiently transport away angular momentum (Bonnell 1994a). The protostar would therefore become stable, and would form a protostellar disk containing a small fraction of the initial mass of the protostar (Figure 1.5; Bonnell 1994a). Although not viewed as a probable formation scenario (e.g. Bonnell 2001), work is still being undertaken exploring the stability of the bar-like structures which form as the result of a rapidly rotating protostar (e.g. Cazes & Tohline 2000; Tohline & Durisen 2001).

1.2 Multiplicity and A-type stars

With temperatures ranging from 7,500K to 10,000K (Habets & Heintze 1981), A-type stars are among the most massive and luminous spectral classes of stars with a non-negligible frequency within the solar neighbourhood. These early-type stars account for many of the stars visible at night with the naked eye, and as such have played a prominent role in the history of astronomy. Two such A-type stars have provided a significant number of firsts in the study of binary stars, ζ Ursae Majoris (Mizar and Alcor). The wide binary of Mizar and Alcor, physically separated by approximately 0.36 pc (Mamajek et al. 2010), has been known since antiquity. Mizar, the

Image Copyrighted
Figure can be found in Bonnell 1994a
(Figure 3, p 841)

Figure 1.5: A smoothed particle hydrodynamical simulation of a rapidly rotating protostar (Bonnell 1994a). The rapid rotation leads to the formation of a protostellar disk, allowing a dissipation of angular momentum, and preventing the fission of the protostar into two objects. The panels, each ~ 117 AU across, are at times of $1.34246t_{\text{ff}}$, $1.42765t_{\text{ff}}$, $1.47347t_{\text{ff}}$, $1.50543t_{\text{ff}}$, $1.52804t_{\text{ff}}$, $1.54843t_{\text{ff}}$, $1.57281t_{\text{ff}}$, $1.64444t_{\text{ff}}$, where $t_{\text{ff}} = 1.2622 \times 10^{11}$ seconds (4×10^3 years).

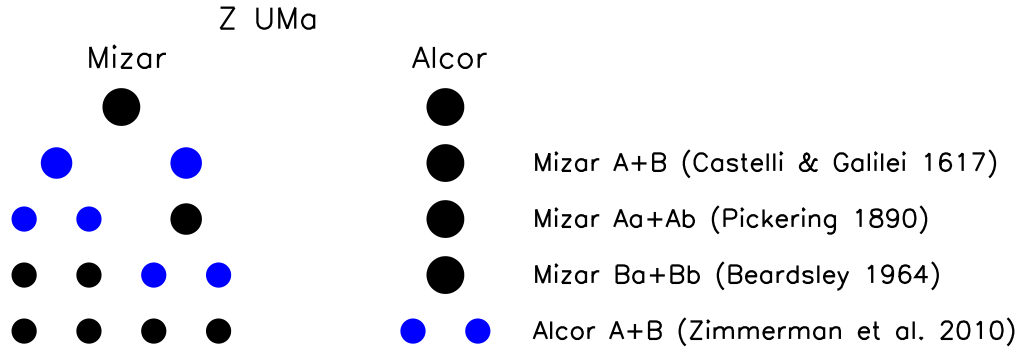


Figure 1.6: The evolution of the membership of the ζ Ursae Majoris system. Known as a binary since antiquity (Mizar and Alcor), Mizar was the first star to be resolved into a binary using a telescope (Castelli & Galilei 1617). Mizar A and B were both subsequently resolved into spectroscopic binaries (Pickering 1890; Beardsley 1964). Recently, a low-mass companion to Alcor was resolved using adaptive optics (Zimmerman et al. 2010).

brighter of the two stars, was itself resolved as a binary system by Benedetto Castelli and Galileo Galilei in 1617, the first binary to be resolved telescopically. Mizar also produced the first binary resolved through an analysis of the spectrum of a star (Pickering 1890), Mizar A, which was subsequently imaged with an optical interferometer (Hummel et al. 1998). More recently, the fainter companion Alcor was itself resolved into a binary using adaptive optics imaging, and was the first to be confirmed as gravitationally bound through an analysis of the parallactic motion of both components (Zimmerman et al. 2010). Presently, the ζ Ursae Majoris system is known to contain at least six stellar components, ranging from spectral type A through M (Figure 1.6). While this system provides an interesting insight into the history of binary star research, and demonstrates the variety of techniques used to resolve binary stars, it does not answer fundamental questions regarding the frequency of A-type stars within multiple systems.

Comprehensive work has been done characterising the multiplicity, and various binary statistics, of Solar-type stars (e.g. Abt & Levy 1976; Duquennoy & Mayor 1991; Raghavan et al. 2010), and the more abundant, lower-mass M-dwarfs (e.g. Fischer & Marcy 1992; Bergfors et al. 2010). Sensitivity to companions over the full range of separations, from 10^{-2} to 10^4 AU, was achieved through the combination of various detection techniques, with spectroscopy providing sensitivity to close companions $a \lesssim 10^2$ AU, and with imaging techniques sensitive to wider companions $a \gtrsim 10^2$ AU. While successful at detecting companions to Solar-type and lower-mass stars, these techniques struggle when used to resolve companions to brighter, more active A-type stars.

The intrinsic brightness of A-type stars (e.g. Figure 2.1) causes a significant increase in the contrast ratio between the star and any resolved companion, with a maximum contrast of 10^4 between an A0 primary and an M9 companion, an order of magnitude higher than for Solar-type stars Siess et al. (2000). Early direct imaging and high-resolution instrumentation were not able to achieve these high contrast levels, and as such a survey of A-type stars, fully

Images Copyrighted
Left figure can be found at:
[http://keckobservatory.org/news/
nsf_awards_1.72_million_to_improve_keck_LGSAO](http://keckobservatory.org/news/nsf_awards_1.72_million_to_improve_keck_LGSAO)
Right figure can be found at:
<http://www.eso.org/public/news/eso0842/>

Figure 1.7: (*left panel*): Three of the four known extrasolar planets orbiting the A-type star HR 8799 (Marois et al. 2008, 2010). The flux from the central star has been removed through image processing (Lafrenière et al. 2007b), revealing three gravitationally bound planetary-mass objects. Image credit: C. Marois, NRC, and B. Macintosh, LLNL. (*right panel*): The extrasolar planet (inset) and circumstellar disk imaged around the A-type star β Pic (Lagrange et al. 2009). Image credit: ESO.

sensitive to all stellar companions, was not possible. The rapid rotation of A-type stars also reduces the sensitivity of spectroscopic companion searches, due to the rotationally broadened spectral lines within the stellar spectrum. Although notable examples of spectroscopic A-type stars exist (e.g. Mizar, Castor), these systems are typically equal mass, which produce the greatest variation in the radial velocity of the primary. The detection of lower-mass companions becomes increasingly challenging as the amplitude of the radial velocity variations decreases. Metallic-line A-type stars are an exception to this, their spectra consist of spectral features of light-absorbing elements which are pushed towards the surface (Sargent 1964). This effect only takes place if the star has a low rotational velocity, typically caused by tidal breaking of a close binary companion (Abt & Levy 1985). As such, the multiplicity of these stars has been extensively studied with spectroscopy (e.g. Abt & Levy 1985; Debernardi et al. 2000; Carquillat et al. 2003).

Development in the field of adaptive optics instrumentation and imaging sensors, has advanced sufficiently such that the detection and characterisation of extrasolar planets is now possible around bright A-type stars (e.g. Kalas et al. 2008; Lafrenière et al. 2010). The recent detection of extrasolar planets orbiting three A-type stars; β Pic (Figure 1.7, right panel; Lagrange et al. 2009), Fomalhaut (Kalas et al. 2008), and HR 8799 (Figure 1.7, left panel; Marois et al. 2008), and the observed trend of increasing planet frequency as a function of primary mass (Johnson et al. 2007), raise important questions regarding the influence a binary companion may have on the formation and stability of planetary systems and circumstellar disks. By utilising high-resolution adaptive optics observations, the multiplicity of A-type stars can be determined within a separation range crucial to the formation of planets, in addition to

providing constraints on the various binary formation theories described in §1.1.

1.3 Adaptive optics

Adaptive optics is a technique designed to overcome the limits on ground-based observing imposed by the Earth's atmosphere, a technique essential for the detection of faint stellar companions and exoplanets at close angular separations ($\rho \leq 15''$). The fundamental limit to the minimum resolvable angular separation of any telescope is defined by its diffraction limit. Caused by the interference due to the passage of an incident plane wave through a circular aperture, the diffraction limit is defined as

$$\frac{\lambda}{D_{\text{tel}}} \quad (1.1)$$

where D_{tel} is the diameter of the telescope's aperture and λ is the wavelength of observation. As D_{tel} increases the light collection sensitivity scales as D_{tel}^2 , while the angular resolution scales as $1/D_{\text{tel}}$. For larger telescopes the angular resolution is limited further by atmospheric turbulence, which causes distortions on the incoming wavefront as it passes through the atmosphere. Typically, turbulence becomes a limiting factor when the aperture size becomes larger than r_0 , a value known as the turbulence coherence length. Adaptive optics provides a solution to this problem by attempting to correct in real time the effect atmospheric turbulence has upon the incoming wavefront, increasing the angular resolution to the diffraction limit.

1.3.1 Atmospheric turbulence

The Earth's atmosphere provides significant problems for ground-based observations. Firstly, the atmosphere is only transparent at certain wavelengths and while a large window exists between 0.3 and 1 μm covering UV, visible and near-IR bands, the atmosphere is opaque to the vast majority of wavelengths. Absorption by certain molecules within the atmosphere restrict the transparency between 1 and 10 μm , leaving only certain bands such as the J-band at 1.25 μm and the H-band at 1.6 μm . Wavelengths below 0.3 and above 30 μm are also unable to pass through the atmosphere, although the atmosphere does become transparent to radio waves above ~ 1 mm (Hardy 1998). Secondly, the atmosphere itself is luminous, either by scattered light from the Sun and Moon or by airglow via excitation processes occurring in the upper atmosphere. The atmosphere will therefore never be totally dark, and this background radiation will set a fundamental limit to the detection of faint objects.

Caused by thermal heating from the Sun, turbulence is present in all layers of the atmosphere, tending to be greater in intensity closer to sea-level. Atmospheric heating causes localised variations of the refractive index of the air, the magnitude of which is dependent on both the density of air and the scale of the temperature variations. Within the atmospheric model proposed by Tatarski (1961), based upon work on turbulence by Kolmogorov (1941), atmospheric turbulence can be subdivided into distinct turbulent cells, each of which has a different value of the refractive index, causing a phase distortion of the incoming wavefront. These cells

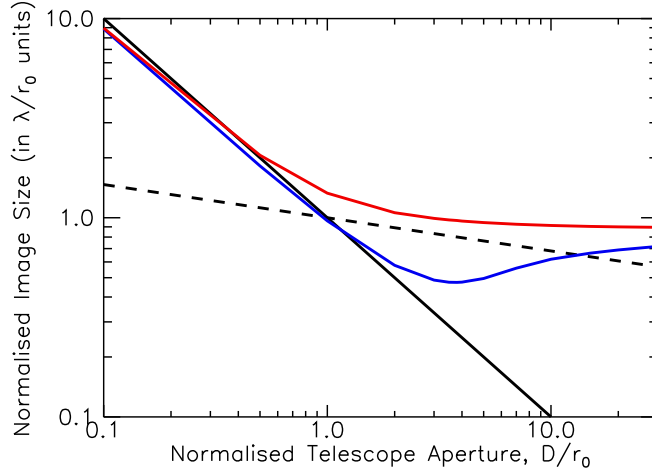


Figure 1.8: Plot showing how the angular size of an image varies for long ($> \tau_0$) and short exposures (red and blue lines respectively). These are plotted alongside the fundamental diffraction limit of the aperture which is $\propto \lambda/D_{\text{tel}}$, and the limiting factor of image motion, $\propto D_{\text{tel}}^{-1/6}$, (solid and dashed lines respectively) (Fried 1966).

are defined by a characteristic turbulence coherence length r_0 which defines the length over which the phase adjustment to the wavefront is identical. It is also possible to define both a turbulence time constant τ_0 , the time scale over which the turbulent cells can be considered fixed, and an isoplanatic angle θ_0 which defines the angle over which wavefront phase distortions are correlated (Hardy 1998). As shown by Equation 1.2 these three characteristic parameters are all dependent on the wavelength of the incoming wavefront (Fried 1966; Beckers 1993), with the temporal coherence also dependent on \bar{V} , the wind velocity averaged over the altitude, and the isoplanatic angle dependent on \bar{h} , the characteristic average turbulence altitude.

$$\begin{aligned}
 r_0 &\propto \lambda^{6/5} \\
 \tau_0 &\propto \frac{r_0}{\bar{V}} \propto \frac{\lambda^{6/5}}{\bar{V}} \\
 \theta_0 &\propto \frac{r_0}{\bar{h}} \propto \frac{\lambda^{6/5}}{\bar{h}}
 \end{aligned} \tag{1.2}$$

As an example, the atmosphere above the Keck observatory in Hawaii typically has a coherence length of 0.2 m at a wavelength of $0.5\mu\text{m}$ (Chanan et al. 2000) corresponding to a minimum angular resolution of 0.5 arcseconds. This value is significantly poorer than the diffraction limit, which fundamentally limits the angular resolution to 0.01 arcseconds at the same wavelength.

Figure 1.8 shows the three distinct regimes where atmospheric turbulence has a differing effect upon the angular resolution of the images obtainable by a telescope. Within the first regime, where $D_{\text{tel}}/r_0 < 1$, the image size is only limited by the intrinsic diffraction limit of the telescope, with turbulence only causing a displacement of the peak of the image. The timing of the exposure becomes important within the second regime where $1 < D_{\text{tel}}/r_0 < 10$; for exposures greater than τ_0 the image becomes a blurred disc with angular resolution limited by

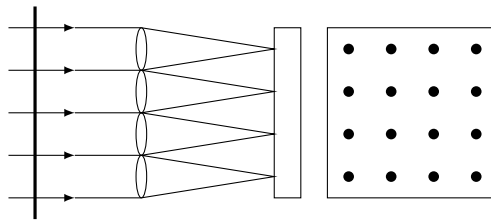


Figure 1.9: A perfect plane wave incident upon the lenslet array of an Shack-Hartmann wavefront sensor producing a periodic repetition of the object image on the detector.

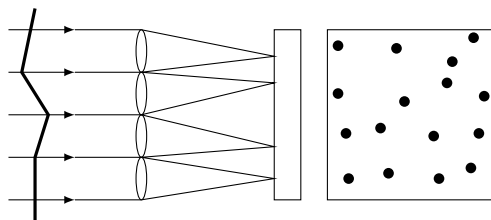


Figure 1.10: A wavefront which has been distorted through atmospheric turbulence incident upon the lenslet array of an Shack-Hartmann wavefront sensor producing a non-periodic repetition of the object image on the detector.

λ/r_0 , while for shorter exposures an image consisting of a large number of speckles, the size of which is limited by λ/D_{tel} , extended over a size limited by λ/r_0 . In the final regime, where $D_{\text{tel}}/r_0 > 10$, the angular size of both short and long exposure images become asymptotic to λ/r_0 .

1.3.2 Wavefront detection

The variations of a wavefront caused by its passage through the turbulent atmosphere must first be measured before a correction can be applied. The Shack-Hartmann wavefront sensor, the most prevalent in AO systems, takes the incoming wavefront at the entrance pupil of the telescope and passes it through an array of identical lenslets (Hardy 1998). This forms an array of images of the target onto a detector array that is placed in the focal plane of the lenslet array. For a perfect wavefront passing through the lenslet array a periodic pattern of images corresponding to the geometry of the array will be produced on the detector as shown in Figure 1.9. If a distorted wavefront is passed through the lenslet array, an irregular pattern will be recorded, as shown in Figure 1.10. The displacement from the expected location (shown in Fig 1.11) of these spots is directly proportional to the average wave-front slope within the xy plane over each individual lenslet. The incident planar wavefront can then be reconstructed from this array of measured slopes with the use of a deformable mirror.

An alternative to measuring the spatial displacement of the images within the focal plane is to instead measure the relative intensity either side of the focal plane using a wavefront curvature sensor (Roddi 1988). Detecting defocused images at displacements of $\pm z$ along the axis of the beam and comparing their relative intensities allows for a determination of the curvature of the incoming wavefront. Figure 1.12 depicts a simplified wavefront curvature sensor,

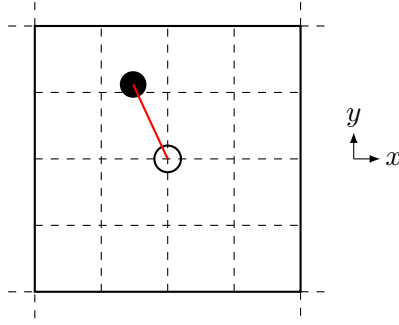


Figure 1.11: The i^{th} element of the CCD detector at the focal position of the i^{th} lenslet. The deviation of the image from its expected location is indicated by the red line. The values of the displacement can be used to correct the wavefront with a deformable mirror.

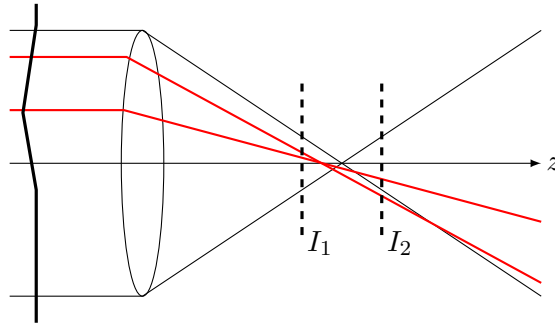


Figure 1.12: A wavefront curvature sensor depicting how the intensities per unit area at the two detection planes would vary when a distorted wavefront is incident. In this situation $I_1 \neq I_2$. A typical sensor will consist of an array of such lenses and detectors, similar to the Shack-Hartmann design.

an ideal plane wavefront would focus in the midpoint between the two detectors, producing equal intensities on either side of the focal plane. Any deviation in the wavefront will manifest itself as a displacement of the focus location along the beam plane detected by the relative difference in intensities per unit area between I_1 and I_2 .

To achieve the best possible reconstruction of the original wavefront in the Shack-Hartmann setup, the number of lenslets should be equal to the number of turbulent cells through which the light has travelled, $n_{\text{lenslet}} = (D_{\text{tel}}/r_0)^2$. It follows that the intensity of the light through each lenslet will scale as I_0/n_{lenslet} . The error on the measurement of the slope of the wavefront is $\propto n^{-1/2}$, where n represents the number of photons incident on the detector. If the number of lenslets is doubled, the number of photons incident on each portion of the detector will be halved, and the error will increase by a factor of $\sqrt{2}$, similarly the error will also increase when attempting to observe a fainter object. Given that the accuracy of the corrections is directly related to the number of lenslets, a trade-off between this and the magnitude limit of the AO system must be made; observations of very distant galaxies would not be possible on a large n_{lenslet} AO system without utilising a guide star located within the isoplanatic angle of the target galaxy. If no guide star is present it is possible to use a laser mounted upon the telescope to excite atoms to emit photons within a specific layer of the atmosphere, providing

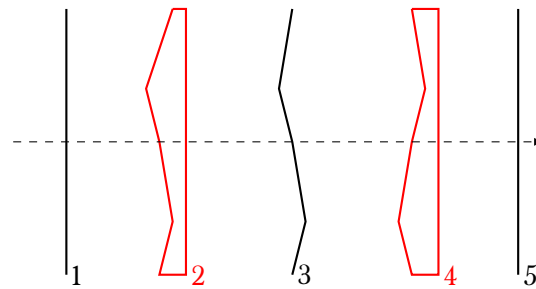


Figure 1.13: The propagation of an initially planar wavefront (1), through atmospheric turbulence which introduces optical path length errors (2), producing a distorted wavefront (3). Corrections to the path length are detected using the wavefront sensor and are introduced by the wavefront corrector at (4) resulting in an approximation to the original planar wave (5).

a bright enough source for the wavefront detector to perform the necessary corrections (Fugate et al. 1991).

1.3.3 Wavefront correction

The principle of wavefront correction is inverting the effect of the atmospheric turbulence by passing the distorted wavefront through an optical device which introduces a path length correction that is opposite and equal to the path length error introduced by the atmosphere, as shown schematically in Figure 1.13. Early wavefront correctors consisted of an optically dynamic lens whose refractive index can be locally adjusted through an applied voltage. Such correctors had a limited range and required a substantial voltage for operation, limitations which led to the developments of reflective correctors (Hardy 1998). Currently, three principal types of reflective correctors exist, the segmented, deformable and bimorph mirror, with the deformable mirror being preferred in the current generation of adaptive optics instrumentation (e.g. Dohlen 2006; Macintosh 2006).

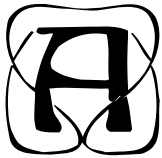
Deformable mirrors are constructed from a thin faceplate which can be deformed by a periodic arrangement of piezoelectric actuators that can displace the mirror either outwards or inwards (Beckers 1993). The amplitude of the maximum possible stroke on a deformable mirror is limited by the stress such an action has upon the faceplate, with values of the order of $1 \mu\text{m}$ (Hardy 1998). The number of actuators determines the number of wavefront inflections that the mirror can correct. Typically, the separation between these actuators is of the order of 1 mm (Hardy 1998). The continuous nature of the deformable mirror, and the greater degrees of freedom offered by the actuators in this design, allow for the creation of smooth wavefront corrections.

Irrespective of the mirror design, the dynamical nature of atmospheric turbulence requires continuous, real-time correction to the wavefronts at a frequency greater than $1/\tau_0$, with modern AO instruments achieving a cadence of 1 kHz (e.g. Macintosh 2006). Similarly, corrections must be on a spatial scale equal to or less than the projection onto the deformable mirror of the turbulence coherence length r_0 . Given the wavelength dependence of these values, wavefront measurement and correction is typically performed in a lower wavelength band than the

Image Copyrighted
Figure can be found at:
<http://www.astro.caltech.edu/palomar/AO/>

Figure 1.14: (*left panel*): A seeing-limited image of the binary star IW Tau, observed with the Hale Telescope at the Palomar Observatory. The binary star is not resolved in this observation, due to the turbulence within the atmosphere. The separation of the system, $0''.3$, is larger than the diffraction limit of the telescope, $0''.089$. (*right panel*): With the adaptive optics instrument activated, the binary star can be clearly resolved into two components. The wavefront correction has sharpened the image such that the central intensity is significantly higher than in the previous image, with the resolution of the image approaching the diffraction limit of the telescope. Image credit: Caltech.

scientific measurements. The incident light is split using a dichroic, with visible light directed towards the lenslet array of the wavefront sensor, and the near-infrared light directed towards the science camera. An example of the improvement to the image quality achievable with an adaptive optics instrument is shown in Figure 1.14.



large, unbiased sample of A-type stars was drawn from the *Hipparcos* catalogue (ESA 1997; van Leeuwen 2007), chosen due to the high quality parallax and visual photometry measurements. The sample was initially limited to targets within 75pc (parsecs), corresponding to an *Hipparcos* parallax of $\pi \geq 13.3$ mas (van Leeuwen 2007). Targets with significant parallax uncertainties ($\sigma_\pi/\pi > 6\%$) were removed to ensure accurate estimations of both the distance to the primary, and the absolute magnitude of any resolved companion candidates. A further restriction was applied to limit the sample to targets within the A-type star range, achieved by selecting those stars with a colour index between $0.0 \leq B_T - V_T \leq 0.33$ (Gray 1992). The individual B_T and V_T magnitudes for each target, and corresponding uncertainties, were obtained from the *Tycho2* catalogue (Høg et al. 2000). For systems where multiple binary components were resolved within the *Tycho2* catalogue, e.g. HIP 20995, the component with the brightest V_T magnitude is identified as the primary, and used for the sample selection process. Finally, a magnitude cut-off ($M_V < 4$) was used to remove contamination from faint white dwarfs which have a colour consistent with A-type stars. A total of 660 targets within the *Hipparcos* catalogue satisfy the stated criteria, and the complete sample is plotted on a colour-magnitude diagram in Figure 2.1.

2.1 Sample completeness

High angular resolution adaptive optics observations were obtained for a total of 371 members of the VAST sample, as described in Chapter 4, out of an original sample of 660. In order to ensure the multiplicity statistics derived from the observations obtained as a part of the VAST survey, a more complete subsample of the original sample was selected to remove the effect of any completeness biases. The completeness of the sample was explored for targets above a declination of $\delta = -30^\circ$, as a function of both the distance cut-off, and the lower $B_T - V_T$ cut-off (at the red end). The remaining sample selection criteria ($B_T - V_T \geq 0.0$, $M_V < 4$, and $\sigma_\pi/\pi \leq 6\%$) were held constant. The corresponding completeness contour is shown in

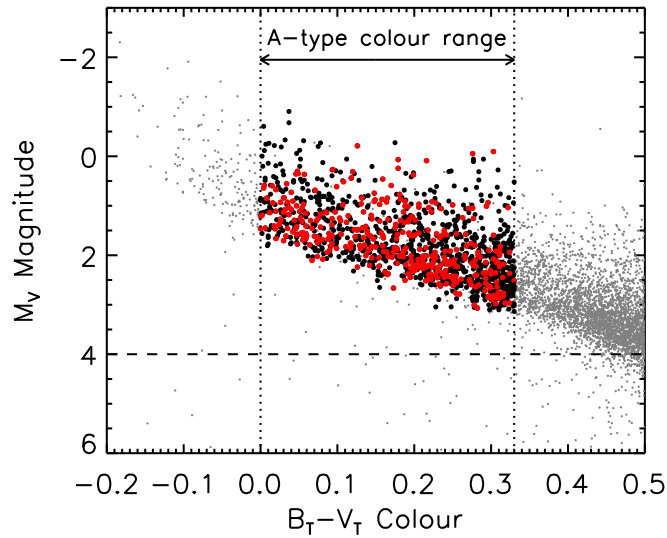


Figure 2.1: A colour-magnitude diagram of the 660 members of the VAST sample, distinguished between those stars with high-resolution adaptive optics observations (red filled circles - 371), and those without (black filled circles - 289). Over-plotted for reference are all *Hipparcos* stars within 75 parsecs (grey points). The $B_T - V_T$ colour criterion is denoted by the vertical dashed lines, and the $M_V = 4$ magnitude cut-off is denoted by the horizontal dashed line.

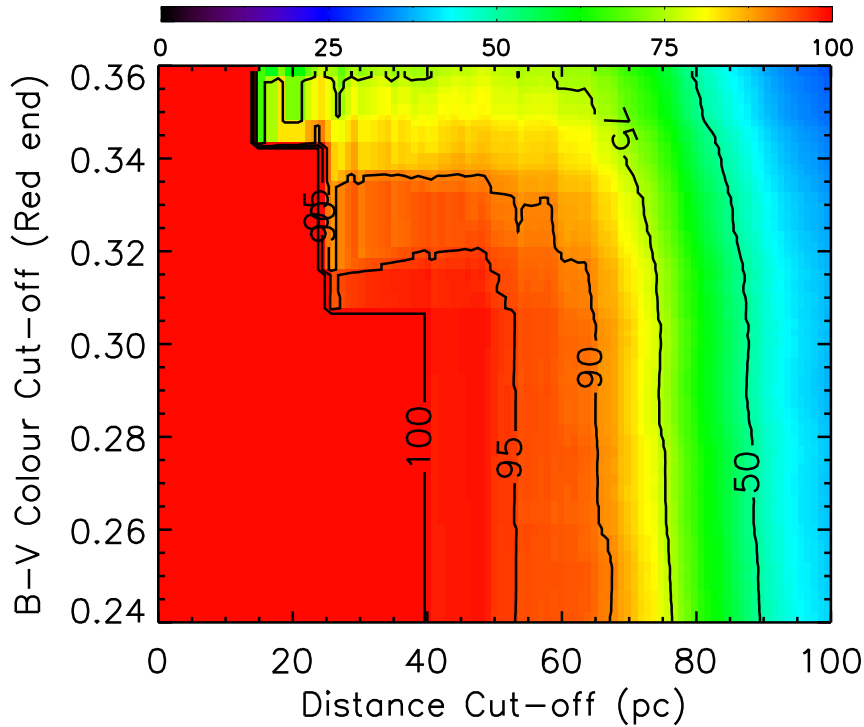


Figure 2.2: The completeness of the survey, in terms of targets with a declination of $\delta \geq -30^\circ$, as a function of both the upper distance limit, and the $B_T - V_T$ colour cut-off at the red end. The contour levels of 100%, 95%, 90%, 75%, and 50% are over-plotted for clarity.

Table 2.1: Metallicity subsamples

N Stars	Metallicity Range		Isochrone Metallicity	
			[Fe/H]	Z
32	[Fe/H] < -0.124	$Z < 0.015$	-0.300	0.01
25 (+139)	$-0.124 \leq$ [Fe/H] < 0.098	$0.015 \leq Z < 0.025$	0.001	0.02
21	$0.098 \leq$ [Fe/H] < 0.244	$0.025 \leq Z < 0.035$	0.177	0.03
18	$0.244 \leq$ [Fe/H]	$0.035 \leq Z$	0.302	0.04

Figure 2.2. The sample was further restricted to only include those targets with a declination of $\delta \geq -30^\circ$, a distance of $D < 60$ pc, and a colour cut-off of $B_T - V_T \leq 0.30$, leading to a final sample of 233 targets, of which 216 have been observed - a 93% completeness level. Each of the final sample members are listed in the table at the end of this chapter, alongside their parallax, $B_T - V_T$ colour index, and *2MASS* JHK_S magnitudes.

2.2 Sample properties

2.2.1 Distance and absolute photometry estimates

The distance to each target in parsecs D , distance modulus μ , and absolute magnitude M , were estimated from the target parallax in milliarcseconds π , and apparent magnitude m , using

$$\begin{aligned}
 D &= \frac{1000}{\pi} \\
 \mu &= 5 [\log(D) - 1] \\
 M &= m - \mu
 \end{aligned} \tag{2.1}$$

with the corresponding uncertainties on each value estimated as

$$\begin{aligned}
 \sigma_D &= 1000 \frac{\sigma_\pi}{\pi^2} \\
 \sigma_\mu &= \frac{\sigma_D}{D} 5 \ln(10) \\
 \sigma_M &= \sqrt{m^2 \sigma_m^2 + \mu^2 \sigma_\mu^2}
 \end{aligned} \tag{2.2}$$

2.2.2 Metallicity estimates

Prior to using theoretical isochrones to estimate the age and mass of the sample members (Section 2.2.3), an estimate of the metallicity of each star must be determined. An incorrect assumption of the metallicity of a target has a significant effect on the information drawn from the position of the target on a colour-magnitude diagram. For example, a Solar-metallicity star with an incorrectly estimated sub-solar metallicity, will appear significantly older when the position on the colour-magnitude diagram is compared with theoretical sub-solar isochrones. Metallicity measurements for 96 targets within the sample were obtained from a combination of the *PASTEL* catalogue (Soubiran et al. 2010), the *XHIP* compilation (Anderson & Francis 2011),

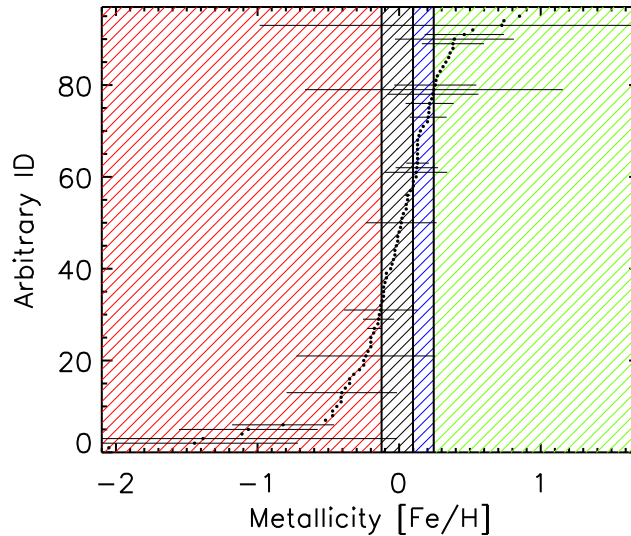


Figure 2.3: Metallicity estimates for 96 of the targets within the VAST sample, obtained from the *PASTEL* catalogue (Soubiran et al. 2010) and the *XHIP* compilation (Anderson & Francis 2011). Shading indicates the metallicity of the isochrone used to estimate the age and mass of each sample member using the Siess et al. (2000) models. For targets with multiple metallicity estimates, the average of the estimates is used as the metallicity value, and the range of the estimates is denoted by the a horizontal error bar.

and metallicity estimates for known moving group and stellar cluster members (AB Doradus - Ortega et al. 2007, Hyades - Paulson et al. 2003, Tucana-Horologium - Makarov 2007, UMa - Boesgaard & Friel 1990). A cumulative distribution of the metallicity estimate for each target within the sample is shown in Figure 2.3, demonstrating how the complete sample will be divided into four subsamples based on the metallicity of the Siess et al. (2000) models (Table 2.1. The age and mass of each subsample member will then be estimated based on a comparison to the theoretical isochrone corresponding to the subsample metallicity. For those targets with no metallicity measurement presented within the literature, a solar value of $[\text{Fe}/\text{H}] = 0$ is assigned, consistent with the average metallicity of the sample of $\langle [\text{Fe}/\text{H}] \rangle = -0.04$, with a standard deviation of 0.46. A colour-magnitude diagram of the four metallicity subsamples is presented in Figure 2.4, alongside theoretical isochrones from the Siess et al. (2000) evolutionary models.

2.2.3 Age and mass estimates

Multiplicity surveys of lower-mass Solar-type primaries (e.g. Raghavan et al. 2010) typically study nearby targets at ages of several billion years. These targets are at an age sufficient such that the primary, and any resolved secondary, has fully contracted onto the Main Sequence, thus ensuring the mass estimate of each component is completely degenerate with respect to the age of the system. The intrinsic youthfulness of A-type stars, having typical lifespans of ~ 1 Gyr, introduces an additional complication when estimating the mass of any resolved companion within this study. Considering an M-dwarf companion to an A-type star with a

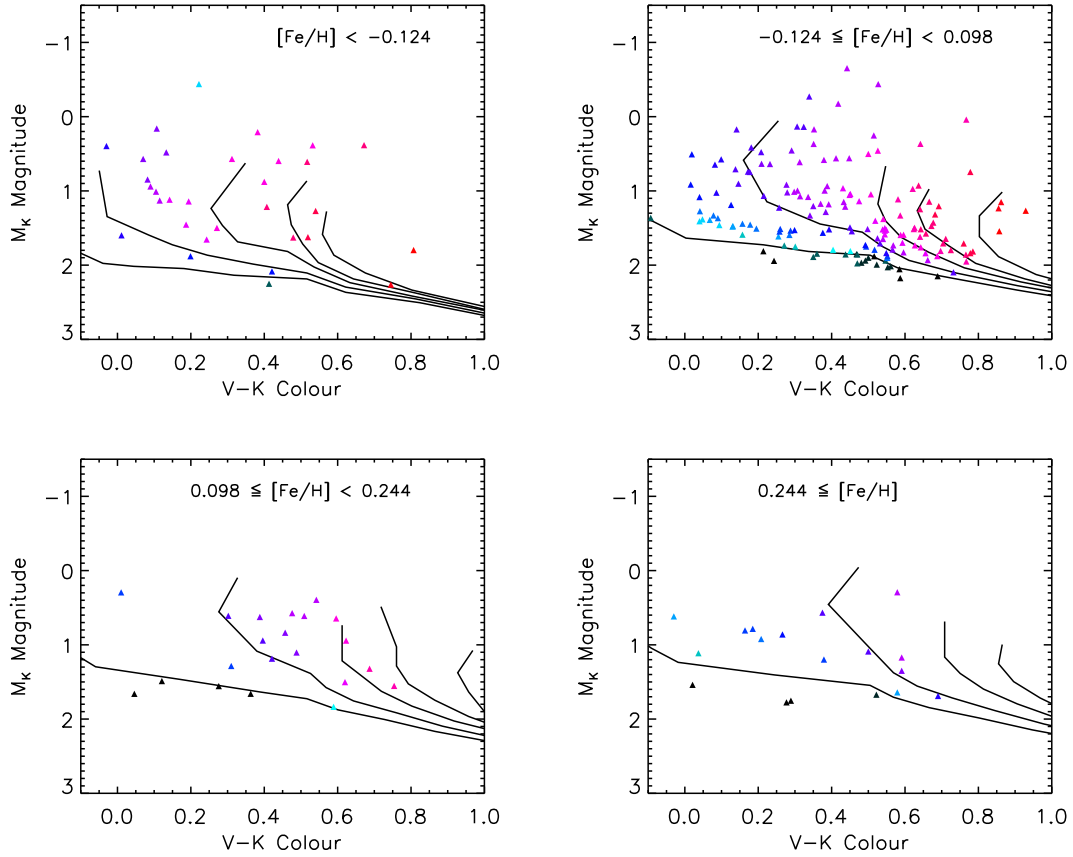


Figure 2.4: The age and mass of each member of the VAST sample were estimated based on the position of the star on a colour-magnitude diagram relative to theoretical isochrones of 100, 400, 630, 800 and 1000 Myrs (Siess et al. 2000). The sample is divided into four subsamples, based on estimates of their metallicity (see Section 2.2.2).

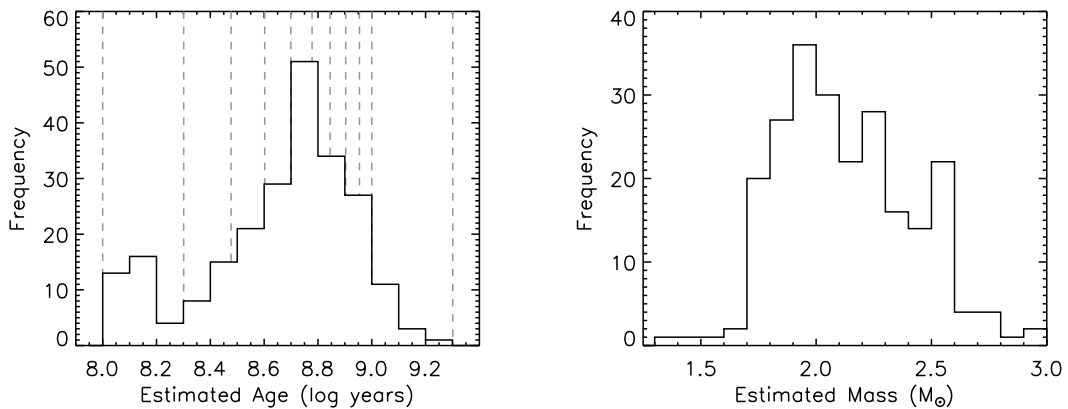


Figure 2.5: (*left panel*): An age distribution histogram of the VAST sample, estimated using the Siess et al. (2000) isochrones. Over-plotted for reference as dashed grey lines are the ages 100 Myr to 1100 Myr in 100 Myr steps. (*right panel*): A mass distribution histogram of the VAST sample, estimated using the Siess et al. (2000) isochrones.

measured magnitude difference of $\Delta K \sim 6$, the companion mass estimate will increase by a factor of two as the age estimate of the system is increased from 10 to 100 Myrs, demonstrating the need for a consistent age estimation technique for each target within the sample.

The rapid evolution of A-type stars away from the Main Sequence allows for an estimation of the age and mass of each target within the VAST sample based on a comparison with theoretical isochrones on the colour-magnitude diagram. Using the *Tycho* V_T and *2MASS* K_S magnitudes, each target was placed on an M_K vs. $V - K$ colour-magnitude diagram. The $V - K$ colour index was chosen due to the large wavelength difference between the photometric bands, increasing the overall sensitivity of the age estimation of each target. The overall distribution of age and mass estimates for the overall sample is shown in Figure 2.5, while the estimates for each individual target are given in the sample table at the end of this chapter.

The ages estimated based on this procedure are subject to significant biases, causing an over-estimate of the age based on the position on the colour-magnitude diagram relative to theoretical models. The rapid rotation of A-type stars causes a gradient in the surface gravity as a function of stellar latitude, with the poles having a significantly lower surface gravity. The surface brightness and local effective temperature are therefore lower at the equator than at the poles, such that a rapidly rotating star will appear cooler than a non-rotating star of the same mass (Song et al. 2001). The inclination angle of the star with respect to the observer has a significant effect on the apparent luminosity change, with a rapidly rotating pole-on star appearing brighter, and an edge-on star appearing dimmer, than a non-rotating star of the same mass (Kraft 1970). This effect is most pronounced for B- and A-type stars with rapid rotation rates ($v \sin i \geq 100 \text{ km s}^{-1}$), causing the age determination to be over-estimated by approximately 40% (Figueras & Blasi 1998).

2.2.4 Spectral type distribution

The spectral type estimation of each sample member was obtained from the *SIMBAD* database, and the resulting distribution of spectral types of the sample members is plotted in Figure 2.6. The majority of the sample are Main Sequence dwarves; 178 have a luminosity subtype V or IV (76.4%), and 40 are of an undetermined luminosity type (17.2%). The remaining 15 targets are either giants (III - 6.0%), or supergiants (Ib/II - 0.4%). The distribution of spectral subtypes within the VAST sample is representative of the overall population of nearby A-type stars, with the paucity of A6, A8, and A9 spectral subtypes reflected in previous studies (e.g. Cowley et al. 1970).

2.2.5 Spatial distribution

The VAST sample is uniformly distributed throughout the celestial sphere, with the notable exception of the clustering of sample members within the Hyades open cluster at a Right Ascension of $4^{\text{h}}28^{\text{m}}$, and a distance of $\sim 45 \text{ pc}$ (Figure 2.7). The distribution of the sample, plotted only as a function of distance (Figure 2.8), leads to an average population density of A-type stars satisfying the sample selection criteria of $2.79 \times 10^{-4} \text{ stars pc}^{-3}$. This estimate is based on a logarithmic fit to the cumulative distribution of *Hipparcos* stars which satisfy the

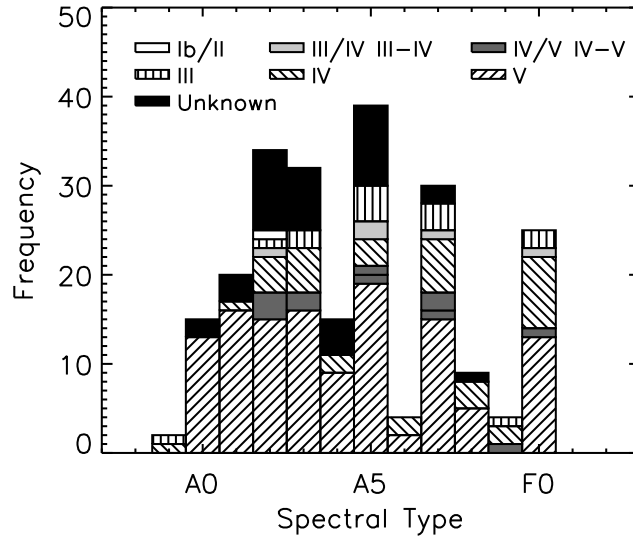


Figure 2.6: Spectral type distribution of the targets within the VAST sample, obtained from the *SIMBAD* database. Each spectral classification has been subdivided into the spectral subclass (A0, A1, etc.), and luminosity class (V, IV, etc.). Four targets with no estimate of either the spectral subclass, or luminosity, are not included within the distribution.

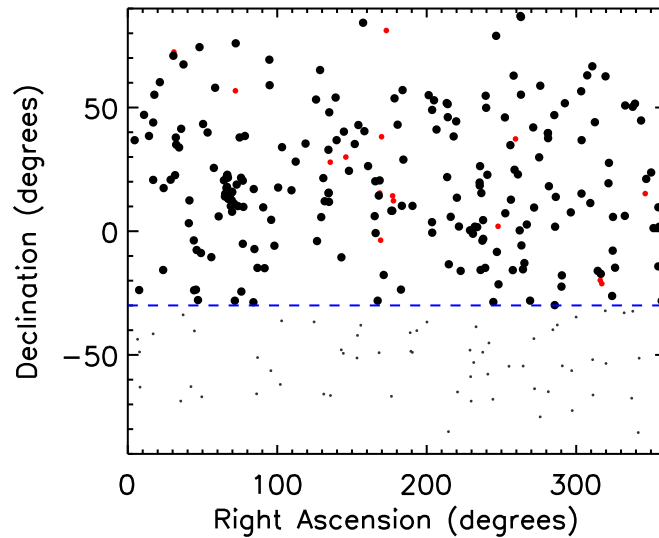


Figure 2.7: The VAST sample plotted as a function of right ascension and declination. Those targets with high angular resolution adaptive optics observations are plotted as black filled circles. The incompleteness of the sample is depicted by the red filled circles, representing the targets for which no high-resolution observations exist. The dashed blue line denotes the lower declination limit of the sample at $\delta \geq -30^\circ$, and the grey points below this limit line are stars which otherwise satisfy the sample selection criteria described previously.

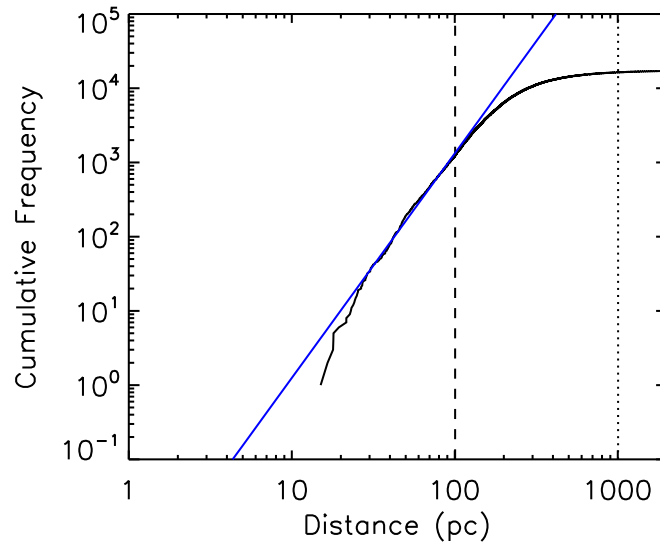


Figure 2.8: The cumulative frequency of *Hipparcos* stars which satisfy the selection criteria described previously, as a function of distance (black line). A logarithmic fit to the cumulative frequency up to a distance of 100 pc is over-plotted (blue line). The fit leads to an estimate of spatial density of A-type stars of 2.79×10^{-4} stars pc^{-3} . The dashed line indicates the completeness limit of the *Hipparcos* catalogue to the faintest A-type stars (spectral type A9). The dotted line indicates the distance at which the *Hipparcos* catalogue is magnitude limited to the faintest A-type stars.

sample selection criteria, to a distance of 100pc, at which the *Hipparcos* catalogue becomes incomplete to the faintest A-type stars (Figure 2.8).

Table 2.2: VAST sample table

HIP	Spectral Type	Parallax (mas)	$B_T - V_T$	J (mag)	H (mag)	K_S (mag)	Age $\log(t)$	Mass M_\odot
HIP1473	A2V	24.20±0.21	0.078±0.076	4.345±0.270	4.421±0.180	4.464±0.290	8.3	2.26
HIP2381	A3V	18.83±0.29	0.139±0.088	5.282±0.244	4.877±0.076	4.830±0.017	8.7	2.09
HIP3414	A5V	18.63±0.32	0.192±0.085	4.910±0.256	4.765±0.242	4.584±0.016	8.7	2.19
HIP4436	A5V	25.14±0.86	0.158±0.066	3.621±0.256	3.652±0.182	3.636±0.214	8.7	2.40
HIP5310	A3V	21.14±0.77	0.142±0.095	5.277±0.018	5.269±0.038	5.220±0.020	8.1	1.88
HIP5317	A3m	16.96±0.28	0.144±0.086	5.098±0.208	4.997±0.206	4.769±0.016	8.7	2.27
HIP5542	A7Vvar	24.42±0.24	0.193±0.075	4.449±0.296	4.277±0.252	4.128±0.396	8.6	2.24
HIP6686	A5Vv	32.81±0.14	0.179±0.046	2.336±0.256	2.367±0.186	2.245±0.282	8.7	2.50
HIP7345	A1V	16.84±0.28	0.074±0.094	5.487±0.020	5.528±0.020	5.458±0.020	8.2	2.09
HIP7447	F0IV	17.22±0.37	0.275±0.106	5.413±0.037	5.364±0.055	5.336±0.016	8.9	1.80
HIP8903	A5V...	55.60±0.58	0.176±0.046	2.340±0.232	2.351±0.164	2.270±0.242	8.7	2.15
HIP9480	A3IV	28.36±0.44	0.140±0.097	4.350±0.252	4.125±0.036	4.254±0.268	8.6	1.96
HIP9598	A2V	20.76±0.14	0.022±0.066	3.885±0.204	3.898±0.202	3.921±0.242	8.5	2.74
HIP9836	A2m	17.96±0.37	0.155±0.086	5.221±0.308	4.738±0.036	4.740±0.018	8.7	2.19
HIP9977	A5IV-V	17.04±0.27	0.131±0.082	4.619±0.240	4.571±0.226	4.425±0.017	8.7	2.36
HIP10064	A5III	25.71±0.34	0.179±0.052	2.738±0.318	2.768±0.252	2.678±0.346	8.6	2.70
HIP10670	A1Vnn	29.04±0.25	0.026±0.067	3.802±0.268	3.862±0.228	3.958±0.026	8.4	2.30
HIP11090	F0III-IV	21.27±0.31	0.293±0.100	5.200±0.037	5.126±0.018	5.069±0.026	8.9	1.69
HIP11569	A5p Sr	24.55±0.81	0.105±0.078	3.981±0.428	4.290±0.036	4.248±0.031	8.4	2.19
HIP12706	A3V	40.97±0.63	0.093±0.060	3.241±0.256	3.104±0.214	3.076±0.264	8.8	2.04
HIP12832	A7III-IV	27.52±0.40	0.239±0.089			4.562±0.029	8.8	1.73
HIP13717	A3Vn	17.49±0.25	0.093±0.090	5.019±0.030	4.980±0.044	4.858±0.017	8.7	2.17
HIP13782	A5IV/V	20.97±0.35	0.266±0.094	5.062±0.037	5.015±0.027	4.915±0.020	8.8	1.86
HIP14146	A4V	36.80±0.18	0.186±0.070	3.657±0.268	3.539±0.220	3.573±0.238	8.8	1.92
HIP14293	A8V	24.06±0.40	0.204±0.090	4.869±0.048	4.834±0.042	4.741±0.024	8.7	1.83
HIP14551	A3V	18.30±0.50	0.188±0.109	5.891±0.020	5.851±0.053	5.772±0.018	8.5	1.45
HIP14862	A2Vnn	19.72±0.20	0.054±0.081	5.074±0.270	4.779±0.024	4.714±0.021	8.5	2.26
HIP15197	A5m	29.72±0.29	0.246±0.083	4.419±0.250	4.255±0.220	4.225±0.020	8.8	1.81

HIP	Spectral Type	Parallax (mas)	$B_T - V_T$	J (mag)	H (mag)	K_S (mag)	Age $\log(t)$	Mass M_\odot
HIP15648	A3V	21.66±0.33	0.073±0.083	4.796±0.037	4.864±0.016	4.776±0.021	8.4	2.12
HIP16591	A5m	17.84±0.46	0.154±0.098	5.505±0.023	5.502±0.015	5.493±0.021	8.2	1.94
HIP17395	A5m	23.57±0.49	0.222±0.099	5.208±0.024	5.166±0.061	5.077±0.020	8.1	1.75
HIP17954	A2V	17.71±0.55	0.239±0.090	4.841±0.037	4.902±0.021	4.813±0.018	8.8	2.08
HIP18217	A5m	19.80±0.41	0.202±0.099	5.445±0.019	5.412±0.020	5.372±0.016	8.1	1.83
HIP18907	A1V	27.89±0.19	0.051±0.065	3.752±0.198	3.842±0.190	3.783±0.304	8.7	2.00
HIP19990	A3m	34.55±0.38	0.280±0.086	4.786±0.272	4.577±0.256	4.362±0.020	8.0	1.69
HIP20219	F3V...	21.88±0.36	0.299±0.105	5.002±0.037	4.927±0.047	4.853±0.015	8.8	1.81
HIP20261	F0V	21.30±0.39	0.247±0.091	4.750±0.048	4.973±0.282	4.689±0.016	8.8	1.90
HIP20542	A7V	20.21±0.40	0.187±0.082	4.561±0.268	4.513±0.210	4.414±0.020	8.6	2.26
HIP20635	A7IV-V	21.19±0.21	0.165±0.072	4.093±0.284	4.064±0.228	4.077±0.470	8.6	2.44
HIP20641	A7V	22.03±0.35	0.266±0.091	5.086±0.250	4.921±0.230	4.607±0.016	8.8	1.92
HIP20648	A2IV	21.96±0.51	0.056±0.072	4.338±0.316	4.381±0.238	4.098±0.029	8.4	2.50
HIP20711	A8Vn	21.21±0.25	0.296±0.075	3.859±0.250	3.793±0.232	3.761±0.348	8.7	2.42
HIP20713	F0V...	20.37±0.60	0.276±0.078	4.167±0.252	3.954±0.236	4.028±0.236	8.7	2.35
HIP20842	Am	21.22±0.41	0.300±0.099	5.163±0.017	5.103±0.017	5.055±0.018	8.6	1.83
HIP20894	A7III	21.69±0.46	0.216±0.059	2.994±0.206	2.997±0.212	2.880±0.264	8.7	2.50
HIP20901	A7V	20.47±0.28	0.242±0.087	4.793±0.198	4.656±0.204	4.534±0.033	8.6	2.15
HIP21029	A6IV	23.15±0.31	0.197±0.082	4.773±0.224	4.677±0.200	4.364±0.036	8.6	2.14
HIP21036	F0V	22.12±0.35	0.293±0.094	5.221±0.312	4.834±0.036	4.748±0.017	8.9	1.81
HIP21039	Am	22.26±0.49	0.280±0.095	5.458±0.242	4.967±0.036	4.903±0.022	8.3	1.91
HIP21273	A8V	20.61±0.57	0.263±0.081	4.311±0.262	4.288±0.228	4.074±0.036	8.8	2.20
HIP21402	A5m	20.88±0.94	0.182±0.073	3.702±0.228	3.883±0.036	3.693±0.248	8.7	2.46
HIP21589	A6V	21.24±0.56	0.148±0.073	4.117±0.258	4.078±0.228	4.105±0.334	8.6	2.43
HIP21670	A5m	20.34±0.35	0.283±0.093	5.180±0.254	4.928±0.029	4.808±0.020	8.7	1.99
HIP21673	A4m	22.18±0.93	0.145±0.086	4.823±0.018	4.856±0.036	4.805±0.024	8.4	2.01
HIP21683	A5Vn	20.97±0.27	0.182±0.080	4.682±0.294	4.547±0.222	4.229±0.036	8.7	2.27
HIP22044	F0V	21.82±0.30	0.279±0.093	4.962±0.248	4.732±0.027	4.733±0.020	8.9	1.83
HIP22192	A2IV/V	17.80±0.33	0.195±0.105	5.801±0.023	5.730±0.038	5.715±0.017	8.1	1.79
HIP22287	A3m	18.95±0.52	0.268±0.091	5.108±0.240	4.769±0.040	4.725±0.016	8.8	1.99

HIP	Spectral Type	Parallax (mas)	$B_T - V_T$	J (mag)	H (mag)	K_S (mag)	Age $\log(t)$	Mass M_\odot
HIP22361	A9IV	21.25±0.29	0.298±0.103	5.347±0.023	5.293±0.022	5.221±0.016	8.9	1.64
HIP22565	A7IV-V	19.51±0.71	0.229±0.088	4.972±0.264	4.566±0.036	4.492±0.016	8.8	2.12
HIP22845	A0V	28.04±0.25	0.090±0.079	4.846±0.246	4.517±0.047	4.416±0.047	8.8	1.66
HIP23179	A1V	19.13±0.79	0.018±0.083	4.903±0.470	4.980±0.021	4.922±0.026	8.4	2.24
HIP23497	A7V	18.88±0.30	0.192±0.079	4.333±0.320	4.375±0.208	4.245±0.021	8.7	2.38
HIP23554	A2IV	17.19±0.31	0.118±0.095	5.428±0.059	5.401±0.042	5.336±0.016	8.4	2.04
HIP23871	A5V	17.21±0.39	0.124±0.090	5.107±0.037	5.075±0.026	5.047±0.016	8.6	2.15
HIP23875	A3IIIvar	36.50±0.42	0.170±0.048	2.470±0.258	2.439±0.204	2.397±0.220	8.8	2.00
HIP23983	A2m	18.28±0.36	0.274±0.094	4.965±0.025	4.929±0.022	4.861±0.022	8.7	2.06
HIP24340	A4m	21.32±0.81	0.218±0.083	4.376±0.194	4.389±0.036	4.396±0.031	8.8	2.09
HIP26309	A2III/IV	18.94±0.43	0.173±0.110	5.958±0.024	5.936±0.033	5.864±0.018	8.1	1.64
HIP26382	F0V	20.58±0.37	0.247±0.098	5.062±0.020	5.002±0.024	4.935±0.029	8.8	1.89
HIP26563	A4V	22.42±0.44	0.157±0.082	4.694±0.186	4.545±0.076	4.420±0.016	8.7	2.10
HIP27288	A2Vann	46.28±0.16	0.130±0.060	3.390±0.280	3.314±0.252	3.286±0.282	8.3	2.01
HIP28614	Am...	21.05±0.68	0.181±0.071	3.730±0.308	3.598±0.276	3.637±0.260	8.7	2.48
HIP28910	A0V	18.88±0.54	0.054±0.078	4.743±0.234	4.593±0.236	4.523±0.021	8.6	2.35
HIP29997	A0Vn	18.64±0.23	0.020±0.079	4.973±0.214	4.767±0.036	4.672±0.017	8.6	2.35
HIP30060	A2Vs	20.83±0.40	0.037±0.074	4.282±0.274	4.287±0.192	4.347±0.018	8.7	2.00
HIP30419	A5IV	26.67±0.90	0.206±0.076	3.870±0.246	3.716±0.194	3.916±0.036	8.8	2.05
HIP31167	F0Vnn+...	23.90±0.24	0.272±0.097	5.116±0.020	5.007±0.020	4.905±0.017	8.9	1.68
HIP32104	A2V	22.92±0.67	0.074±0.088	5.026±0.037	5.070±0.021	5.011±0.020	8.0	1.99
HIP33018	A3III	17.25±0.19	0.126±0.061	3.246±0.220	3.229±0.194	3.163±0.296	8.7	2.50
HIP35350	A3V...	32.33±0.20	0.134±0.061	3.540±0.330	3.495±0.284	3.535±0.262	8.5	2.38
HIP36393	A4V	18.51±0.25	0.137±0.086	4.818±0.037	4.793±0.016	4.744±0.021	8.7	2.15
HIP38723	A3p	16.95±0.49	0.281±0.111	5.547±0.021	5.438±0.021	5.397±0.017	9.1	1.70
HIP41152	A3V	19.83±0.28	0.137±0.093	5.252±0.023	5.292±0.033	5.249±0.016	8.2	1.96
HIP41375	A5III-IV	19.99±0.38	0.242±0.096	5.161±0.043	5.133±0.045	4.992±0.018	8.8	1.83
HIP42080	A2m	21.39±0.41	0.225±0.094	5.044±0.037	5.020±0.026	4.934±0.995	8.8	1.84
HIP42313	A1Vnn	20.34±0.63	0.020±0.069	4.147±0.284	4.126±0.256	4.033±0.036	8.6	2.59
HIP42806	A1IV	18.00±0.21	0.026±0.078	4.799±0.180	4.788±0.186	4.638±0.024	8.5	2.49

HIP	Spectral Type	Parallax (mas)	$B_T - V_T$	J (mag)	H (mag)	K_S (mag)	Age $\log(t)$	Mass M_\odot
HIP43121	AIV	18.53±0.43	0.126±0.100	5.647±0.044	5.642±0.044	5.550±0.017	8.1	1.88
HIP43932	A7IV	16.79±0.29	0.178±0.093	5.312±0.256	5.079±0.016	5.024±0.020	8.7	2.06
HIP43970	A5III	21.87±0.26	0.173±0.092	4.910±0.037	4.971±0.220	4.865±0.016	8.5	1.95
HIP44001	F0IV	21.68±0.33	0.237±0.106	5.271±0.023	5.208±0.018	5.156±0.024	8.6	1.76
HIP44066	A5m	17.32±0.97	0.159±0.073	3.979±0.252	4.027±0.192	3.944±0.274	8.6	2.70
HIP44127	A7IV	68.92±0.16	0.230±0.055	2.781±0.230	2.763±0.184	2.660±0.240	8.1	1.82
HIP44342	A8Vn	17.24±0.39	0.261±0.113	5.537±0.021	5.521±0.034	5.435±0.022	8.8	1.78
HIP45493	A5V	27.90±0.20	0.212±0.083	4.481±0.198	4.353±0.178	4.291±0.020	8.8	1.87
HIP45688	AIV	26.13±0.78	0.047±0.066	3.480±0.284	3.464±0.256	3.416±0.350	8.8	2.20
HIP46744	F0Vn	19.45±1.06	0.284±0.115	5.579±0.024	5.436±0.024	5.371±0.021	8.9	1.65
HIP47300	F0V	26.61±0.32	0.244±0.091	4.969±0.234	4.845±0.036	4.752±0.018	8.4	1.76
HIP47701	A2IV	20.40±0.38	0.133±0.095	5.394±0.023	5.439±0.016	5.394±0.016	8.0	1.95
HIP48390	A5IV	24.12±1.41	0.256±0.092	4.858±0.354	4.717±0.036	4.662±0.020	8.9	1.78
HIP49593	A7V	35.41±0.18	0.209±0.077	4.269±0.250	4.046±0.036	4.004±0.036	8.4	1.83
HIP50372	A2IV	23.72±0.78	0.048±0.058	3.437±0.282	3.459±0.212	3.418±0.330	8.4	2.90
HIP51384	F0IV	24.61±0.39	0.251±0.095	4.945±0.037	4.928±0.029	4.853±0.022	8.8	1.69
HIP51658	A7IV	28.88±0.52	0.228±0.082	4.122±0.228	4.059±0.234	4.197±0.015	8.8	1.88
HIP52422	A4Vn	20.67±1.13	0.196±0.094	5.114±0.037	5.072±0.036	5.051±0.022	8.9	1.54
HIP53824	A5III	21.57±0.26	0.177±0.085	4.862±0.242	4.696±0.017	4.614±0.016	8.7	2.04
HIP53954	AIm	25.73±0.18	0.067±0.074	4.315±0.228	4.324±0.176	4.315±0.036	8.4	2.22
HIP54027	F0V	17.88±0.45	0.279±0.114	5.632±0.027	5.485±0.045	5.445±0.022	8.9	1.72
HIP54477	AIV	17.97±0.53	0.077±0.091	5.313±0.030	5.352±0.033	5.235±0.022	8.4	2.09
HIP54688	A5V	17.80±0.35	0.242±0.117	5.845±0.023	5.830±0.042	5.762±0.022	8.1	1.72
HIP54872	A4V	55.82±0.25	0.166±0.044	2.238±0.258	2.191±0.188	2.144±0.206	8.8	1.94
HIP54879	A2V	19.76±0.17	0.018±0.055	3.115±0.276	3.190±0.240	3.082±0.308	8.3	3.30
HIP55084	A7IVn	17.71±0.25	0.226±0.077	4.318±0.298	4.186±0.242	4.126±0.284	8.7	2.40
HIP55266	A2V	17.00±0.34	0.123±0.081	4.655±0.232	4.518±0.036	4.460±0.036	8.7	2.33
HIP55705	A9V	39.62±0.20	0.211±0.071	3.648±0.426	3.523±0.570	3.546±0.526	8.8	1.86
HIP56253	A2m	16.89±0.27	0.286±0.109	5.655±0.025	5.604±0.018	5.560±0.021	8.8	1.78
HIP57328	A4V	26.73±0.25	0.181±0.083	4.634±0.204	4.542±0.076	4.409±0.045	8.6	1.92

HIP	Spectral Type	Parallax (mas)	$B_T - V_T$	J (mag)	H (mag)	K_S (mag)	Age $\log(t)$	Mass M_\odot
HIP57562	A1	16.90±0.28	0.035±0.089	5.276±0.023	5.301±0.038	5.251±0.017	8.3	2.24
HIP57606	F0V	16.74±0.58	0.281±0.106	5.269±0.019	5.162±0.016	5.115±0.018	9.0	1.84
HIP57779	A5m	19.38±0.40	0.292±0.113	5.802±0.024	5.750±0.020	5.712±0.024	8.0	1.62
HIP58001	A0V	39.21±0.40	0.057±0.041	2.381±0.290	2.487±0.174	2.429±0.288	8.6	2.50
HIP58684	A7m	29.18±0.75	0.293±0.091	4.711±0.180	4.841±0.036	4.553±0.016	8.8	1.67
HIP59394	A1V	17.00±0.56	0.057±0.091	5.336±0.024	5.357±0.036	5.321±0.020	8.3	2.15
HIP59608	A2m	19.93±0.29	0.290±0.101	5.405±0.021	5.325±0.040	5.236±0.017	8.8	1.75
HIP59774	A3Vvar	40.51±0.15	0.112±0.056	3.316±0.248	3.306±0.252	3.104±0.338	8.8	1.89
HIP59923	A4m	18.20±0.35	0.186±0.097	5.370±0.023	5.374±0.016	5.359±0.020	8.0	2.01
HIP61960	A0V	27.57±0.21	0.081±0.082	4.986±0.272	4.761±0.018	4.678±0.022	8.5	1.62
HIP65477	A5V	39.91±0.13	0.196±0.069	3.291±0.226	3.295±0.228	3.145±0.244	9.0	1.87
HIP66200	Alp SrCrEu	17.65±0.20	0.059±0.083	5.185±0.278	4.980±0.268	4.879±0.020	8.2	2.49
HIP66234	A5V	18.09±0.19	0.155±0.080	4.525±0.262	4.461±0.020	4.273±0.036	8.7	2.37
HIP66249	A3V	44.03±0.19	0.142±0.058	3.257±0.274	3.154±0.284	3.223±0.274	8.4	2.14
HIP66634	A3Vn	18.66±0.28	0.130±0.093	5.221±0.019	5.196±0.024	5.173±0.017	8.5	2.02
HIP67194	A5V	19.03±0.37	0.230±0.101	5.426±0.019	5.374±0.020	5.336±0.017	8.7	1.78
HIP69483	A8IV	19.96±0.63	0.219±0.078	4.208±0.290	4.157±0.238	4.096±0.298	8.8	2.00
HIP69592	A7V	16.70±0.46	0.215±0.118	5.933±0.020	5.901±0.016	5.879±0.018	8.1	1.74
HIP69713	A9V	34.40±0.19	0.239±0.082	4.638±0.202	4.320±0.036	4.293±0.036	8.1	1.81
HIP69732	A0sh	32.94±0.16	0.093±0.071	3.983±0.304	4.030±0.254	3.910±0.036	8.8	1.69
HIP69974	A1V	17.49±0.27	0.148±0.077	4.395±0.226	4.282±0.212	4.241±0.016	8.7	2.48
HIP70400	A5V	20.51±0.23	0.147±0.087	4.864±0.037	4.921±0.016	4.771±0.020	8.7	2.06
HIP71075	A7IIIvar	37.58±0.14	0.223±0.053	2.646±0.284	2.571±0.250	2.511±0.378	8.8	2.00
HIP71618	A1V	17.54±0.40	0.033±0.090	5.196±0.037	5.277±0.038	5.260±0.020	8.3	2.15
HIP71759	F0V	19.68±0.40	0.250±0.105	5.447±0.024	5.402±0.017	5.365±0.016	8.2	1.81
HIP71795	A3IVn	18.56±0.76	0.082±0.075	3.738±0.228	3.747±0.198	3.697±0.208	8.8	2.20
HIP72220	A0V	24.25±0.18	0.004±0.062	3.683±0.244	3.628±0.202	3.646±0.190	8.7	2.26
HIP72622	A3IV	43.03±0.19	0.188±0.048	2.467±0.276	2.439±0.184	2.440±0.280	8.6	2.47
HIP74689	A4V	21.67±0.42	0.198±0.096	5.729±0.322	5.250±0.026	5.177±0.020	8.1	1.82
HIP75342	F0V	19.56±0.35	0.274±0.114	5.629±0.032	5.485±0.026	5.475±0.022	8.7	1.67

HIP	Spectral Type	Parallax (mas)	$B_T - V_T$	J (mag)	H (mag)	K_S (mag)	Age $\log(t)$	Mass M_\odot
HIP75761	A8IV	25.16±0.31	0.252±0.089	4.748±0.037	4.776±0.026	4.590±0.021	8.8	1.81
HIP76291	F0III	17.73±0.41	0.297±0.122	6.000±0.025	5.930±0.024	5.853±0.021	8.6	1.60
HIP76852	AIV	17.16±0.67	0.071±0.076	4.413±0.228	4.482±0.218	4.305±0.016	8.6	2.55
HIP76878	A2m	18.84±0.39	0.224±0.103	5.371±0.023	5.327±0.020	5.296±0.016	8.1	1.93
HIP76952	AIVs	22.33±0.50	0.015±0.064	3.620±0.194	3.691±0.206	3.670±0.226	8.6	2.57
HIP77060	A6IV	21.86±0.23	0.239±0.093	5.041±0.037	4.976±0.076	4.816±0.016	8.8	1.82
HIP77233	A3V	21.03±0.26	0.094±0.062	3.440±0.290	3.539±0.276	3.546±0.318	8.7	2.30
HIP77464	A5IV	18.51±0.27	0.142±0.094	5.328±0.023	5.267±0.031	5.256±0.020	8.4	2.00
HIP77622	A2m	46.30±0.19	0.171±0.064	3.564±0.258	3.440±0.234	3.425±0.266	8.0	2.15
HIP77660	A3Vn	20.10±0.33	0.144±0.087	5.172±0.282	4.849±0.049	4.699±0.018	8.9	1.69
HIP78078	A2Ib/II	19.57±0.40	0.251±0.114	5.495±0.021	5.390±0.051	5.339±0.015	9.2	1.31
HIP78180	F0IV	29.78±0.16	0.293±0.086	4.384±0.280	4.330±0.017	4.276±0.031	8.9	1.73
HIP78286	F0IV	20.41±0.25	0.296±0.104	5.434±0.024	5.324±0.018	5.289±0.017	8.9	1.64
HIP78554	A3V	18.22±0.26	0.085±0.081	5.012±0.266	4.658±0.036	4.619±0.017	8.4	2.42
HIP79881	A0V:	24.22±0.22	0.030±0.080	4.855±0.037	4.939±0.076	4.739±0.018	8.0	2.27
HIP80480	F0V	23.32±0.25	0.254±0.096	5.071±0.018	5.000±0.031	4.989±0.021	8.7	1.73
HIP80628	A3m	24.42±0.91	0.201±0.080	4.271±0.244	4.155±0.200	4.165±0.036	8.7	2.13
HIP80883	A2V	18.84±0.55	0.043±0.070	3.913±0.288	3.794±0.256	3.795±0.272	8.7	2.45
HIP80975	Ap	19.34±0.21	0.149±0.076	3.922±0.188	3.849±0.176	4.137±0.015	8.8	2.00
HIP82321	A2p...	18.10±0.34	0.097±0.082	4.775±0.256	4.581±0.036	4.572±0.018	8.5	2.41
HIP82402	A3m	18.38±0.33	0.129±0.093	5.241±0.018	5.237±0.024	5.226±0.031	8.4	2.03
HIP83494	A5V	18.19±0.31	0.227±0.108	5.654±0.021	5.675±0.038	5.601±0.017	8.1	1.79
HIP83613	A4IV	24.47±0.38	0.150±0.083	5.072±0.232	4.722±0.024	4.613±0.024	8.0	2.10
HIP84012	A2.5Va	36.91±0.80	0.120±0.043	2.369±0.276	2.409±0.216	2.336±0.242	8.6	2.63
HIP84183	F0IV	23.23±0.19	0.219±0.095	5.093±0.037	5.105±0.045	5.050±0.018	8.0	1.79
HIP84379	A3IVv	43.41±0.15	0.104±0.053	2.834±0.238	2.976±0.178	2.808±0.304	8.7	2.19
HIP84606	A2V	18.59±0.33	0.034±0.077	4.773±0.284	4.462±0.036	4.438±0.017	8.4	2.49
HIP85157	F0IV	23.42±0.45	0.232±0.098	5.244±0.018	5.215±0.022	5.180±0.018	8.1	1.72
HIP85537	A8V	16.77±0.26	0.255±0.094	4.813±0.037	4.883±0.018	4.805±0.021	8.9	2.00
HIP85699	A2m	21.33±0.19	0.248±0.099	5.341±0.020	5.306±0.018	5.293±0.020	8.1	1.79

HIP	Spectral Type	Parallax (mas)	$B_T - V_T$	J (mag)	H (mag)	K_S (mag)	Age $\log(t)$	Mass M_\odot
HIP85819	A6...	33.06±0.15	0.272±0.085	4.832±0.248	4.579±0.202	4.243±0.020	8.8	1.70
HIP85822	AIVn	18.95±0.14	0.040±0.073	4.052±0.182	4.331±0.036	4.258±0.029	8.6	2.55
HIP85922	A5V	20.79±0.33	0.205±0.096	5.253±0.025	5.251±0.034	5.139±0.015	8.5	1.84
HIP86263	F0IIIp	30.98±0.19	0.294±0.063	3.065±0.242	2.913±0.176	2.911±0.244	8.8	2.20
HIP86565	A2Va	18.83±0.25	0.099±0.072	4.248±0.248	4.181±0.168	4.107±0.248	8.7	2.29
HIP87108	A0V	31.73±0.21	0.052±0.063	3.587±0.230	3.661±0.206	3.622±0.232	8.7	1.96
HIP87836	A7III/IV	19.49±0.39	0.223±0.099	5.345±0.019	5.309±0.027	5.257±0.020	8.6	1.82
HIP88565	F0V	18.28±0.64	0.292±0.114	5.764±0.024	5.693±0.020	5.641±0.018	8.8	1.62
HIP88771	A4IVs	37.55±0.21	0.159±0.064	3.509±0.226	3.426±0.216	3.412±0.192	8.4	2.17
HIP89925	A5m	17.80±0.30	0.255±0.097	5.119±0.025	5.042±0.021	4.994±0.018	8.9	1.91
HIP90156	A3V	17.71±0.35	0.073±0.085	4.938±0.438	4.874±0.020	4.779±0.021	8.7	2.21
HIP91919	FIV	20.09±0.78	0.139±0.085	4.198±0.220	4.298±0.033	4.230±0.018	8.9	2.00
HIP91926	A8Vn	20.97±0.50	0.189±0.090	4.026±0.240	4.209±0.026	4.157±0.018	9.1	1.80
HIP91971	Am	20.89±0.17	0.228±0.075	4.061±0.284	4.014±0.220	3.967±0.230	8.6	2.45
HIP92161	A5III	34.61±0.46	0.145±0.074	4.498±0.324	4.447±0.230	4.079±0.026	8.0	2.15
HIP93408	A7V	26.71±0.17	0.205±0.086	4.776±0.282	4.578±0.036	4.505±0.016	8.7	1.84
HIP93506	A3IV	36.98±0.87	0.118±0.045	2.319±0.236	2.318±0.200	2.293±0.234	8.6	2.69
HIP93580	A4V	18.22±0.31	0.196±0.099	5.462±0.020	5.362±0.024	5.320±0.018	8.9	1.51
HIP93747	A0Vn	39.28±0.16	0.035±0.050	3.084±0.330	3.048±0.280	2.876±0.360	8.7	2.17
HIP95077	A6:m...	18.06±0.35	0.297±0.102	5.100±0.037	5.054±0.022	4.922±0.021	8.9	1.87
HIP95168	F0III/IV	25.69±0.19	0.250±0.068	3.608±0.244	3.412±0.224	3.409±0.244	8.8	2.20
HIP95853	A5Vn	26.88±0.11	0.164±0.065	3.735±0.288	3.691±0.228	3.598±0.282	8.6	2.43
HIP97229	A3IV	18.65±0.41	0.195±0.101	5.565±0.021	5.471±0.040	5.457±0.022	8.2	1.84
HIP99655	A3IV-Vn	20.48±0.12	0.132±0.073	4.275±0.274	4.166±0.268	4.078±0.378	8.7	2.39
HIP99742	A2V	21.75±0.26	0.074±0.083	4.865±0.270	4.801±0.034	4.767±0.017	8.8	1.76
HIP99770	A2V	23.42±0.22	0.159±0.084	4.886±0.306	4.688±0.242	4.422±0.017	8.9	1.64
HIP101093	A7III	23.90±0.60	0.222±0.073	3.744±0.254	3.756±0.246	3.719±0.322	8.7	2.33
HIP101800	A2V	17.26±0.33	0.060±0.091	5.407±0.021	5.372±0.034	5.303±0.021	8.0	2.24
HIP102253	A8V	23.37±0.21	0.230±0.096	5.180±0.037	5.134±0.049	5.059±0.016	8.4	1.75
HIP102843	A4me...	24.41±0.22	0.216±0.087	4.882±0.238	4.614±0.036	4.576±0.026	8.7	1.90

HIP	Spectral Type	Parallax (mas)	$B_T - V_T$	J (mag)	H (mag)	K_S (mag)	Age $\log(t)$	Mass M_\odot
HIP103460	A2/A3III	18.23±0.47	0.199±0.109	5.592±0.017	5.458±0.031	5.489±0.017	8.2	1.87
HIP104019	A5V	20.20±0.82	0.185±0.083	4.473±0.268	4.334±0.262	4.437±0.040	8.8	2.12
HIP104139	AIV	20.11±0.28	0.005±0.068	4.372±0.280	4.316±0.216	4.100±0.036	8.3	2.80
HIP104365	A0V	18.14±0.31	0.010±0.089	5.313±0.044	5.334±0.047	5.305±0.021	8.6	1.86
HIP105199	A7IV-V	66.50±0.11	0.267±0.044	2.154±0.298	2.134±0.176	2.066±0.242	8.7	2.08
HIP105860	A8m	21.57±0.56	0.254±0.108	5.677±0.067	5.488±0.027	5.506±0.026	8.0	1.68
HIP105966	AIV	17.14±0.28	0.053±0.090	5.276±0.032	5.368±0.051	5.290±0.018	8.3	2.19
HIP106654	A7/A8IV	17.11±0.47	0.240±0.099	5.318±0.017	5.261±0.018	5.212±0.018	8.8	1.91
HIP106786	A7V	18.26±0.24	0.188±0.080	4.359±0.248	4.219±0.196	4.252±0.017	8.7	2.38
HIP106856	A9IV-Vn	18.28±0.30	0.283±0.098	5.157±0.037	5.104±0.029	5.007±0.022	8.9	1.84
HIP107302	A7IV/V	18.87±0.44	0.236±0.111	5.565±0.025	5.459±0.027	5.411±0.021	8.7	1.77
HIP109427	A2V	35.34±0.85	0.093±0.060	3.455±0.268	3.390±0.206	3.377±0.264	8.8	1.90
HIP109521	A5V	17.81±0.73	0.160±0.092	5.013±0.037	5.016±0.045	4.959±0.016	8.7	2.04
HIP11169	AIV	31.79±0.12	0.026±0.063	3.830±0.238	3.867±0.208	3.851±0.274	8.1	2.45
HIP111674	A8IV	19.00±0.19	0.271±0.081	3.745±0.210	3.693±0.188	3.990±0.036	8.9	1.80
HIP113048	A3m	17.57±0.51	0.277±0.103	5.169±0.018	5.051±0.020	5.043±9.995	9.1	1.78
HIP113963	B9.5III	24.46±0.19	0.004±0.041	2.535±0.270	2.744±0.220	2.647±0.306	8.3	3.50
HIP114189	A5V	25.38±0.70	0.278±0.111	5.383±0.027	5.280±0.018	5.240±0.018	9.0	1.24
HIP115250	A5V	20.17±0.40	0.186±0.079	4.331±0.294	4.362±0.222	4.085±0.020	8.9	1.80
HIP115738	A0p	21.25±0.29	0.059±0.083	5.317±0.270	4.984±0.016	4.902±0.018	8.0	2.38
HIP116758	A7IV	22.94±1.05	0.268±0.087	4.886±0.248	4.629±0.220	4.342±0.024	8.9	1.95
HIP116768	A2m	18.38±0.85	0.241±0.103	5.563±0.024	5.488±0.045	5.471±0.017	8.4	1.81
HIP116928	A7V	30.59±0.19	0.227±0.078	4.372±0.298	4.204±0.244	4.064±0.036	8.6	1.94
HIP117452	A0V	23.73±0.22	0.006±0.076	4.801±0.262	4.643±0.076	4.532±0.021	8.3	2.26
HIP117730	A4Vn	17.85±0.96	0.194±0.091	4.854±0.030	4.812±0.038	4.714±0.017	8.8	2.05

CHAPTER 3

PRIMARY COMPARISON SAMPLES



In order to place the results of this volume-limited multiplicity of A-type stars into context, it is necessary to consider samples against which the results will be compared (Figure 3.1, Table 3.1). Primarily, the results will be compared to previous volume-limited multiplicity surveys of lower-mass primaries, allowing for an investigation of the various multiplicity statistics as a function of primary mass. In addition, the results will also be compared with environment-specific surveys with samples containing A-type stars, allowing for a comparison of the multiplicity statistics between cluster and field populations. Each comparison sample, either derived from a volume-limited or environment-specific study, must be convolved with the detection limits of the VAST survey to allow for a fair statistical comparison.

3.1 Volume-limited surveys

3.1.1 Solar-type primaries

The multiplicity of Solar-type primaries is well understood, with the seminal work by Duquennoy & Mayor (1991) providing the benchmark against which most multiplicity surveys are compared. This study was recently expanded upon by Raghavan et al. (2010), increasing the sample size from 165 to 454 nearby Solar-type stars, and providing robust estimates of the multiplicity statistics over a wide range of physical separations through a combination of spectroscopy, speckle interferometry, and direct imaging techniques to resolve stellar companions. As with the VAST sample, the Raghavan et al. (2010) Solar-type sample was drawn from the *Hipparcos* catalogue, selecting a sample of 454 stars with a parallax of $\pi > 40$ mas, corresponding to a volume-limited sample within 25 parsecs. The sample was restricted to Main Sequence stars within the \sim F6 - K3 spectral type range by applying both a $B - V$ colour cut-off, and an absolute V -band magnitude cut-off.

The observed fraction of single, double, triple, and higher order systems was reported as $56\% \pm 2\%$, $33\% \pm 2\%$, $8\% \pm 1\%$, and $3\% \pm 1\%$, respectively (Raghavan et al. 2010). The

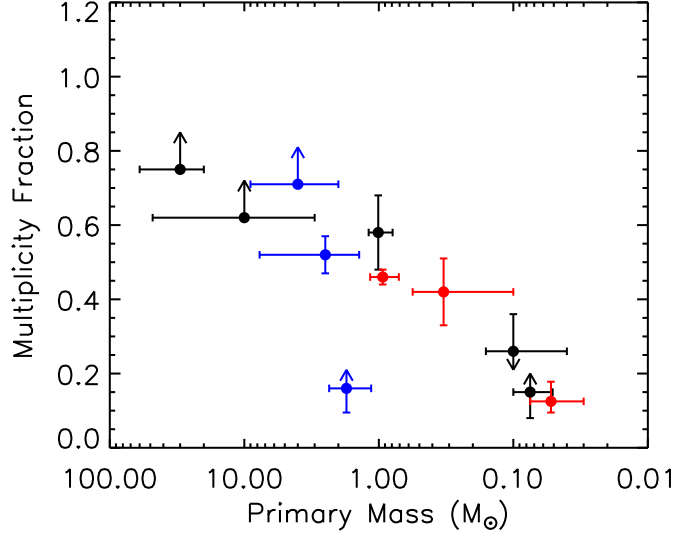


Figure 3.1: The multiplicity of various samples of stars as a function of primary mass. From lowest to highest mass, the black points represents the surveys of Close et al. (2003), Basri & Reiners (2006), Duquennoy & Mayor (1991), Preibisch (1999), and Mason et al. (1998). The red points represent volume-limited surveys of, from lowest to highest mass, brown dwarfs (Reid et al. 2008), M-dwarfs (Fischer & Marcy 1992), and Solar-type stars (Raghavan et al. 2010). The blue points represent surveys studying the multiplicity of early-type stars, with a survey of Austral early-type stars at 16% (Ehrenreich et al. 2010), a survey of Sco OB2 association members at 52% (Kouwenhoven et al. 2005), and an ongoing survey of Herbig Ae/Be stars at 71% (Thomas et al. 2007). The trend of increasing multiplicity as a function of primary mass is apparent, with the notable exception of the Ehrenreich et al. (2010) and Thomas et al. (2007) measurements, discussed further in §3.3.1 and §3.3.2.

Table 3.1: Primary comparison samples

Reference	Spectral Type Range	Notes
Raghavan et al. (2010)	F6 – K3	Volume limited
Fischer & Marcy (1992)	M0 – M8	Volume limited
Reid et al. (2008)	L0 – L8	Volume limited
Ehrenreich et al. (2010)	B9 – F7	Southern Hemisphere
Kouwenhoven et al. (2005)	B2 – A9	Sco OB2 association
Thomas et al. (2007)	B0 – A7	Herbig AeBe

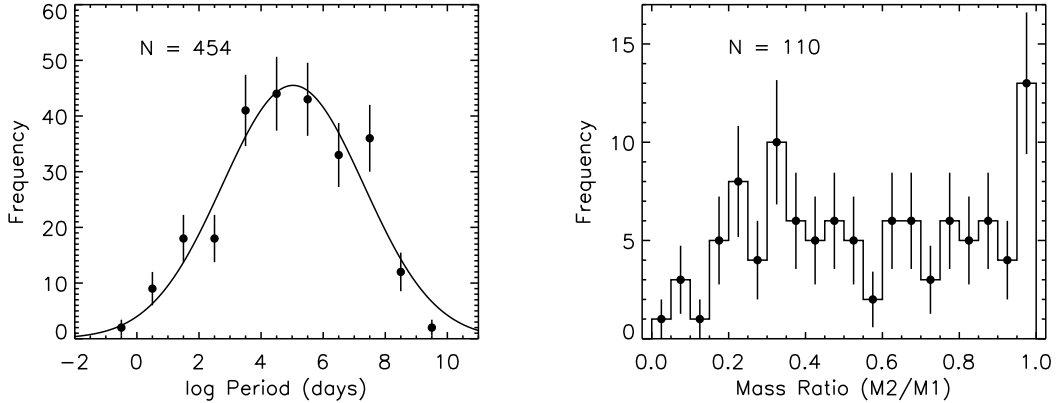


Figure 3.2: (*left panel*): Period distribution of the 259 confirmed companions to Solar-type primaries resolved by Raghavan et al. (2010) from a sample of 454 stars, with associated Poisson uncertainties. A Gaussian fit to the data, with a mean value of $\langle \log P_d \rangle = 5.03$ and a standard deviation of $\sigma_{\log P_d} = 2.28$, is over-plotted with a solid line. (*right panel*): Mass ratio distribution of the 110 multiple systems reported by Raghavan et al. (2010) with only two resolved components. The distribution is flat between a mass ratio of 0.2 and 0.95, with a significant lack of lower-mass companions, and relative abundance of equal-mass companions.

fraction of single Solar-type stars was relatively unchanged compared with the value measured by Duquennoy & Mayor (1991), who had suggested that a significant number of unresolved companions would further decrease this value, despite the comprehensive monitoring of these targets using a variety of detection methods. The fraction of Solar-type stars with multiple components has more than doubled between the two surveys, indicating that the majority of the newly resolved companions are additional components to previously resolved binary systems.

The separation distribution measured by Raghavan et al. (2010), plotted in Figure 3.2 (left panel), is consistent with the measurement of Duquennoy & Mayor (1991), with the mean of the distribution increasing from $\langle \log P_d \rangle = 4.8$ to $\langle \log P_d \rangle = 5.03$, and the standard deviation decreasing from $\sigma_{\log P_d} = 2.3$ to $\sigma_{\log P_d} = 2.28$, with P_d measured in days. The distribution is well sampled, with significant overlap existing between the different detection techniques in all but the widest separations, indicating the multiplicity survey is complete to a significant level. The drop in the number of companions detected at the widest separations ($\log P_d > 8$), is present within a region of the separation distribution which is well sampled by the observations, and is considered to be physical. Although companions with separations of the order of 0.1 pc have been resolved (e.g. Latham et al. 1991), they are unlikely to be stable within the dynamical environment of a stellar cluster (Parker et al. 2009).

The Raghavan et al. (2010) survey significantly improves the sensitivity to lower-mass companions populating the lowest extreme of the mass ratio distribution ($M_2/M_1 < 0.2$), detecting significantly fewer lower-mass companions than expected by the incompleteness study of Duquennoy & Mayor (1991). No distinct trend was observed in the shape of the mass ratio distribution for the complete ensemble of companions to Solar-type stars, with the distribution being roughly flat between a mass ratio of 0.2 and 0.95 (Figure 3.2, right panel). Equal-mass

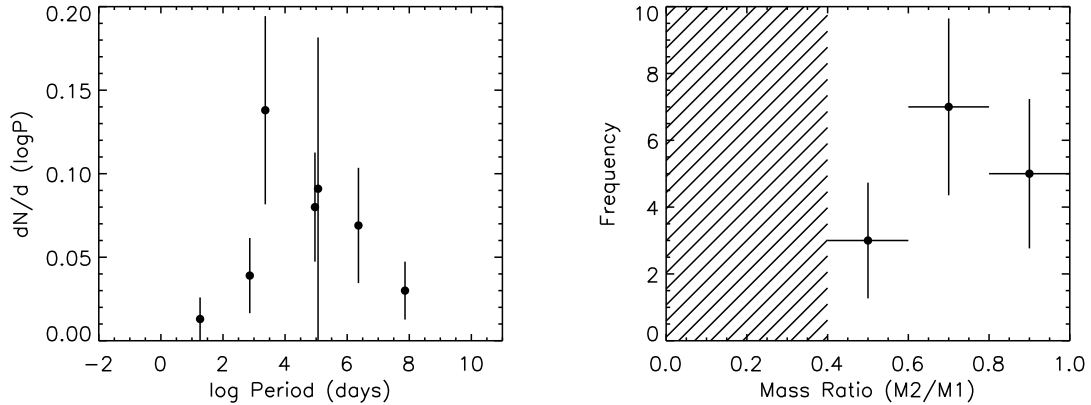


Figure 3.3: (*left panel*): Period distribution of the confirmed companions to nearby M-dwarf primaries presented within the Fischer & Marcy (1992) survey. Although no functional form to the data was estimated, the peak of the distribution is observed to be between $\log P_d = 3.47$ and $\log P_d = 5.00$. (*right panel*): The mass ratio distribution of the 15 binary systems with a primary of mass between 0.30 and $0.55 M_\odot$, with a lower mass ratio limit of 0.4 . These restrictions were applied to remove the bias introduced by binary systems with low-mass primaries.

binaries were found preferentially on shorter periods, with $\log P_d < 2$, consistent with the theoretical predictions of preferential accretion of gas onto the lower-mass companion within a proto-binary system, causing an equalisation of the final component masses of the system (Bate 2000). Dynamical interactions within the formation environment may also produce close binaries systems of equal component masses, with a wider tertiary component enhancing the accretion of the circumbinary material onto the inner binary (Tokovinin 2000). The apparent deficiency of low-mass companions in short-period orbits is consistent with the inward migration, and eventual destruction, of brown dwarf companions within the protoplanetary disk (Armitage & Bonnell 2002).

3.1.2 M-dwarf primaries

The preponderance of M-dwarfs within the Solar neighbourhood ($D < 20$ pc), combined with the ease of companion detection, has led to the multiplicity of these low-mass stars being well characterised (Fischer & Marcy 1992). The low contrast ratio between primary and secondary, in the case of direct imaging detection methods, and the sharp absorption lines within the spectrum of the primary, in the case of companion detection through Doppler shift spectroscopy, have both enabled the detection of a significant number of companions to nearby M-dwarfs (e.g. Skrutskie et al. 1989; Marcy & Benitz 1989.) Unlike the Duquennoy & Mayor (1991) and Raghavan et al. (2010) surveys of Solar-type primaries, the results presented by Fischer & Marcy (1992) are based on the combination of a number of individual studies of M-dwarf primaries. The sensitivity to companions on short period orbits provided by radial velocity measurements (Marcy & Benitz 1989), was supplemented by infrared speckle interferometric observations (Henry & McCarthy 1990), infrared CCD imaging observations (Skrutskie et al. 1989), and a search for common proper motion companions (Fischer & Marcy 1992) to provide sensitivity to

companions at a wide range of separations. The selection criteria used within each of the four studies differed slightly, although all studies are typically complete to a specific distance, and are limited to targets of M-type spectral classification.

The overall fraction of M-dwarfs with stellar companions between $10^{-1.4}$ and 10^4 AU was reported as $42\% \pm 9\%$, including corrections for observational incompleteness. While the combination of observational techniques allows for a coverage of a significant portion of the separation distribution, it does not allow for an investigation of the higher-order multiplicity of M-dwarfs due to the limited overlap between the samples within each study. There were no targets which were observed by each observational technique individually, and only three out of the twenty-four systems with a resolved companion were observed with at least three of the four observational techniques. Therefore, an estimate of fraction of triple, quadruple and higher order multiple systems with M-dwarf primaries is not possible with this combined dataset.

The separation distribution reported by Fischer & Marcy (1992), plotted in Figure 3.3 (left panel), was constructed from a combination of the four observational techniques. The variation in the overall sample size for each original study is apparent from the significant change in the size of the Poisson uncertainties. A functional fit to the observed separation distribution is not estimated by Fischer & Marcy (1992), although the peak of the distribution is observed to be between $\log P_d = 3.47$ and $\log P_d = 5.00$, consistent with the results of a previous multiplicity survey of M-dwarf primaries (Henry 1991). The observed separation distribution is consistent with a unimodal distribution of one distinct population, suggestive of a single mechanism responsible for the formation of companions to M-dwarf primaries (Fischer & Marcy 1992). The selection criteria for the radial velocity sample were chosen to exclude those targets with known wide companions (Marcy & Benitz 1989), and an assumption was adopted by Fischer & Marcy (1992) in their analysis that the frequency of close companions (0-4 AU) would only weakly depend on the presence of companions at wider separations. This assumption is inconsistent with the conclusions of a study investigating the statistics of spectroscopic sub-systems within visual multiple stars, suggesting that an outer companion would act to remove angular momentum from the inner system, allowing orbital energy to be removed through tidal dissipation (Tokovinin & Smekhov 2002). The selection bias introduced by this assumption may therefore reduce the number of companions detected through radial velocity observations, causing the $\log P_d = 1.3$ and $\log P_d = 2.9$ bins within Figure 3.3 to be systematically lower than the true separation distribution.

A companion mass ratio distribution was constructed from the individual component masses of the resolved binary systems listed in Fischer & Marcy (1992), considering only those systems with a primary mass of between 0.3 and $0.55 M_{\odot}$, and mass ratios between 0.4 and 1.0 (Figure 3.3, right panel). This restriction was applied to remove the bias introduced by the mass ratio of binary systems with low-mass primaries being skewed towards unity. Fifteen binary systems within the study satisfied these conditions, and the resulting mass ratio distribution was observed to have no significant trend. This result is consistent with the flat mass ratio distribution for Solar-type primaries measured by Raghavan et al. (2010), although the relative

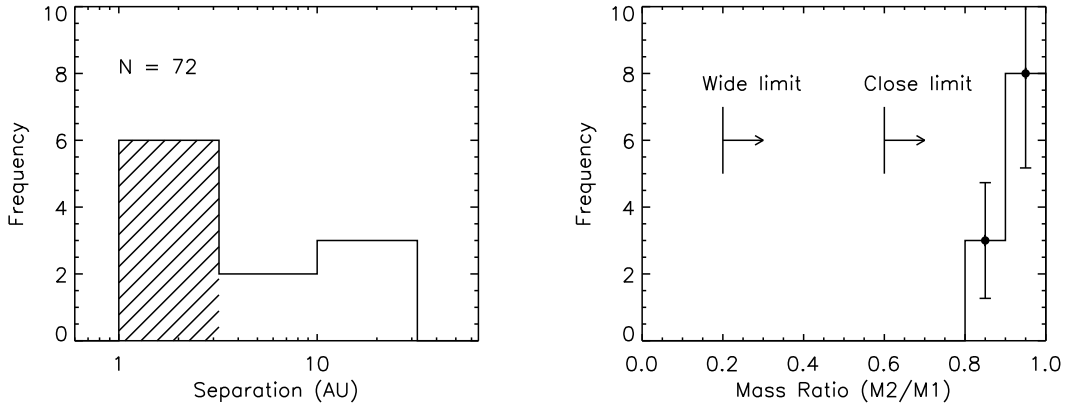


Figure 3.4: (*left panel*): Separation distribution of the 11 confirmed companions resolved within the Reid et al. (2008) survey of 72 L-type brown dwarfs within 20 parsecs. The inner-most bin has been shaded to signify the incompleteness of the observations to companions within ~ 2 AU. (*right panel*): The corresponding mass ratio distribution, showing the abundance of equal-mass systems. The data are sensitive to a mass ratio of $q = 0.6$ at separations ≥ 3 AU (denoted by the close limit), and to a mass ratio of $q = 0.2$ at separations ≥ 6 AU (denoted by the wide limit). The steep decline as a function of decreasing mass ratio is consistent with the mass ratio distribution observed in a larger sample of 30 brown dwarf binaries (Burgasser et al. 2006).

frequency is significantly lower.

3.1.3 Brown dwarfs primaries

The recent discovery of nearby brown dwarfs (e.g. Becklin & Zuckerman 1988; Nakajima et al. 1995), objects of insufficient mass for the continued burning of hydrogen (Hayashi & Nakano 1963), was further augmented with the publication of the *2MASS* all-sky survey dataset (e.g. Kirkpatrick et al. 1999; Burgasser et al. 1999). The near-infrared photometric bands of the survey were ideally suited to the detection of these faint brown dwarfs, with over two hundred such objects being identified from this dataset within the past twenty years. The frequency of binary companions to nearby brown dwarfs can provide certain observational constraints to the various formation scenarios theorised for these low mass objects (e.g. Whitworth et al. 2007, references therein).

With a large population of brown dwarfs within the Solar neighbourhood resolved in all-sky surveys such as *2MASS* and *SDSS*, the multiplicity of these objects, and the corresponding separation and mass ratio distributions, can be significantly constrained. A multiplicity survey of 72 L-type brown dwarfs (Kirkpatrick 2005) within 20 parsecs was carried out by Reid et al. (2008) using the *Hubble Space Telescope (HST)* to resolve companions beyond a projected separation of ~ 2 AU. A total of eleven companions were resolved, corresponding to a multiplicity fraction of $12.5^{+5.3}_{-3.0}\%$ for these nearby L-dwarfs, once corrected for survey incompleteness. This fraction is plotted in Figure 3.1, alongside the frequency of binaries observed for Solar-type and M-dwarf primaries, showing the significant trend of increasing multiplicity as a function of

increasing primary mass.

The separation distribution of the eleven binary companions to nearby L-type brown dwarfs resolved by Reid et al. (2008) is shown in Figure 3.4 (left panel). The data from which the distribution is drawn are incomplete to companions at separations of < 2 AU, although the data do show an abundance of binaries within ~ 3 AU, relative to wider systems. Subsequent radial velocity observations of the sample will allow for a further constraint of the frequency of binary companions within the sensitivity limit of the *HST* observations. The paucity of companions at wide separations is consistent with the embryo-ejection scenario (Billères et al. 2005), where very low-mass objects are ejected without accreting a substantial amount of material from the surrounding reservoir (Bate et al. 2003; Delgado-Donate et al. 2004). Within this scenario, wide companions to these ejected objects would be susceptible to dynamical disruption, consistent with the observed separation distribution. The detection of brown dwarf binaries with separations beyond ~ 200 AU (e.g. Luhman 2004; Billères et al. 2005), systems which could not survive three body interactions, suggests a small subset of the overall brown dwarf binary population are formed through an alternative mechanism. The frequency of these wide systems is observed to be extremely low, with an upper limit on the multiplicity of 2.3% between a separation of ~ 40 AU and ~ 1000 AU (Allen et al. 2007).

The companion mass ratio distribution, shown in Figure 3.4 (right panel), is significantly skewed towards equal-mass companions. The data were sensitive to companions to a mass ratio of $q = 0.6$ at separations ≥ 3 AU, and $q = 0.2$ at separations ≥ 6 AU, demonstrating that the measured peak of the mass ratio distribution at unity is not biased by the sensitivity limits of the observations (Allen 2007). The shape of the distribution resolved by Reid et al. (2008) is consistent with results from previous multiplicity studies of brown dwarfs (e.g. Burgasser et al. 2006). The mass ratio distribution of brown dwarf binaries resolved in hydrodynamical simulations of stellar clusters appears consistent with these observations (Bate 2009, 2012), although only three brown dwarf binary systems are formed within the simulations due to the relative dearth of such systems (Bate 2012). The mass ratio distribution is also shown to vary as a function of time (Bate 2009), with the mass ratio of a binary system tending to become more equalised as the simulation evolves, consistent with theories of preferential accretion and dynamical interaction within the formative environment (Bate et al. 2002).

3.2 Environment-specific surveys

Star formation predominately occurs within stellar clusters (Lada & Lada 2003), with the majority of stars forming within multiple systems (Mathieu 1994; Larson 2001). For the latter hypothesis to be consistent with the low observed multiplicity fraction of field stars (e.g. Fischer & Marcy 1992; Raghavan et al. 2010), a significant proportion of these nascent binary systems must be gravitationally disrupted prior to the effective cessation of dynamical interactions, brought on by the fragmentation and eventual dispersion of the star formation region (Kroupa 1995; Reipurth 2000). The efficiency of this dynamical process would necessarily be dependent on the density of the star formation region (Simon et al. 1999); the frequency of

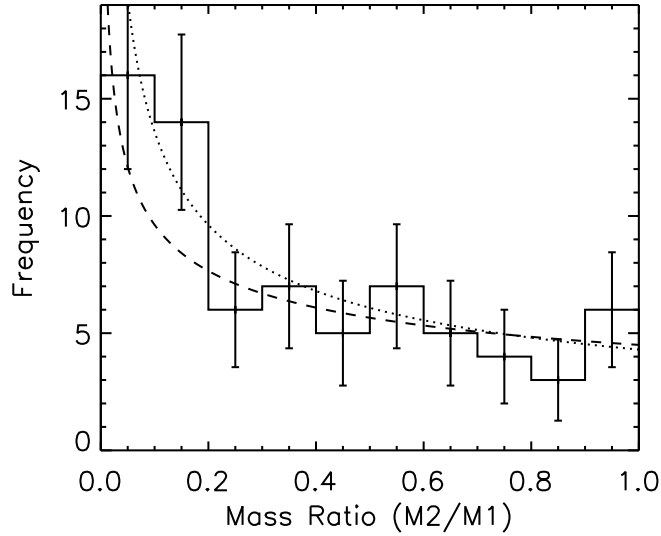


Figure 3.5: The mass ratio distribution of the 73 binary systems resolved within the Sco OB2 association (Kouwenhoven et al. 2005). This distribution includes both B- and A-type stars, spanning a range of primary mass between 1.4 and 7.7 M_{\odot} . A power law fit of $q^{-0.33}$ is over-plotted (dashed line - Kouwenhoven et al. 2005). This result is consistent with previous studies of the mass ratio distribution of binary systems with B-type primaries within the Sco OB2 association, with the corresponding power law fit of $q^{-0.50}$ over-plotted (dotted line - Shatsky & Tokovinin 2002).

binary systems within the Taurus, Ophiuchus, Lupus, and Chamaleon star-forming regions is approximately twice that of the field frequency resolved by Raghavan et al. (2010) (Simon & Prato 1995; Ghez et al. 1997; Kohler & Leinert 1998), while the frequency observed within the denser Orion Nebula Cluster (ONC) shows no such increase relative to the field population (e.g. Petr et al. 1998). Alternatively, the primordial frequency of binary systems may be dependent on the initial conditions within the molecular cloud (Köhler et al. 2006), with the binary frequency remaining relatively unchanged throughout the dynamical evolution of the cluster (Moeckel & Bate 2010).

Constraints on the effect of dynamical interactions within the formation environment can be determined through observations of the binary fraction within the formation environment over a specific primary mass range, and a comparison to the corresponding observed binary fraction within the field. For A-type stars, the nearest formation environment with a significant population of these early-type stars, is the Scorpius OB2 association. Based on an analysis of *Hipparcos* measurements, the stellar population of the Sco OB2 association has been well defined, consisting of ~ 160 A-type stars (de Zeeuw et al. 1999). At a distance of between 120 and 150 pc (de Zeeuw et al. 1999), and an age of between 5 and 18 Myrs (Preibisch et al. 2002; Mamajek et al. 2002), the Sco OB2 association is an ideal target to resolve the binary frequency of a sample of young early-type stars within their formation environment. A recent multiplicity survey of 199 Sco OB2 B- and A-type star members, combining dedicated adaptive optics observations with literature data, measured the binary fraction of these early-type stars within

the association to be $52\pm 5\%$ within a separation range of 29 to 1612 AU (Kouwenhoven et al. 2005). The companion mass ratio distribution was observed to be strongly skewed towards lower-mass companions, with a power law fit of $q^{-0.33}$ (Figure 3.5). Kouwenhoven et al. (2005) find that the observed mass ratio distribution is inconsistent with a random pairing of binary companions from the cluster mass distribution (Kouwenhoven et al. 2009), suggesting an alternative means of formation is required to explain the relative deficit of lower-mass companions (e.g. Kratter et al. 2010b).

3.3 Other surveys

3.3.1 Southern early-type stars

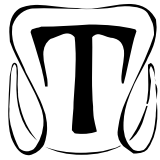
The recent detection of planetary companions to nearby A-type stars (e.g. Marois et al. 2008; Kalas et al. 2008) has prompted an investigation into the formation and frequency of low-mass companions to these stars. An adaptive-optics imaging survey of 38 nearby, Southern A- and F-type stars revealed a lower limit on the multiplicity of these early-type stars of 16% (Ehrenreich et al. 2010). The survey was sensitive to faint stellar companions within a projected separation range of $10 \lesssim \rho \lesssim 1000$ AU. Known binaries were excluded from the sample selection process, introducing a significant bias in the overall multiplicity fraction observed. The data obtained as a part of the VAST survey in the Northern Hemisphere, have been complemented by obtaining the observations of the Southern A-type stars within the Ehrenreich et al. (2010) survey from the ESO Science Archive Facility.

3.3.2 Herbig AeBe stars

Constraints on the binary formation processes within the dynamical nascent environment can be determined through an investigation of the multiplicity of pre-Main Sequence stars. Significant work on this field has been undertaken for low mass pre-Main Sequence T Tauri stars (e.g. Duchêne 1999), showing a significant excess in binary companions, excluding dense clusters such as the ONC, relative to corresponding surveys of field stars (e.g. Raghavan et al. 2010). The evolution in the multiplicity fraction is suggestive of a dynamical process which causes a significant reduction in the frequency of binary companions (Ghez et al. 1993; Patience et al. 1998). Equivalent studies of more massive pre-Main Sequence Herbig AeBe stars are challenging, due to the relative paucity of these objects within the Solar neighbourhood. Two recent high-resolution adaptive optics imaging surveys of Herbig AeBe stars, the majority within ~ 1000 pc, observe a significant fraction of Herbig AeBe stars with a binary companion ($\sim 40\%$ – Bouvier & Corcoran 2001, $\sim 70\%$ – Thomas et al. 2007). The observed multiplicity fraction in both instances, due to the limited physical separation over which the observations are sensitive, are considered to be lower limits to the true multiplicity of these pre-Main Sequence objects.

CHAPTER 4

OBSERVATIONS AND DATA REDUCTION



The data obtained as a part of the VAST survey are the result of a large international collaboration, utilising a wide range of telescopes to obtain dedicated high-resolution adaptive optics observations of the sample members. Table 4.1 lists the instruments used to obtain the dedicated high-resolution observations, and the number of observations obtained at each. The total number of observations is greater than the number of targets within the overall sample, due to the repeat observations of a significant number of targets. The observing strategy was chosen so as to be sensitive to stellar companions to the bottom of the Main Sequence for the majority of the VAST sample, corresponding to a magnitude difference of $\Delta K = 10.0$ (Figure 4.1). The data obtained were reduced through a standard near-infrared reduction pipeline, as described in Chapter 4.3, and companion candidates identified through a visual inspection of the reduced data. The relative position and brightness of each companion candidate were determined (Chapter 4.5), from which the projected separation and companion mass can be estimated.

Table 4.1: List of instruments used to obtain observations

Telescope	Primary Mirror Diameter	Instrument	Number of Observations
Canada-France-Hawai'i-Telescope	3.58m	PUEO/AOB + KIR	88
Gemini North Telescope	8.10m	ALTAIR + NIRI	73
Lick Observatory - Shane Telescope	3.00m	IRCAL	67
Palomar Observatory - Hale Telescope	5.10m	PHARO	60

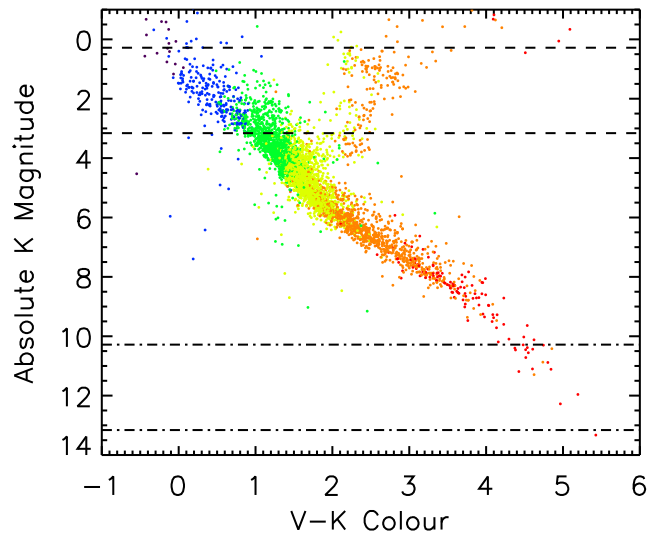


Figure 4.1: A colour-magnitude diagram of the stars within the *Hipparcos* catalogue with a parallax of $\pi > 13.3$ mas, corresponding to a distance of $D < 75$ pc. V -band magnitudes obtained from the *Tycho2* catalogue, and K -band magnitudes obtained from the *2MASS* catalogue. The colour of the data is representative of the spectral type of the star as reported within the *Hipparcos* catalogue; purple - O- and B-type, blue - A-type, green - F-type, yellow - G-type, orange - K-type, and red- M-type. For clarity only one in three stars is plotted on the colour-magnitude diagram, although the relative population of each spectral type is preserved. The dashed lines denote the 2σ range of K -band magnitudes of the VAST sample members, and the dot-dashed lines represented the observational strategy of a $\Delta K = 10$ dynamic range, corresponding to the bottom of the Main Sequence at $M_K = 10$ for the majority of the VAST sample members.

Image Copyrighted
 Figure can be found at:
<http://www.cfht.hawaii.edu/en/news/CFHT30/>

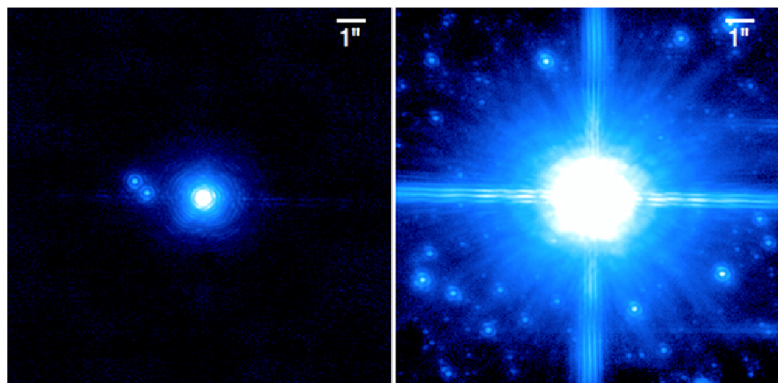


Figure 4.2: (*left panel*): An image of the CFHT observatory on the summit of Mauna Kea, Hawai'i (image credit CFHT). (*middle panel*): An unsaturated image of the A7V star HIP 44127 obtained using the KIR detector at the CFHT with the $H2_{1-0}$ narrow-band filter, resolving the system into a hierarchical triple. (*right panel*): A saturated image of the A7V star HIP 87836 obtained using the KIR detector and the K' wide-band filter. The high stellar background density within the vicinity of this target due to its low Galactic latitude is apparent within these deep exposures.

Image Copyrighted
Figure can be found at:
<http://www.gemini.edu/node/271>

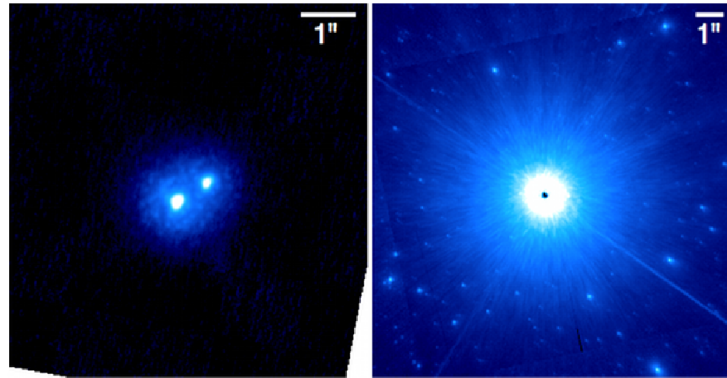


Figure 4.3: (*left panel*): An image of the Gemini North observatory on the summit of Mauna Kea, Hawai'i (image credit John Randrup). (*middle panel*): An unsaturated image of the A3IV star HIP 9480 obtained using the NIRI detector at Gemini North with the Br γ narrow-band filter, resolving the system into a binary. (*right panel*): A saturated image of the A7V star HIP 87836 obtained using the NIRI detector and the K' wide-band filter.

4.1 Dedicated observations

4.1.1 CFHT - PUEO/AOB + KIR

Accounting for 27.2% of the total number of observations obtained as a part of the VAST survey, the PUEO/KIR instrument package mounted upon the Canada-France-Hawaii Telescope (CFHT) is the largest source of data for this survey, obtained exclusively in visitor mode observations. Located on the summit Mauna Kea, Hawai'i, the CFHT is a 3.58 metre telescope which has been operational since 1979. Mounted upon the Cassegrain focus of the CFHT, the Probing the Universe with Extreme Optics adaptive optics bonnette (PUEO/AOB - Arsenault et al. 1994) instrument was used in conjunction with the KIR near-infrared detector (Doyon et al. 1998) to search for stellar companions to 88 members of the VAST sample. The KIR instrument provides an angular field-of-view on the sky of $35''.6 \times 35''.6$, corresponding to a maximum physical separation limit to the detection of companions of ~ 1750 AU at a distance of 75 pc, assuming the target is positioned at the centre of the KIR detector. The dither pattern employed within the observational strategy led to a slightly larger effective search radius, as the target was moved between the four quadrants of the detector. The quality of the data obtained using this instrument configuration was excellent, approaching the diffraction limit of $0''.127$ in the K -band ($\lambda = 2.2\mu\text{m}$), corresponding to a minimum separation sensitivity limit to stellar companions of ~ 9 AU at a distance of 75 pc. Examples of both an unsaturated and a saturated exposure obtained using the CFHT are shown in Figure 4.2, demonstrating the capability of the instrument to detect both stellar binary companions (middle panel), and companion candidates at the bottom of the Main Sequence (right panel).

4.1.2 Gemini North - ALTAIR + NIRI

A significant proportion of the survey data, 22.5% of the overall number of observations, were obtained from the Gemini North observatory, also located on the summit of Mauna Kea,

Hawai'i. The 8.1 metre telescope, in science operation since 2000, is home to a significant number of world-class astronomical instruments. Mounted upon the Cassegrain focus of the Gemini North telescope, the ALTitude conjugate Adaptive optics for the InfraRed (ALTAIR - Richardson et al. 1998) adaptive optics package was used in conjunction with the Near-InfraRed Imager and Spectrometer (NIRI - Hodapp et al. 2003) to search for stellar companions to 73 members of the VAST sample. The observations obtained at Gemini North have significantly greater sensitivity to fainter companions, due primarily to the increased primary mirror diameter with respect to the other observatories employed within this study. A significant portion of the observations were this sensitive to companions below the bottom of the Main Sequence, however the frequency of such companions will not be discussed within the context of this work.

The NIRI instrument provides an angular field of view on the sky of $21''.7 \times 21''.7$, corresponding to a maximum physical separation limit to the detection of companions of ~ 1150 AU at a distance of 75 pc, assuming the primary is positioned at the centre of the detector. The observations obtained with the NIRI instrument were scheduled in queue mode, ensuring that the observations were made during favourable atmospheric conditions. As a result, the observations are generally of an excellent quality, approaching the diffraction limit of $0''.056$, corresponding to a physical separation of ~ 4 AU at a distance of 75 pc. The observations were obtained with the Cassegrain rotator disabled, causing the orientation of celestial North to vary on the detector depending on the altitude and azimuth of the target being observed. As a consequence, each science image obtained at Gemini North was de-rotated using the coordinate system information given within the image header file to ensure the angle of celestial North was oriented in the positive y direction on the detector. Examples of both an unsaturated and a saturated exposure obtained using the ALTAIR+NIRI instrument package are shown in Figure 4.3, demonstrating the capability of the instrument to detect both stellar binary companions (middle panel), and companion candidates at the bottom of the Main Sequence (right panel).

4.1.3 Lick Observatory (Shane Telescope) - IRCAL

Data obtained using the 3 metre Shane telescope at the Lick Observatory on the summit of Mount Hamilton, California, constituted 20.7% of the overall number of dedicated observations obtained as a part of the VAST survey. The Infrared Camera for Adaptive optics at Lick observatory (IRCAL - Lloyd et al. 2000) was used in conjunction with the Lick Adaptive Optics System to search for stellar companions to 67 members of the VAST sample. A significant number of observations obtained using the IRCAL instrument were superseded with observations obtained at either CFHT or Gemini North, which have a greater sensitivity to fainter companions. Excluding these, a total of nine targets were only observed with the IRCAL instrument.

The IRCAL instrument provides an angular field of view on the sky of $19''.5 \times 19''.5$, corresponding to a maximum physical separation limit to the detection of companions of ~ 1030 AU at a distance of 75 pc, assuming the primary is positioned at the centre of the detector. The observations obtained with the IRCAL instrument were of good quality, approaching the diffraction limit of $0''.151$, corresponding to a physical separation of ~ 11 AU at a distance of

Image Copyrighted
Figure can be found at:
[http://mtham.ucolick.org/
public/tele_inst/3m/](http://mtham.ucolick.org/public/tele_inst/3m/)

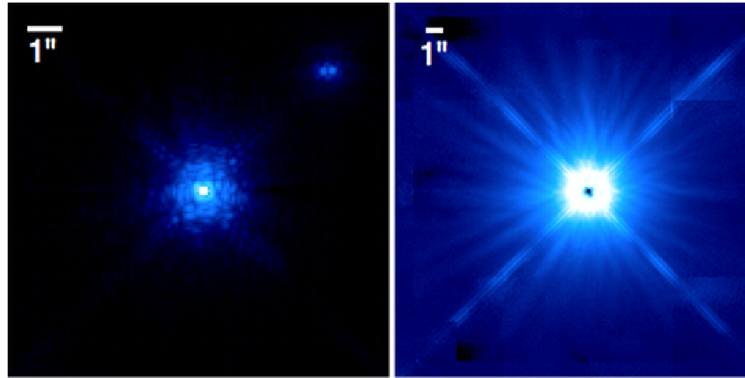


Figure 4.4: (*left panel*): An image of the 3 metre Shane telescope at the Lick Observatory on the summit of Mount Hamilton, California (image credit Laurie Hatch). (*middle panel*): An unsaturated image of the F0V star HIP 21036 obtained using the IRCAL detector at the Lick Observatory with the $\text{Br}\gamma$ narrow-band filter, resolving the system into a hierarchical triple. (*right panel*): A saturated image of the A5m star HIP 21402, increasing the sensitivity to fainter companion candidates, obtained using the wide-band K_S filter.

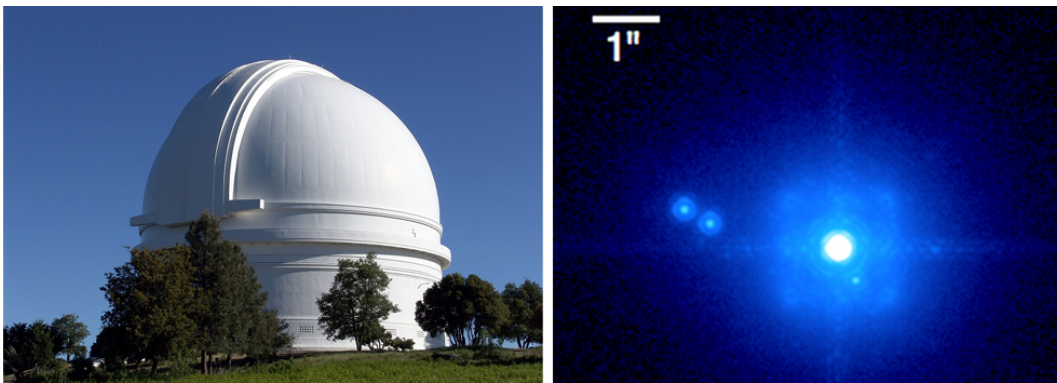


Figure 4.5: (*left panel*): An image of the 5.1 metre Hale telescope at the Palomar observatory on the summit of Mount Wilson, California. (*right panel*): An unsaturated image of the A7V star HIP 44127 obtained using the PHARO detector at Palomar with the $\text{Br}\gamma$ narrow-band filter, resolving the system into a hierarchical triple.

75 pc. Examples of both an unsaturated and a saturated exposure obtained using the IRCAL instrument are shown in Figure 4.4, demonstrating the capability of the instrument to detect both stellar binary companions (middle panel), and candidate companions approaching the bottom of the Main Sequence (right panel).

4.1.4 Palomar Observatory (Hale Telescope) - PHARO

The final source of dedicated observations obtained as a part of the VAST survey was the Hale telescope at the Palomar observatory, on the summit of Mount Wilson, California, providing 18.5% of the total number of observations obtained. The Palomar High Angular Resolution Observer (PHARO - Hayward et al. 2001) detector was used in conjunction with the adaptive optics instrument mounted upon the Hale 5.1 metre telescope to resolve stellar companions to 60 members of the VAST sample. A significant difference between the observing strategy em-

Image Copyrighted
 Figure can be found at:
<http://www.eso.org/public/about-eso/esoglance.html>

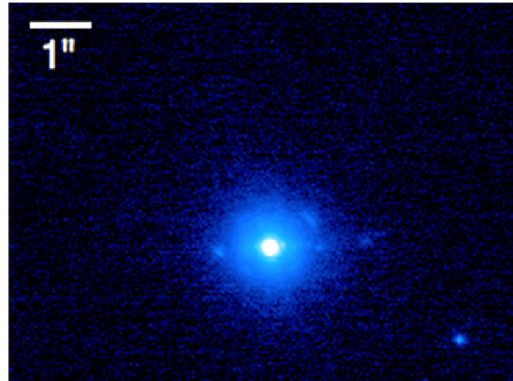


Figure 4.6: (*left panel*): An image of the Very Large Telescope (VLT) at the ESO Paranal Observatory on the summit of Cerro Paranal, Chile (image credit ESO). The NACO instrument is mounted upon the fourth Unit Telescope (UT4), at the far right of the image. (*right panel*): An unsaturated image of the A5V star HIP 70400 obtained using the NACO detector at the VLT with the IB2.18 narrow-band filter, resolving a faint companion candidate.

ployed when using the PHARO instrument was needed due to the requirement that saturation of the detector was prohibited. In order to search for faint companions to the targets observed using the PHARO instrument a significant number, typically 50, of unsaturated observations were obtained of each target to increase sensitivity to faint companions. This strategy was insufficient to achieve the sensitivity required to detect companions at the bottom of the Main Sequence. As a result, a significant number of observations obtained using the PHARO instrument were superseded with observations obtained at either CFHT or Gemini North, which have a greater sensitivity to the faintest companions at the bottom of the Main Sequence. Excluding these, a total of 20 targets were only observed with the PHARO instrument.

The PHARO instrument provides an angular field of view on the sky of $36''.2 \times 36''.2$, corresponding to a maximum physical separation limit to the detection of companions of ~ 1360 AU at a distance of 75 pc, assuming the primary is positioned at the centre of the detector. The observations obtained with the PHARO instrument were of excellent quality, approaching the diffraction limit of $0''.089$, corresponding to a physical separation of ~ 7 AU at a distance of 75 pc. An example of an exposure obtained using the PHARO instrument is shown in Figure 4.5, demonstrating the capability of the instrument to detect stellar binary companions approaching the bottom of the Main Sequence (right panel).

4.2 Archival data

In addition to the dedicated observations described within the previous section, the CFHT and ESO archive facilities were searched for archival observations of VAST sample members within the Northern and Southern celestial hemispheres, respectively. For the Northern hemisphere subsample, targets with declinations of $\delta \gtrsim -28^\circ$, the CFHT archive facility was queried for previous observations obtained using the PUEO/AOB + KIR instrument configuration, which was employed for the dedicated observations described in §4.1.2, during the previous ~ 12 years of operations. Observations of 21 individual VAST sample targets were retrieved from the

CFHT archive facility, dating from between 2001 and 2007, and are summarised in Table 4.2, alongside the filter combinations used, and the principal investigator of the original observing request. Although the archival data were sourced from a number of distinct programmes, with differing scientific goals, the observing strategies are roughly consistent with the observing strategy employed in the dedicated observations described previously; typically consisting of a series of unsaturated exposures, dithered across the detector, followed by a series of deeper exposures to detect faint companion candidates.

Table 4.2: Source of archival observations

Telescope	Proposal ID	PI	Observations
CFHT	2001AF11	Gerbaldi	8
	2001BF21	Catala	1
	2006BF07	Galland	7
	2007BF04	Lagrange	4
	Unknown	Jewitt	1
NACO	074.D-0180(A)	Ivanov	4
	076.D-0108(A)	Ivanov	4
	081.C-0653(A)	Lagrange	2
	272.D-5068(A)	Ivanov	5

For the Southern subsample of the VAST survey targets, with declinations of $\delta \lesssim 28^\circ$, the ESO archive facility was searched for observations obtained using the NAOS+CONICA instrument package mounted upon the 8.2 metre Unit Telescope 4 (UT4) at the Very Large Telescope (VLT), at the summit of Cerro Paranal, Chile. In operation since 1998, the VLT represents one of the most advanced observatories available to the astronomy community, and is host to some of the most sophisticated instruments ever constructed for an observatory of this size. Mounted on UT4, the Nasmyth Adaptive Optics System (NAOS - Rousset et al. 2003), used in conjunction with the Coude Near Infrared Camera (CONICA - Lenzen et al. 2003), provides similar capabilities to detect stellar companions to nearby stars as with the instruments described in the previous section. The archive was searched for observations of the members of the VAST sample which are not observable from the observatories within the Northern Hemisphere, and observations of 15 individual VAST targets were obtained, summarised in Table 4.2. As with the observations obtained from the CFHT archive, the observational strategy was broadly consistent to the strategy employed to obtain the dedicated observations described in the previous section; typically consisting of a series of unsaturated exposures with a narrow- or intermediate-band filter, dithered across the detector. The sensitivity of the CONICA instrument removed the requirement to obtain a set of saturated exposures to achieve the sensitivity necessary to detect faint companions at the bottom of the Main Sequence.

The observations obtained with the CONICA instrument had a field-of-view of $27''.7 \times 27''.7$, corresponding to a maximum physical separation limit to the detection of companions

of ~ 1460 AU at a distance of 75 pc, assuming the primary is positioned at the centre of the detector. The observations obtained with the CONICA instrument were of excellent quality, approaching the diffraction limit of $0''.056$, corresponding to a physical separation of ~ 4 AU at a distance of 75 pc. An example of an exposure obtained using the CONICA instrument are shown in Figure 4.6, demonstrating the capability of the instrument to detect stellar companions approaching the bottom of the Main Sequence (right panel).

4.3 Data reduction pipeline

4.3.1 Image processing

The science images obtained as a part of the dedicated observations described previously were obtained using a consistent observational strategy. Unsaturated exposures of each primary were obtained using a narrow-band filter (e.g. Brackett-Gamma - Br γ), from which the magnitude difference between primary and any resolved companion could be calibrated. These observations were typically taken using a 3- or 5-point dither pattern on the detector, in order to remove the effect of bad pixels and cosmic ray events, and enabling the estimation of the sky background through a combination of the individual exposures. Longer exposures were then obtained using a wide-band filter (e.g. K-prime - K'), causing a saturation of the target on the detector, enabling the detection of companions at the bottom of the Main Sequence ($\Delta K \sim 10$) for the majority of the targets within the sample. These observations were also taken with a dither pattern on the detector, significantly increasing the angular area searched for companions in the vicinity of each target. The only exceptions to this strategy within the dedicated observations were those obtained from the Palomar observatory, on which the saturation of the detector was not permitted. Instead of obtaining saturated exposures, an average of 50 short unsaturated exposures were obtained in order to extend the sensitivity to companions towards the bottom of the Main Sequence. Each science image obtained as a part of this survey was calibrated using the standard near-infrared data reduction process, which is described in detail below. This reduction pipeline removes systematic biases present within the data caused by non-linearities of the detector, or spurious detections caused by either bad pixels or cosmic ray events.

Dark current and bias removal

The imaging detectors used to obtain the observations described within this section consist of either mercury cadmium telluride (HgCdTe), or indium antimonide (InSb). The basic principles of photon detection are the same regardless of the materials used in construction of the detector; an incoming photon from the source to be imaged excites an electron from the valance band to the conduction band within the detector. These electrons are collected in the individual pixels of the detector, and converted into a digital signal to be read by a computer. The thermal excitation of electrons within the valance band of the detector material can cause these electrons to jump the band gap, becoming collected within the potential well of an individual pixel (Howell 2000). These electrons are then indistinguishable from electrons created due to

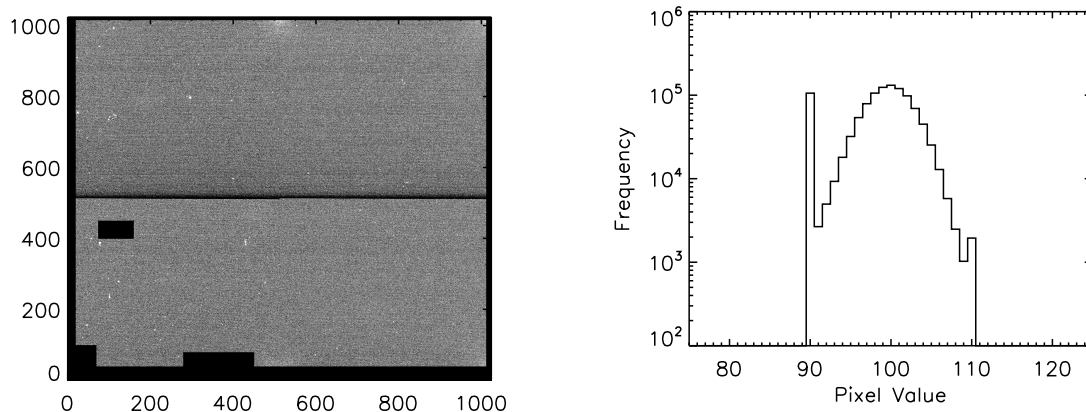


Figure 4.7: (*left panel*): A 10 second dark frame obtained using the KIR detector at the CFHT in 2010. The division between the upper and lower half of the detector has a significantly lower dark current than the average value. A pixel mask is used to remove cosmetic defects near the edges of the detector. (*right panel*): A histogram of the pixel values within the dark frame image. The values are normally distributed about the average value, with a notable peak at ~ 90 counts due to the lower pixel values within the boundary between the upper and lower halves of the detector.

the photoelectric effect caused by photons from astronomical sources, and constitute the dark current of the detector. Cryogenic cooling of the detector is used to significantly reduce the thermal excitation of electrons within the valance band, decreasing the number of dark current electrons by several orders of magnitude compared relative to the room temperature value (Howell 2000), however it is still non-negligible and needs to be removed from any science images obtained. In addition to the dark current, a significant source of noise is introduced when the individual pixels of the detector are read out by the detector electronics, and converted into digital values. This readout noise - or bias - is caused by the inherent inaccuracies of an analogue to digital conversion process, and the introduction of spurious electrons into the signal of interest by the detector electronics.

These two sources of noise must be estimated and removed from all science images obtained before any analysis can be completed. The dark current and bias can be simultaneously estimated by taking an exposure with the detector whilst keeping the camera shutter closed, hereafter called a dark frame. The two components of noise will be included within this dark frame, the duration of the exposure will introduce a certain amount of dark current into the resulting image, depending on the duration of the exposure, and the bias will be introduced as the individual pixels are read by the detector electronics. As the dark current is highly dependent on the duration of the exposure, a dark frame must be obtained for each unique exposure time used to obtain the science images - for example, 0.1 seconds for an unsaturated exposure, and 10 seconds for a saturated exposure. To remove both the random fluctuations in the dark current and bias level, and the effect of cosmic rays penetrating the closed shutter, a large number of dark frames are obtained, and are averaged through a median combination to obtain the final dark frame estimate. An example of the dark frame for a 10 second exposure of

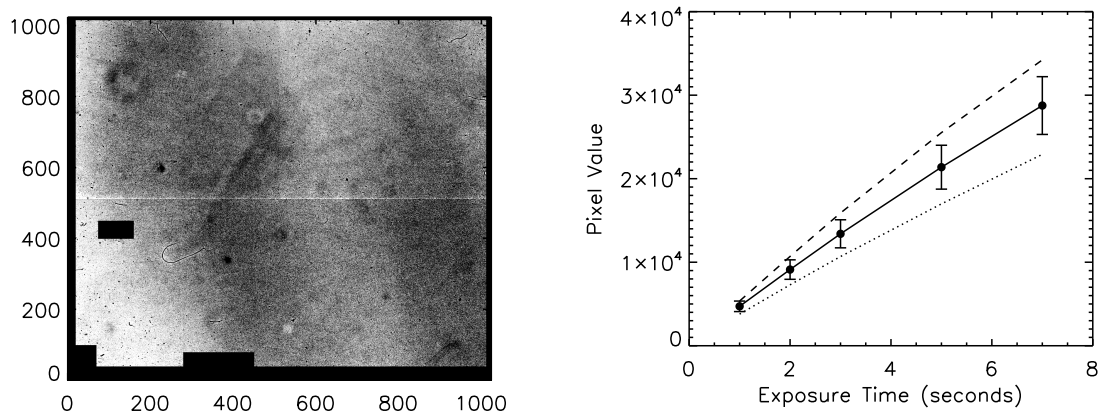


Figure 4.8: (*left panel*): An example flat field image obtained with the wide-band K' filter using the KIR detector at the CFHT in 2010. The flat field depicts how efficient each pixel is at converting photons into a digital signal, with white pixels being twice as efficient as average, and black pixels being only half as efficient. Each science image must be divided by this frame to correct for these non-linearities within the detector. Numerous cosmetic defects are apparent on this image, including an eyelash and numerous dust particles. (*right panel*): The average pixel value as a function of exposure time when the KIR detector is uniformly illuminated with the dome flat field lamps (solid line), and corresponding standard deviation (error bars). A pixel with a high (dashed line) and low (dotted line) photon to data-unit efficiency are plotted for reference. Each pixel of the flat field frame contains the gradient of a linear fit to the pixel value as a function of exposure time, normalised so the average gradient is unity.

the KIR detector on the CFHT is shown in Figure 4.7 (left panel), alongside a histogram of the pixel counts in Figure 4.7 (right panel). In more general terms, for a set of science exposures $I(t_{\text{exp}})$ with exposure time t_{exp} , an estimate of the dark frame $D(t_{\text{exp}})$ must be obtained for each unique value of t_{exp} from a median combination of n individual dark frames $d_i(t_{\text{exp}})$ obtained with exposure time t_{exp} ,

$$D(t_{\text{exp}}) = \text{Median} [d_0(t_{\text{exp}}), d_1(t_{\text{exp}}), \dots, d_{n-1}(t_{\text{exp}}), d_n(t_{\text{exp}})] \quad \forall t_{\text{exp}} \in S \quad (4.1)$$

where $S = \{t_{\text{exp}}^0, t_{\text{exp}}^1, \dots, t_{\text{exp}}^{m-1}, t_{\text{exp}}^m\}$ is the set of m exposure times for which a dark frame estimate is required. The corresponding estimate for the dark frame is then subtracted from each science exposure, constituting the first part of the reduction process.

Detector linearity

The number of photons required to excite an electron out of the valance band of the detector, defined as the quantum efficiency, varies per pixel across the detector due to imperfections in the manufacturing process (Howell 2000). Defects on the detector surface can also cause individual pixels to be either unresponsive to incoming photons, or have a significantly non-linear behaviour. To ensure that photometric measurements are not affected by such variations, the response of each pixel to incoming photons must be calibrated relative to every other pixel on the detector. By uniformly illuminating the detector, typically using a lamp mounted on the

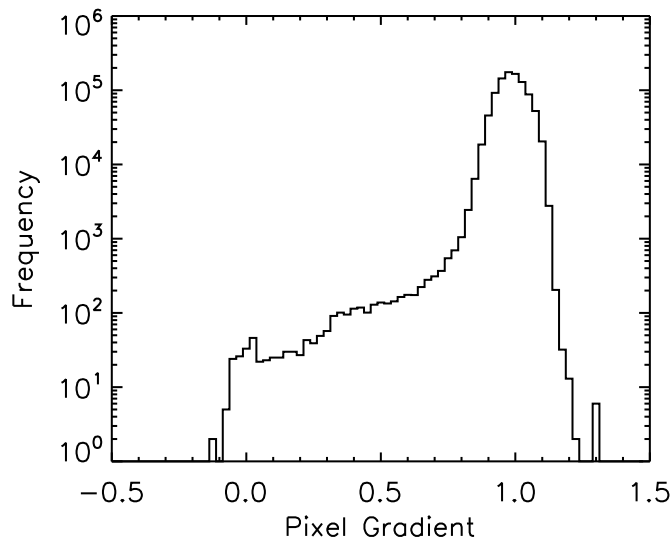


Figure 4.9: The histogram of pixel values within the example flat field frame shown in Figure 4.8. The flat field has been normalised such that the average value is unity, with the distribution skewed towards a higher frequency of less efficient pixels. Those pixels exhibiting a strong non-linearity, e.g. < 0.5 , are flagged as bad pixels and interpolated over.

inside of the telescope done, a flat field can be obtained from which the response of each pixel can be estimated.

The flat field frame can be estimated by obtaining a series of exposures of incrementally increasing exposure times (e.g. 5s, 10s, ... 25s) whilst the detector is uniformly illuminated. As with the process for obtaining the dark frame, a series of exposures are taken at each given exposure time, and are averaged through median combination to remove both the variations in pixel counts introduced by the imperfect analogue to digital conversion carried out when the detector is read, and the effect of cosmic ray strikes on the detector. For each pixel in the detector, a linear curve is fit to the number of counts registered within the pixel as a function of the exposure time, as shown in Figure 4.8 (right panel). The gradient of the fit for each pixel is normalised so that the average gradient is unity, and saved as the flat field as shown in 4.8 (left panel). Each science image, after the dark frame has been subtracted, is divided by this flat field to remove the inter-pixel variations of the sensitivity to incoming photons. Those pixels exhibiting strongly non-uniform behaviour, as described in Figure 4.9, are flagged as bad pixels during this step of the reduction process, and are further discussed in the following section. The wavelength dependence of the quantum efficiency requires this procedure to be repeated for each filter set used during the science observations. Each science image, following the subtraction of the dark frame, is then divided by the flat field frame corresponding to the filter used to obtain the observation.

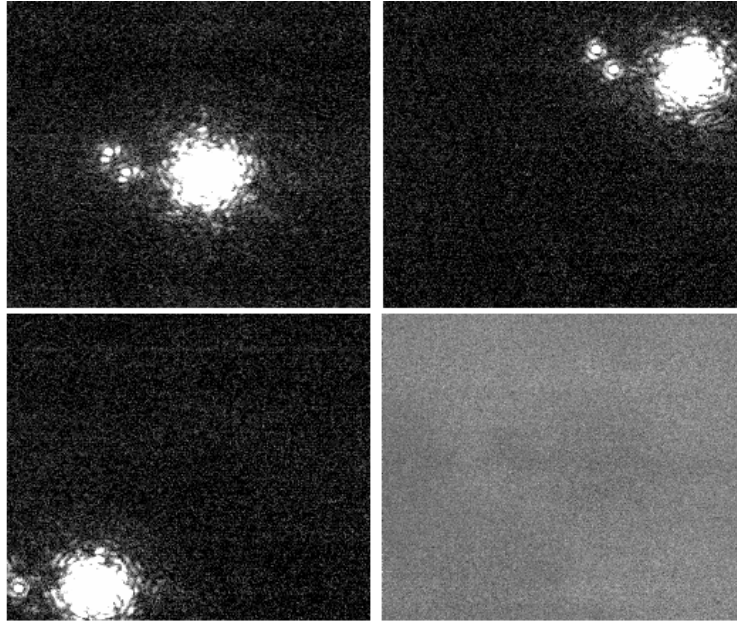


Figure 4.10: (*top row and bottom left panel*): Three example images of the A7V star HIP 44127 at different dither positions on the KIR detector. Each image has a linear scale between -5 (black) and 50 (white). (*bottom right panel*): The sky background can be estimated from a combination of all the images obtained of an individual target, before registration to a common centre. The resulting sky background image is linearly scaled between -5 (black) and 5 (white).

Bad pixels and cosmic rays

Defects on the surface of the detector, and the presence of foreign objects (e.g. Figure 4.8), can cause pixels to exhibit strongly non-linear behaviour when exposed to incident photons. These pixels, identified during the estimation of the flat field described previously, are typically non-transient and need to be removed from each science image obtained. A bad pixel map is constructed from the location of each of these errant pixels, and their values within the science images are replaced by a cubic interpolation of the surrounding functional pixels. Transient events, such as a cosmic ray striking the detector, also need to be located and removed. A cosmic ray will typically cause the pixel it strikes to become saturated, significantly higher than the background level. These cosmic ray events are located by applying a standard deviation cut-off to each pixel, with the value of each pixel compared with the standard deviation of an area on the detector of width 20 pixels centred on the pixel of interest. Each pixel with a value discrepant from the surrounding pixels by at least 5σ is flagged and its value replaced with a cubic interpolation of the neighbouring pixels. The dithering strategy employed in the observations also helps to minimise the likelihood that a bad pixel or cosmic ray falls onto the same pixel as a companion candidate.

Sky background

Typically, near-infrared observations involve obtaining an image of the science target, followed by an image of the sky background in the vicinity of the target which can be used to estimate

the level of the sky background in the science image. Due to the large overheads this would introduce into a programme as large as the VAST survey, the sky background for each target was instead estimated from a median combination of each science image obtained of the target. As the target was dithered across the detector, an average of the individual science images through median combination will remove the target, leaving an estimate of the sky background. This procedure is demonstrated in Figure 4.10, with three example images at different dither positions shown of the 150 images obtained for this target, alongside an estimate of the sky background obtained through a median combination of the science images. The sky background is subtracted from each science image; after the dark current, non-linearities, and bad pixels have been removed; completing the reduction pipeline.

4.3.2 Image registration

Unsaturated images

To increase sensitivity to faint companions, and increase the signal-to-noise ratio (SNR) of any detection, the individual science images obtained for each target are aligned to a common centre and averaged through a median combination. The registration of the unsaturated images obtained using a narrow-band filter, such as Br γ , is achieved by determining the centroid of the star within each image based on a fit of the PSF to a Gaussian profile. An initial estimate of the centroid of the primary is achieved by finding the highest valued pixel within the image. Taken as the initial guess of the centroid, the image is passed to the IDL Gaussian centroid algorithm GCNTRD. The centroids returned by the algorithm, typically accurate to a sub-pixel level, are used to register each image of an individual target to a common centre using a cubic interpolation of the data. The images are then averaged through a median combination, to create the final science image. A complication can arise when the target has a close binary companion close to the resolution limit of the data. In this case, the PSF of the target is contaminated by the PSF of the companion, often leading to a failure of the Gaussian centroid algorithm. In this case, the centroid of the target is found by performing a least squares minimisation of a Gaussian fit to the core of the PSF, with the companion obscured using a pixel mask.

Saturated images

The saturation of the target within the science exposures obtained using wide-band filters prevent the registration of the individual images based on the centroid of the PSF of the target. An estimate of the centroid of the target can be determined through an analysis of the diffraction spikes present within the saturated exposures, caused by the presence of the secondary mirror supports on each telescope. By cross-correlating the position of the diffraction spikes within each individual saturated exposure of a given target, the offsets required to register each image to a common centre can be calculated (e.g. Lafrenière et al. 2007a). The position of the diffraction spikes in each saturated science image was correlated with the position in a given reference science image, typically the first saturated exposure obtained of a given target, the

centroid of which is determined manually to an uncertainty of ~ 1 pixel. The presence of a binary companion, or a background object, can introduce a significant bias in the magnitude of the correlation, leading to a poor estimate of the true centroid of the primary. To reduce the effect of other objects within the field on the correlation calculation, and to significantly reduce the computational requirement of the calculation, an image mask is applied which sets all pixels outside the locale of the diffraction spikes to zero. The correlation between each image and the corresponding reference image is then calculated based on the normalised cross-correlation function, removing any bias introduced by changes in the intensity of the diffraction spike due to seeing variations. The set of offsets resulting in the largest value of the cross-correlation parameter is used as the offset required to register the image to a common centre with respect to the reference image.

4.4 Astrometric calibration

To ensure that the differential positions between primary and any resolved companions are accurately converted into angular separations and position angles on the sky, each detector must be calibrated based on an observation of an astrometric calibration field; either the Trapezium cluster, or binary systems with well determined orbital parameters.

4.4.1 Trapezium observations

Using the absolute positions of the Trapezium cluster members determined in the high-resolution near-infrared observations by McCaughrean & Stauffer (1994), the expected separation and position angle between each pair of stars within the cluster can be calculated. Observations of the Trapezium were obtained, either through dedicated observations or from archival data, at numerous epochs with KIR (CFHT), NIRI (Gemini North), and NACO (VLT). For each observation of the Trapezium, the data were reduced in the same manner as described previously, and the relative position of each Trapezium cluster member was estimated using the IDL GCNTRD algorithm. Typically, the number of Trapezium cluster members resolved within the AO observations was between $10 \lesssim n \lesssim 25$ (e.g. Figure 4.11). A comparison of the separation in pixels on the detector of each Trapezium cluster member pair to the expected angular separation and position angle is then used to estimate the plate scale of the detector p , measured in milliarcseconds per pixel, and the orientation of the detector relative to celestial north β , referred to as the true north correction. Given the large number of pairs, calculated as $n(n-1)/2$, and their wide spatial distribution, a significant number of paths across the detector are sampled. This ensures that any non-uniformities in the plate scale and the orientation across the detector are accounted for within the uncertainties of the calibration values (Figure 4.12).

4.4.2 Calibration binary observations

For detectors where no observations of the Trapezium cluster were obtained, such as PHARO (Palomar) and IRCAL (Lick) in 2008, the plate scale and the orientation relative to celestial north of the detector were estimated from observations of binary systems obtained near-

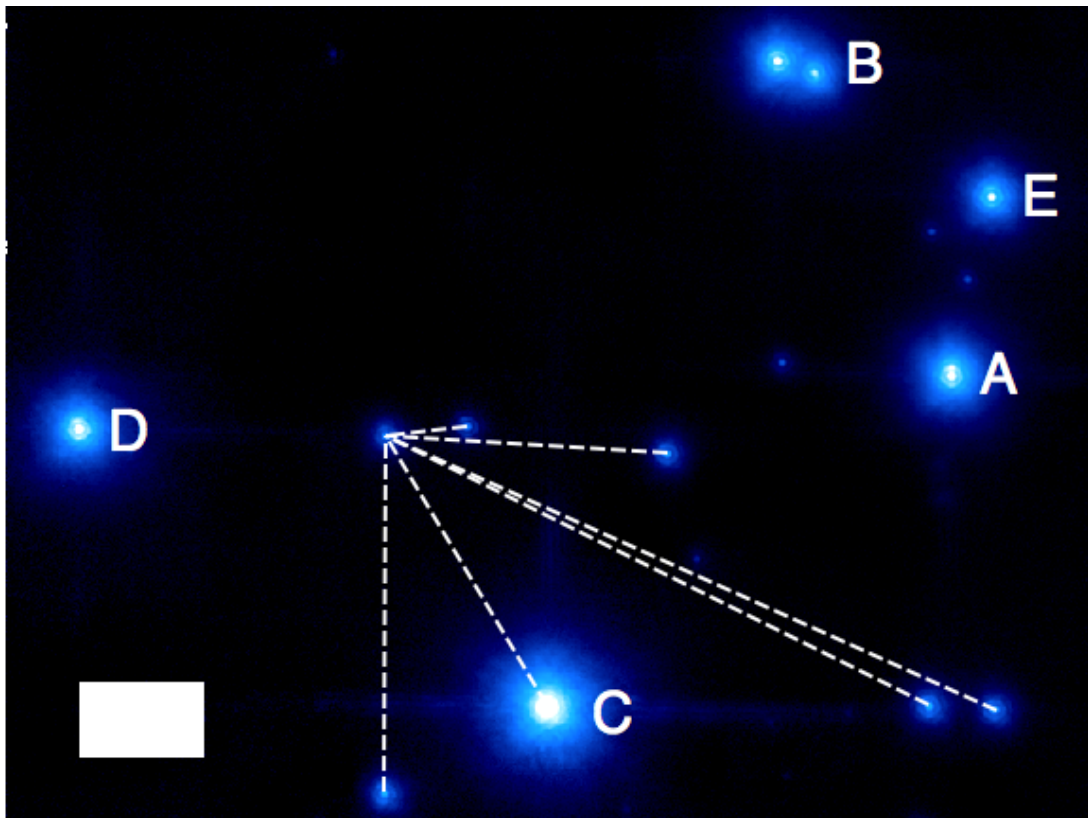


Figure 4.11: An observation of the Trapezium cluster obtained at the CFHT in 2007. The stars θ Ori A, θ Ori B, θ Ori C, θ Ori D, and θ Ori E are labelled for reference. The relative pixel offsets between each pair of resolved Trapezium cluster members (e.g. dashed lines) are compared with the offsets published within McCaughrean & Stauffer (1994), from which the plate scale and orientation of the detector are estimated.

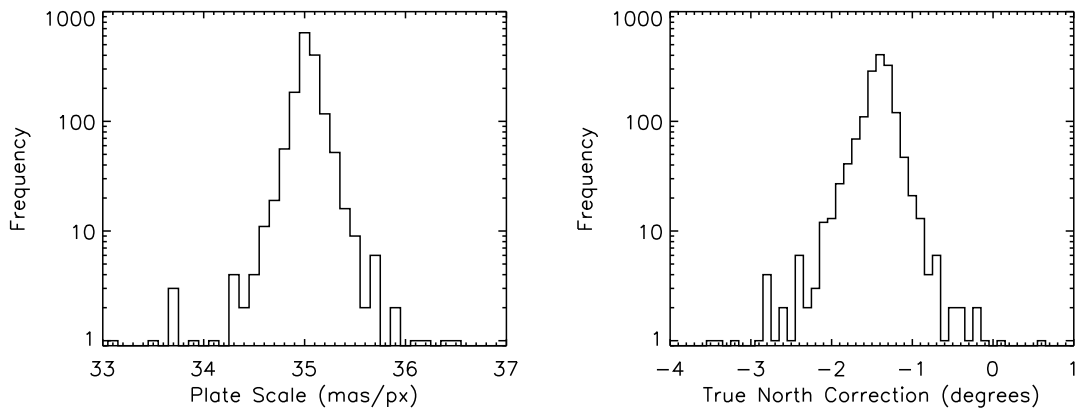


Figure 4.12: A total of 56 members of the Trapezium cluster are resolved within the observation shown in Figure 4.11, corresponding to 1540 unique pairs. For each pair, the plate scale and orientation of the detector is estimated from the relative pixel offset between each star and the published separation and position angle presented in McCaughrean & Stauffer (1994). The mean value of each distribution is used as the estimate for the plate scale and true north correction, and the standard deviation of each distribution is used as the corresponding statistical uncertainty.

simultaneously with detectors calibrated using observations of the Trapezium cluster. For IR-CAL, the plate scale and orientation were calibrated using an observation of the HIP 2355 binary system, which was observed on the same night, 16 October 2008, at the Lick Observatory and with NIRI at Gemini North. A wider binary, HIP 55705, was used to calibrate the PHARO detector, with an observation at the Palomar observatory on 11 April 2008, followed by an observation with KIR at the CFHT on 13 June 2008. The large separation between the two components of the HIP 55705 system results in a negligible orbital motion between the two components on the time scale of the two observations.

4.5 Candidate identification

Companion candidates are identified through a visual examination of the final combined science image (c.f. Raghavan et al. 2010). The position and relative brightness of each companion candidate is estimated, as described in the following section, and stored within a database for future analysis.

4.5.1 Separation and position angle estimates

The absolute pixel position of the companion candidates is determined using the IDL Gaussian centroid algorithm GCNTRD. The resulting pixel centroids (x_b, y_b) are converted to a relative position of the companion candidate with respect to the primary using

$$\begin{aligned}\Delta x &= x_b - x_a \\ \Delta y &= y_b - y_a\end{aligned}\tag{4.2}$$

where x_a and y_a are the centroid of the primary determined during the image registration procedure described previously. The uncertainty on the relative position is therefore

$$\begin{aligned}\sigma_{\Delta x} &= \sqrt{x_a^2 \sigma_{x_a}^2 + x_b^2 \sigma_{x_b}^2} \\ \sigma_{\Delta y} &= \sqrt{y_a^2 \sigma_{y_a}^2 + y_b^2 \sigma_{y_b}^2}\end{aligned}\quad (4.3)$$

The relative offsets are then converted into a pixel separation r , and a position angle ϕ using the mathematical function `atan2`, as

$$\begin{aligned}r &= \sqrt{\Delta x^2 + \Delta y^2} \\ \phi &= [\text{atan2}(-\Delta x, \Delta y) + 2\pi] \bmod 2\pi\end{aligned}\quad (4.4)$$

The additional terms on the ϕ expression are required to express ϕ in the standard astronomical convention of the position angle increasing counter-clockwise from north. These values are converted into an angular separation ρ and position angle θ using the estimated detector plate scale p and the true north correction β , described in 4.4, along with their corresponding uncertainties, as

$$\begin{aligned}\rho &= pr = p\sqrt{\Delta x^2 + \Delta y^2} \\ \theta &= \phi + \beta = [\text{atan2}(-\Delta x, \Delta y) + 2\pi + \beta] \bmod 2\pi\end{aligned}\quad (4.5)$$

with a corresponding uncertainty in the angular separation σ_ρ of

$$\begin{aligned}\sigma_\rho^2 &= \left[\frac{\partial}{\partial p} \left(p\sqrt{\Delta x^2 + \Delta y^2} \right) \right]^2 \sigma_p^2 + \left[\frac{\partial}{\partial \Delta x} \left(p\sqrt{\Delta x^2 + \Delta y^2} \right) \right]^2 \sigma_{\Delta x}^2 \\ &\quad + \left[\frac{\partial}{\partial \Delta y} \left(p\sqrt{\Delta x^2 + \Delta y^2} \right) \right]^2 \sigma_{\Delta y}^2 \\ \sigma_\rho &= \sqrt{\sigma_p^2 (\Delta x^2 + \Delta y^2) + \frac{p^2}{\Delta x^2 + \Delta y^2} (\Delta x^2 \sigma_{\Delta x}^2 + \Delta y^2 \sigma_{\Delta y}^2)}\end{aligned}\quad (4.6)$$

and an uncertainty in the position angle of σ_θ of

$$\begin{aligned}\sigma_\theta^2 &= \left[\frac{\partial}{\partial \Delta x} (\text{atan2}(-\Delta x, \Delta y) + \beta) \right]^2 \sigma_{\Delta x}^2 + \left[\frac{\partial}{\partial \Delta y} (\text{atan2}(-\Delta x, \Delta y) + \beta) \right]^2 \sigma_{\Delta y}^2 \\ &\quad + \left[\frac{\partial}{\partial \beta} (\text{atan2}(-\Delta x, \Delta y) + \beta) \right]^2 \sigma_\beta^2 \\ \sigma_\theta &= \sqrt{\frac{\sigma_{\Delta x}^2 \Delta y^2 + \sigma_{\Delta y}^2 \Delta x^2}{(\Delta x^2 + \Delta y^2)^2} + \sigma_\beta^2}\end{aligned}\quad (4.7)$$

The angular separation is then converted into a projected separation a , in Astronomical Units (AU), based on the *Hipparcos* parallax π as

$$a = \frac{1000\rho}{\pi}\quad (4.8)$$

Table 4.3: Photometric filter transmission estimates

Observatory	Narrow-band Filter	Wide-band Filter	Relative Transmission (Γ)
CFHT	FeII	H	23.61 ± 1.18
CFHT	H2 ₁₋₀	K'	25.91 ± 1.30
Gemini	Br γ	K'	14.50 ± 0.72
Lick	H2 ₁₋₀	K	16.71 ± 0.84

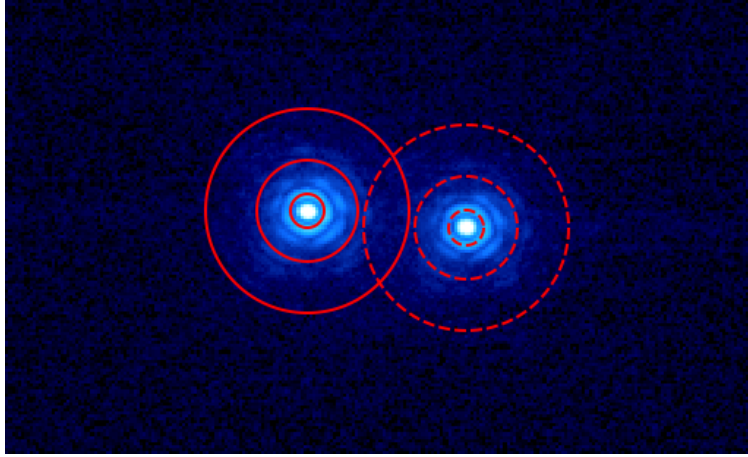


Figure 4.13: Flux estimates of the target star and a resolved companion candidate are based on aperture photometry. The value of the pixels within the inner annulus, of radius twice the FWHM of the target star, are summed to estimate the flux of the primary (solid line) and the resolved companion candidate (dashed line). The sky background, which is subtracted from the estimate of the flux, is estimated based on the pixel values within the inner sky annulus at three times the FWHM, and the outer sky annulus at six times the FWHM. The magnitude difference between the two stars is estimated from the logarithm of the flux ratio (Equation 4.10). The image is logarithmically scaled, with $\sim 90\%$ of the flux within the central annulus, and the separation of the pair is measured to be $1''.84$.

with a corresponding uncertainty in the projected separation σ_a of

$$\sigma_a = 1000 \sqrt{\frac{\sigma_\rho^2 \pi^2 + \sigma_\pi^2 \rho^2}{\pi^4}} \quad (4.9)$$

4.5.2 Photometry estimates

For companion candidates identified in narrow-band images, within which the PSF of the target star is not saturated, the magnitude difference is estimate using the flux of the target star F_a and companion candidate F_b as

$$\Delta m = 2.5 \log \left(\frac{F_a}{F_b} \right) \quad (4.10)$$

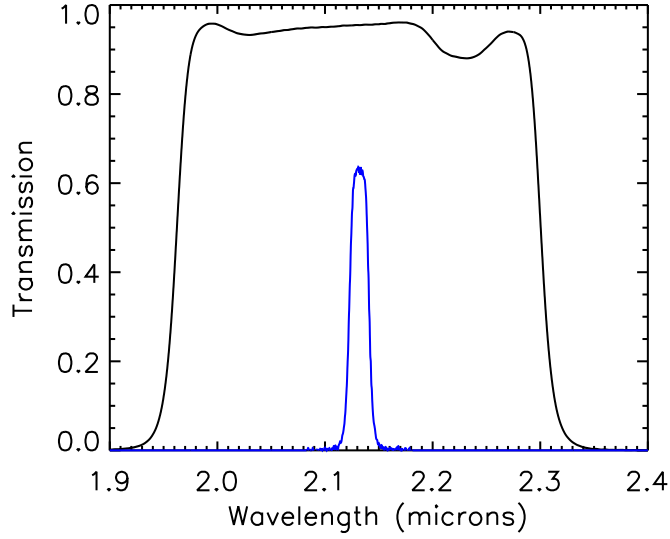


Figure 4.14: The transmission of the narrow-band $H2_{1-0}$ filter (blue line) and wide-band K' filter (black line) as a function of wavelength. The relative transmission of both filters is required to calibrate the photometry of companion candidates resolved within the wide-band images.

The fluxes F_a and F_b are estimated using aperture photometry, with an aperture of radius twice the full-width at half-maximum (FWHM) of the target star. Contamination from the sky background was estimated, and subtracted from the flux estimates, using an annulus with an inner radius of three times the FWHM, and an outer radius of six times the FWHM (Figure 4.13). The magnitude difference estimated from the average median combined image is used as the true value, with the statistical uncertainty being estimated from the standard deviation of the magnitude difference estimated within the individual images.

In order to estimate the relative flux of a companion candidate resolved within an image where the target star is saturated, an estimate of the expected brightness of the target star must first be made from the corresponding image taken with a narrow-band filter where the target is not saturated. The expected flux of the target star within the wide-band image F_w , is estimated using the flux measured within the narrow-band image F_n , and the ratio of the exposure times of the narrow-band and wide-band images t_w/t_n .

$$F_w = \Gamma \frac{t_w}{t_n} F_n \quad (4.11)$$

with the factor Γ estimated from the relative transmission of the narrow-band, T_n , and wide-band, T_w , filters (Figure 4.14), as

$$\Gamma = \frac{\int_0^\infty T_w d\lambda}{\int_0^\infty T_n d\lambda} \quad (4.12)$$

Values of Γ are calculated for all pairs of narrow-band and wide-band filters used to obtain the observations. The uncertainty in the values of Γ is conservatively estimated as $\sigma_\Gamma = 5\%$, with the final uncertainty on the estimate of the flux of the target in the wide-band image, F_w , being

determined as

$$\begin{aligned}\sigma_{F_w}^2 &= \left[\frac{\partial}{\partial \Gamma} \left(\Gamma \frac{t_w}{t_n} F_n \right) \right]^2 \sigma_{\Gamma}^2 + \left[\frac{\partial}{\partial F_n} \left(\Gamma \frac{t_w}{t_n} F_n \right) \right]^2 \sigma_{F_n}^2 \\ \sigma_{F_w} &= \sqrt{\frac{t_w}{t_n} (F_n \sigma_{\Gamma} + \Gamma \sigma_{F_n})}\end{aligned}\quad (4.13)$$

The magnitude difference of a companion candidate resolved within a wide-band image is then estimated based on the flux of the companion candidate F_b and the calculated flux of the primary F_w as

$$\Delta m = 2.5 \log \left(\frac{F_w}{F_b} \right) \quad (4.14)$$

with the corresponding uncertainty estimated as

$$\sigma_{\Delta m} = \sqrt{1.17882 \left(\frac{\sigma_{F_w}}{F_w} + \frac{\sigma_{F_b}}{F_b} \right)} \quad (4.15)$$

The absolute magnitude of a resolved companion candidate M_b is then estimated from the absolute magnitude of the primary as

$$M_b = M_a + \Delta m \quad (4.16)$$

with a corresponding uncertainty σ_{M_b} estimated as

$$\sigma_{M_b} = \sqrt{\sigma_{M_a}^2 + \sigma_{\Delta m}^2} \quad (4.17)$$

4.5.3 Mass-magnitude relations

The mass of each companion candidate resolved is estimated using the magnitude of the companion M_b , and the mass-magnitude relations presented in Siess et al. (2000). The companion is assumed to be of the same age and metallicity (Chapters 2.2.2 and 2.2.3) as the primary, and as such would lie on the same mass-magnitude relation, as shown in Figure 4.15. The mass ratio q of the system is therefore calculated as the ratio of the secondary M_2 to primary M_1 masses as

$$q = \frac{M_2}{M_1} \quad (4.18)$$

4.5.4 Background probability

The large number of targets within the sample excluded the possibility of obtaining a second epoch observation of each companion candidate resolved within the survey. It is therefore necessary to establish a statistical cut-off to exclude background objects from the binary statistics. An estimate of the probability of each companion candidate being an optical binary was made based on the local stellar densities for each target, measured from the *2MASS* source catalogue. The number of sources within a $2^\circ \times 2^\circ$ box of each target was determined in magnitude bins 1 magnitude in width from 0–14 mag for the J , H , and K_S bandpasses. An example plot of

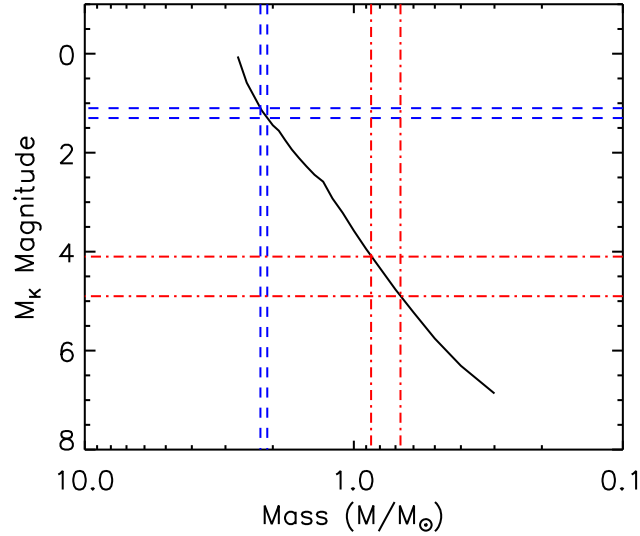


Figure 4.15: The mass-magnitude relation with an age of $\log t = 8.6$ and a metallicity of $Z = 0.02$ from Siess et al. (2000) (black line). The absolute magnitude and corresponding uncertainty of the primary, $M_a \pm \sigma_{M_a}$, and the resolved companion candidate, $M_b \pm \sigma_{M_b}$, are used to estimate the mass of each component from the mass magnitude relation. In this example, a star with an absolute magnitude of 1.2 ± 0.1 , corresponding to a mass of $2.16 \pm 0.06 M_\odot$ (blue dashed line), has a resolved companion candidate with an absolute magnitude of 4.5 ± 0.4 , corresponding to a mass of $0.77 \pm 0.10 M_\odot$ (red dashed line).

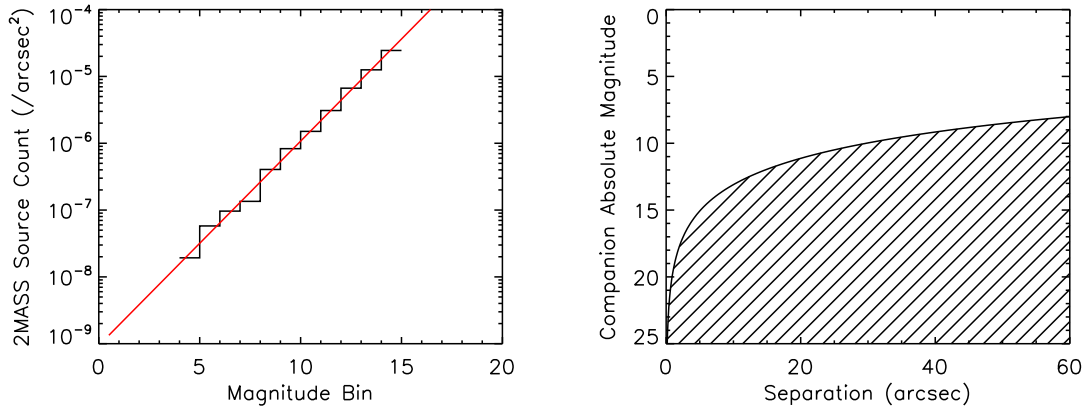


Figure 4.16: (*left panel*): The *2MASS* source count per square arcsecond as a function of source magnitude in the vicinity of HIP 57646 (black line). A logarithmic fit to the data is overplotted (red line). (*right panel*): The probability cut-off applied for companion candidates resolved within this study is shown for the star HIP 57646. Companion candidates with absolute magnitudes within the shaded region are classified as background objects, and are not included within the binary statistics. The boundary between the shaded and open region denotes the 95% probability based on the *2MASS* source density.

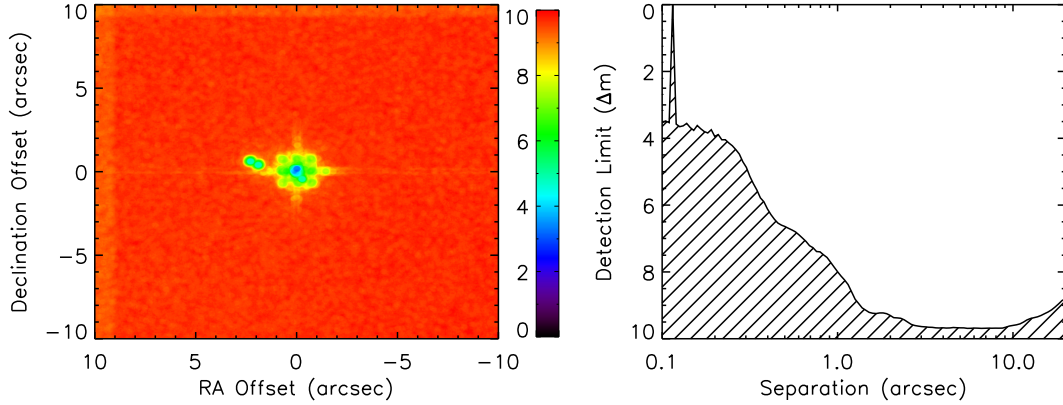


Figure 4.17: (*left panel*): The 3σ detection limit for the observation of HIP 44127 obtained using PHARO at the Palomar observatory in 2008. The colour scale indicates the faintest companion to which the data are sensitive. (*right panel*): The corresponding radial average of the sensitivity to faint companions for the observation of HIP 44127. The data are not sensitive to companions within the shaded region of the plot.

the *2MASS* source count for the star HIP 57646 as a function of source magnitude is given in Figure 4.16. A power law fit was applied to the counts such that

$$N = \pi\rho^2 10^{b+am} \quad (4.19)$$

where N is the number of sources within a separation ρ from the target, with an apparent magnitude of m , expressed as a function of the two fit parameters a , the gradient, and b , the intercept. The approximately 300 candidates with $N > 0.05$ are assumed to be background objects, and are not considered within any aspect of this study. After a sufficient time baseline has elapsed, second epoch observations of these candidate companions, specifically those with lower mass ratios, will reveal their true physical nature.

4.6 Detection limits

The sensitivity of each data set obtained is estimated in order to quantify the sensitivity of the data to faint companions. For each pixel within the final combined science image, the standard deviation of all surrounding pixels within a radius of twice the FWHM of the target star is determined. To remove the effect of the bright primary on the inter-pixel variance in the vicinity of the stellar PSF, a radial subtraction was first performed on each image. The faintest companion to which the data are sensitive is conservatively estimated as a signal five times this standard deviation σ , and can be quantified in terms of the peak flux of the target star A as

$$\Delta m_{\max} = 2.5 \log \left(\frac{A}{5\sigma} \right) \quad (4.20)$$

An example of this technique is given in Figure 4.17, with the companion sensitivity shown as a function of detector position (left panel), and angular separation (right panel). The sensitivity of images obtained using a wide-band filter, within which the primary is saturated, the peak value is obtained from the corresponding narrow-band image, and scaled using the filter transmission parameter described previously.

Subsequent to the reduction of the observations obtained as a part of the VAST survey, companion candidates were identified by a visual inspection of the final data. Prior to a statistical analysis of the distribution of the various properties of the resolved companion candidates, an estimate of the overall completeness of the survey is required. This will allow for a correction to be applied to the multiplicity fraction, and the mass ratio and separation distributions, to take into account the number of companions missed due to the varying nature of the survey completeness as a function of separation and magnitude difference.

5.1 Survey completeness

It is necessary to consider the completeness of the high-resolution adaptive optics observations prior to the discussion of resolved companion candidates, in order to statistically quantify the frequency of companions and the shape of the mass ratio and separation distributions. The detection limit of each observation is characterised based on the procedure described in §4.6, in terms of the position on the imaging detector relative to the central star (Figure 5.1, left panel). The square geometry of the detector leads to a varying level of completeness as a function of position angle, and as such the detection limit must be expressed in terms of separation and position angle relative to the central star. Figure 5.1 (right panel) demonstrates this coordinate transform, showing the clear dependence of the detection limit on the position angle relative to the central star. The completeness of the observation is then determined as a function of separation and magnitude difference, as shown in Figure 5.2. The completeness of the observation is then converted into a completeness distribution as a function of either the angular separation or physical separation on the x -axis, and a function of either the magnitude difference, or companion mass, or mass ratio on the y -axis, resulting in six distinct completeness distributions. For targets with multiple observations, the observation with the greatest sensitivity at each grid position within the sensitivity distribution is used, prior to the calculation of

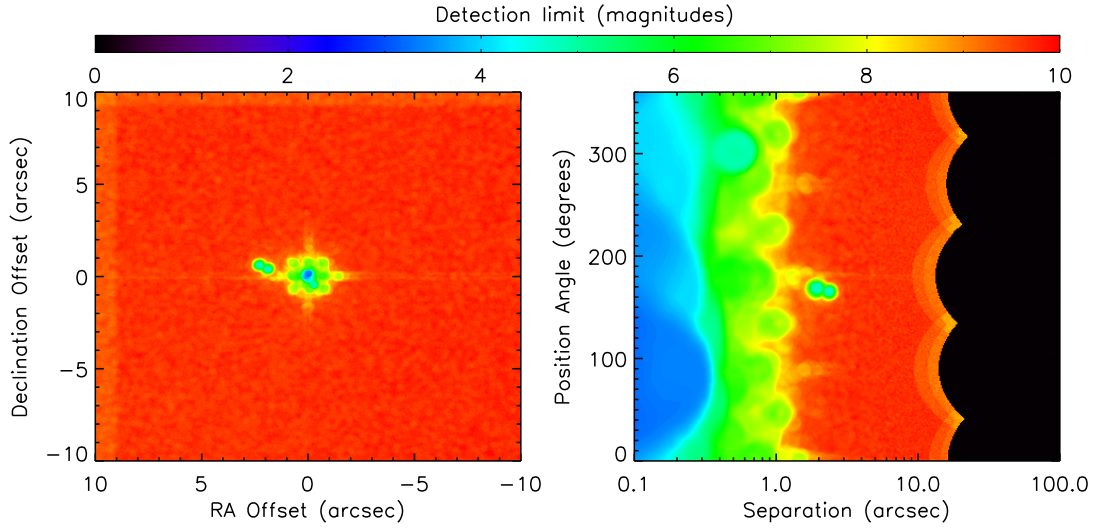


Figure 5.1: (*left panel*): The 3σ detection limit for the observation of HIP44127 obtained using PHARO at the Palomar observatory in 2008. The colour scale indicates the faintest companion to which the data are sensitive. (*right panel*): The same detection limit expressed in terms of polar coordinates (ρ and θ).

the various completeness distributions.

This process to determine the completeness, as a function of angular separation and magnitude difference, for example $c_i(\rho, \Delta m)$, is repeated for each target within the VAST sample described in Chapter 2. The overall completeness of the sample, e.g. $C(\rho, \Delta m)$, is then calculated using

$$C(\rho, \Delta m) = \frac{1}{N} \sum_{i=1}^N c_i(\rho, \Delta m) \quad (5.1)$$

with N representing the total number of targets within the sample, 233. The resulting completeness distribution of the overall sample is shown in Figure 5.3 - $C(\rho, \Delta m)$ and $C(a, \Delta m)$, Figure 5.4 - $C(\rho, M_2)$ and $C(a, M_2)$, and Figure 5.5 - $C(\rho, q)$ and $C(a, q)$. As the two primary statistical results of the survey, the mass ratio and separation distribution, are measured in terms of projected physical separation a and companion mass ratio q , it follows that a specific region of the $C(a, q)$ distribution suffering minimally from incompleteness should be selected from which the two distributions are estimated. Based on the level of completeness, only those companion candidates with $56 < a[\text{AU}] \leq 891$ and $0.05 \leq q \leq 1.00$ are considered in terms of the statistical analysis presented throughout this chapter.

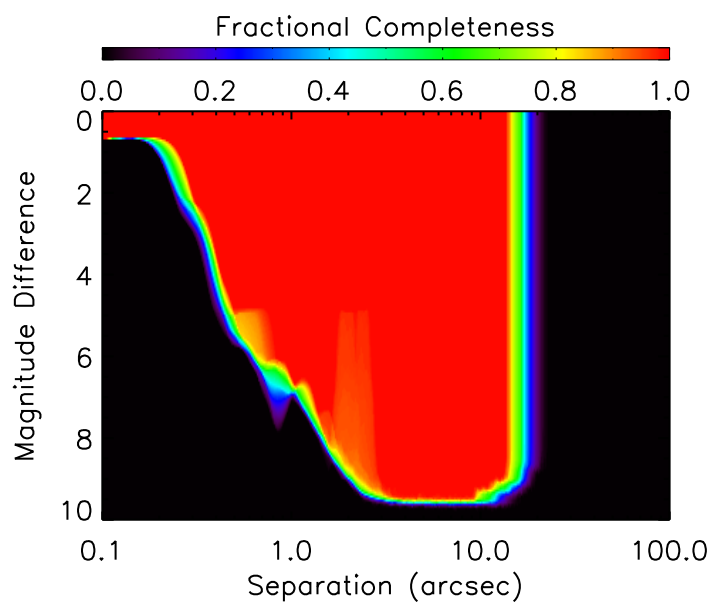


Figure 5.2: The completeness of the observation of HIP 44127 (see Figure 5.1) as a function of angular separation and magnitude difference. For each position within the $(\rho, \Delta m)$ grid, the fractional completeness of the observation is determined, with a value of 1.0 indicating that the observation is sensitive to companions at this separation and magnitude difference at all position angles relative to the central star.

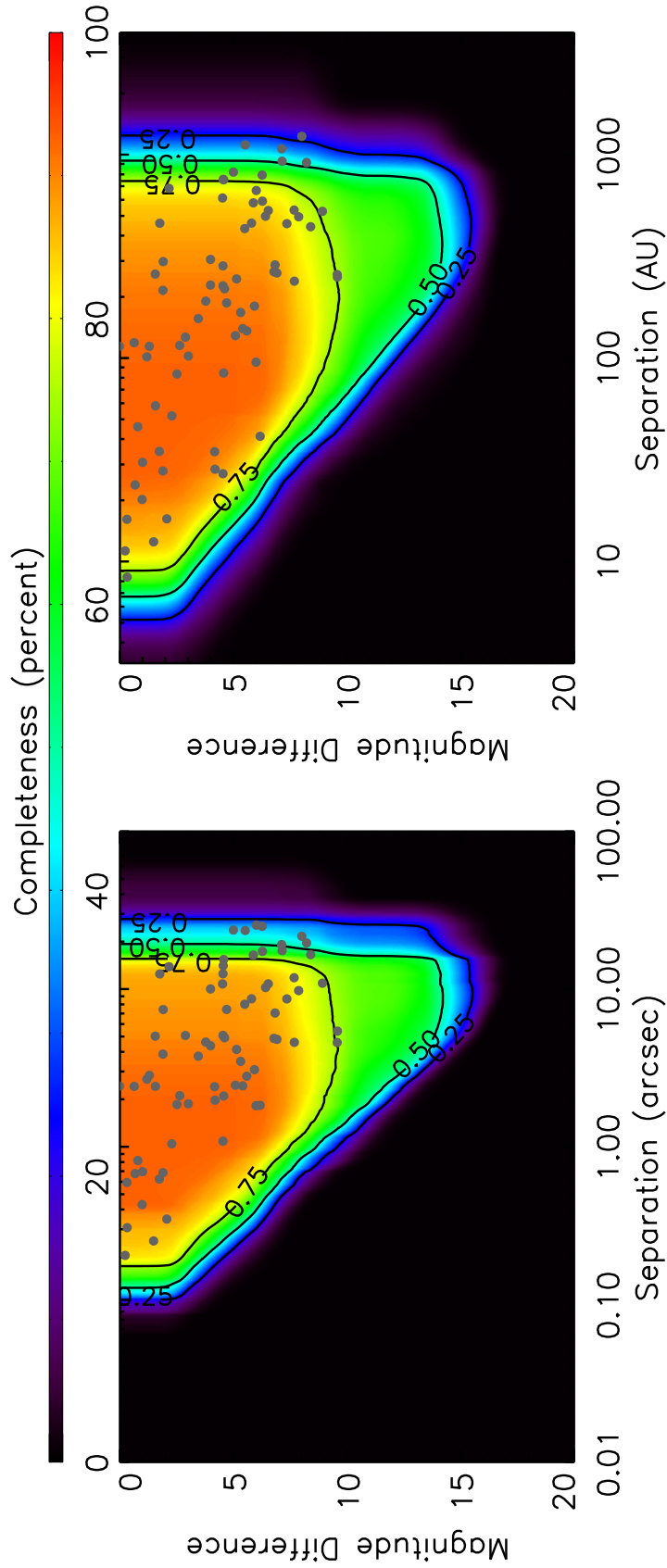


Figure 5.3: The completeness of the survey measured as a function of separation and magnitude difference. (*left panel*): As a function of angular separation, and (*right panel*): as a function of projected separation. The colour-scale denotes the percentage completeness of the survey, with the lack of observations of 17 stars within the 233 star sample leading to a maximum completeness of 92.7%. Over-plotted for clarity are the 75%, 50%, and 25% contours, and the resolved companion candidates listed in Table 5.1

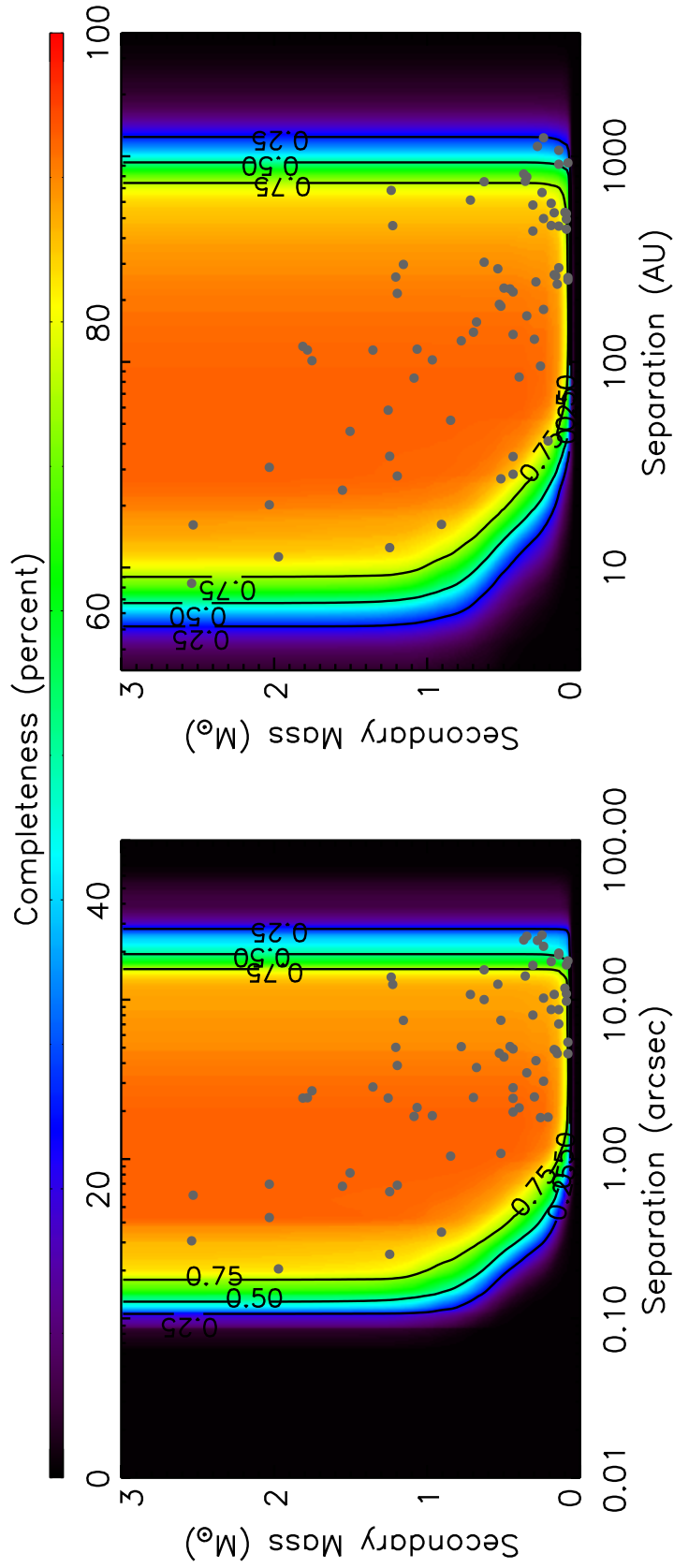


Figure 5.4: The completeness of the survey measured as a function of separation and companion mass. (*left panel*): As a function of angular separation, and (*right panel*): as a function of projected separation. The colour-scale denotes the percentage completeness of the survey, with the lack of observations of 17 stars within the 233 star sample leading to a maximum completeness of 92.7%. Over-plotted for clarity are the 75%, 50%, and 25% contours, and the resolved companion candidates listed in Table 5.1

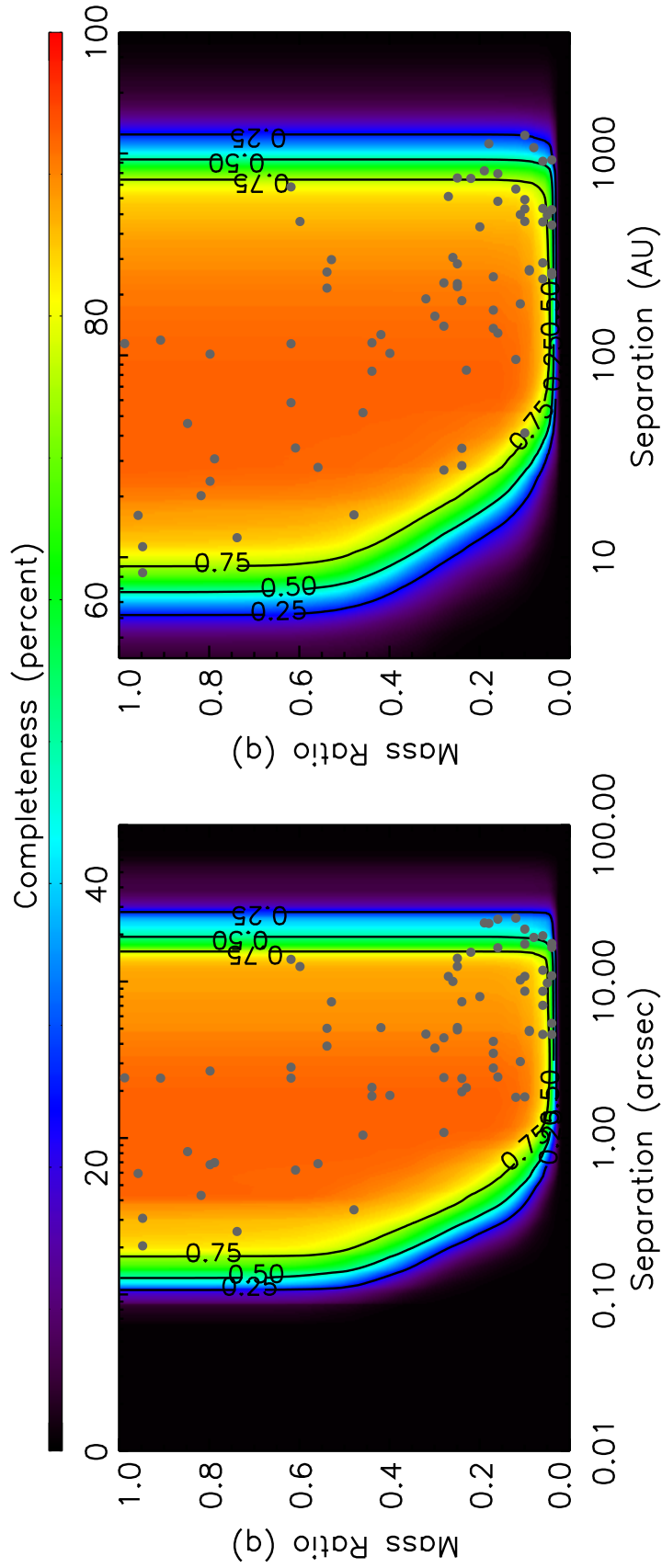


Figure 5.5: The completeness of the survey measured as a function of separation and mass ratio. (*left panel*): As a function of angular separation, and (*right panel*): as a function of projected separation. The colour-scale denotes the percentage completeness of the survey, with the lack of observations of 17 stars within the 233 star sample leading to a maximum completeness of 92.7%. Over-plotted for clarity are the 75%, 50%, and 25% contours, and the resolved companion candidates listed in Table 5.1

5.2 Correction for incompleteness

The synthesis of observations from a variety of different instruments, each with a different field-of-view and sensitivity (see Chapter 4), and the varying distances to each target, led to a significant non-uniformity in the completeness distribution of the survey as a function of projected separation and mass ratio (Figure 5.6). Considering the completeness of the survey within the restricted projected separation range of $56 < a[\text{AU}] \leq 891$ and mass ratio range of $0.05 \leq q \leq 1.00$, the level of completeness varies from 92.7% - where all stars observed are sensitive to companions - to $\sim 60\%$ at $a = 56$ AU and $q = 0.05$. In order to better quantify the level of incompleteness as a function of the two parameters, a and q , and to determine the level of correction which is to be applied, a coarse resolution completeness distribution was created. The distribution was divided into a grid of spacing $\Delta \log(a) = 0.10$ and $\Delta q = 0.20$, with the average completeness within each grid cell being used as the level of completeness between the parameter boundaries, as shown in Figure 5.7).

From this coarse completeness distribution, $C'(a, q)$, the weighting of each companion candidate detection can be determined. Considering a companion candidate at a separation of 125 AU and a mass ratio of 0.25, for example, the fraction of stars to which observations were sensitive to such a companion is found to be $C'(125, 0.25) = 94.2\%$. This corresponds to an effective sample size of 219 stars for this companion candidate, and as such it will contribute a frequency of $1/219 = 0.46\%$ to the overall binary frequency, and the separation and mass ratio distributions. In more general terms, the contribution of a companion candidate at a projected separation a and mass ratio q to the overall binary frequency is

$$(C'(a, q) N)^{-1} \quad (5.2)$$

where N is the number of stars within the overall sample, 233. Upper limits to the overall binary frequency, and the separation and mass ratio distributions can be determined in a similar way, using the effective sample size obtained from the coarse completeness distribution.

5.3 Identified companion candidates

Table 5.1 lists each companion candidate identified through a visual inspection of the high-resolution adaptive optics observations described in Chapter 4. Only those companion candidates satisfying the selection criteria described in §4.5.4 are listed. The literature was searched for references to each companion candidate, and if previously resolved, the component designation and the physical nature of the system are additionally listed. In order to retain a consistent analysis technique, any information regarding the physicality of each companion candidate is ignored when constructing the final mass ratio and separation distributions, as this extra information is not available for the majority of the companion candidates resolved within this study. The distribution of companion candidate detections as a function of physical separation and mass ratio is shown in Figure 5.8, with the hashed area denoting region of the phase space with insufficient completeness to construct reliable mass ratio or separation distributions (see §5.1).

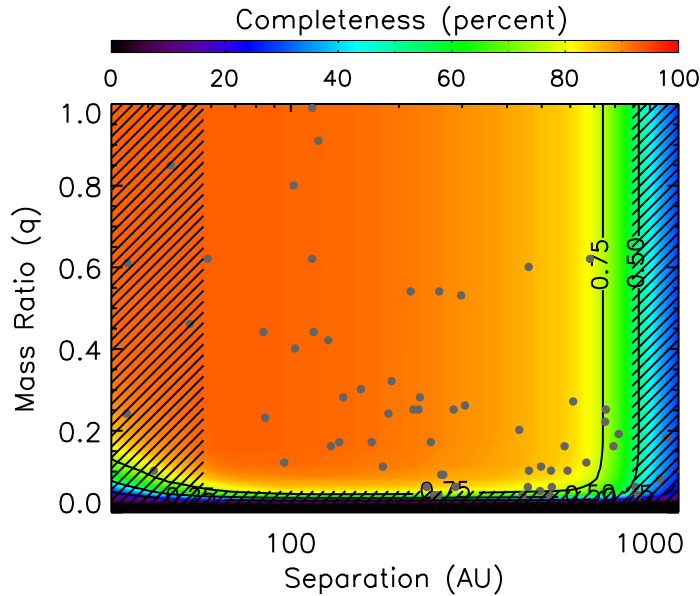


Figure 5.6: The region of the (a, q) phase space used to construct the binary statistics discussed within the remainder of this work. As with Figure 5.5, the completeness of the survey is plotted as a function of projected separation, a , and mass ratio, q . The figure has been centred and zoomed into the separation range $56 < a[\text{AU}] \leq 891$, to highlight the variability of the level of completeness. The hashed region denotes projected separations and mass ratios outside of the region of the phase space considered within the overall binary statistics.

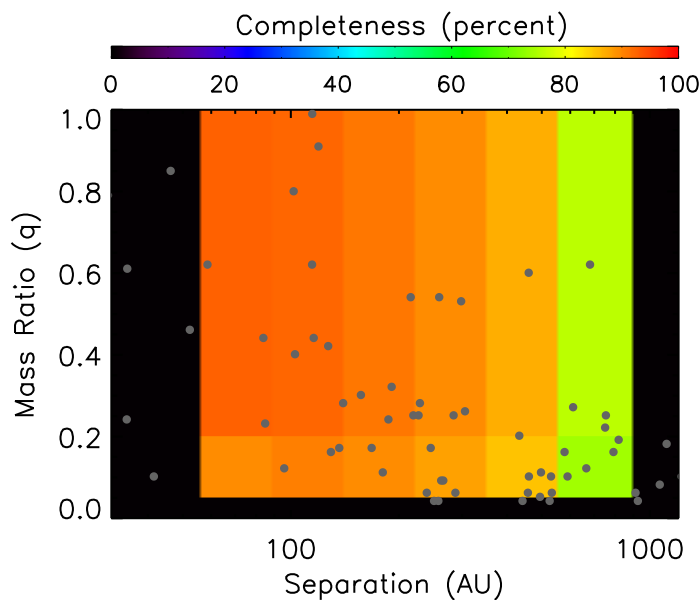


Figure 5.7: A coarse resolution version of the completeness distribution shown in Figure 5.6. The non-uniformity of the distribution must be taken into account when estimating the overall binary frequency, and a weighting of each resolved companion candidate can be obtained from this coarse distribution.

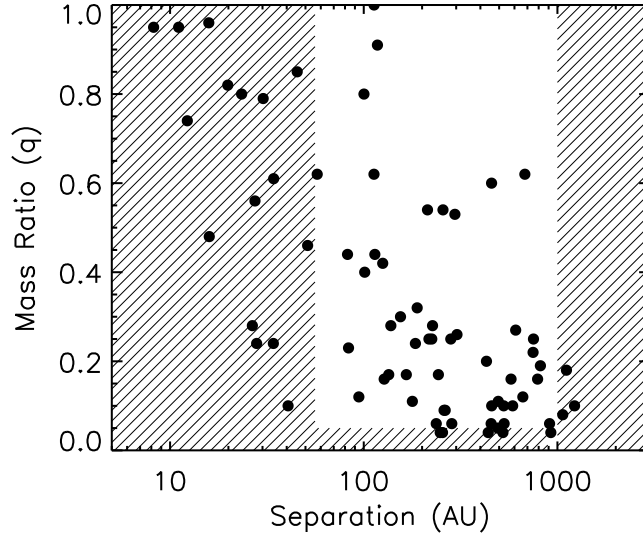


Figure 5.8: The companion candidates resolved within this study, plotted as a function of their projected separation and mass ratio. The hashed region denotes projected separations and mass ratios not considered within the overall binary statistics. Four candidate companions within the unshaded region were excluded based on the statistical cut-off described in §4.5.4.

There are two different quantities which can be used to express the fraction of stars within multiple systems; the multiplicity fraction (MF, e.g. Reipurth & Zinnecker 1993), defined as

$$\text{MF} = \frac{B + T + Q \dots}{S + B + T + Q \dots} \quad (5.3)$$

and the companion star fraction (CSF, e.g. Goodwin et al. 2004b), defined as

$$\text{CSF} = \frac{B + 2T + 3Q \dots}{S + B + T + Q \dots} \quad (5.4)$$

where B , T , and Q are the number of binary, triple, and quadruple systems, respectively. The multiplicity fraction is a more robust measure of the true multiplicity, as it is unchanged if a binary system is resolved to have additional components (Hubber & Whitworth 2005; Bate 2012). When taking into account the variable nature of the survey completeness as a function of physical separation and mass ratio as described in §5.2, the overall multiplicity fraction of the sample, within the separation range of $56 < a[\text{AU}] \leq 891$ and mass ratio range of $0.05 \leq q \leq 1.00$, is $24.2\% \pm 3.5\%$, with a corresponding companion star fraction of $28.1\% \pm 4.1\%$. The multiplicity fraction is slightly lower than the companion star fraction due to the detection of 4 triple systems within the sample. A lower-limit to the overall multiplicity fraction of the sample, over the full range of companion separations, can be estimated through a combination of these results and the known binary companions within the literature. Using the Ninth Catalogue of Spectroscopic Orbits (SB9; Pourbaix et al. 2004), and the Washington Double Star Catalog (WDS; Mason et al. 2001), an additional 45 known binary companions can be included, leading to a lower-limit of the multiplicity fraction of 45.2%.

Table 5.1: List of companion candidates resolved within the survey observations

HIP	Desig.	Position Angle θ (°)	Sky Separation ρ (")	Projected Separation ρ (AU)	Magnitude Difference Δm	Companion Mass M_2 (M_\odot)	Mass Ratio q	Date	Observatory	Filter	Notes
1473		146.18±0.21	6.89±0.02	284.69±2.61	6.85±0.04	0.14	0.06	2009-08-31	CFHT	H21-0	U
2381		279.50±0.21	1.78±0.01	94.31±1.51	6.01±0.02	0.26	0.12	2007-09-26	NACO	IB218	P*
5310		175.79±0.31	0.34±0.00	15.93±0.59	2.07±0.78	0.91	0.48	2008-10-16	Gemini	Br γ	U
9480	B	302.20±0.30	0.66±0.00	23.40±0.39	0.67±0.19	1.56	0.80	2010-08-26	Gemini	Br γ	P
11569	B	231.25±0.59	2.77±0.02	112.89±3.78	1.30±0.05	1.36	0.62	2008-10-16	Lick	Br γ	P
11569	C	115.49±0.64	7.25±0.05	295.45±9.96	1.91±0.01	1.16	0.53	2008-10-16	Lick	Br γ	P
12706	B	298.38±0.60	2.36±0.02	57.48±0.97	1.57±0.01	1.26	0.62	2008-10-17	Lick	Br γ	P
14551		123.49±0.24	13.76±0.05	752.00±20.72	4.56±0.00	0.36	0.25	2008-08-20	NACO	K $_S$	U
17954		200.86±0.31	0.20±0.00	11.07±0.35	0.23±0.01	1.98	0.95	2008-11-14	Gemini	Br γ	P
18217		60.04±0.57	1.02±0.01	51.29±1.11	2.29±0.01	0.85	0.46	2008-10-17	Lick	Br γ	U
20542		85.47±0.02	10.00±0.01	494.67±9.80	6.43±0.02	0.24	0.11	2007-11-17	CFHT	Br γ z	U
20648	B	340.91±0.11	1.81±0.00	82.44±1.92	2.52±0.00	1.09	0.44	2010-02-04	CFHT	H21-0	P
21036		311.23±0.11	4.97±0.01	224.46±3.59	4.55±0.01	0.46	0.25	2010-02-05	CFHT	H21-0	U
21036		313.67±0.11	4.80±0.01	217.01±3.47	4.62±0.01	0.44	0.25	2010-02-05	CFHT	H21-0	U
23179	B	3.33±0.54	4.91±0.04	256.44±10.75	1.56±0.01	1.21	0.54	2008-10-17	Lick	Br γ	P
28614	B	18.83±0.29	0.42±0.00	19.85±0.65	0.98±0.00	2.04	0.82	2009-12-19	Gemini	Br γ	P
30419	B	28.84±0.20	12.19±0.04	456.93±15.48	1.76±0.03	1.23	0.60	2009-09-01	CFHT	H21-0	P
31167	B	91.92±0.20	4.51±0.01	188.67±1.97	3.79±0.00	0.53	0.32	2002-01-24	CFHT	H21-0	P
33018		295.67±0.12	2.38±0.01	137.97±1.56	5.42±0.01	0.70	0.28	2010-02-05	CFHT	H21-0	U
35350	B	33.74±1.00	9.79±0.39	302.91±12.26	4.00±0.01	0.63	0.26	2008-04-12	Palomar	Br γ	P
41375		95.57±0.43	10.55±0.08	527.79±10.81	6.55±0.01	0.17	0.10	2011-12-08	Lick	H21-0	U
42313	B	263.19±0.02	2.74±0.00	134.55±4.17	5.60±0.00	0.44	0.17	2007-11-17	CFHT	Br γ z	P
43121		48.87±0.24	8.48±0.04	457.52±10.83	5.81±0.39	0.19	0.10	2001-05-06	CFHT	Hcont	U
43121		76.87±0.21	17.13±0.07	924.34±21.78	7.16±0.23	0.08	0.04	2001-05-06	CFHT	Hcont	U
44066	B	321.15±0.53	10.54±0.06	608.60±34.26	4.53±0.01	0.72	0.27	2011-12-09	Lick	H21-0	P
44127	B	76.02±1.00	2.35±0.09	34.13±1.37	4.18±0.00	0.44	0.24	2008-04-12	Palomar	Br γ	P

HIP	Desig.	Position		Sky Separation ρ (")	Projected Separation ρ (AU)	Magnitude Difference Δm	Companion		Date	Observatory	Filter	Notes
		Angle θ (°)	Separation ρ (")				Mass M_2 (M_\odot)	Ratio q				
44127	C	79.35±1.00	1.93±0.08	27.98±1.12	4.20±0.00	0.44	0.24	2008-04-12	Palomar	Br γ	P	
45688	B	224.22±1.00	2.62±0.10	100.23±5.00	1.19±0.01	1.76	0.80	2008-04-12	Palomar	Br γ	P	
51384		212.78±1.00	2.05±0.08	83.41±3.59	4.58±0.02	0.40	0.23	2008-04-12	Palomar	Br γ	U	
52422		108.09±0.04	23.00±0.02	1112.88±60.85	5.53±0.01	0.28	0.18	2007-01-27	CFHT	Br γ z	O	
55705	B	92.88±0.11	4.96±0.01	125.27±0.70	2.89±0.01	0.78	0.42	2010-02-05	CFHT	H21-0	P	
57562		293.26±0.30	3.01±0.02	178.20±3.10	5.94±0.09	0.24	0.11	2008-02-14	NACO	IB218	P*	
65477	Cb [†]	209.01±1.00	1.06±0.04	26.59±1.07	4.55±0.03	0.52	0.28	2008-04-11	Palomar	CH4s	P	
66249	B	154.29±0.12	1.79±0.00	40.66±0.20	6.19±0.02	0.21	0.10	2010-02-05	CFHT	H21-0	P	
69483	B	235.49±1.00	13.55±0.54	678.85±34.59	2.17±0.01	1.24	0.62	2008-04-11	Palomar	CH4s	P	
69592		174.83±1.00	4.05±0.16	242.78±11.79	5.15±0.01	0.29	0.17	2008-07-12	Palomar	CH4s	U	
70400		244.12±0.30	3.40±0.02	165.82±2.06	5.33±0.09	0.35	0.17	2008-02-24	NACO	IB218	P*	
76878		86.35±1.00	2.40±0.10	127.48±5.74	5.10±0.06	0.30	0.16	2008-07-13	Palomar	Ks	U	
76952	B	112.43±1.00	0.68±0.03	30.24±1.39	1.00±0.00	2.04	0.79	2008-04-11	Palomar	CH4s	P	
77660	B	71.87±0.31	0.247±0.01	12.27±0.21	1.487±0.01	1.25	0.74	2004-06-30	NACO	IB218	P	
80628	Ab	20.40±1.00	0.67±0.03	27.43±1.50	1.90±0.01	1.20	0.56	2008-04-12	Palomar	Br γ	P	
82321	B	33.66±1.00	1.83±0.07	101.12±4.47	3.02±0.01	0.97	0.40	2008-07-12	Palomar	CH4s	P	
82321	C	37.89±1.00	2.06±0.08	114.08±5.04	2.64±0.01	1.07	0.44	2008-07-12	Palomar	CH4s	P	
84012	B	236.88±1.02	0.58±0.02	15.84±0.72	0.31±0.01	2.54	0.96	2008-04-12	Palomar	Br γ	P	
84379	B	285.30±0.53	12.22±0.09	281.42±2.19	4.55±0.00	0.54	0.25	2008-07-25	Lick	Br γ	O	
85822		67.07±0.24	4.49±0.02	236.68±2.03	7.70±0.25	0.15	0.06	2009-09-01	CFHT	H21-0	U	
90156	B	348.64±0.29	3.78±0.02	213.35±4.39	1.90±0.00	1.20	0.54	2008-06-24	Gemini	Br γ	P	
91919	B	347.94±0.30	2.36±0.01	117.65±4.62	0.63±0.01	1.82	0.91	2008-06-19	Gemini	Br γ	P	
91926	Cb [†]	259.42±0.29	2.37±0.01	113.03±2.77	-0.02±0.00	1.79	0.99	2008-06-19	Gemini	Br γ	P	
93506	B	285.58±0.71	0.30±0.01	8.22±0.23	0.32±0.04	2.55	0.95	2011-04-22	CFHT	H21-0	P	
93580		274.45±1.00	7.83±0.31	430.01±18.69	5.51±0.01	0.31	0.20	2008-07-12	Palomar	CH4s	U	
93747		46.56±0.02	7.26±0.01	184.77±0.77	4.71±0.01	0.52	0.24	2007-11-17	CFHT	Br γ z	P	
104139		125.70±0.25	15.05±0.06	748.36±10.78	4.58±0.04	0.63	0.22	2008-08-21	NACO	Ks	U	
107302		229.20±0.60	4.27±0.03	226.47±5.45	4.00±0.01	0.50	0.28	2008-07-24	Lick	Br γ	U	
113048	B	235.69±0.20	0.80±0.00	45.32±1.32	0.79±0.02	1.51	0.85	2009-08-31	CFHT	H21-0	P	

HIP	Desig.	Position		Sky Separation ρ (")	Projected Separation ρ (AU)	Magnitude Difference Δm	Companion		Date	Observatory	Filter	Notes
		Angle θ (°)					Mass M_2 (M_\odot)	Ratio q				
117452	B	237.94±0.21	3.67±0.01	154.73±1.51	3.46±0.01	0.68	0.30	2009-08-30	CFHT	H2 ₁₋₀	P	
117730		352.59±0.45	0.61±0.01	34.25±1.86	1.74±0.01	1.25	0.61	2011-12-16	Lick	H2 ₁₋₀	P	
Companion candidates resolved in wide-band data												
9480	C	52.55±0.13	23.16±0.07	816.60±12.89	5.01±0.10	0.37	0.19	2009-09-01	CFHT	K'	P	
14146		147.63±0.13	16.16±0.05	439.10±2.50	8.42±0.10	0.09	0.04	2009-08-31	CFHT	K'	U	
18907		182.46±0.11	16.06±0.04	575.92±4.14	5.89±0.10	0.31	0.16	2010-02-05	CFHT	K'	U	
20713		145.14±0.79	10.65±0.11	523.07±16.41	8.94±0.10	0.09	0.04	2009-08-31	CFHT	K'	U	
24340		255.14±0.14	5.29±0.02	248.06±9.45	9.60±0.10	0.08	0.04	2011-11-23	CFHT	K'	U	
28614		283.83±0.29	19.17±0.11	910.57±29.88	8.24±0.10	0.14	0.06	2009-12-19	Gemini	K'	U	
29997		218.60±0.29	8.47±0.06	454.59±6.43	7.37±0.10	0.14	0.06	2009-09-01	CFHT	K'	U	
33018		297.79±0.11	21.14±0.05	1225.38±13.79	8.03±0.10	0.24	0.10	2010-02-05	CFHT	K'	U	
46744		240.44±0.51	9.56±0.06	491.61±26.96	7.89±0.10	0.09	0.05	2011-12-09	Lick	K	U	
51658		357.52±0.11	16.96±0.04	587.09±10.66	6.29±0.10	0.19	0.10	2010-02-04	CFHT	K'	O	
86263	B	78.65±0.13	24.47±0.07	789.73±5.35	6.28±0.10	0.35	0.16	2008-06-13	CFHT	K'	P	
88771	B	297.61±0.11	24.88±0.06	662.67±4.01	6.02±0.10	0.25	0.12	2010-02-05	CFHT	K'	P	
95077		322.31±0.30	4.76±0.03	263.30±5.34	6.80±0.10	0.17	0.09	2008-06-27	Gemini	K'	U	
95077		327.06±0.29	4.69±0.03	259.74±5.26	6.93±0.10	0.16	0.09	2008-06-27	Gemini	K'	U	
99742		116.14±0.13	11.54±0.03	530.49±6.53	7.69±0.10	0.10	0.06	2009-08-30	CFHT	K'	U	
113048		306.46±0.16	4.48±0.02	255.06±7.45	9.59±0.10	0.08	0.04	2009-08-31	CFHT	K'	U	
113048		303.23±0.13	18.71±0.05	1064.76±31.06	7.14±0.10	0.14	0.08	2009-08-31	CFHT	K'	U	

† - The primary in this system is HIP 65378

‡ - The primary in this system is HIP 91919

O - Confirmed to be an optical binary, not physically associated

P - Confirmed to be physically associated based on historical observations

P* - Confirmed to be physically associated based on multiple observations

U - Unconfirmed physical nature

5.4 Mass ratio distribution

The measured distribution of mass ratios, considering only those systems with a projected separation of $56 < a[\text{AU}] \leq 891$, is shown in Figure 5.9. The distribution includes the mass ratio of 49 companion candidates, with a variable weighting applied to each dependent on the non-uniform completeness of the survey (see §5.2). The distribution shows a significant population of lower-mass companions to the stars within the overall sample, with the frequency of companions with a mass ratio of $q < 0.4$ being approximately three times as great as those with a mass ratio of $q \geq 0.4$. Following the multiplicity study of early-type stars within the Sco OB2 association by Kouwenhoven et al. (2005), a power-law of the form $f(q) \propto q^{-\alpha}$ is fit to the observed distribution, with a power index of $\alpha = 0.83$ fitting the data best (Figure 5.9). The distribution does suffer from incompleteness to the lowest-mass companions, those with a mass ratio of $q < 0.05$ corresponding to a companion mass of $\sim 0.10 M_{\odot}$, however, and as such the lowest mass bin of the distribution ($0.0 \leq q < 0.2$) should be considered a lower-limit. If the lowest mass bin of the distribution is ignored, the overall trend remains, suggesting that this incompleteness is not significantly altering the overall result. Systems with more equal mass ratios ($q > 0.75$) are exclusively found at close separations ($a < 200$ AU), suggesting that the mass ratio distribution is strongly dependent on the range of separations over which the distribution is constructed (Figure 5.8, c.f. Tokovinin 2000).

5.5 Separation distribution

The measured distribution of projected separations, shown in Figure 5.10 (left panel), is constructed for each resolved companion with a mass ratio of $q \geq 0.05$ between 56 and 891 AU ($1.75 \leq \log(a) < 2.95$). As with the mass ratio distribution described previously, the distribution includes the projected separation of 59 companion candidates, with a variable weighting applied to each dependent on the non-uniform completeness of the survey (see §5.2). The distribution is shown to be relatively flat over the complete range of projected separations, with the exception of a significant decrease in the frequency of companions within the closest bin ($1.75 \leq \log(a) < 1.95$). The cumulative form of the distribution, shown in Figure 5.10 (right panel), removes any artificial bias introduced due to the selected bin size. The distribution is shown to be flat beyond $\log(a) = 2.00$, with no discernable peak. The relative lack of companions between $2.48 < \log(a) < 2.64$ is most likely an observational effect, rather than some physical mechanism excluding the presence of companions within this separation range.

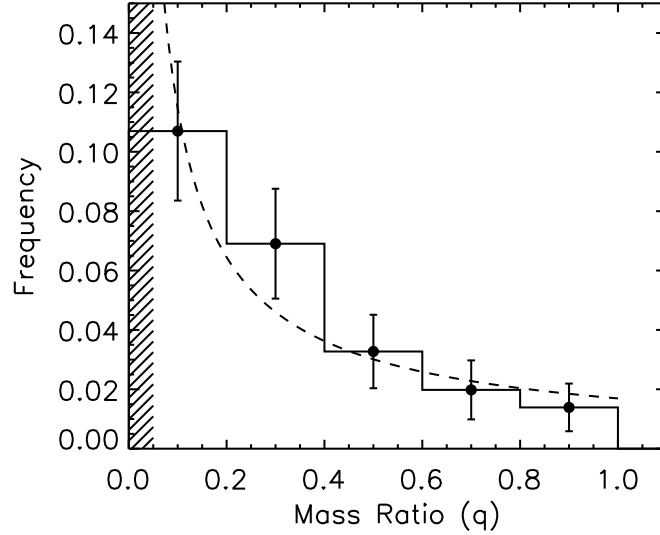


Figure 5.9: The measured mass ratio distribution, taking into account the completeness of the survey as discussed in §§5.1 and 5.2. The shaded region denotes mass ratios of $q < 0.05$, to which very few observations are sensitive. The lowest mass bin of the distribution, with a mass ratio between $0.0 \leq q < 0.2$, should therefore be considered incomplete. A power law fit to the measured distribution has been over-plotted, with $f(q) \propto q^{-0.83}$.

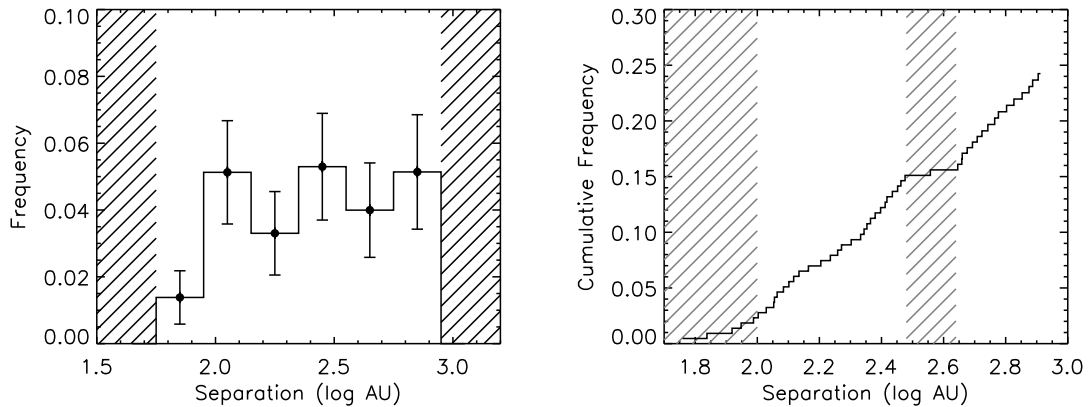
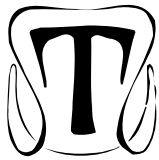


Figure 5.10: (*left panel*): The measured projected separation distribution, taking into account the completeness of the survey as discussed in §§5.1 and 5.2. The shaded regions denote projected separation ranges to which the survey observations are not complete ($a < 56$ AU and $a \geq 891$ AU). (*right panel*): The corresponding cumulative projected separation distribution. The distribution is shown to be flat, corresponding to a line of constant gradient in a cumulative distribution, with the notable exception of companion candidates with projected separations of $a < 2.0$, and $2.48 < a < 2.64$ (hashed regions).

CHAPTER 6

COMPARISON WITH PREVIOUS OBSERVATIONS AND THEORETICAL PREDICTIONS



The primary statistical results of this survey, the overall multiplicity fraction, and the separation and mass ratio distributions, provide key constraints to binary formation theories. A comparison with previous surveys can also provide insight into the dependence on binary formation as a function of primary mass. Although the observations presented within this work are not sensitive to companions at the full range of companion separations, there is sufficient information to both resolve the increase in multiplicity as a function of primary mass, and compare the shape of the mass ratio distribution to both observations and theoretical predictions.

6.1 Multiplicity as a function of primary mass

The companion star fraction (CSF) measured from the results of the VAST survey is plotted alongside the observed companion star fraction for Solar-type (Raghavan et al. 2010) and M-dwarf (Fischer & Marcy 1992) primaries in Figure 6.1. The companion star fractions obtained from the literature surveys have been estimated from a truncated form of the reported separation distributions between 56 and 891 AU, to ensure a fair comparison with the value reported for A-type stars. Although the companion star fractions estimated for Solar-type and M-dwarfs are statistically indistinguishable between 56 and 891 AU, a significant increase in the CSF is measured for A-type stars relative to these lower mass primaries. No comparison is made to the frequency of companions within 56 to 891 AU to brown dwarf primaries, as no such companions were resolved within a survey of L-type brown dwarfs within 20 parsecs. Companions to brown dwarfs at these wide projected separations are known, but at a significantly low frequency relative to the bulk of the companion separation distribution (Allen et al. 2007). The observed increase in the multiplicity as a function of increasing primary mass is consistent with the results of surveys of more distant massive stars (e.g. Preibisch 1999; Mason et al. 1998).

The measured companion star fraction for A-type primaries is consistent with the ob-

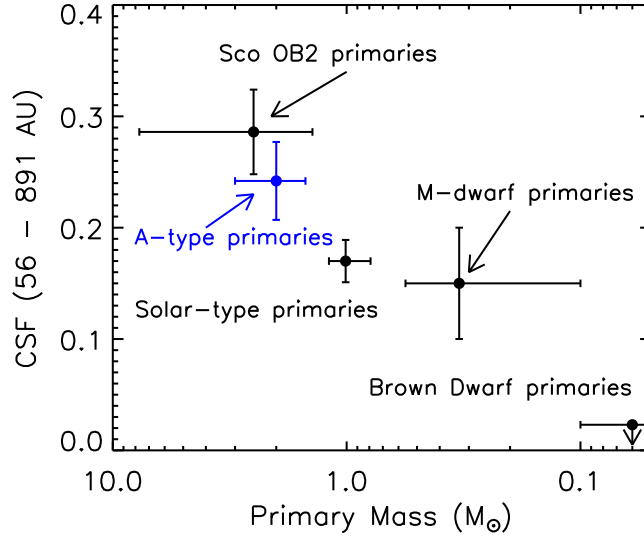


Figure 6.1: The observed companion star fraction observed between 56 and 891 AU as a function of primary mass (blue data point). The data point for; Solar-type stars is taken from the separation distribution presented in Raghavan et al. (2010) between 50 and 1000 AU, and for M-dwarf primaries is estimated from the number of companions per AU per primary presented within Fischer & Marcy (1992). As no companions were resolved between 56 and 891 AU as a part of a survey of nearby brown dwarfs (Reid et al. 2008), the upper limit of 2.3% calculated by Allen (2007) is used instead. The companion star function between 56 and 891 AU for early-type stars within the Sco OB2 association is also shown (Kouwenhoven et al. 2005).

served CSF for early-type stars within the young Sco OB2 stellar association (Kouwenhoven et al. 2005), as shown in Figure 6.1. Two observational biases exist within the measurement of the CSF within the Sco OB 2 association. Firstly, the distance to the association, approximately 130 parsecs, leads to an increase in the minimum projected separation at which faint companions at the bottom of the Main Sequence ($q \sim 0.05$) can be resolved. The observations are not sensitive to faint companions with a projected separation of $a < 130$ AU, and are not sensitive to any companions below $a \lesssim 20$ AU. The estimated CSF between 56 and 891 AU, plotted in Figure 6.1, should therefore be considered a lower limit, due to potentially missing companions with projected separations of $a < 130$ AU.

Hydrodynamical (Bate 2009, 2012) and numerical N -body (Durisen et al. 2001; Sterzik & Durisen 2003) simulations of stellar clusters reproduce the observed trend of increasing multiplicity as a function of mass, as shown in Figure 6.2. For the hydrodynamical simulations, a $500 M_{\odot}$ spherical cloud with an initial decaying velocity field was allowed to collapse due to self-gravity with (Bate 2012) and without (Bate 2009) radiation feedback. In each case, the computationally intensive calculation was stopped at an age of $\sim 10^5$ years, at which point the multiplicity fraction as a function of mass was measured (Figure 6.2). The subsequent dynamical evolution of the cluster, and resulting effect on the multiplicity fraction, was studied through an N -body evolution of the final state of the hydrodynamical simulation by Moeckel & Bate (2010) for a period of 10 Myrs. The multiplicity fraction as a function of mass between 10^5

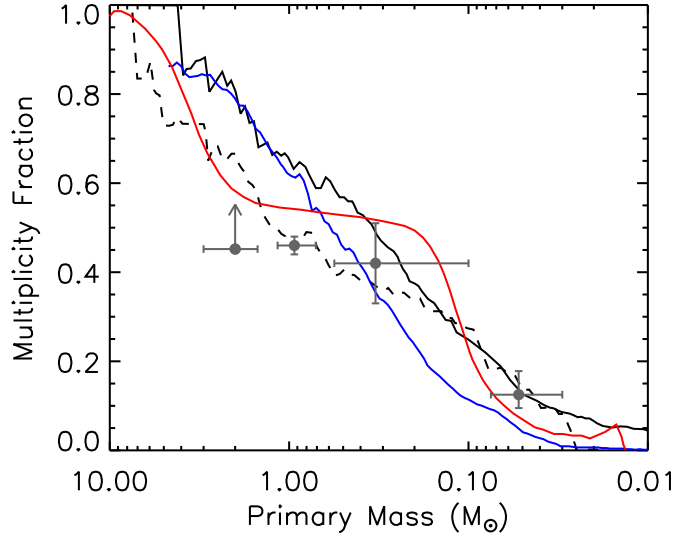


Figure 6.2: The measured multiplicity fraction of four stellar clusters simulations as a function of primary mass. The results of barotropic and radiation hydrodynamical simulations are plotted as black solid and dashed lines, respectively (Bate 2009, 2012), a numerical Monte-Carlo calculation looking at small- N interactions are plotted as a solid blue line (clusters with $N < 10$ stars; Sterzik & Durisen 2003), and an ensemble of small N -body clusters are plotted as a solid red line (a ring of $N = 6$ stars, with mass dispersion of $\sigma_{\log M} = 0.2$; Hubber & Whitworth 2005). Over-plotted for reference are, from left to right, the lower limit on the multiplicity fraction of A-type stars measured within this survey, and the observed multiplicity fraction of nearby Solar-type, M-dwarf, and brown dwarf primaries (see Figure 3.1).

and 10^7 years did not vary in a statistically significant manner, suggesting that the primordial binary population within this realisation of a stellar cluster is stable against future dynamical evolution. N -body simulations of larger stellar clusters, however, have shown a significant decrease in the multiplicity due to dynamical interactions as the cluster evolves (Parker et al. 2011). The large number of stars within the calculation of Parker et al. (2011), $N = 1500$, relative to the number within the hydrodynamical/ N -body simulation of Bate (2012) and Moeckel & Bate (2010), $N = 158$, and the required assumption of an initial distribution of binary stars for the former calculation, are possible reasons for the discrepancy.

Full radiative hydrodynamical simulations of star cluster formations are computationally intensive calculations, requiring 10^6 CPU hours to evolve a $500 M_{\odot}$ cluster for 10^5 years. An alternative approach is to simulate a large ensemble of small- N clusters, the combination of which being used to estimate various binary statistics (e.g. Sterzik & Durisen 2003; Hubber & Whitworth 2005), or several realisations of large- N clusters (e.g. Kroupa 1995; Parker et al. 2009). This N -body approach requires assumptions of the formation processes, as the calculations must be seeded with an initial population of stars with various masses, velocities, and locations, before simulating the dynamical evolution (Duchêne et al. 2007). Crucially, an initial multiplicity fraction is often assigned based on observations of field stars (e.g. Parker et al. 2009), or at a specific value (e.g. unity; Kroupa 1995). These assumptions neglect some of the

more complex modelling of gas fragmentation, collapse, and accretion (Duchêne et al. 2007), which may be significant to the properties of binary stars (e.g. Bate & Bonnell 1997), and the formation of additional companions within the cluster (e.g. Kratter et al. 2010b; Bate 2011). As such, N -body simulations are often used to study the effects of the dynamical evolution of a stellar cluster (e.g. van den Berk et al. 2007; Fregeau et al. 2009), rather than considering the initial formation of the cluster. The multiplicity fractions, as a function of primary mass, measured within two N -body simulations are shown in Figure 6.2 (Sterzik & Durisen 2003; Hubber & Whitworth 2005). Both simulations display the same increase in multiplicity as observed in the field, and measured within hydrodynamical simulations, with the Hubber & Whitworth (2005) calculation not based on an assumption of the initial multiplicity fraction.

6.2 Comparison of mass ratio distributions

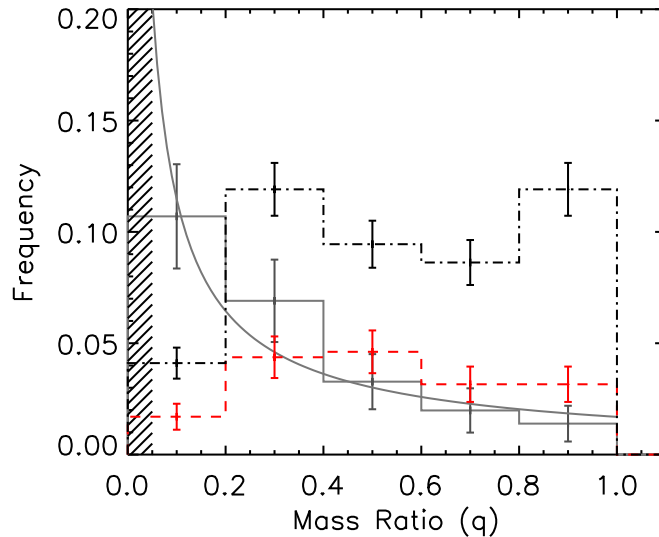


Figure 6.3: The observed mass ratio distribution presented in Figure 5.9 (grey histogram), and corresponding power-law fit (grey curve), compared with the observed companion mass ratio distribution for Solar-type primaries presented in Raghavan et al. (2010) (red dashed histogram). Both histograms are limited to companions within the limited separation range of this survey, 56 to 891 AU. The complete mass ratio distribution for Solar-type primaries over the full range of companion separations is shown for reference (black dot-dashed histogram).

The observed companion mass ratio distribution is significantly different from the distribution resolved by Raghavan et al. (2010) of companions to Solar-type primaries (Figure 6.3), with both distributions limited to companions resolved within the separation range of $56 < a[\text{AU}] \leq 891$. Raghavan et al. (2010) report no significant trend in the complete mass ratio distribution between $0.20 < q < 0.95$ (black histogram, Figure 6.3), with a significant deficiency in lower-mass companions $q < 0.2$, and a greater frequency of equal-mass binaries at close separations $q > 0.95$. When the range of separations considered is restricted (red histogram, Figure 6.3), the overall shape of the distribution remains the same; flat between

$0.20 < q < 0.95$, with a significant deficiency of lower-mass companions. Notably, the frequency of equal-mass companions has decreased by a greater amount relative to the bulk of the distribution, due to the greater frequency of equal-mass binaries at separations within 56 AU (Lucy & Ricco 1979; Tokovinin 2000; Bate et al. 2002). The restricted Solar-type distribution is significantly different than the distribution observed within this study, suggestive of a different dominant mode of binary formation within this separation regime for more massive stars (e.g. disk fragmentation; Kratter et al. 2010b).

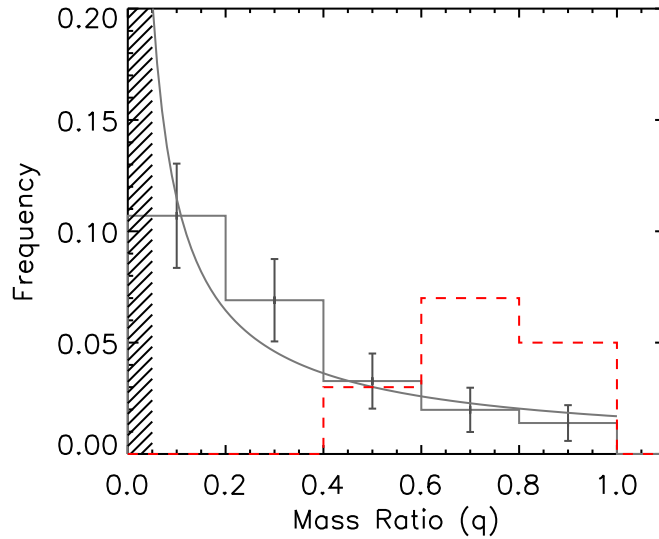


Figure 6.4: The observed mass ratio distribution presented in §5.4 (grey histogram), and corresponding power-law fit (grey curve), compared with the observed companion mass ratio distribution for M-dwarf primaries presented in Fischer & Marcy (1992) (red dashed histogram). The frequencies of M-dwarf binary companions have been scaled to the companion star fraction presented in Figure 6.1, as the population from which the distribution was drawn is not known. Similarly, statistical uncertainties are not presented, although Fischer & Marcy (1992) report no significant trend within the distribution. The distribution, covering the complete range of companion separations, only includes those systems with a companion mass ratio of $q > 0.4$.

A comparison with the companion mass ratio distribution of M-dwarfs measured by Fischer & Marcy (1992) is presented in Figure 6.4. Due to the synthesis of various techniques used to produce the binary statistics, the absolute frequency of each bin of the distribution is not known. The distribution has therefore been scaled using the multiplicity fraction of M-dwarfs presented in Figure 6.1. Fischer & Marcy (1992) report no significant trend within the observed distribution, limited to companions of M-dwarfs with a mass between 0.30 and 0.55 M_{\odot} . Larger surveys of nearby M-dwarfs, with sensitivity to companions extending down to $q = 0.2$, have revealed a distribution peaked at $q = 1$ (Bergfors et al. 2010), broadly consistent with the distribution observed by Fischer & Marcy (1992).

The mass ratio distribution of companion candidates to A-type stars resolved within this study can also be compared with the distribution of companion mass ratios within the Sco OB 2 association (Figure 6.5; Kouwenhoven et al. 2005). The two distributions have a similar power-

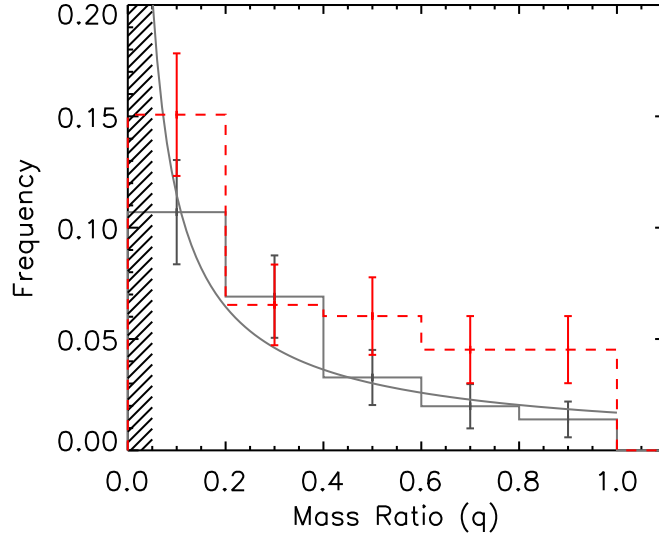


Figure 6.5: The observed mass ratio distribution presented in §5.4 (grey histogram), and corresponding power-law fit (grey curve), compared with the observed companion mass ratio distribution for early-type primaries within the Sco OB2 association presented in (Kouwenhoven et al. 2005) (red dashed histogram). The distribution covers the full range of companion separations sampled by the survey, $25 \lesssim a[\text{AU}] \lesssim 1500$.

law shape, $f(q) \propto q^{-\alpha}$, skewed preferentially towards lower-mass companions. The value of the best fit power-law index is lower for the companion mass ratio distribution observed within this study, indicating a greater frequency of lower mass companions ($q < 0.2$) relative to more equal-mass companions ($q > 0.8$) than measured within the Sco OB2 association. Unfortunately, as the mass ratio and separation of each companion resolved within the survey of Sco OB2 members is not listed by Kouwenhoven et al. (2005), the distribution cannot be limited to the separation range over which this study is sensitive, $56 < a[\text{AU}] \leq 891$, instead it includes all companions resolved within the study, with separations of $26 < a[\text{AU}] \leq 1612$. The situation is complicated further by the limited sensitivity to faint companions with separations of $a < 130$ AU, and incompleteness due to detector geometry at separations of $a > 1250$ AU. The survey of the Sco OB2 members can therefore only be considered complete with the separation range of $130 < a[\text{AU}] \leq 1250$. The larger measured frequency of equal mass companions resolved to Sco OB2 members, with mass ratios of $q > 0.8$, relative to those resolved within this study, can be attributed to the observed preference for equal-mass companions being found at closer separations (Figure 5.8). As the Sco OB2 companion mass ratio distribution includes systems at separations to which the observations are not complete, $a < 130$ AU, separations at which low-mass ratio companions may have been missed, a significant bias may be introduced to the relative level of each bin within the overall distribution. This bias would act to overstate the relative frequency of equal-mass companions, consistent with the overpopulation observed relative to the companion mass ratio distribution measured within this study. With access to the mass ratio and separation of each individual companion resolved within the Sco OB2 study,

a more thorough comparison can be made over the separation range complementary to both studies.

Two binary formation scenarios are thought to predominate over the separation range to which this study is complete, the initial fragmentation of a pre-stellar molecular cloud (e.g. Boss & Bodenheimer 1979; Bonnell et al. 1991), and the fragmentation of a large circumstellar disk (e.g. Adams et al. 1989; Bonnell 1994a; Woodward et al. 1994). The initial fragmentation of a cloud prior to the formation of protostellar objects can produce binary systems with separations ranging between 10^1 and 10^4 AU (Bate et al. 1995). A scale-free fragmentation model, in which the companion mass ratio distribution is independent of the initial clump mass (Clarke 1996), can be tested against the observations presented here. This model predicts a multiplicity fraction which is weakly dependent on primary mass, and a mass ratio distribution which is independent, or weakly dependent on primary mass. These predictions are inconsistent with both the observed trend in multiplicity as a function of primary mass (Figures 3.1 and 6.1), and the observed variation in the companion mass ratio distribution for Solar-type and A-type primaries (Figure 6.3). Star formation within a more clustered environment may introduce a dependence on primary mass, with more massive primaries having mass ratio distributions skewed towards less massive companions (Bonnell & Bastien 1992; Bate 2001). Simulations of the dynamical decay of small clusters, formed through the fragmentation of an initial cloud (Sterzik & Durisen 1998), are consistent with the observed companion mass ratio distribution, and its dependence on primary mass.

Subsequent to the fragmentation of an initial cloud, leading to the formation of a number of protostellar objects, the conservation of angular momentum can cause the infall of material from the surrounding cloud to form a protostellar disk (Bonnell 1994a). These disks can fragment to produce substellar and stellar companions within the plane of the disk, providing a mechanism for the disk to become gravitationally unstable, and subsequently cool efficiently, is present (e.g. Kratter et al. 2010b). This formation process is thought to be more significant for more massive stars (Kratter 2011), due primarily to the large reservoir of material within the massive disks of these stars (e.g. Smith & Terrile 1984). Current disk fragmentation theories have not produced strong predictions for the separation and mass ratio distribution of binaries (Kratter 2011). Competitive accretion may cause an equalisation of the mass ratios of binaries with close separations (Bate & Bonnell 1997; Bate 2000), while at wider separations a dearth of lower-mass companions to massive stars may be resolved (Kratter et al. 2010b; Stamatellos et al. 2011). The resolved mass ratio distribution presented within this study, with a greater abundance of lower-mass companions, is consistent with these theoretical predictions, and are resolved within a separation range coincident with the sizes of known circumstellar disks of pre-Main Sequence A-type stars (e.g. Dent et al. 2006; Hamidouche et al. 2006; Fukagawa et al. 2010).

Although the efficiency of dynamical capture events within the formation environment is not thought to be sufficient to explain the observed frequency of binary stars (Clarke & Pringle 1991), it is prudent to test the observed mass ratio distribution against the prediction of random capture from the initial mass function (IMF). To achieve this, two stars were drawn

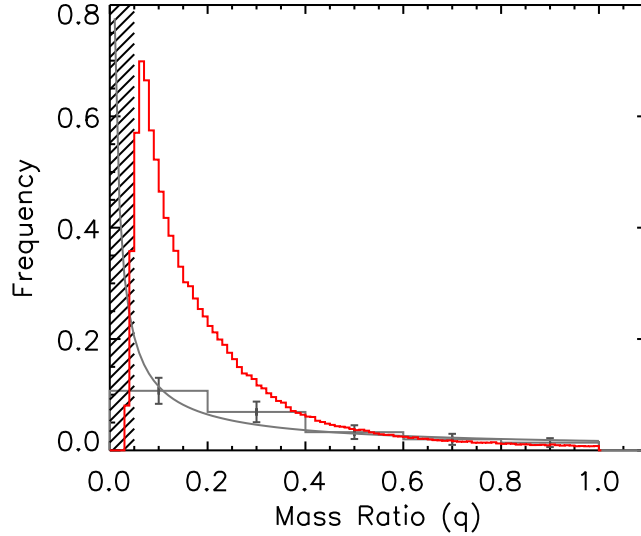


Figure 6.6: The observed mass ratio distribution presented in §5.4 (grey histogram), and corresponding power-law fit (grey curve), compared with the predicted mass ratio distribution from a simple random capture simulation (red histogram, see text for a complete description). The distributions are normalised between $0.4 < q \leq 1.0$, demonstrating the significant population of lower-mass companions predicted by simple random capture, inconsistent with the observations. A Kolmogorov-Smirnov test of the two distributions exclude the possibility that the two populations are drawn from the same distribution at a 4σ confidence level.

from a Kroupa IMF (Kroupa 2001) within the mass range of 0.1 to $3.0 M_{\odot}$, the most massive of which is assigned as the primary. Rejecting systems with primaries of mass below $1.5 M_{\odot}$, the mass ratio of the system is calculated, and added to the overall companion mass ratio distribution. This process is then repeated 10^5 times, and the resulting distribution is scaled to the multiplicity fraction discussed in §5.3 between $0.4 < q \leq 1.0$. The observed companion mass ratio distribution is not consistent with a random pairing from the IMF at a 4σ level, as shown in Figure 6.6, however this does not exclude the possibility that such pairing occurred, and the distribution was altered through dynamical evolution within the formation environment (e.g. Valtonen 1998). The random capture scenario is also found to be inconsistent with the companion mass ratio distribution observed in the Sco OB2 association (Reggiani & Meyer 2011), placing an upper limit for the age at which significant dynamical evolution occurs of ~ 10 Myrs. The observations presented here also do not exclude the probable dependence of the capture efficiency on the masses and separation of the stars involved, and as such a more comprehensive simulation technique is required before random capture can be ruled out.

The variation in the shape of the mass ratio distribution as a function of separation can be demonstrated by dividing the separation range covered into two equally sized sub-samples in $\log a$ ($56 \leq a[\text{AU}] < 224$ and $224 \leq a[\text{AU}] < 891$, Figure 6.7). A Kolmogorov-Smirnov test of the two distributions leads to the rejection of the hypothesis that both samples are drawn from the same population. No companion candidate with a mass ratio of $q > 0.6$ is found within the wider of the two subsamples, consistent with observations of Solar-type primaries

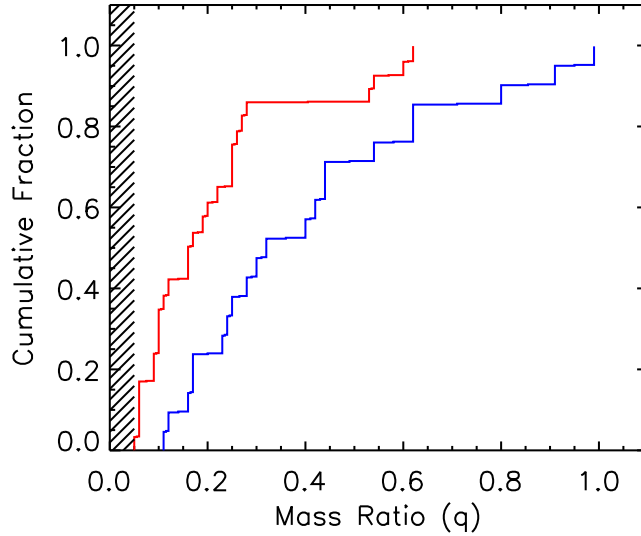


Figure 6.7: The cumulative mass ratio distribution for companion candidates resolved between $56 \leq a[\text{AU}] < 224$ (blue histogram) and between $224 \leq a[\text{AU}] < 891$ (red histogram). A Kolmogorov-Smirnov test of the two cumulative distributions reject the hypothesis that they are drawn from the same population, demonstrating the dependence of the mass ratio distribution on the separation of the companion candidate. The p -value measured from the Kolmogorov-Smirnov test, at 1.3%, indicates a low probability that the two distributions are drawn from the same population, assuming that the two measured distributions are accurate representations of the true mass ratio distributions.

showing equal-mass binaries typically have smaller separations (Tokovinin 2000), and the observed decrease in the median mass ratio as a function of separation (Raghavan et al. 2010). The greater frequency of equal-mass companions at close separations is consistent with the accretion of material onto a protobinary system preferentially equalising the mass ratios of close binary systems (Bate 2000; Bate et al. 2002). This paucity of equal-mass companions at wider separations is physical, with the completeness of the survey decreasing only at the widest separations searched (e.g. Figure 5.6). The survey does suffer from an incompleteness to low-mass companions at close separations, where the completeness decreases to approximately 50%, and as such the frequency of low-mass companions at close separations may have been somewhat underestimated. Future observations with high angular resolution instruments, such as the Gemini Planet Imager, should help to constrain the frequency of these lower-mass companions within this region of the search phase space.

6.3 Comparison of separation distributions

The observed companion separation distribution, limited to the separation range of $56 < a[\text{AU}] \leq 891$ ($1.75 < \log a \leq 2.95$), is compared with the separation distribution of companions to Solar-type primaries (Figure 6.8). While the separation distribution of the companions to Solar-type stars presented by Raghavan et al. (2010) is sensitive to companions at all separations,

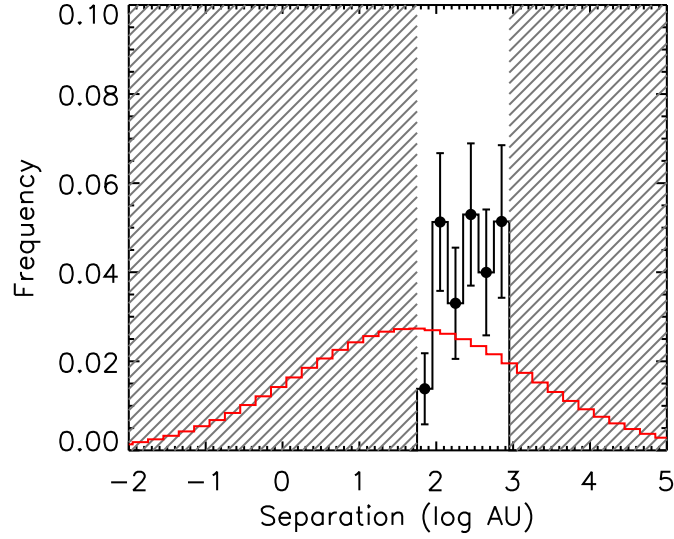


Figure 6.8: The observed companion separation distribution presented in Section 5.5 (black histogram), compared with the functional form of the separation distribution of companions to Solar-type primaries (red histogram; Raghavan et al. 2010). The sum of the frequencies of each distribution is equal to the companion star fraction plotted in Figure 6.1. The disparity in the separation coverage in both samples is apparent, with the shaded region indicating separations to which the observations within this study are not sensitive to companions. Coverage at wider separations will be added through common proper motion search using available historical observations (see Chapter 9).

the results from this survey are substantially limited by the angular resolution of the adaptive optics observations. Due to these limitations, and the relative flat shape of the distribution across the separation range to which the observations are sensitive, the overall shape of the distribution remains unknown. Further observations of the members of the VAST sample are required using high angular resolution techniques to resolve the frequency of companions within ~ 50 AU (e.g. interferometry - Patience et al. 2008, spectroscopy - Abt 1965), and a common proper motion search for companions with separations of $a > 1000$ AU (e.g. Makarov et al. 2008).

Simulations of dynamical interactions within stellar clusters, and numerical calculations of companion formation through disk fragmentation, both predict an increase in the location of the peak of the separation distribution as a function of increasing primary mass (Sterzik & Durisen 2003; Whitworth & Stamatellos 2006). Measurements of the position of the peak of the companion separation distribution for M-dwarf and Solar-type primaries are consistent with these predictions (Figure 6.9; Fischer & Marcy 1992; Raghavan et al. 2010). Assuming that the peak of the separation distribution for A-type stars is within the range of separations over which this survey is sensitive, the observational data points can be extended to higher mass, remaining consistent with the theoretical predictions (Figure 6.9). If the peak of the A-star companion separation distribution is within this range, it will have a significant impact on the formation and stability of circumstellar disks and planetary systems which are known to occupy

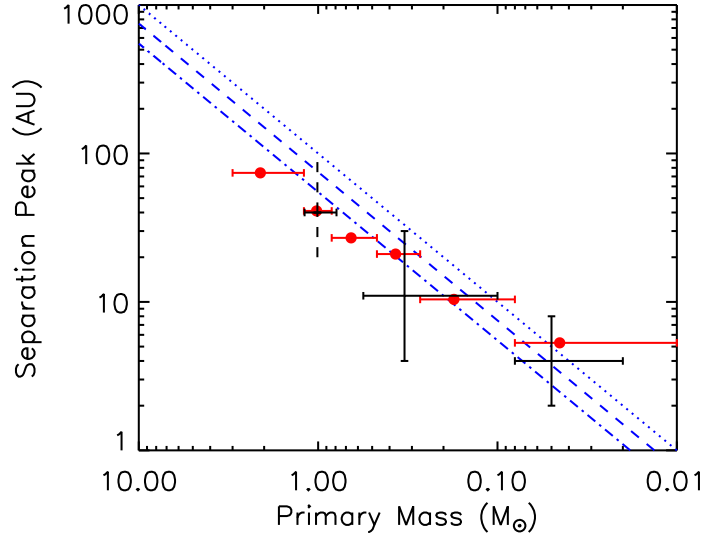


Figure 6.9: The location of the peak of the separation distribution as a function of primary mass for, black data points from right to left; brown dwarf primaries (Burgasser et al. 2006), M-dwarf primaries (Fischer & Marcy 1992), and Solar-type primaries (Raghavan et al. 2010). As the uncertainty in the location of the peak of the separation distribution was not provided by Raghavan et al. (2010), the corresponding vertical error bar is dashed. The observations show a clear trend of an increase in the peak of the distribution as a function of primary mass, consistent with theoretical predictions from dynamical simulations (red points; Sterzik & Durisen 2003), and from disk fragmentation models (blue curves - dotted $q = 1.0$, dashed $q = 0.5$, dot-dashed $q = 0.1$; Whitworth & Stamatellos 2006). The increase in the peak of the separation distribution has also been observed in SPH simulations of stellar clusters (e.g. Bate 2009).

this separation range (e.g. Fukagawa et al. 2010; Marois et al. 2008).

6.4 Summary

The observations presented within this study cover a key separation range, between so-called *hard* binaries which are not susceptible to dynamical removal ($a \lesssim 10^1$ AU), and *weak* binaries which are loosely bound, and are possibly the result of simultaneous ejection during the evaporation phase of the formative stellar cluster ($a \gtrsim 10^2$ AU, e.g. Kouwenhoven et al. 2010). The companions resolved within this study are therefore the most susceptible to being dynamically processed within the formative environment, while being sufficiently bound as to not cause the ejection of the lower-mass component. As the sample of stars searched is drawn from the field population, the mass ratio and separation distributions will be a synthesis of the individual distributions found within clusters of varying stellar densities, ranging from those found within the ONC, to those found within Taurus.

The observed mass ratio distribution shows a significant abundance of lower-mass companions, with $q < 0.5$, relative to more equal-mass companions (Figure 5.9). This distribution is shown to have a clear dependence on the companion separation, with the median mass ratio

decreasing as a function of separation (Figure 6.7). Comparing with similar surveys of lower-mass primaries, the mass ratio distribution has a significant dependence on primary mass, with Solar-type primaries exhibiting a flat distribution (Raghavan et al. 2010), and a mass ratio distribution skewed towards a greater frequency of equal-mass companions for brown dwarf and M-dwarf primaries (Reid et al. 2008; Bergfors et al. 2010). The observed mass ratio distribution is consistent with the formation of unequal mass ratio binary companions within a large circumstellar disk (e.g. Kratter et al. 2010b). The separations of the candidate companions resolved within this study, although limited in terms of the range of separations surveyed, are similar to the radii of extended debris disks resolved around A-type stars (e.g. Dent et al. 2006).

The overall shape of the separation distribution, and location of its peak, cannot be determined from the observations presented within this study due to the limitations of adaptive optics observations. A combination of historical photographic measurements dating from the 1950s, and new direct imaging observations will provide sensitivity to companions beyond 891 AU to the majority of the targets within the sample. A search for companions interior to the detection limits of the AO imaging data can be performed using a number of complementary techniques, including radial velocity monitoring, interferometry, and synthetic aperture masking. While these techniques may be unable to achieve uniform sensitivity to companions at the bottom of the Main Sequence, their combination will provide comprehensive binary companion statistics over the complete separation range for mass ratios as low as $q \sim 0.2$, allowing a more robust comparison with similarly complete surveys of lower-mass primaries (e.g. Raghavan et al. 2010). The potential dynamical evolution of any natal mass ratio and separation distributions prevents the confirmation or rejection of any individual binary formation mechanism with the currently available data. As the dynamical evolution of these natal distributions is likely strongly dependent on the density of the formation environment (e.g. King et al. 2012), and as the observed mass ratio and separation distributions within this survey of field A-type stars are constructed from a synthesis of numerous distributions resulting from formation environments of varying densities, any individual binary formation scenario for A-type stars will only be confirmed or rejected with observations of these early type stars within their formation environments.

CHAPTER 7

COMPANIONS AND THE UNEXPLAINED X-RAY DETECTION OF B6 – A7 STARS



With an adaptive optics imaging survey of 148 B6-A7 stars, the hypothesis that unresolved lower-mass companions are the source of the unexplained X-ray detection of stars within this spectral type range has been tested. The sample is composed of 63 stars detected in X-rays within the *ROSAT* All-Sky Survey and 85 stars that form a control sample; both subsets have the same restricted distribution of spectral type, age, X-ray sensitivity and separation coverage. A total of 68 companion candidates are resolved with separations ranging from $0''.3$ to $26''.2$, with 23 new detections. The multiple star frequency of the X-ray sample based on companions resolved within the *ROSAT* error ellipse is found to be $43^{+6}_{-6}\%$. The corresponding control sample multiple star frequency is three times lower at $12^{+4}_{-3}\%$ - a difference of $31 \pm 7\%$.

7.1 X-ray emission of Main Sequence stars

The detection of X-ray emission from Main Sequence stars is common (Vaiana et al. 1981), with the notable exception of late B- and early A-type stars (e.g. Stauffer et al. 1994). Two distinct generation mechanisms are responsible for the X-ray emission, related to the different stellar structure of massive O- and B-type stars and lower mass F- to M-type stars. For the massive stars, the hot stellar winds cause X-ray emission, while the lower mass stars produce X-rays from the confinement of superheated plasma within their magnetic fields.

Radiative winds driven by line-absorption and re-emission within the extended atmospheres of O- and early B-type stars form a key component of the model for X-ray emission from these massive stars (e.g. Lucy & White 1980). Wind shocks caused either through instability generated through radiative driving (Owocki et al. 1988), or due to collisions of magnetically driven wind streams (Feldmeier et al. 1997) are thought to be the primary X-ray generation mechanisms. Interaction between stellar winds and surrounding material is also thought to produce X-rays (e.g. Giampapa et al. 1998).

For lower mass stars, stellar winds are too weak to generate X-rays, and the stellar corona is responsible for the emission of X-rays and is intrinsically linked to the magnetic field. For late A- to early M-type stars, magnetic fields arise from the $\alpha\Omega$ dynamo caused by the differential rotation at the interface between the convective envelope and the radiative core (Spiegel & Weiss 1980). The magnetic field generated by the dynamo process is essential for confining the superheated plasma necessary for X-ray generation (G del 2004). The heating mechanism required to maintain the corona at temperatures greater than 10^6 K was originally thought to be acoustic waves (e.g. Schwarzschild 1948; Schatzman 1949), while current models involve Alfvén waves travelling perpendicular to the magnetic field (e.g. De-Pontieu et al. 2007; Jess et al. 2009). Localised magnetic reconnection events within the chromosphere are also a potential source of coronal heating through Joule heating (e.g. Sturrock 1999). Beginning at a spectral type of M3 ($\sim 0.35M_{\odot}$), the stars become fully convective (Chabrier & Baraffe 1997) and the high level of magnetic activity observed (e.g. Randich 2000) may be due to an α^2 -type dynamo generation mechanism (Chabrier & Küker 2006), in which turbulent motions are able to generate large-scale magnetic fields.

In addition to the emission mechanisms intrinsic to the star, X-rays can be generated by processes involving binary systems. Accretion of material within cataclysmic variable systems (e.g. Patterson & Raymond 1985) and compact object binaries (e.g. Shapiro et al. 1976) can produce X-ray fluxes. For stars between spectral types B6 to A7, which are expected to be X-ray quiet, the presence of a low-mass companion can lead to the detection of X-rays which are assigned to the primary if the companion is unknown. This study is designed to explore the hypothesis that unresolved lower mass companions are the true source of the unexpected X-ray detections from B6-A7 stars.

7.2 Previous observations

7.2.1 X-ray detection of B6-A7 stars

Early studies of stellar X-ray emission conducted with the *Einstein Observatory* measured a notable decrease in the fraction of X-ray detected A-type stars ($0.00 \lesssim B - V \lesssim 0.25$) compared to bluer and redder stars (Topka et al. 1982; Schmitt et al. 1985). Out of the 35 A-type stars observed by Schmitt et al. (1985), only 7 were detected and 4 were listed as having a secondary component which could be the source of the X-ray emission. *Einstein* observations of coeval stellar groups also showed a similar decrease in the fraction of X-ray detections of A-type stars between $0.00 \lesssim B - V \lesssim 0.3$ (e.g. Micela et al. 1985; Schmitt et al. 1990).

The increased sensitivity provided by the *ROSAT* mission and all-sky coverage led to the detection and characterisation of a significant number of stellar X-ray sources (Voges et al. 1999). A search by Huensch et al. (1998b) of the Bright Star Catalogue (Hoffleit 1964) and the *ROSAT* Bright Source Catalogue for objects within $90''$ of the same position defined a population of 232 B6-A7 X-ray detected stars. To investigate possible sources of the X-ray emission for this sample, the X-ray luminosity was compared with spectral type, spectral peculiarities and rotational velocities (e.g. Simon et al. 1995; Schröder & Schmitt 2007). The lack of a

dependence on any of these factors was taken as evidence of unresolved companions. Without a comprehensive binary survey of A-type stars, it was not possible to test the companion hypothesis directly. Similarly, X-ray data from *Chandra* which could resolve the emission source in tight ($\rho \sim 0''.5$) binary systems do not exist for a significant sample of X-ray B6-A7 stars.

7.2.2 High-resolution imaging companion searches

High-resolution AO imaging studies of X-ray detected B- and A-type stars have been employed to search for lower mass stars capable of producing X-rays. Pointed observations of late B-type stars with known lower mass companions (e.g. Schmitt et al. 1993; Berghofer & Schmitt 1994) wide enough to be resolved with the *ROSAT* High Resolution Imager were obtained to determine the source of the X-ray emission. These observations typically identified the B-type star as the source of X-ray emission, although subsequent high-resolution AO imaging has revealed additional components to several of these systems (e.g. Shatsky & Tokovinin 2002). Sub-arcsecond binary companions have also been resolved with high-resolution AO imaging of pre-Main Sequence companions to late B-type stars (e.g. Hubrig et al. 2001).

Recent discoveries of low-mass companions to Alcor (Mamajek et al. 2010; Zimmerman et al. 2010) and ζ Virginis (Hinkley et al. 2010) have both noted that the unexplained X-ray emission from the primary can be explained by the lower-mass companion, and demonstrate how X-ray emission from A-type stars could be a useful tool in searching for low-mass companions. The current study expands upon the existing imaging results of X-ray detected B6-A7 stars by observing a large sample of both X-ray stars and a control sample.

Table 7.1: X-ray detected sample

HIP	Name	<i>Hipparcos</i> Spectral Type	Distance μ c	ROSAT Source		Observations		Band	Integration <i>sec</i>	2MASS Sources <i>arcmin</i> ⁻²	
				Designation B - BSC, F - FSC	Offset <i>arcsec</i>	Error Radius <i>arcsec</i>	Tel.				Date
5310	ψ^2 Psc	A3V	49.4 \pm 2.0	B - J010757.4+204424	4.9	14	Gemini	16/10/2008	K	200	0.156
9480	48 Cas	A3IV	35.8 \pm 0.7	B - J020156.9+705432	7.6	8	CFHT	01/09/2009	K	480	0.868
11569	ι Cas	A5p	43.4 \pm 1.5	B - J022902.9+672407	6.4	8	CFHT	05/02/2010	K	330	1.088
13133	RZ Cas	A3Vv+	62.5 \pm 2.4	B - J024854.7+693804	4.3	7	Gemini	14/11/2008	K	400	0.767
17608	Merope	B6IVe	110.1 \pm 12.6	F - J034620.7+235713	24.5	13	AEOS	04/02/2002	I	300	0.207
17664		B9.5V	150.1 \pm 22.3	F - J034659.4+243049	23.5	23	AEOS	02/03/2003	I	599	0.216
17923		A0V	158.7 \pm 36.8	B - J034958.2+235109	13.8	14	AEOS	03/02/2002	I	289	0.212
19949		A2Vn	108.2 \pm 8.8	F - J041642.9+533649	6.7	16	AEOS	05/02/2002	I	300	0.749
20070	b Per	A2V	97.6 \pm 8.3	B - J041814.8+501747	3.7	7	AEOS	05/02/2002	I	300	0.800
20156		A7V	79.4 \pm 5.3	B - J041913.6+500254	3.6	8	AEOS	05/02/2002	I	300	0.781
20380		A3V	95.0 \pm 6.1	F - J042149.8+563020	16.8	27	AEOS	05/02/2002	I	300	0.677
20400	60 Tau	A3m	45.7 \pm 2.0	F - J042204.5+140440	14.7	27	AEOS	04/02/2002	I	300	0.150
20484	63 Tau	A1m	47.2 \pm 1.8	F - J042325.5+164633	8.1	28	AEOS	04/02/2002	I	300	0.180
20648	δ^3 Tau	A2IV	45.3 \pm 1.6	F - J042528.4+175512	31.8	14	AEOS	04/02/2002	I	300	0.189
21402	88 Tau	A5m	46.1 \pm 1.7	B - J043538.5+100941	11.6	8	CFHT	04/02/2010	K	352	0.317
22287	4 Cam	A3m	49.7 \pm 2.0	F - J044758.6+564531	14.6	18	AEOS	04/02/2002	I	300	0.171
23040	7 Cam	AIV	115.2 \pm 10.8	B - J045714.3+534442	34.8	10	AEOS	05/02/2002	I	300	0.506
23179	ω Aur	AIV	48.8 \pm 2.2	B - J045915.4+375330	5.2	7	Gemini	15/11/2008	K	200	0.545
23875	β Eri	A4III	27.2 \pm 0.6	B - J050750.5-050455	17.3	10	Gemini	19/12/2009	K	200	1.125
24019		A5m	54.7 \pm 3.9	F - J050945.2+280209	20	12	AEOS	04/02/2002	K	200	0.274
26126	38 Ori	A2V	105.8 \pm 8.3	F - J053416.4+034623	23.4	17	AEOS	05/02/2002	I	300	0.466
28614	μ Ori	AIVm	46.5 \pm 1.8	B - J060222.9+093854	4.6	9	Gemini	19/12/2009	I	300	0.322
29997		A0Vn	53.9 \pm 1.9	F - J061849.6+691929	18.7	14	Gemini	19/12/2009	K	200	0.995
30060	2 Lyn	A2Vs	45.7 \pm 2.0	F - J061938.6+590019	22.4	20	CFHT	01/09/2009	K	480	0.310
							AEOS	05/02/2002	I	300	0.243
30419	ϵ Mon	A5IV	39.4 \pm 1.6	B - J062346.2+043544	9.9	10	CFHT	01/09/2009	K	480	0.364
							CFHT	01/09/2009	K	480	1.133

HIP	Name	<i>Hipparcos</i> Spectral Type	Distance μc	ROSAT Source		Observations		Magnitude	Band	Integration <i>sec</i>	2MASS Sources <i>arcmin⁻²</i>	
				Designation B - BSC, F - FSC	Offset <i>arcsec</i>	Tel.	Date					
35643		A7s	34.5±0.9	F - J072119.0+451327	20.9	22	AEOS	02/02/2002	5.38±0.01	I	300	0.183
39095		A1V	73.1±4.3	F - J075951.6-182353	7.4	17	AEOS	02/02/2002	4.51±0.02	I	300	0.756
39847	27 Lyn	A2V	66.8±3.1	F - J080828.5+513040	19.3	16	AEOS	02/02/2002	4.71±0.04	I	300	0.126
41564		A5m	85.2±6.8	B - J082828.5-023051	13.9	9	AEOS	03/02/2002	6.06±0.01	I	300	0.235
42313	δ Hya	A1Vnn	54.9±2.7	B - J083740.1+054217	11.2	11	AEOS	04/02/2002	4.12±0.02	I	300	0.166
44127	ι Uma	A7V	14.6±0.2	B - J085913.0+480227	5.9	11	Palomar	01/03/2003	4.12±0.02	I	300	0.166
45688	38 Lyn	A3V	37.4±1.1	B - J091850.2+364814	7.5	8	CFHT	12/04/2008	2.66±0.24	K	71	0.145
51200		A2V	66.3±3.1	F - J102728.3+413613	9.7	13	CFHT	05/02/2010	2.66±0.24	K	352	0.145
52913	40 Sex	A2IV	95.9±10.8	F - J104917.1-040123	4.7	14	AEOS	06/02/2002	3.81±0.03	I	300	0.081
57646		A3m	62.7±3.2	F - J114915.1+161430	6.4	12	Palomar	12/04/2008	3.42±0.35	K	71	0.124
58001	Phecda	A0Ve	25.6±0.4	B - J115352.3+534153	25	16	CFHT	04/02/2010	5.53±0.02	K	440	0.104
59504		A5m	33.7±0.6	B - J121210.1+773702	7.3	20	AEOS	02/03/2003	6.38±0.01	I	300	0.083
62394	34 Vir	A3V	74.6±5.2	F - J124714.4+115723	12.5	19	AEOS	02/03/2003	5.75±0.01	I	300	0.058
62572		A1IIIsh	93.0±15.1	F - J124909.8+832448	6.7	13	CFHT	05/02/2010	5.35±0.02	K	352	0.091
65198		A2V	65.3±3.4	B - J132141.7+020521	7.2	8	Palomar	11/04/2008	2.49±0.17	H	71	0.090
65241	64 Vir	A2m	63.7±2.9	B - J132209.8+050918	2.6	10	CFHT	05/02/2010	2.43±0.29	K	352	0.102
65477	Alcor	A5V	24.9±0.3	F - J132513.8+545920	3.9	13	AEOS	29/05/2002	4.77±0.00	I	300	0.103
66249	ζ Vir	A3V	22.5 ± 0.4	F - J133442.6-003550	19.6	14	AEOS	29/05/2002	5.98±0.00	I	300	0.059
66727	1 Boo	A1V	92.8±7.8	B - J134040.2+195708	12.8	11	AEOS	29/05/2002	5.26±0.00	I	300	0.126
71618	33 Boo	A1V	60.4±2.0	B - J143850.0+442418	3.7	7	AEOS	02/03/2003	5.64±0.00	I	300	0.075
							CFHT	13/06/2008	5.60±0.05	H	450	0.103
							CFHT	04/02/2010	5.51±0.02	K	440	0.115
							AEOS	03/03/2003	5.82±0.03	I	319	0.066
							CFHT	14/06/2008	5.67±0.03	H	450	0.094
							Palomar	11/04/2008	3.30±0.23	H	71	0.100
							AEOS	03/03/2003	3.27±0.02	I	300	0.079
							CFHT	05/02/2010	3.22±0.27	K	352	0.122
							AEOS	03/03/2003	5.72±0.01	I	300	0.064
							CFHT	14/06/2008	5.28±0.04	H	450	0.098

HIP	Name	Hipparcos Spectral Type	Distance ρc	ROSAT Source		Observations		Magnitude	Band	Integration sec	2MASS Sources $arcmin^{-2}$	
				Designation	Offset $arcsec$	Tel.	Date					
76376		A2V	75.5 ± 3.0	B - J153556.8+54375	3.3	9	AEOS	29/05/2002	5.72 \pm 0.00	I	300	0.089
76878	τ^7 Ser	A2m	53.2 ± 2.3	B - J154154.9+182744	6.9	15	AEOS	29/05/2002	5.61 \pm 0.03	I	300	0.096
77336	ν Ser	A3V	77.2 ± 6.0	F - J154717.7+140652	6.9	15	Palomar	13/07/2008	5.30 \pm 0.02	K	62	0.149
80628	ν Oph	A3m	37.5 ± 1.2	B - J162748.2-082213	4.8	9	AEOS	29/05/2002	5.61 \pm 0.00	I	300	0.108
82321	52 Her	A2Vspe	53.7 ± 1.5	F - J164914.1+455848	12	12	Palomar	12/04/2008	4.17 \pm 0.04	K	47	0.401
83223		A7V	73.1 ± 4.6	F - J170028.6+063456	13.4	29	AEOS	12/07/2008	4.58 \pm 0.04	H	71	0.174
85829	ν^2 Dra	A4m	30.6 ± 0.5	F - J173216.1+551023	1	15	AEOS	29/05/2002	6.33 \pm 0.01	I	300	0.232
87045		A2Vs	131.6 ± 14.2	B - J174707.6+473648	5.2	8	Palomar	12/04/2008	4.16 \pm 0.02	K	71	0.203
87212	30 Dra	A2V	66.5 ± 2.1	F - J174904.5+504651	2.6	34	CFHT	05/02/2010	4.16 \pm 0.02	K	264	0.223
88771	72 Oph	A4IVs	25.4 ± 0.5	F - J180719.8+093411	26.4	16	AEOS	29/05/2002	6.37 \pm 0.01	I	300	0.183
89925	108 Her	A5m	57.6 ± 2.0	F - J182057.4+295146	14.8	12	Gemini	24/06/2008	4.88 \pm 0.02	K	200	0.259
91971	ζ^1 Lyr	Am	47.1 ± 1.2	B - J184446.1+373620	3.7	9	Palomar	12/07/2008	4.88 \pm 0.02	K	71	0.259
93747	ζ Aql	A0Vn	25.5 ± 0.5	B - J190526.0+135136	22.8	12	Palomar	12/04/2008	3.41 \pm 0.19	K	71	0.990
98103	ϕ Aql	A1IV	63.1 ± 3.0	F - J195613.8+112526	8.5	13	CFHT	05/02/2010	3.41 \pm 0.19	K	264	0.990
102033		A2V	82.0 ± 4.4	F - J204036.8+294822	6.1	15	AEOS	31/05/2002	5.37 \pm 0.03	I	300	0.348
106711	74 Cyg	A5V	63.3 ± 2.5	F - J213656.7+402440	8.9	14	Gemini	24/06/2008	4.99 \pm 0.02	K	200	0.540
109521		A5V	54.8 ± 1.7	B - J221109.0+504929	8.7	14	CFHT	01/09/2009	4.99 \pm 0.02	K	720	0.540
110787	ρ^1 Cep	A2m	62.6 ± 2.0	F - J22264.9+784709	4.5	12	CFHT	13/06/2008	3.97 \pm 0.23	K	180	0.566
117452	δ Scl	A0V	44.0 ± 2.2	B - J234854.7-280751	11.2	13	CFHT	13/06/2008	3.05 \pm 0.28	H	180	5.932
							Gemini	18/06/2008	5.26 \pm 0.02	K	200	1.778
							AEOS	31/05/2002	5.87 \pm 0.00	I	300	0.993
							Gemini	08/09/2008	4.51 \pm 0.02	K	200	1.218
							Gemini	08/09/2008	4.96 \pm 0.02	K	200	2.059
							Gemini	17/08/2008	5.54 \pm 0.03	K	200	0.435
							CFHT	30/08/2009	4.53 \pm 0.02	K	480	0.112

Table 7.2: Control sample

HIP	Name	<i>Hipparcos</i> Spectral Type	Distance μ c	Tel.	Observations Date	Magnitude	Band	Integration <i>sec</i>	2MASS Sources <i>arcmin</i> ⁻²
159		A3	59.1±2.8	Gemini	17/10/2008	6.21±0.02	K	200	0.115
2852		A5m	49.7±2.2	Gemini	17/10/2008	5.42±0.02	K	200	0.100
3414	π Cas	A5V	53.5±2.1	AEOS	02/03/2003	4.79±0.01	I	300	0.334
5317	41 And	A3m	60.2±2.7	Gemini	16/10/2008	4.58±0.02	K	200	0.505
8122		A3	71.7±3.8	CFHT	30/08/2009	4.77±0.02	K	200	0.404
9487	α Psc	A2	42.6±1.9	CFHT	01/09/2009	6.17±0.02	K	640	0.229
13717		A1Vn	57.9±3.1	Gemini	18/10/2008	3.62±0.33	K	480	0.115
17489	Celeno	B7IV	102.6±11.1	AEOS	03/02/2002	4.86±0.02	K	200	0.115
17572		A0V	103.3±11.0	AEOS	04/02/2002	5.43±0.03	I	300	0.207
17588	22 Tau	A0Vn	108.6±10.9	AEOS	02/02/2002	6.77±0.01	I	300	0.192
17791		A1V	144.9±20.8	AEOS	04/02/2002	6.41±0.03	I	300	0.213
17847	Atlas	B8III	116.7±14.0	AEOS	04/02/2002	6.83±0.02	I	300	0.217
20507	ξ Eri	A2V	63.9±3.3	Gemini	17/10/2008	3.64±0.03	I	300	0.214
20641	κ^2 Tau	A7	44.2±1.6	CFHT	05/02/2010	4.93±0.02	K	200	0.187
20894	θ^2 Tau	A7III	45.7±1.7	CFHT	04/02/2010	4.61±0.02	K	352	0.362
21039	81 Tau	Am	44.3±2.1	CFHT	05/02/2010	2.88±0.26	K	440	0.307
22192	EX Eri	A3IV	57.5±2.2	Gemini	14/11/2008	4.90±0.02	K	352	0.311
23554		A2IV	60.1±2.3	Gemini	19/12/2009	5.72±0.02	K	200	0.172
23983	16 Ori	A2m	53.9±2.4	Gemini	05/11/2008	5.34±0.02	K	200	0.209
25197	16 Cam	A0Vne	104.3±8.4	AEOS	05/02/2002	4.86±0.02	K	200	0.403
26309		A2III-IV	56.6±2.3	Gemini	14/11/2008	5.23±0.00	I	300	0.337
28360	Menkalinan	A2IV+	25.2±0.5	CFHT	05/02/2010	5.86±0.02	K	200	0.255
28910	θ Lep	A0V	52.2±1.9	Gemini	25/11/2008	1.78±0.19	K	352	0.651
29711		A5IVs	66.5±3.4	Gemini	25/11/2008	4.52±0.02	K	200	0.472
31119		A3V	64.8±3.6	AEOS	04/02/2002	5.86±0.02	K	200	0.729
31290		A3V	136.1±18.0	Gemini	11/11/2008	5.04±0.01	I	300	0.706
				AEOS	05/02/2002	4.77±0.04	K	200	1.198
				AEOS	05/02/2002	6.46±0.01	I	300	0.402

HIP	Name	<i>Hipparcos</i> Spectral Type	Distance μ c	Observations Tel.	Date	Magnitude	Band	Integration <i>sec</i>	2MASS Sources <i>arcmin</i> ⁻²
34897		A5	66.4±3.4	Gemini	10/05/2010	5.99±0.02	K	200	0.293
35341	65 Aur	A5Vn	82.1±6.2	AEOS	02/02/2002	5.69±0.01	I	300	0.207
35350	λ Gem	A3V	28.9±0.8	Palomar	12/04/2008	3.54±0.26	K	68	0.489
38723		A3p	60.4±3.4	CFHT	04/02/2010	3.54±0.26	K	440	0.489
40646	29 Lyn	A7IV	93.2±5.9	Gemini	11/11/2008	5.40±0.02	K	200	0.241
41152		A3V	51.4±1.9	AEOS	03/02/2002	5.46±0.00	I	300	0.116
42806	Asellus Borealis	A1IV	48.6±2.0	AEOS	06/02/2002	5.39±0.01	I	300	0.113
43570		A5V	167.8±38.8	AEOS	02/03/2002	4.64±0.00	I	300	0.123
43932	σ^2 Cnc	A7IV	59.8±3.3	AEOS	04/02/2002	6.21±0.01	I	300	0.138
44066	α Cnc	A5m	53.2±2.8	AEOS	06/02/2002	5.26±0.01	I	300	0.099
44901	15 UMa	A1m	29.3±0.7	AEOS	01/03/2003	4.13±0.03	I	300	0.119
45493	18 UMa	A5V	36.3±1.0	AEOS	01/03/2003	4.19±0.03	I	300	0.087
49593	21 LMi	A7V	28.0±0.7	Palomar	12/04/2008	4.04±0.28	K	69	0.138
51658		A7IV	34.3±0.9	CFHT	05/02/2010	4.04±0.28	K	352	0.138
53910	Merak	A1V	24.4±0.4	AEOS	03/03/2003	4.58±0.03	I	300	0.094
53954	60 Leo	A1m	37.9±1.2	Palomar	12/04/2008	4.29±0.02	K	85	0.138
54063		A5	61.8±3.3	Palomar	12/04/2008	4.00±0.04	K	44	0.108
54136	51 UMa	A3III-IV	80.6±4.6	Palomar	12/04/2008	4.20±0.02	K	69	0.106
57328	ξ Vir	A4V	36.6±1.1	CFHT	04/02/2010	4.20±0.02	K	440	0.106
57632	β Leo	A3V	11.1 ± 0.1	Palomar	04/02/2010	2.29±0.24	K	440	0.106
58510	7 Vir	A1V	84.8±5.4	Palomar	12/04/2008	4.32±0.04	K	71	0.103
58590	π Vir	A5V	109.2±10.1	CFHT	14/06/2008	6.29±0.02	H	450	0.079
59394	3 Crv	A1V	56.1±2.1	AEOS	03/03/2003	5.86±0.01	I	300	0.065
				Palomar	03/03/2003	4.67±0.00	I	300	0.067
				CFHT	11/04/2008	4.41±0.05	K	71	0.104
				CFHT	13/06/2008	4.54±0.08	H	180	0.091
				CFHT	05/02/2010	1.88±0.19	K	352	0.099
				AEOS	02/03/2003	5.34±0.00	I	290	0.068
				AEOS	02/03/2003	4.53±0.02	I	300	0.067
				CFHT	14/06/2008	5.36±0.04	H	450	0.165

HIP	Name	Hipparcos Spectral Type	Distance μ c	Observations		Magnitude	Band	Integration <i>sec</i>	2MASS Sources <i>arcmin</i> ⁻²
				Tel.	Date				
59608	12 Vir	A2m	49.5±1.8	AEOS	03/03/2003	5.61±0.03	I	200	0.060
59774	Megrez	A3V	25.0±0.4	CFHT	04/02/2010	5.24±0.02	K	440	0.097
		Palomar		11/04/2008	3.31±0.25	H	71	0.094	
60746	16 Com	A4V	86.5±5.6	CFHT	13/06/2008	3.31±0.25	H	180	0.094
61960	ρ Vir	A0V	36.9±1.1	AEOS	03/02/2003	4.93±0.03	I	300	0.058
		Palomar		02/03/2003	4.80±0.03	I	300	0.064	
62933	41 Vir	A7III	61.0±2.9	AEOS	11/04/2008	4.76±0.02	H	57	0.092
				CFHT	04/02/2010	4.68±0.02	K	440	1.040
68520	τ Vir	A3V	66.9±3.9	CFHT	05/02/2010	5.47±0.02	K	352	0.097
69592	λ Boo	A7V	59.0±2.6	AEOS	03/03/2003	4.11±0.02	I	300	0.075
		A0p		12/07/2008	5.90±0.02	H	71	0.093	
69951	λ Vir	A5	73.5±3.4	AEOS	03/03/2003	4.15±0.03	I	300	0.069
				Palomar	11/04/2008	4.03±0.25	H	71	0.095
69974	γ Boo	A7III	26.1±0.5	Palomar	12/07/2008	6.40±0.04	H	71	0.097
				AEOS	03/03/2003	4.43±0.02	I	669	0.114
71075	ϵ Ser	A4V	65.3±2.2	Gemini	24/06/2008	4.24±0.02	K	200	0.177
75043	60 Her	A4V	58.9±2.7	Palomar	11/04/2008	2.57±0.25	H	71	0.089
		A4V		29/05/2002	5.52±0.00	I	300	0.082	
76852	ι Ser	A3V	46.9±1.9	Palomar	13/07/2008	4.31±0.02	K	71	0.142
		A5IV		12/04/2008	3.55±0.32	K	67	0.161	
77464	β Ser	A2IV-V	25.8±0.6	Gemini	27/06/2008	5.26±0.02	K	200	0.238
		A2Va		12/04/2007	3.43±0.27	K	71	0.203	
77622	ϵ Ser	A2m	21.6±0.3	Palomar	12/04/2008	4.61±0.02	K	71	0.347
		A4IV		12/04/2008	2.34±0.24	K	71	1.436	
84012	η Oph	A2IV-V	51.5±2.8	Palomar	12/04/2008	4.11±0.25	K	200	3.249
		A0V		28/06/2008	3.62±0.23	K	71	0.919	
86565	γ Oph	A0V	29.0±0.8	Palomar	12/04/2008	3.62±0.23	K	71	0.919
92161	III Her	A5III	28.4±0.6	CFHT	31/08/2009	3.62±0.23	K	480	0.919
		A2III _s		13/06/2008	4.08±0.03	H	180	1.472	
95081	π Dra	A2III _s	68.9±2.2	Gemini	24/06/2008	4.45±0.02	K	200	0.380
		Palomar		12/07/2008	4.58±0.17	H	71	0.348	

HIP	Name	<i>Hipparcos</i> Spectral Type	Distance μ c	Observations		Magnitude	Band	Integration <i>sec</i>	2MASS Sources <i>arcmin</i> ⁻²
				Tel.	Date				
95853	ι^2 Cyg	A5Vn	37.5 \pm 0.6	CFHT	12/06/2008	3.69 \pm 0.23	H	280	0.583
99655	33 Cyg	A3IV-Vn	46.7 \pm 1.0	CFHT	14/06/2008	4.17 \pm 0.27	H	450	0.767
99742	ρ Aql	A2V	47.1 \pm 1.7	CFHT	30/08/2009	4.77 \pm 0.02	K	480	1.353
99770	29 Cyg	A2V	41.0 \pm 0.9	CFHT	31/08/2009	4.42 \pm 0.02	K	480	7.030
100108	36 Cyg	A2V	59.7 \pm 1.9	AEOS	31/05/2002	5.51 \pm 0.00	I	300	2.521
100526		A2	69.2 \pm 2.2	Gemini	08/09/2009	5.49 \pm 0.02	K	200	6.666
101093	θ Cep	A7III	41.6 \pm 0.9	Gemini	08/09/2008	6.20 \pm 0.02	K	200	1.137
101300		Am	81.1 \pm 4.6	AEOS	31/05/2002	6.08 \pm 0.01	I	300	0.980
101483	η Del	A3IVs	53.0 \pm 2.3	Gemini	08/09/2008	5.24 \pm 10.00	K	200	0.796
105966	35 Vul	AIV	55.7 \pm 2.2	Gemini	08/09/2008	5.29 \pm 0.02	K	200	0.630
109427	θ Peg	AIVa	29.6 \pm 0.8	CFHT	14/06/2008	3.39 \pm 0.21	H	450	0.193
109667		A3V	58.1 \pm 2.7	Gemini	10/09/2008	5.74 \pm 0.02	K	200	0.157
111169	α Lac	AIV	31.4 \pm 0.5	CFHT	31/08/2009	5.74 \pm 0.02	K	720	0.157
116354	15 And	AIII	71.6 \pm 3.2	Palomar	12/07/2008	3.87 \pm 0.21	H	71	1.384
				CFHT	30/08/2009	3.85 \pm 0.27	K	480	1.516
				Gemini	08/09/2008	5.28 \pm 0.02	K	200	0.405

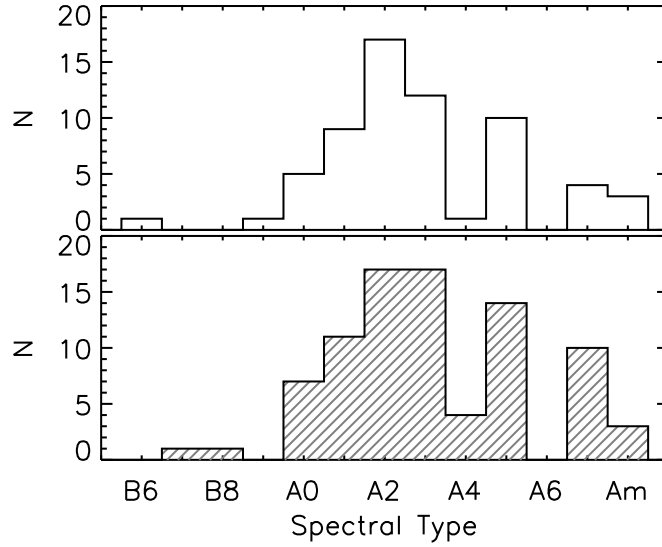


Figure 7.1: Distribution of the spectral type for each target reported within the *Hipparcos* catalogue for the X-ray (white histogram) and control (grey histogram) samples.

7.3 Sample

Two samples were constructed in order to test the companion hypothesis: a 63-star X-ray detected sample, and an 85-star control sample. The distributions of spectral types reported in the *Hipparcos* catalogue for both samples are shown in Figure 7.1, and a K-S test confirms that both are drawn from the same distribution. Both the X-ray and control samples include targets spanning a similar range of ages, as shown in the colour-magnitude diagram in Figure 7.2. To perform a robust test of the companion hypothesis, it was ensured that each sample had a similar distribution of sensitivity to X-ray sources. Background X-ray counts were extracted from the *ROSAT* All Sky Survey (RASS) observations at the coordinates of each target within both samples. A minimum detectable X-ray flux at each coordinate was estimated as five times the background level. These minimum fluxes were calculated assuming a hardness ratio of 0.5, typical of low-mass stellar sources (e.g. Huélamo et al. 2000). The X-ray luminosity (L_X) was then calculated based on a distance equal to that of the target. The distributions of minimum detectable L_X for both samples are shown in Figure 7.3.

The latest spectral type companion to which the RASS observations are sensitive depends on the age of the target, derived from theoretical isochrones (Fig. 7.2 - Marigo et al. 2008), and the X-ray luminosity sensitivity of the observations (Fig. 7.3). The distribution of this spectral type sensitivity is given in Figure 7.4. Most of the targets within both samples had RASS observations sensitive to M-type companions and above: 75% of the X-ray sample and 85% of the control sample. Nearly all the RASS observations were sensitive to K-type companions – 87% of the X-ray and 93% of the control sample – and the few remaining targets were sensitive to F- or G-type companions.

The targets within the X-ray detected sample were chosen based on the presence of a

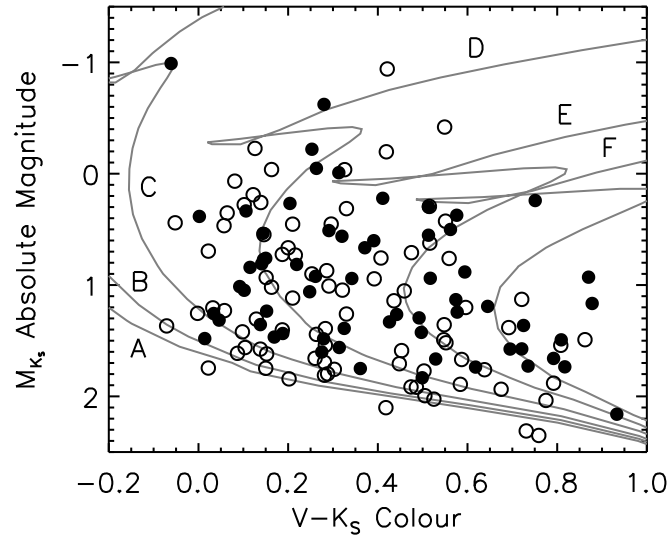


Figure 7.2: A colour-magnitude diagram of the X-ray (filled circles) and control (open circles) samples. Theoretical isochrones are plotted for A - 10Myrs, B - 100 Myrs, C - 250 Myrs, D - 500 Myrs, E - 800 Myrs, F - 1 Gyrs (Marigo et al. 2008).

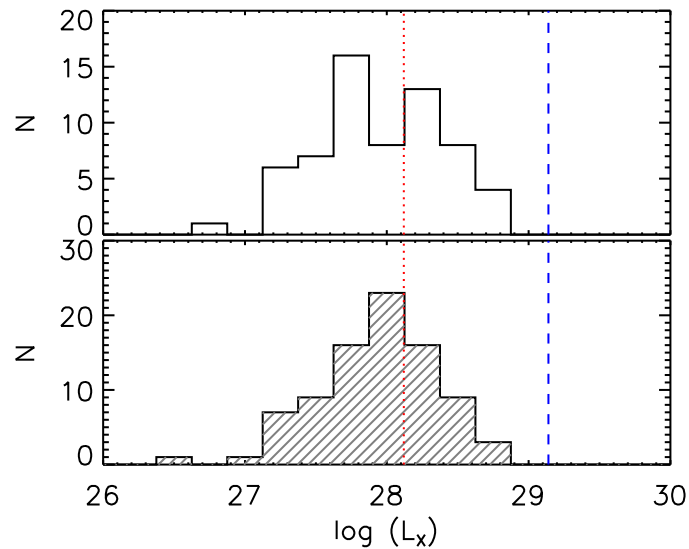


Figure 7.3: Histogram of the *RASS* detection limits for the targets within the X-ray (white histogram) and control (grey histogram) samples. Mean L_x values for Pleiades (100 Myr) and Hyades (650 Myr) M-dwarfs as blue dashed and red dotted lines respectively (Micela et al. 1996; Stern et al. 1995).

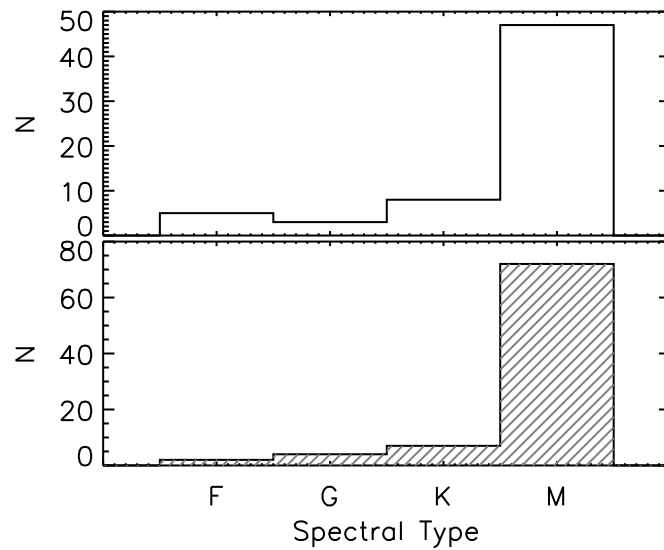


Figure 7.4: Histogram showing the distribution of the sensitivity of RASS observations to lower-mass companions for targets in the X-ray (white histogram) and control (grey histogram) samples. The evolution of L_X as a function of stellar age was derived from observations of open clusters (G del 2004, and references therein).

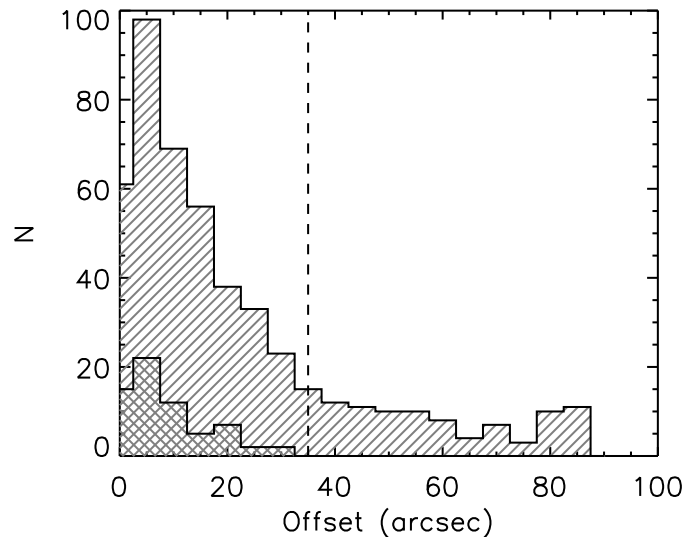


Figure 7.5: Distribution of *Hipparcos* - *ROSAT* offsets for 479 X-ray detected early-type stars (hatched histogram). These stars have a *ROSAT* source within $90''$ using the same criteria as Huensch et al. (1998a). The tail of the distribution was removed by selecting a more stringent maximum offset of $35''$ (dashed line). The offset distribution for the 63 early-type stars within the X-ray detected sample is overplotted (cross-hatched histogram).

ROSAT Bright Source Catalogue (Voges et al. 1999 – BSC) or *ROSAT* Faint Source Catalogue (Voges et al. 2000 – FSC) source within $35''$ of the *Hipparcos* coordinate of each target. As noted in Table 7.5, 51% are from the Faint Source Catalogue. Previous correlations between BSC sources and optical star catalogues (e.g. Huensch et al. 1998a) have typically used a maximum offset of $90''$ between the catalogue positions, to define an X-ray source. The distribution of the offsets between X-ray source position and *Hipparcos* position is given in Figure 7.5 and a more stringent maximum offset cut-off than previous studies has been applied, $35''$. All of the A-type stars within the X-ray sample were also identified as X-ray stars in previous studies of X-ray detected A-type stars (e.g. Schröder & Schmitt 2007).

Table 7.3: Instruments used to obtain observations

Telescope	Proposal ID	Dates	N	Filter	λ/D	Field of view	Pixel Scale	North
AEOS	-	02-02-2002 - 03-03-2003	101	I_C	0''.05	24''.6 × 24''.6	0''.048 ± 0''.003	0.0° ± 1.0°
CFHT	2008A-C22	12-06-2008 - 14-06-2008	14	H (FeII)	0''.09	35''.6 × 35''.6	0''.035 ± 0''.0001	-2.4° ± 0.1°
	2008A-C22	13-06-2008 - 14-06-2008	1	K' (H2 ₁₋₀)	0''.13	35''.6 × 35''.6	0''.035 ± 0''.0001	-2.4° ± 0.1°
	2009B-C06	30-08-2009 - 01-09-2009	18	K' (H2 ₁₋₀)	0''.13	35''.6 × 35''.6	0''.035 ± 0''.0001	-2.4° ± 0.1°
	2010A-C14	04-02-2010 - 05-02-2010	29	K' (H2 ₁₋₀)	0''.13	35''.6 × 35''.6	0''.035 ± 0''.0001	-2.4° ± 0.1°
Gemini	GN-2008A-Q-74	18-06-2008 - 24-06-2008	8	K' (Br γ)	0''.06	21''.7 × 21''.7	0''.021 ± 0''.0001	0.5° ± 0.3°
	GN-2008B-Q-119	17-08-2008 - 25-11-2008	26	K' (Br γ)	0''.06	21''.7 × 21''.7	0''.021 ± 0''.0001	0.5° ± 0.3°
	GN-2009B-Q-120	08-09-2009 - 19-12-2009	6	K' (Br γ)	0''.06	21''.7 × 21''.7	0''.021 ± 0''.0001	0.5° ± 0.3°
	GN-2010A-Q-75	10-05-2010	1	K' (Br γ)	0''.06	27''.7 × 21''.7	0''.021 ± 0''.0001	0.5° ± 0.3°
Palomar	-	11-04-2008 - 13-07-2008	13	H (CH4s)	0''.07	25''.4 × 25''.4	0''.025 ± 0''.002	-0.7° ± 0.1°
Palomar	-	11-04-2008 - 13-07-2008	22	K_S (Br γ)	0''.09	25''.4 × 25''.4	0''.025 ± 0''.002	-0.7° ± 0.1°

7.4 Observations

High-resolution AO images were obtained for all 148 stars in order to compare the binary statistics of the X-ray and control samples. The data were acquired with several instruments listed in Table 7.3 – VisIm (Roberts & Neyman 2002) on AEOS, KIR (Doyon et al. 1998) on CFHT, NIRI (Hodapp et al. 2003) on Gemini North, and PHARO (Hayward et al. 2001) on Palomar. The resolution limit λ/D ranged from $0''.05$ for the I_C -band AEOS images to $0''.13$ for the K' CFHT images. The filter used for observations with each instrument is given in Table 7.3, alongside the corresponding narrowband filter in parentheses. The FWHM of the image cores typically matched the diffraction-limit, due to the high quality AO correction on these bright stars. Given the nearby distances of the targets ($D < 170$ pc), the resolution limit corresponds to projected separations of $\sim 10 - 20$ AU. The field-of-view ranges from $21''.7 \times 21''.7$ to $35''.6 \times 35''.6$, making binary systems as wide as ~ 3000 AU detectable. The effective field-of-view for the combined science images was increased by dithering the target on the detector. The search range covers the peak of the binary separation distribution of lower mass stars (e.g. Duquennoy & Mayor 1991; Fischer & Marcy 1992), important for resolving the bulk of the binary population.

The observing strategy was consistent for all targets. To search for close companions, unsaturated exposures were obtained of each target using either a narrow-band or neutral-density filter. Exposure times ranged from 0.01s to 4.0s, with stacks of 3 to 500 frames. To detect wider, fainter objects approaching the bottom of the Main Sequence, longer exposures in a wide-band filter were recorded with total integration times ranging from 41s to 720s. Details of the filter combinations are given in Table 7.3 and exposure times of individual targets are listed in Tables 7.1 and 7.2. Because of the brightness of the targets, all-sky survey images from *2MASS* are saturated over a significant fraction of the separation range covered by the images within this study.

7.5 Data analysis

The science images were processed with standard image reduction steps including dark subtraction, flat fielding, interpolation over bad pixels, and sky subtraction. Alignment of short exposure images was achieved through Gaussian centroiding, while the saturated exposures were aligned by cross-correlating the diffraction spikes (e.g. Lafrenière et al. 2007a). To improve the measurable contrast ratios, a radial subtraction was performed on the saturated images to suppress the seeing halo of the central star. Finally, all the processed images were median-combined to increase the signal-to-noise ratio of any detection.

Candidates were identified by visual inspection, and the separation and magnitude difference were measured for each candidate, as reported in Tables 7.4 and 7.5. The projected separation between the central star and candidate was calculated from the positions of the centroids of each component in the final median-combined image. The uncertainty of the separation incorporates both the uncertainty in the instrument pixel scale, given in Table 7.3, and the standard deviation of the measurements from each individual exposure. An estimate of

the physical separation in AU was then determined from the *Hipparcos*-derived distance to the primary. The position angle of each candidate was measured based on the instrument field orientation, given in Table 7.3, and the rotation angle on the sky for all Gemini and a subset of the AEOS data. For data obtained at Palomar and CFHT, there is no instrument or sky rotation. Typically, the total uncertainty is dominated by the measurement uncertainty, however the lack of calibration measurements within some of the observation runs requires a more conservative estimate of the plate scale and angle of true north uncertainty.

The magnitude difference between each candidate and target star was measured with aperture photometry. Using an aperture of twice the FWHM, the fluxes for the candidate and unsaturated star were measured. If the candidate was only detected in the saturated image, then the comparison flux of the central star was scaled according to the exposure time of the saturated image and the appropriate filter bandpass. The reported magnitude difference uncertainty was estimated as the standard deviation of the values from each processed image before combination. Using the magnitudes of the target from the *Hipparcos* and *2MASS* (Skrutskie et al. 2006) source catalogues, the apparent magnitude of the candidate was determined. An estimate of the physical properties of both primary and candidate companion was made using a combined set of theoretical solar-metallicity isochrones (Marigo et al. 2008; Baraffe et al. 1998). Each target was plotted on a colour-magnitude diagram (Fig. 7.2) from which an estimate of the age was derived. Estimated colours and bolometric luminosities were obtained for the companion candidates based on the measured magnitude difference, using an isochrone of the same age as the primary.

7.6 Results

Table 7.4: Candidate binary systems within control sample

Designation	Separation <i>arc sec</i>	Position Angle <i>degrees</i>	Magnitude Difference	Filter	Observation Date
HIP2852 B [†]	0.93 ± 0.01	260.6 ± 0.3	5.07 ± 0.03	Br γ	17/10/2008
HIP9487 B	1.83 ± 0.01	266.9 ± 0.2	0.33 ± 0.01	H2 ₁₋₀	01/09/2009
HIP17572 B	3.4 ± 0.1	333.0 ± 1.0	2.54 ± 0.01	I _C	04/02/2002
HIP28360 C	13.9 ± 0.3	155.0 ± 0.1	8.5 ± 0.2	K'	05/02/2010
HIP29711 B	~4.2	~239.7	< 2.5	K'	25/11/2008
HIP35350 B	9.7 ± 0.1	33.8 ± 0.1	3.8 ± 0.1	Br γ	12/04/2008
HIP43570 B	0.66 ± 0.02	310.0 ± 1.0	2.58 ± 0.01	I _C	04/02/2002
HIP44066 B	10.3 ± 0.3	320.9 ± 1.0	5.5 ± 0.2	I _C	01/03/2003
HIP44901 B [†]	26.2 ± 0.1	33.9 ± 0.1	6.0 ± 0.1	K'	05/02/2010
HIP51658 B	16.9 ± 0.04	357.6 ± 0.1	6.0 ± 0.2	K'	04/02/2010
HIP54136 B	7.7 ± 0.3	110.7 ± 1.0	4.6 ± 0.2	I _C	03/03/2003
HIP58510 B [†]	3.2 ± 0.1	218.4 ± 1.0	9.2 ± 0.3	I _C	02/03/2003
HIP68520 Aa [†]	14.4 ± 0.5	41.9 ± 1.0	7.7 ± 0.1	I _C	03/03/2003
HIP69592 B [†]	4.05 ± 0.03	174.5 ± 0.1	5.1 ± 0.1	CH4 _S	12/07/2008
HIP75043 B	0.26 ± 0.01	227.6 ± 2.0	6.0 ± 0.4	I _C	29/05/2002
HIP84012 B	0.58 ± 0.01	236.0 ± 0.2	0.6 ± 0.1	Br γ	12/04/2008
HIP95081 B [†]	13.1 ± 0.1	16.9 ± 0.3	8.7 ± 0.1	K'	24/06/2008

Designation	Separation <i>arc sec</i>	Position Angle <i>degrees</i>	Magnitude Difference	Filter	Observation Date
HIP101300 B	0.26 ± 0.01	241.7 ± 1.3	1.0 ± 0.1	I_C	31/05/2002
HIP109667 B [†]	1.12 ± 0.01	285.2 ± 0.3	4.1 ± 0.1	Br γ	10/09/2008
	1.11 ± 0.01	284.7 ± 0.2	4.2 ± 0.1	H2 ₁₋₀	31/08/2009

† - Previously unresolved companion candidate

Table 7.5: Candidate binary systems within X-ray detected sample

Designation	Separation <i>arc sec</i>	Position Angle <i>degrees</i>	Magnitude Difference	Filters	Observation Date	Estimated $V - I$	Estimated $\log(L_X/L_{\text{Bol}})$
5310 B ^{†*}	0.36 ± 0.01	175.3 ± 0.3	3.91 ± 0.04	Br γ	16/10/2008	1.98	-3.01
9480 B*	0.67 ± 0.01	297.3 ± 0.2	1.18 ± 0.02	H2 ₁₋₀	01/09/2008	0.64	-4.24
11569 B*	2.77 ± 0.01	230.0 ± 0.2	1.60 ± 0.02	H2 ₁₋₀	05/02/2010	0.64	-4.32
11569 C	7.22 ± 0.01	115.3 ± 0.1	1.98 ± 0.01	H2 ₁₋₀	05/02/2010	0.75	-4.08
13133 C [†]	~ 6.6	~ 70.5	< 1.9	K'	14/11/2008	0.86	-3.00
13133 D ^{†*}	3.87 ± 0.03	229.8 ± 0.3	9.4 ± 0.3	K'	14/11/2008	4.94	1.16
17608 Ab [†]	0.25 ± 0.02	111.0 ± 1.1	4.0 ± 0.4	I _C	04/02/2002	0.54	-4.32
17923 B	3.1 ± 0.1	232.3 ± 1.0	2.66 ± 0.01	I _C	03/02/2002	0.65	-3.29
17923 Ca	9.7 ± 0.3	233.7 ± 1.0	2.8 ± 0.1	I _C	03/02/2002	0.68	-3.23
17923 Cb	10.2 ± 0.3	235.0 ± 1.0	4.5 ± 0.2	I _C	03/02/2002	1.08	-2.52
19949 B [†]	13.5 ± 0.4	146.9 ± 1.0	7.3 ± 0.3	I _C	05/02/2002	1.88	-2.63
20648 B	1.7 ± 0.1	337.9 ± 1.0	3.12 ± 0.02	I _C	04/02/2002	0.80	-4.84
22287 Ab*	1.80 ± 0.01	341.4 ± 0.1	2.55 ± 0.01	H2 ₁₋₀	04/02/2010		
22287 B*	0.46 ± 0.01	41.6 ± 1.2	3.8 ± 0.1	I _C	05/02/2002	1.13	-4.41
23179 B*	13.2 ± 0.5	238.7 ± 1.0	5.5 ± 0.2	I _C	05/02/2002	1.82	-3.78
24019 B*	~ 4.7	~ 4.0	< 2.6	K'	15/11/2008	1.12	-2.81
28614 BaBb*	~ 11.2	~ 26.1	< 2.4	I _C	04/02/2002	0.86	-4.38
29997 B [†]	0.40 ± 0.01	22.1 ± 0.3	1.27 ± 0.01	K'	19/12/2009	0.27	-5.36
30419 B*	8.47 ± 0.05	218.1 ± 0.4	6.8 ± 0.1	K'	01/09/2009	2.43	-2.16
39095 B*	12.20 ± 0.04	29.0 ± 0.2	1.72 ± 0.03	H2 ₁₋₀	01/09/2009	0.65	-4.95
39847 Aa [†]	5.3 ± 0.2	65.8 ± 1.0	9.5 ± 0.7	I _C	02/02/2002	2.32	-2.63
42313 Ab [†]	4.6 ± 0.2	114.0 ± 1.0	9.5 ± 0.5	I _C	02/02/2002	2.39	-2.26
44127 B*	2.6 ± 0.1	265.1 ± 1.0	6.6 ± 0.2	I _C	04/02/2002	1.79	-3.08
	2.6 ± 0.1	262.7 ± 3.1	7.3 ± 0.2	I _C	01/03/2003		
	2.35 ± 0.02	76.6 ± 0.1	4.22 ± 0.02	Br γ	12/04/2008	2.08	-3.55
44127 C*	2.40 ± 0.01	78.8 ± 0.1	4.36 ± 0.02	H2 ₁₋₀	05/02/2010		
	1.94 ± 0.02	79.8 ± 0.1	4.26 ± 0.02	Br γ	12/04/2008	2.09	-3.53
	1.92 ± 0.01	87.2 ± 0.1	4.30 ± 0.02	H2 ₁₋₀	05/02/2010		

Designation	Separation <i>arc. sec</i>	Position Angle <i>degrees</i>	Magnitude Difference	Filters	Observation Date	Estimated $V - I$	Estimated $\log(L_X/L_{\text{Bol}})$
45688 B*	2.5 ± 0.1	222.6 ± 1.0	1.64 ± 0.03	I_C	06/02/2002	0.48	-4.79
51200 B*	2.60 ± 0.02	224.0 ± 0.1	1.2 ± 0.1	Br γ	12/04/2008		
52913 B*	2.41 ± 0.01	304.1 ± 0.1	3.08 ± 0.01	H2 $_{1-0}$	04/02/2010	1.42	-3.63
62394 Ab [†] *	2.3 ± 0.1	13.8 ± 1.1	0.31 ± 0.01	I_C	02/03/2003	0.31	-5.13
65241 B [†] *	3.2 ± 0.1	348.8 ± 1.4	7.0 ± 0.2	I_C	29/05/2002	2.16	-2.37
65477 B*	0.34 ± 0.02	41.7 ± 3.2	4.3 ± 0.4	I_C	03/03/2003	1.40	-3.16
66249 B	1.07 ± 0.01	209.0 ± 0.1	5.6 ± 0.1	CH4s	11/04/2008	2.19	-3.46
66727 B	1.81 ± 0.01	154.4 ± 0.1	6.4 ± 0.1	H2 $_{1-0}$	05/02/2010	2.45	-3.18
76376 C [†] *	4.4 ± 0.1	338.5 ± 1.2	2.95 ± 0.02	I_C	03/03/2003	0.74	-3.72
76878 B*	9.6 ± 0.4	350.1 ± 1.0	11.9 ± 0.3	I_C	29/05/2002	3.6	-1.52
	2.3 ± 0.1	53.4 ± 1.7	7.3 ± 0.2	I_C	29/05/2002	2.24	-2.31
	2.4 ± 0.02	86.4 ± 0.1	5.1 ± 0.4	K_S	13/07/2008		
80628 B*	0.67 ± 0.01	22.6 ± 0.1	2.26 ± 0.03	Br γ	12/04/2008	0.90	-3.78
82321 B	1.82 ± 0.01	34.1 ± 0.1	2.2 ± 0.1	CH4s	12/07/2008	0.77	-4.66
82321 C	2.06 ± 0.02	38.4 ± 0.1	2.69 ± 0.03	CH4s	12/07/2008	0.90	-4.39
87045 B*	0.32 ± 0.01	144.1 ± 1.1	2.45 ± 0.04	I_C	29/05/2002	0.62	-3.71
88771 B*	24.83 ± 0.06	297.6 ± 0.1	5.2 ± 0.1	K'	05/02/2010	2.18	-3.83
88771 D	24.20 ± 0.06	48.4 ± 0.1	8.1 ± 0.1	K'	05/02/2010	3.40	-2.53
91971 B	23.28 ± 0.07	51.3 ± 0.2	9.7 ± 0.2	K'	13/06/2008	4.27	-0.33
93747 B	7.27 ± 0.02	47.0 ± 0.2	4.88 ± 0.02	FeII	13/06/2008	1.99	-3.23
98103 C [†] *	2.8 ± 0.1	184.7 ± 0.2	4.7 ± 0.1	K'	18/06/2008	2.05	-2.96
102033 B*	0.72 ± 0.02	345.4 ± 1.1	2.36 ± 0.01	I_C	31/05/2002	0.72	-4.62
106711 B [†]	6.98 ± 0.04	58.1 ± 0.3	8.5 ± 0.1	K'	08/09/2008	3.00	-2.14
109521 B [†] *	9.98 ± 0.06	241.3 ± 0.3	8.1 ± 0.1	K'	08/09/2008	3.27	-1.18
110787 B [†] *	0.29 ± 0.01	211.1 ± 0.6	4.3 ± 0.1	Br γ	17/09/2008	2.03	-3.18
117452 Ba [†] *	3.7 ± 0.1	237.3 ± 0.4	3.48 ± 0.04	H2 $_{1-0}$	30/08/2009	1.61	-3.01
117452 Bb [†] *	3.5 ± 0.1	238.5 ± 0.5	3.7 ± 0.1	H2 $_{1-0}$	30/08/2009	1.73	-2.90

[†] - Previously unresolved companion candidate

* - Companion candidate falls within RASS error ellipse

Table 7.6: Multiplicity fraction within both samples

	<i>Total Field-of-View</i>		<i>RASS Error Ellipse Search Area</i>	
	X-Ray	Control	X-Ray	Control
A8 - M9 Companion ¹	60 ⁺⁶ ₋₆ %	20 ⁺⁵ ₋₄ %	43 ⁺⁶ ₋₆ %	12 ⁺⁴ ₋₃ %
B6 - A7 Companion	2 ⁺⁴ ₋₁ %	2 ⁺³ ₋₁ %	3 ⁺⁴ ₋₁ %	2 ⁺³ ₋₁ %
No Resolved Companion	38 ⁺⁶ ₋₆ %	78 ⁺⁴ ₋₅ %	56 ⁺⁶ ₋₆ %	86 ⁺³ ₋₄ %

¹ - Expected spectral type based on measured magnitude difference and assuming the same distance as the target.

7.6.1 Detections

Among the 148 targets, a total of 68 candidate companions were imaged around 59 members of the total sample. One-third of the candidate companions, 23 systems, are newly resolved. The binary angular separations range from $0''.3$ to $26''.2$, and the magnitude differences range from 0.3 to 11.9, corresponding to spectral types of mid-A to late-M for associated companions. The measured magnitude difference of the candidates is plotted as a function of separation in Figure 7.6. Properties of the companion candidates in the X-ray and control samples are listed in Tables 7.4 and 7.5, respectively. Candidate companions are limited to those with less than 5% probability of being a background object, based on the star density analysis described in §7.6.3.

7.6.2 Detection limits

The sensitivity to companions varies with angular separation from the central star due to the significant residual halo from the bright targets. Detection limits for each image are quantified by determining the flux level in a 5×5 pixel aperture that would produce a signal 5σ above the noise within the aperture. The median magnitude difference sensitivity curve for each instrument is plotted in Figure 7.6. Since the data were obtained at several wavelengths, the bottom of the Main Sequence corresponds to a different magnitude difference for each instrument. For an A0 primary, a companion at the bottom of the Main Sequence would have an absolute magnitude of 14.3 at I_C , 10.5 at H , and 10.2 at K_S at an age of 700 Myr. The infrared data obtained at CFHT and Gemini are sensitive to the bottom of the Main Sequence at separations beyond $\sim 2''$. The achieved contrast for the Palomar data was less due to the shorter exposure times, and reached a companion mass limit of $0.12 M_\odot$ to $0.2 M_\odot$, depending on the age of the target. The AEOS data have a sensitivity limit to companions ranging from $0.08 M_\odot$ to $0.1 M_\odot$. The sensitivity to companions for both the X-ray and control samples is similar, making the difference between the two measured binary frequencies a valid test of the companion hypothesis.

7.6.3 Probability of chance superpositions

An estimate of the probability of each companion candidate being an optical binary was made based on the local stellar densities for each target, measured from the *2MASS* source catalogue. The number of sources within a $2^\circ \times 2^\circ$ box of each target was determined in magnitude bins

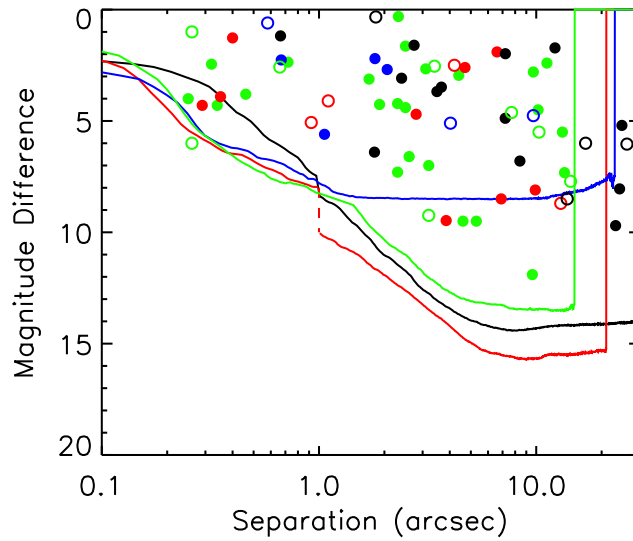


Figure 7.6: The magnitude difference of the candidate companions detected within this study as a function of angular separation from the central star. Filled and open circles represent companions within the X-ray and control samples, respectively. Colours represent each of the instruments used: AEOS (green), CFHT (black), Gemini (red), Palomar (blue). Over-plotted are the detection limits for each instrument (see §7.6.2). The dashed portion of the Gemini sensitivity curve represents the edge of the field of view for the unsaturated exposures.

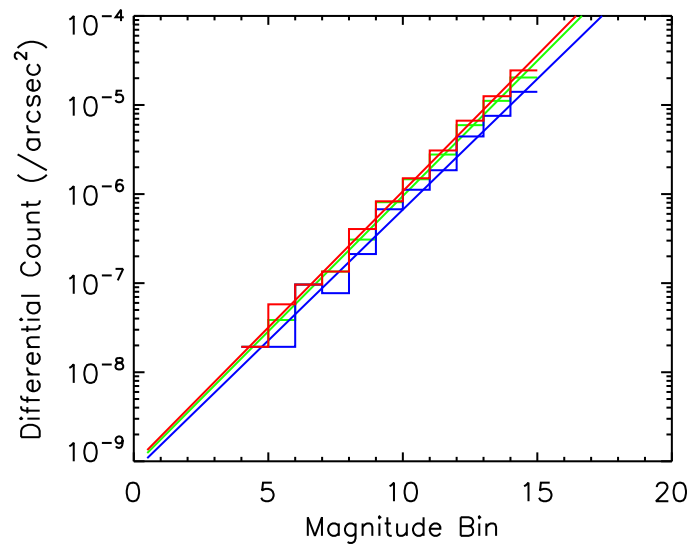


Figure 7.7: Histogram of differential source counts and corresponding logarithmic fits within the *2MASS* source catalogue in the vicinity of HIP 57646 in *J*, *H* and *K_S* filters (blue, green and red respectively).

1 magnitude in width from 0–14 mag for the J , H , and K_S bandpasses. An example plot of this differential source count per area is given in Figure 7.7. A power law fit was applied to the counts such that

$$N = \pi\rho^2 10^{b+am} \quad (7.1)$$

where N is the number of sources within a separation ρ from the target, with an apparent magnitude brighter than m , expressed as a function of the two fit parameters a , the gradient, and b , the intercept. For the I_C band observations obtained at the AEOS, the local stellar density is approximated using the J band *2MASS* data. Candidates with $N > 0.05$ were assumed to be a background object, and not counted for any aspect of this study – a total of 492 candidates were rejected through this process. To compare the stellar density across the samples, Tables 7.1 & 7.2 give the number of objects brighter than 14th magnitude expected per square arcminute in the vicinity of each target. In order to prove physical association of the companion candidates which satisfy this criterion, a second epoch measurement will be required.

7.7 Discussion

7.7.1 Multiplicity comparison

The frequency of multiple systems in the X-ray and control sample was determined by two methods. In the first calculation, the total field-of-view of each observation was used, and, in the second calculation, the search area was restricted to the RASS position error box. For each approach, candidate companions with a small magnitude difference, consistent with a spectral type in the B6–A7 range, were excluded from the X-ray companion hypothesis test and are listed separately in Table 7.6. This criterion of a companion capable of generating X-rays eliminated one binary companion from the X-ray sample and two companions from the control sample. All multiple systems considered also satisfied the background object probability of $< 5\%$, as described in §7.6.3.

Considering the total field-of-view of the combined dithered observations, candidates satisfying the magnitude and background probability criteria were included in the multiple frequency measurement. Among the X-ray sample, $60_{-6}^{+6}\%$ were multiple, compared to $20_{-4}^{+5}\%$ for the control sample – a difference of $40 \pm 8\%$, a 5σ result. These and subsequent reported errors are estimated from a binomial distribution (e.g. Burgasser et al. 2003). Spectroscopic binaries – unresolved with these observations – constitute a significant fraction of both samples ($\sim 15\%$, Pourbaix et al. 2004). This estimate represents a lower limit on the frequency since the sample of stars observed with the radial velocity monitoring is not known, and the large $v \sin i$ of the primary and less massive unseen companions make such observations challenging. These spectroscopically resolved binaries are not considered within the statistics.

The multiplicity of the X-ray sample was also measured by considering only companion candidates that were located within the confines of the RASS error ellipse. For each target, the AO data covered a portion of the RASS error ellipse ranging from 25 to 100 percent. This

additional restriction lowered the multiple frequency to $43_{-6}^{+6}\%$. To determine a comparable frequency for the control sample, a series of companion searches were performed by randomly assigning the RASS-optical offset and corresponding error ellipse of an X-ray target to a control target and determining the number of candidate companions which fall within the error ellipse. Based on a large number of simulations (100,000), the frequency of multiples was estimated as $12_{-3}^{+4}\%$. These two frequencies are different by $31 \pm 7\%$, a 4σ result.

A summary of the multiplicity calculations is given in Table 7.6. The high statistical significance of the difference in frequencies for the X-ray and control samples provides strong support of the companion hypothesis as an explanation of the X-ray detection of B6-A7 stars. Further evidence for individual systems with separations of a few arcseconds could be provided by high-resolution *Chandra* observations which would have the pointing accuracy to assign the X-ray flux to the companion unambiguously. One target, Merope in the Pleiades, was observed with the high-resolution mode of *Chandra*, but the binary separation is only $0''.25$, making the discrepancy between the *Chandra* and *2MASS* coordinates ambiguous in this case. Targets within the X-ray sample for which no companions have been resolved will make prime targets for future interferometric and spectroscopic study in a search for lower-mass companions with angular separations low enough to render them undetectable with AO observations.

7.7.2 *ROSAT* positional uncertainty

Previous studies of the unexplained X-ray detection of early-type stars (e.g. Schröder & Schmitt 2007) have used the same definition of an X-ray detected early-type star as presented by Huensch et al. (1998a) – any X-ray source within $90''$ of an optical source can be attributed to the optical source. This value was based on estimating the frequency of false attribution by means of a Monte Carlo simulation, and was selected at the radius at which the probability of correctly attributing an X-ray source is ~ 50 percent. A significantly lower offset of $25''$ was calculated by Voges et al. (1999) from a correlation of the *Tycho* catalogue and *ROSAT* Bright Source Catalogue positions, a radius within which 90 percent of the optical targets have an X-ray source attributed. This measurement represents the empirical positional uncertainty of the RASS source catalogue positions.

The sample investigated within this study was initially selected in the same manner as Huensch et al. (1998a) – using a maximum offset of $90''$. The tail of the offset distribution was removed by applying a more stringent maximum offset at $35''$, as described in §7.3. Variations in the field-of-view size between instruments caused the coordinates of the X-ray source given within the RASS to be outside of the field-of-view within a small subset of the observations. In order to investigate any biases this may have had upon the results presented previously, the sample was further restricted to only include those targets for which the RASS source position was within the field-of-view and at least 50 percent of the RASS error ellipse was covered – a total of 45 stars. For this sample a marginally higher frequency of companions located within the RASS error ellipse was recorded, $53_{-7}^{+7}\%$, reinforcing the result obtained with the unrestricted sample.

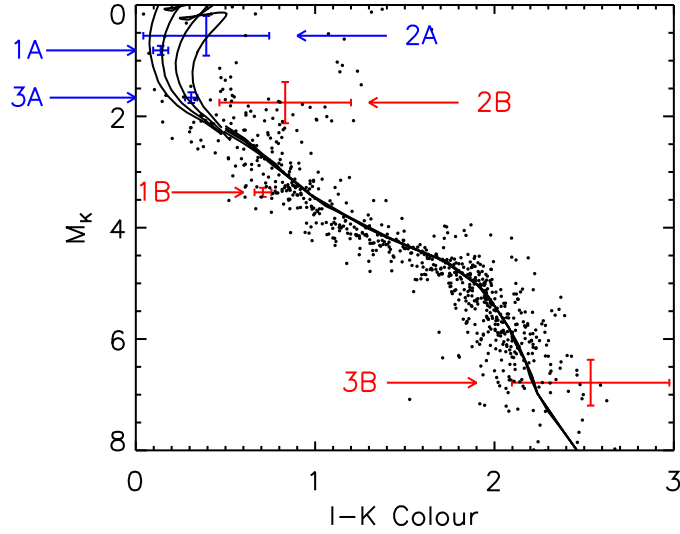


Figure 7.8: A colour-magnitude diagram of 792 nearby Gliese stars. Overplotted are four theoretical isochrones of ages $\log t = 8.7, 8.8, 8.9, 9.0$ (Marigo et al. 2008; Baraffe et al. 1998). Three of the targets within the X-ray sample are plotted in blue: HIP 20648 (1), HIP 45688 (2) and HIP 76878 (3). The corresponding resolved companions for each primary are shown in red.

7.7.3 Comparison of measured and expected X-ray luminosities

Candidate companions with measured colours

Several of the candidate companions to X-ray targets have a measured $I - K$ colour from this study, and are plotted in Figure 7.8. The colour provides additional information to estimate the spectral type of the object and to test further the capacity of the second object to generate X-ray emission. The three systems with colours are: (1) HIP 20648, (2) HIP 45688, and (3) HIP 76878. The $I - K$ colours of the candidate companions are all consistent with X-ray emitting companions: 0.71 ± 0.05 or late F-/early G-type for HIP 20648 B, 0.83 ± 0.37 or mid G-type for HIP 45688 B, and 2.54 ± 0.44 or late M-type for HIP 76878 B.

With the assumption of a distance and age equivalent to the primary distance, the X-ray luminosity associated with the *ROSAT* detection can be checked for consistency with the spectral type. The position on the colour-magnitude diagram for each primary star and its imaged candidate companion is given in Figure 7.8, assuming the distance to each component is the same. Each case is examined individually, and the colour and proper motion measurements clearly support the assignment of the X-ray emission to the candidate companion in two cases, while one case remains uncertain.

The theoretical isochrone that best fits the first target, HIP 20648A, corresponds to an age of ~ 650 Myr, and the candidate companion position in Figure 7.8 is as expected for an associated companion. The companion X-ray luminosity is $\log L_X = 28.71$, and this value falls between the X-ray luminosities of Hyades F- and G-type stars. The assessment of the second target, HIP 45688, is complicated by the presence of a known close companion to the

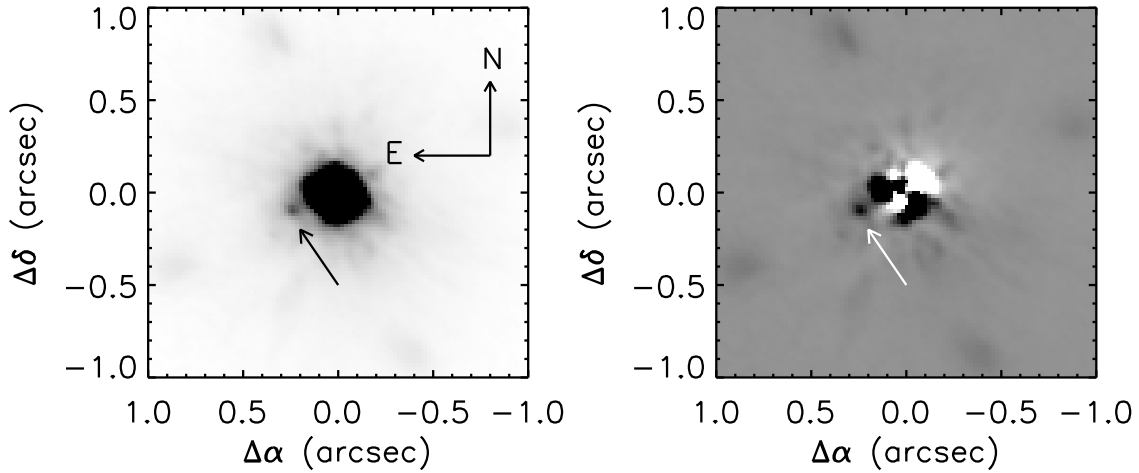


Figure 7.9: A sub-arcsecond companion candidate is resolved around HIP 17608 (Merope), a member of the Pleiades cluster. A faint ($\Delta I = 4.0 \pm 0.4$) companion candidate at $\rho = 0''.25$, $\theta = 110^\circ$ is visible within the median combined image of the 500, 0.048 second unsaturated exposures (*left panel*). The scale is linear from 0 (white) to 45 (black). After radial subtraction the object becomes more prominent (*right panel*), with a linear scale between -15 and 20.

imaged candidate companion ($\rho \sim 0''.06$ – McAlister et al. 1993), unresolved in the current data. The composite colour and magnitude of the BaBb system appear to be more luminous than expected for an object at the 630 Myr age estimated for the primary, even if the pair is an equal magnitude binary. The X-ray luminosity of BaBb would be $\log L_X = 29.43$, significantly higher than younger G-type stars in the Hyades. For the final system, HIP 76878, the best fit age is 700 Myr, similar to the Hyades. The X-ray luminosity of the candidate companion is $\log L_X = 29.26$, if the distance is equal to that of HIP76878. This X-ray level is higher than observed X-ray luminosities of M-dwarfs of similar age within the Hyades (Stern et al. 1995). In this case, the time baseline between the two observations also reveals a significant motion of the candidate relative to the primary on a trajectory different from both a background object and a bound companion. The presence of a foreground M-dwarf in a chance superposition with HIP76878 explains this discrepant proper motion, the red colour of the object, and the unusually high X-ray luminosity.

Candidate companions in open clusters

A subset of the X-ray detected targets with imaged candidate companions are members of stellar clusters. HIP 17608 and HIP 17923 are Pleiades members, while HIP 20648 is a Hyades member. Extensive X-ray population studies of both the Pleiades (e.g. Micela et al. 1985; Stauffer et al. 1994; Daniel et al. 2002) and the Hyades (e.g. Micela et al. 1988; Stern et al. 1995) have been conducted with *Einstein ROSAT* and *Chandra*, providing comparison X-ray luminosities to test the likelihood that the candidate companions are responsible for the detected X-ray emission.

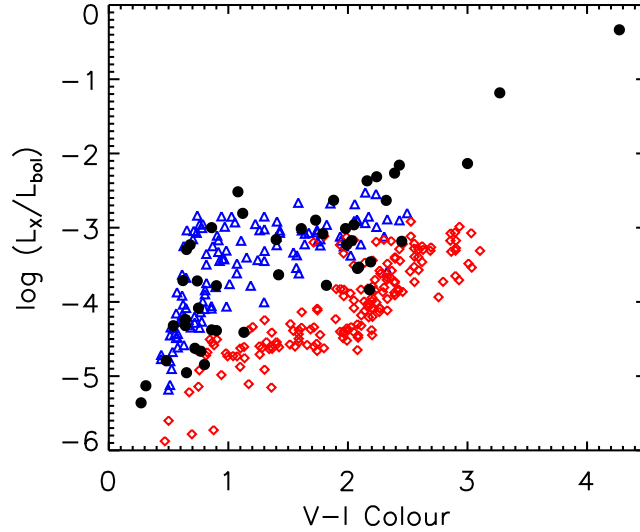


Figure 7.10: The ratio of X-ray to bolometric luminosity is plotted as a function of colour for the candidates resolved within this study. The majority of candidates are constrained by the Pleiades (blue triangles) and Hyades (red diamonds) members, representing the two age extremes of the sample.

The candidate companion to HIP 17608 (Merope in the Pleiades) with $0''.25$ separation is shown in Figure 7.9. With a magnitude difference of $\Delta I_C = 4.0 \pm 0.4$, the second object is a mid F-type star if associated. Assuming a distance to the Pleiades of 133 pc (Pan et al. 2004), the X-ray luminosity for the HIP 17608 system is $\log L_X = 29.91$. The typical X-ray luminosity of F-dwarfs within the Pleiades is estimated to be $\log L_X \sim 29.43 \pm 0.29$ (Stauffer et al. 1994), indicating that the companion to HIP17608, if associated, is on the upper limit of X-ray activity for this class of star.

For the second Pleiades member, the observations resolve three of the companions (B,Ca,Cb) within the HIP17923 quintuple system. Based on the measured magnitude differences, the mass of the components are estimated as follows: B - $1.2 \pm 0.1 M_\odot$ (mid F-type), Ca - $1.2 \pm 0.1 M_\odot$ (mid F-type), Cb - $0.9 \pm 0.1 M_\odot$ (mid G-type). Deeper X-ray observations of the Pleiades (Micela et al. 1999) revealed an estimated X-ray luminosity of $\log L_X = 30.08$ for this system. If the X-ray counts were distributed evenly between the three later-type companions resolved within the AO images, the individual X-ray luminosities would be $\log L_X \sim 29.6$, similar to G- and F-type Pleiades members (Stauffer et al. 1994).

The final cluster X-ray target with a resolved companion is the Hyades member HIP 20648. As described in §7.2, the candidate companion also has a measured I-K colour consistent with a late F-/early G-type star, and the X-ray luminosity assigned to the target is consistent with a Hyades G-type star (Stern et al. 1995).

Remaining candidate companions

For the remaining candidate companions, an estimate of the ratio of X-ray to bolometric luminosity can be made under the assumption that the candidate is a physical companion at the same distance. From the absolute magnitude, the $V - I$ colour and bolometric luminosity were inferred from theoretical isochrones (Baraffe et al. 1998). The ratios of the observed X-ray luminosity to the estimated bolometric luminosity (L_X/L_{bol}) are plotted as a function of $V - I$ colour in Figure 7.10, with Pleiades and Hyades members (Zuckerman & Song 2004) overplotted as reference populations spanning the age range of the sample.

All but two of the candidates are within the region bound by the ~ 100 Myr Pleiades and ~ 650 Myr Hyades members. Uncertainty exists on both axes since both the $V - I$ colour and bolometric luminosity are estimated from theoretical isochrones, assuming the distance. Future observations to accurately determine the colour of these candidates will provide a more robust estimate of the bolometric luminosity. The two outlying candidates shown in Figure 7.10 have unphysical high luminosity ratios, significantly higher than the observed luminosity ratios of late M-type stars (e.g. Pizzolato et al. 2003). In these two cases, additional unresolved companions, or background X-ray sources, present a more feasible explanation for the detected X-ray flux. The rate of false-detections, $2/49$, corresponds to the 5% contamination introduced through the statistical method applied to the candidates to remove background sources, as described in §6.3.

7.8 Summary

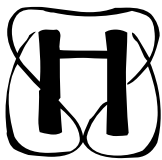
In summary, a total of 148 stars with spectral types in the range B6-A7 and distances of < 200 pc have been observed with AO-equipped cameras on 3.8m-8m telescopes. The high-resolution images were sensitive to companions with angular separations from $\sim 0''.3$ to $26''.2$ and magnitude differences extending to ~ 14 mag. A total of 68 candidate companions to 59 targets were resolved, and the frequency of multiple systems was measured to be substantially higher for the X-ray detected sample. The high frequency of multiples, $43_{-6}^{+6}\%$, compared to $12_{-3}^{+4}\%$ for the control sample is different by 4σ and provides strong evidence that the source of the X-ray emission is the candidate companion. The X-ray detected stars with no resolved companion make ideal candidates for future interferometric observations, as this study has shown that the X-ray detection is indicative of the presence of an unresolved companion, and interferometry can resolve binaries below the resolution of the adaptive optics data presented here.

For three candidate companions to X-ray targets, the $I - K$ colour was also measured, and the colours are consistent with late F- to late M-type stars, supporting the identification of the second object as the X-ray source in two cases. Among the X-ray targets with candidate companions, there are also three cluster members, and the known age, distance, and cluster X-ray properties enabled a further test of the companion X-ray luminosity with other cluster members. In each case, the companions – if associated – would have an X-ray luminosity similar to, or on the upper range of, cluster stars with similar magnitude. Follow-up observations of the

X-ray targets with candidate companions using *Chandra* would provide the angular resolution in the X-ray band necessary to confirm the second object as the true source of the X-ray emission.

CHAPTER 8

ORBITAL MOTION MONITORING OF A-TYPE STAR MULTIPLES



High-resolution observations of 26 binary systems with projected separations <100 AU have been obtained, 13 of which have sufficient historical measurements to allow for refinement of their orbital elements. For each system with an estimated orbit, the dynamical system mass obtained was compared with the system mass estimated from mass-magnitude relations. Discrepancies between the dynamical and theoretical system mass can be explained by the presence of a previously unresolved spectroscopic component, or by a non-solar metallicity of the system. Using this approach to infer the presence of additional companions, a lower limit to the fraction of binaries, triples, and quadruples can be estimated as 39, 46, and 15 per cent, for systems with at least one companion within 100 AU. The fraction of multiple systems with three or more components shows a relative increase compared to the fraction for Solar-type primaries resolved in previous volume-limited surveys. The observations have also revealed a pair of potentially young (<100 Myr) M-dwarf companions, which would make an ideal benchmark for the theoretical models during the pre-Main Sequence contraction phase for M-dwarfs. In addition to those systems with orbit fits, 13 systems which require further orbital monitoring observations are resolved, 11 of which are newly resolved as a part of the VAST survey.

8.1 Introduction

The orbits of binary stars offer one of the few techniques to determine stellar masses, or masses and radii in cases with a favorable geometry (e.g. Andersen et al. 1991). Orbits of binaries with young ages are particularly important to test theoretical evolutionary models, and examples include a double-lined eclipsing binary in Orion (e.g. Stassun et al. 2008). Low mass stars and brown dwarfs also represent a regime requiring empirical calibration, and the visual orbits of nearby M-, L-, and T- dwarfs have been used to measure system masses and compare with theoretical mass-luminosity relations (Dupuy et al. 2009).

Visual orbits also provide a method to search for evidence of additional components and determine higher order multiplicity, by identifying systems with dynamical masses significantly in excess of the theoretical predictions. These visual binaries with an indication of unresolved companions can be monitored with spectroscopy or interferometry to determine the properties such as period and mass ratio of the closer pair and augment the statistics compiled from catalogues (Tokovinin 2008). The properties of higher order multiple systems represent tests of formation scenarios including fragmentation of cores (e.g. Pringle 1989; Bonnell 2001) and disks (e.g. Stamatellos et al. 2007; Kratter et al. 2010b) and may be influenced by processes such as accretion (e.g. Bate 2000) and dynamical interactions (e.g. McDonald & Clarke 1995; Lodato et al. 2007)

In this chapter, a subset of the systems resolved by the ongoing volume-limited A-star (VAST) survey are used to determine dynamical system masses from orbit fits and to compare the results with theoretical models and search for additional unresolved stellar companions. The sample of AO-imaged binaries considered in this study is detailed in §8.2, and a short summary of the new observations is given in §8.3. The data analysis, including the AO image processing to determine the relative positions and the subsequent orbit determination from the compilation of position data, is explained in §8.4. §8.5 reports the astrometric results from the new measurements and the orbital elements and masses based on the orbit fits. The discussion in §8.6 covers a comparison with theoretical mass-magnitude relations, an assessment of the higher order multiplicity, and the identification of a set of targets for continued monitoring. Finally, §8.7 provides a summary and future directions for the project.

8.2 Sample

Table 8.1: Basic properties of sample members

HIP	Name	HR	HD	ADS	Spectral Type	Distance (pc)	V_T (mag)	K_S (mag)
Orbit Subsample								
5300	ν Phe	331	6767		A3IV	57.0±2.0	5.230±0.001	4.78±0.02
9480	48 Cas	575	12111	1598	A3IV	35.3±0.6	4.533±0.002	4.08±0.13 ^a
11569	ι Cas	707	15089	1860	A5p	40.7±1.3	4.496±0.003	4.25±0.03
17954		1188	23985	2799	A2V+...	56.5±1.8	5.259±0.004	4.81±0.02
28614	μ Ori	2124	40932	4617		47.5±1.5	4.150±0.002	3.64±0.26
36850	Castor	2891/2890	60178J	6175	A2Vm	15.6±0.9	1.590±0.020	1.47±0.03 ^a
44127	ι UMa	3569	76644		A7V	14.51±0.03	3.159±0.002	2.67±0.03 ^b
47479		3863	84121		A3IV	72.6±2.2	5.334±0.003	4.80±0.02
76952	γ CrB	5849	140436	9757	B9IV+...	44.8±1.0	3.819±0.002	3.67±0.23
77660	b Ser	5895	141851		A3Vn	49.8±0.8	5.112±0.002	4.70±0.02
80628	ν Oph	6129	148367		A3m	41.0±1.5	4.657±0.003	4.17±0.04
82321	52 Her	6254	152107	10227	A2Vspe...	55.3±1.0	4.833±0.003	4.57±0.02
93506	ζ Sgr	7194	176687	11950	A2.5Va	27.0±0.6	2.617±0.003	2.29±0.23
Monitoring Subsample								
128			224890		Am...	70.8±1.7	6.521±0.004	6.02±0.02
2381		118	2696		A3V	53.1±0.8	5.188±0.003	4.83±0.02

HIP	Name	HR	HD	ADS	Spectral Type	Distance (pc)	V_T (mag)	K_S (mag)
2852	BG Cet	151	3326		A5m...	48.9±0.8	6.093±0.004	5.42±0.01
5310	79 Psc	328	6695		A3V	47.3±1.7	5.581±0.003	5.22±0.02
18217		1192	24141		A5m	50.5±1.1	5.806±0.004	5.37±0.02
29852		2265	43940		A2V	61.9±1.0	5.895±0.003	5.44±0.02
51384		4062	89571		F0IV	40.6±0.6	5.549±0.003	4.85±0.02
65241	64 Vir	5040	116235		A2m	65.9±1.4	5.897±0.003	5.62±0.02
66223		5108	118156	8956	F0IV	69.8±2.0	6.394±0.004	5.88±0.02
103298	16 Del	8012	199254	14429	A4V	60.5±1.1	5.555±0.003	5.19±0.02
109667		8464	210739		A3V	63.5±2.1	6.209±0.005	5.74±0.02
110787	ρ^1 Cep	8578	213403		A2m	63.2±0.9	5.857±0.004	5.54±0.03
116611	75 Peg	8963	222133		AIVn	71.4±1.4	5.483±0.003	5.42±0.02

a - K -band photometry from Ducati (2002)

b - K -band photometry from Morel & Magnenat (1978)

The sample of binaries is drawn from the ongoing VAST survey (De Rosa et al. 2011), an adaptive optics (AO) imaging survey of A-stars within 75 parsecs, and includes the 26 systems with projected separations less than 100 AU. The angular separations of the binaries range from $0''.094$ to $4''.66$, and 11 are newly resolved. Figure 8.2 plots the measured magnitude difference as a function of separation for the complete sample. Of the 26 systems, 13 have a substantial number of previous measurements, and these systems comprise the orbit subsample. For the remaining 13 systems, there is insufficient coverage to fit an orbit, and these binaries comprise the monitoring subsample. Table 8.1 lists each observed binary in the two subsamples, along with basic parameters for each such as distance (van Leeuwen 2007), *Tycho2* V_T -band and *2MASS* K_S -band photometry (ESA 1997; Skrutskie et al. 2006), and spectral type listed within the *SIMBAD* database.

For the brightest stars within the sample, the shortest *2MASS* exposures saturate, requiring a different method for measuring the photometry, resulting in significantly larger uncertainties on the estimated magnitudes (Skrutskie et al. 2006). Therefore for three of these brighter targets, near-infrared photometry was obtained from alternative sources (Ducati 2002; Morel & Magnenat 1978), and converted into the *2MASS* photometric bands using empirical colour transformations (Carpenter 2001). The distribution of the sample on the color magnitude diagram (CMD) is plotted in Figure 8.1. Given the rapid evolution of massive stars off the Main Sequence, the position of an A-star on the CMD provides a method to estimate the age of the system based on a comparison with theoretical isochrones. The inferred age of the system from the CMD is combined with the dynamical system mass from the orbit and system photometry from the literature to test mass-magnitude relations at the corresponding age.

8.3 Observations

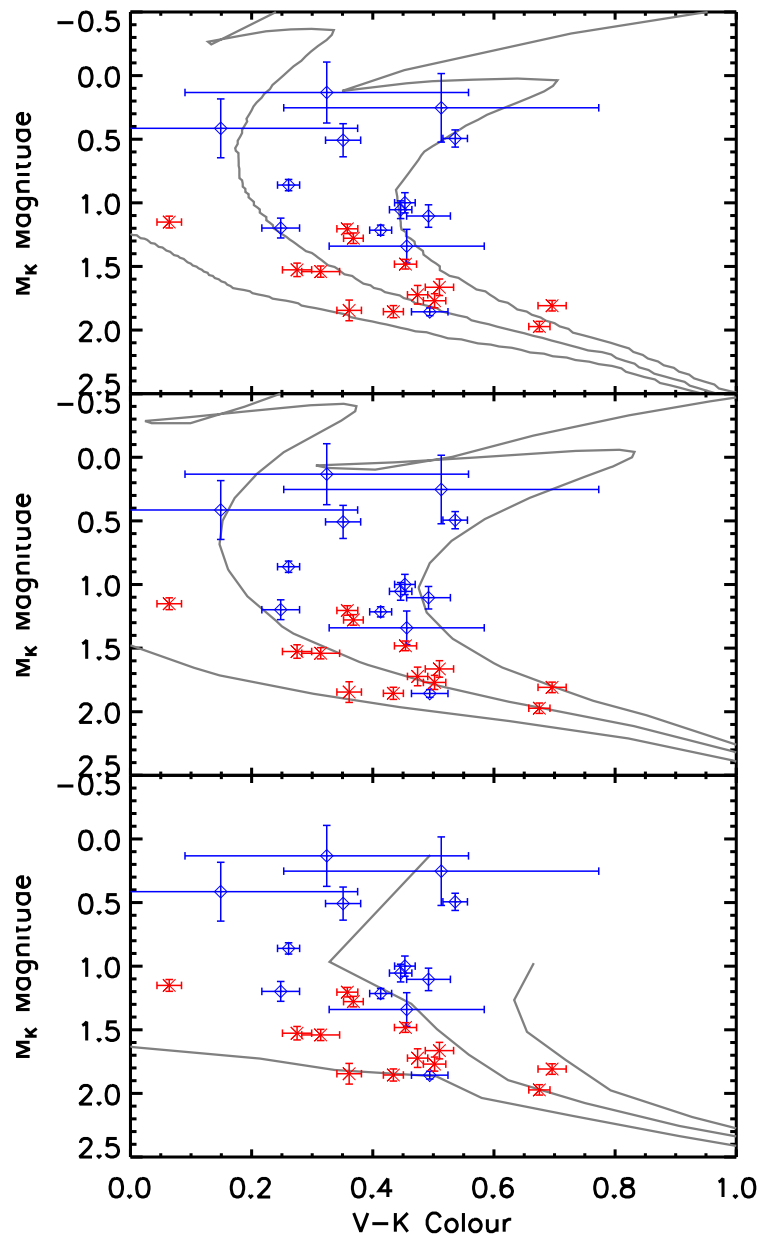


Figure 8.1: A colour-magnitude diagram of the 26 stars discussed within this work, plotted alongside three different sets of theoretical isochrones at 100, 500, and 800 Myrs. Those targets with new or refined orbits are plotted in blue with a diamond symbol (see Table 8.4), and those targets for which further measurements are required are plotted in red with a cross symbol (see Table 8.5 and §6.3). Three different sets of theoretical isochrones are plotted at ages of 100, 500, and 800 Myrs; (*top*) Lejeune & Schaerer (2001), (*middle*) Marigo et al. (2008), and (*bottom*) Siess et al. (2000).

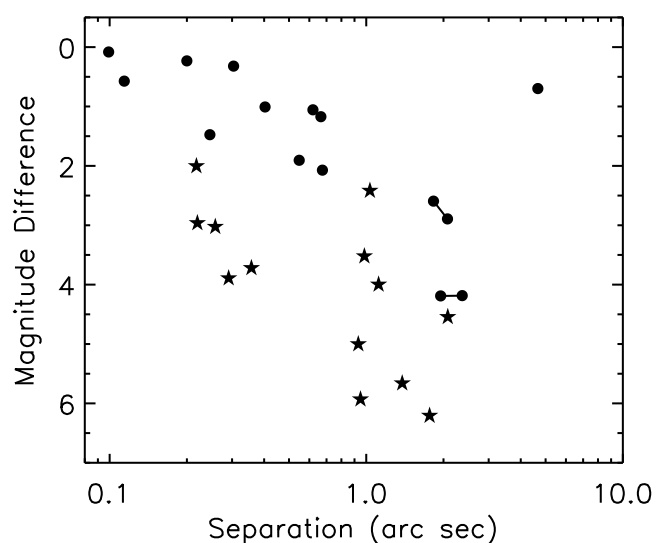


Figure 8.2: The magnitude difference between primary and secondary for each binary system within this study as a function of angular separation. The targets are divided into two distinct subsamples, those with new or refined orbits estimated within this study (filled circles), and those for which further measurements are required before an orbital determination can be attempted (filled stars). The majority of the systems within the second subsample were newly resolved as a part of the VAST survey, demonstrating the higher dynamic range possible with AO imaging. The filled circles connected with a solid line represent companions within the same hierarchical triple (HIP 44127 and HIP 82321).

Table 8.2: Observing run details with calculated astrometric calibration values

Telescope (Instrument)	Date	Filter	Plate Scale (mas/px)	True North ($^{\circ}$)	Proposal ID
CFHT (KIR)	05/05/2001 – 07/05/2001	Hcont	34.87 ± 0.14	1.47 ± 0.19	2001AF11
	06/05/2001	Jcont	34.82 ± 0.15	1.51 ± 0.17	2001AF11
Gemini N (NIR1)	13/06/2008	H ₂ -1-0	34.81 ± 0.10	-2.42 ± 0.13	2008AC22
	14/06/2008	FeII	34.76 ± 0.08	-2.40 ± 0.11	2008AC22
	30/08/2009 – 01/09/2009	H ₂ -1-0	34.78 ± 0.10	-2.40 ± 0.20	2009BC06
	04/02/2010 – 05/02/2010	H ₂ -1-0	34.75 ± 0.08	-2.37 ± 0.11	2010AC14
Gemini N (NIR1)	2011	H ₂ -1-0	34.77 ± 0.06	-2.35 ± 0.09	2011AC11
	08/09/2008 – 14/11/2008	Br γ	21.28 ± 0.12	0.52 ± 0.29	GN-2008A-Q-74
	19/12/2009	Br γ	21.28 ± 0.12	0.52 ± 0.29	GN-2008B-Q-119
	25/06/2010 – 26/08/2010	Br γ	21.28 ± 0.12	0.52 ± 0.29	GN-2010A-Q-75
	24/07/2008 – 25/07/2009	Br γ	74.55 ± 1.00	1.68 ± 0.50	-
	16/10/2008 – 17/10/2008	Br γ	74.55 ± 1.00	1.68 ± 0.50	-
	30/06/2004	IB218	27.02 ± 0.14	0.24 ± 0.30	272.D-5068(A)
	10/01/2005	IB218	27.02 ± 0.15	0.26 ± 0.30	074.D-0180(A)
	08/02/2005	Ks	27.02 ± 0.15	0.26 ± 0.30	074.D-0180(A)
	08/11/2005	Ks	26.98 ± 0.08	0.21 ± 0.20	076.C-0270(A)
Lick (IRCAL) VLT-UT4 (NACO)	10/11/2005	Ks	26.98 ± 0.08	0.21 ± 0.20	076.D-0108(A)
	06/12/2005	IB218	26.98 ± 0.08	0.21 ± 0.20	076.D-0108(A)
	04/01/2006	Ks	27.01 ± 0.13	0.31 ± 0.29	076.D-0108(A)
	07/01/2006	IB218	27.01 ± 0.13	0.31 ± 0.29	076.D-0108(A)
	27/04/2006	IB218	27.00 ± 0.12	0.09 ± 0.26	077.D-0147(A)
	20/09/2007	IB218	26.99 ± 0.12	-0.23 ± 0.21	080.D-0348(A)
	20/09/2007	Ks	26.99 ± 0.12	-0.23 ± 0.21	080.D-0348(A)
	26/09/2007	IB218	26.99 ± 0.12	-0.23 ± 0.21	080.D-0348(A)
	04/11/2007	Ks	27.00 ± 0.10	-0.18 ± 0.20	080.D-0348(A)
	15/02/2008	IB218	27.01 ± 0.14	-0.12 ± 0.29	080.D-0348(A)
Palomar	24/02/2008	Ks	27.01 ± 0.14	-0.12 ± 0.29	080.D-0348(A)
	11/04/2008	CH ₄	25.00 ± 1.00	0.70 ± 1.00	-

Telescope (Instrument)	Date	Filter	Plate Scale (mas/px)	True North ($^{\circ}$)	Proposal ID
(PHARO)	12/04/2008	Br γ	25.00 \pm 1.00	0.70 \pm 1.00	-
	12/07/2008	CH $_4$	25.00 \pm 1.00	0.70 \pm 1.00	-
	13/07/2008	Br γ	25.00 \pm 1.00	0.70 \pm 1.00	-

KIR - (Doyon et al. 1998)
 NIRM (Near InfraRed Imager and Spectrometer) - (Hodapp et al. 2003)
 IRCAL - (Lloyd et al. 2000)
 NACO (Nasmyth Adaptive Optics System/ Near-Infrared Imager and Spectrograph) - (Lenzen et al. 2003; Rousset et al. 2003)
 PHARO (Palomar High Angular Resolution Observer) - (Hayward et al. 2001)

With AO systems operating on telescopes ranging in diameter from the 3m Shane to the 8m Gemini and VLT, near-infrared images were obtained on all targets. In most cases, the filter used for the observations was a narrow or broadband filter within the K bandpass, though some images were taken within the J and H bandpasses. Both the primary and secondary of the pairs were unsaturated in the AO images, simplifying the astrometry measurements. Table 8.2 details the key characteristics of the instruments used to acquire the new AO observations, with the measured pixel scale and orientation for each camera. A subset of the observations were obtained from the CFHT and ESO Science Archive Facilities. One measurement obtained at the Southern Observatory for Astrophysical Research (SOAR) as a part of the VAST survey, and used within this study, has been recently published in Hartkopf et al. (2011, *submitted*).

8.4 Data analysis

8.4.1 AO image processing

The AO science images obtained were processed with standard image reduction steps including dark subtraction, flat fielding, interpolation over bad pixels and sky subtraction. To align all the images, the centroid of the bright primary was obtained in each exposure by fitting a Gaussian to the core of the central point spread function. For each system resolved within the observations, an empirical PSF was determined from the radial profile of the primary, after masking any close companion. The empirical PSF was then fit to the position and intensity of both components of the system, providing a measure of the separation, position angle, and magnitude difference. Uncertainties within the photometry and astrometry were estimated from the standard deviations of the photometric and astrometric measurements from each individual exposure before combination.

To ensure accurate determination of the separation and position angle, the pixel scale and orientation of the detectors were calibrated based on observations of the Trapezium cluster, with the exception of data obtained with IRCAL and PHARO. Depending on the total field-of-view of the detector, the positions of 20 to 40 Trapezium members were compared with the coordinates reported in McCaughrean & Stauffer (1994). The average derived pixel scale and orientation were computed, and the standard deviation of these values was used as the associated error; the results are given in Table 8.2. For the data obtained with IRCAL and PHARO, the pixel scale and orientation were calibrated from binary systems also observed with instruments calibrated with Trapezium measurements.

8.4.2 Orbital determination

For the 13 binaries with sufficient coverage of the orbit, a fit was performed for the orbital elements and an estimate of the dynamical mass was determined. The measurements presented within this study were combined with previous measurements contained within the Washington Double Star (WDS; Mason et al. 2001) Catalog. These archive measurements were obtained using a variety of observational techniques, and date back to the 18th Century. As in some cases the statistical uncertainties were not provided in the WDS Catalog, the literature was searched

for the formal errors for each individual measurement, and only separation and position angle values for which uncertainties could be assigned were included within the fitting procedure. A detailed listing of the individual measurements used for the orbital determination will be made available at the Strasbourg astronomical Data Center (CDS - <http://cds.u-strasbg.fr>).

The orbit fitting approach utilises the method presented by Hilditch (2001), and demonstrated by an application to measurements of the T Tau S system (Köhler et al. 2008). This method is similar to the grid-based search technique developed by Hartkopf et al. (1989). At each epoch of observation t_i , the x_i, y_i position of the companion with respect to the primary is measured in the observed tangent plane. These values are related to the true position of the secondary in the orbital plane (x'_i, y'_i) through the following equations

$$\begin{aligned} x_i &= Ax'_i + Fy'_i \\ y_i &= Bx'_i + Gy'_i \end{aligned} \quad (8.1)$$

where A, B, F and G are the orbital Thiele-Innes elements, with

$$\begin{aligned} A &= a(\cos \omega \cos \Omega - \sin \omega \sin \Omega \cos i) \\ B &= a(\cos \omega \sin \Omega + \sin \omega \cos \Omega \cos i) \\ F &= a(-\sin \omega \cos \Omega - \cos \omega \sin \Omega \cos i) \\ G &= a(-\sin \omega \sin \Omega + \cos \omega \cos \Omega \cos i) \end{aligned} \quad (8.2)$$

where a is the semi-major axis of the orbit, ω the longitude of periastron, Ω the longitude of the ascending node, and i the inclination – four of the seven orbital elements. The position of the companion in the orbital plane (x'_i, y'_i) can also be expressed through the remaining orbital elements (e, P, T_0) as

$$\begin{aligned} x'_i &= \cos E - e \\ y'_i &= \sqrt{1 - e^2} \sin E \end{aligned} \quad (8.3)$$

where e is the eccentricity of the system. The eccentric anomaly (E) can be determined from a numerical solution to Kepler's equation

$$\begin{aligned} M &= E - e \sin E \\ &= (2\pi/P)(t_i - T_0) \end{aligned} \quad (8.4)$$

where M is the mean anomaly, P the period of the system, and T_0 the epoch of periastron passage. At each epoch of observation, the position of the component in the orbital plane can be defined using just three of the orbital elements (e, P , and T_0). The orbital position at each epoch can then be converted into the observed position using the equations in Equation 8.1 through a least-squares determination of the four Thiele-Innes elements.

An initial estimation of the orbital parameters of each system can be determined through an iterative three-dimensional grid search of e, P , and T_0 . A wider range of parameter values was searched, with 100 linear steps searched over a range of $0 \leq e < 1$, 500 linear steps

between $1 \leq \log(P[\text{yrs}]) \leq 3$, and T_0 initially distributed between the years $2000.0 - (P/2)$ and $2000.0 + (P/2)$. At each position within this three-dimensional grid, the fit orbital positions (x'_i, y'_i) were directly calculated (Eqn. 8.3), with the four remaining orbital parameters (a, i, ω, Ω) estimated from a least-squares fit to the observed positions using Equations 8.1 and 8.2. After the χ^2 statistic was calculated at each position within the grid, the range of T_0 values searched was reduced by a factor of 10 centred on the optimum value of T_0 found within the previous iteration. This process was repeated until the step size in T_0 was reduced to less than one day. The values for a, i, ω and Ω can be determined from an inversion of Equation 8.2 (Green 1985),

$$\begin{aligned}\Omega &= \frac{1}{2} \left(\arctan \left(\frac{B-F}{G+A} \right) - \arctan \left(\frac{B+F}{G-A} \right) \right) \\ \omega &= \left(\arctan \left(\frac{B-F}{G+A} \right) - \Omega \right) \\ i &= 2 \arctan \left[\sqrt{\frac{-(B+F) \sin(\omega + \Omega)}{(B-F) \sin(\omega - \Omega)}} \right] \\ a &= \frac{B-F}{\sin(\omega + \Omega) (1 + \cos(i))}\end{aligned}\tag{8.5}$$

The orbital parameters calculated at each position within the (P, e) grid are then used as a starting point for a Levenberg-Marquardt minimisation to ensure the minimum of the χ^2 distribution is found. The set of orbital parameters with the minimum χ^2 statistic was then used as the orbit solution for the system.

The shape of the χ^2 distribution in the vicinity of the global minimum can be used to determine the 1σ uncertainties of each parameter (Press et al. 1992). By perturbing an individual parameter away from the global minimum, and optimising the remaining parameters, a region of the χ^2 distribution can be calculated where the χ^2 statistic is less than $\chi^2_{\min} + 1$. This region encloses 68% of the probability distribution, and is not necessarily symmetric about the minimum χ^2 value. This implementation of the orbit fitting method was tested against four well studied systems (Bonney et al. 2009; Dupuy et al. 2009; Liu et al. 2008), with the resulting parameters being within the published 1σ uncertainties.

8.4.3 Theoretical mass-magnitude relations

Table 8.3: Summary of theoretical model grids

Grid reference	Mass Range (M_{\odot})	Metallicity (Z)
Lejeune & Schaerer (2001)	$0.80 < M < 5.0$	0.02
Marigo et al. (2008)	$0.15 < M < 5.0$	0.02
Siess et al. (2000)	$0.10 < M < 5.0$	0.02
Baraffe et al. (1998)	$0.08 < M < 1.5$	0.02

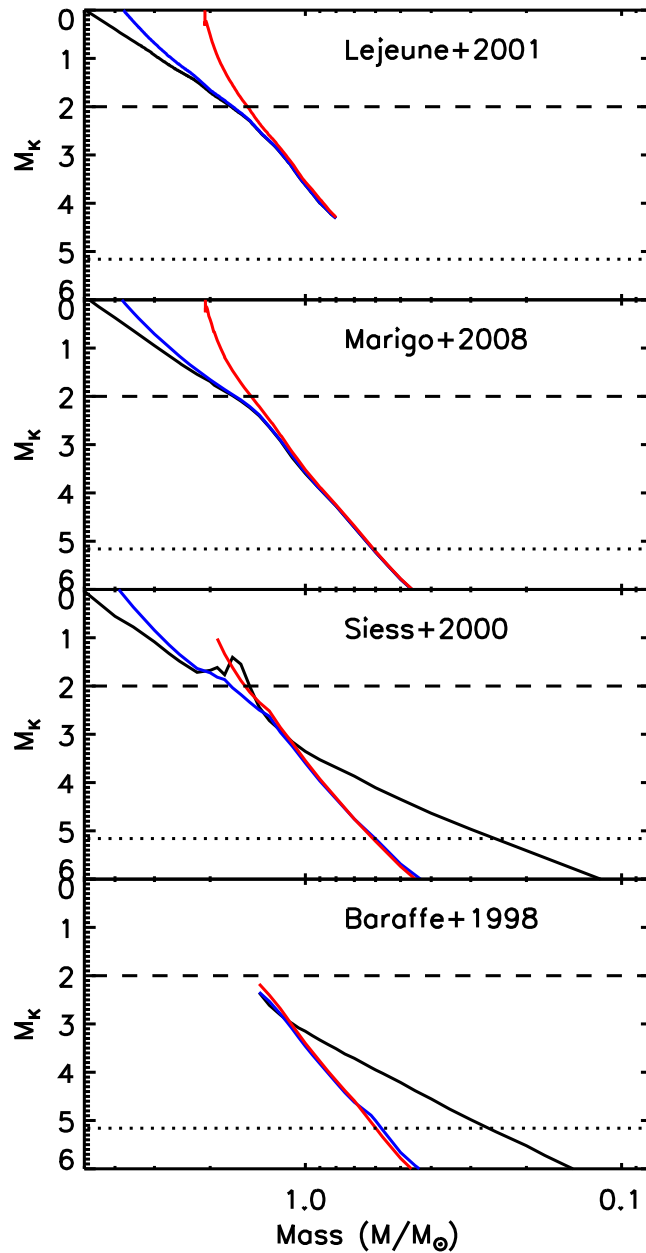


Figure 8.3: Mass-magnitude relations were constructed from each of the four model grids. The evolution of the mass-magnitude relation is shown for each grid, with the 10 Myr (black line), 100 Myr (blue line) and 1 Gyr (red line) relations plotted. For reference the dashed line indicates the faintest A-type star within the sample, and the dotted line indicates the Zero-Age Main Sequence magnitude of an M0 star. A-type stars typically have an absolute K -band magnitude ranging between $M_K = 0$ and $M_K = 2$, where the mass is significantly dependent on the age of the star. Within the Lejeune & Schaerer (2001) and Marigo et al. (2008) models, the mass-magnitude relation of stars fainter than $M_K \sim 2$ is not dependent on the age of the star. The Siess et al. (2000) and Baraffe et al. (1998) models include a description of the contraction phase of lower-mass stars onto the Main Sequence during the early portion of its life.

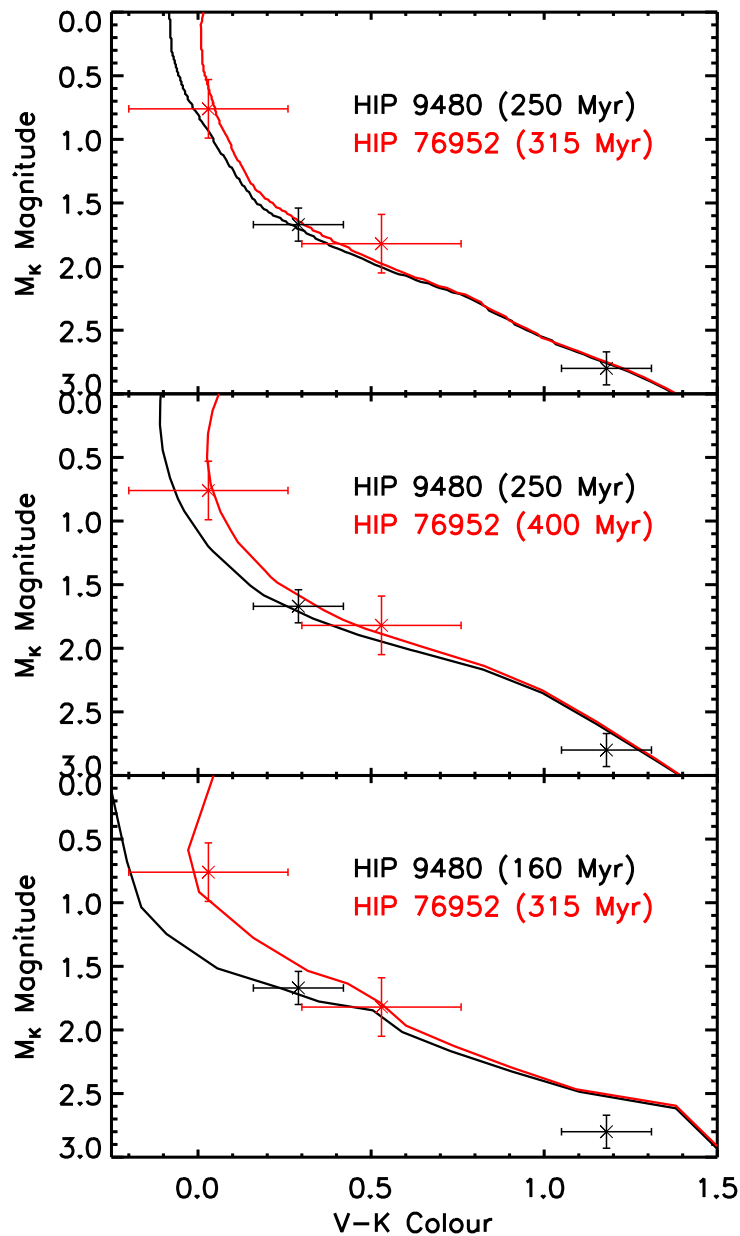


Figure 8.4: The age of each system can be estimated based on the position of each component on the colour-magnitude diagram (top - Lejeune & Schaerer 2001, middle - Marigo et al. 2008, bottom - Siess et al. 2000). This procedure, while demonstrated for only two systems in this figure, was repeated for all the remaining members of the orbit subsample. For each system, the age estimated from each of the three model grids is reported in Table 8.10.

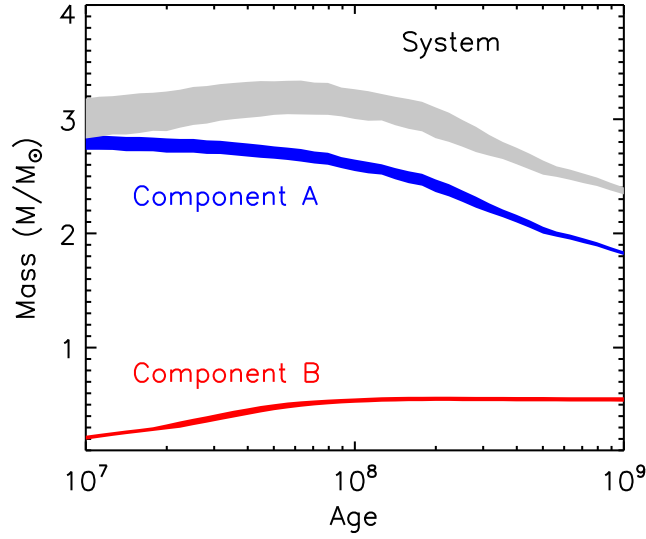


Figure 8.5: The photometric mass of a hypothetical binary system with $M_K(A) = 1.25 \pm 0.05$ and $M_K(B) = 5.50 \pm 0.10$, as a function of system age. The evolution of the mass-magnitude relation is shown for both components (A - blue region, B - red region), and the system as a whole (grey region). The extent of the region in each case represents the uncertainty in the mass estimate due to the uncertainties of the magnitudes of each component.

Four different grids of evolutionary models were obtained with which the dynamical system masses estimated from the fitted orbital parameters were compared. Table 8.3 lists the mass range, metallicity, and literature reference for each of the four grids. The Lejeune & Schaerer (2001), Marigo et al. (2008), and Siess et al. (2000) grids covers a significant portion of the lifespan of a typical A-type star, and as such a maximum age cut-off at 1 Gyr was applied. In addition to these grids, models from Baraffe et al. (1998) were obtained in order to study a pair of lower-mass companions presented in §6.1.2. Each grid was converted into the photometric systems used within this study - *Tycho V* and *2MASS K_S* (Carpenter 2001), before producing a high-resolution ($dM/M_\odot = 0.001$) mass-magnitude relation, created through cubic interpolation of the grid data, as shown in Figure 8.3.

The absolute *V* and *K*-band magnitudes were calculated from the *V*-band magnitude differences obtained from the literature (Table 8.7), and the *K*-band magnitude differences presented within this study (Table 8.4). The individual component magnitudes and *V* – *K* colour for each system are presented in Table 8.6. Within the A-type star mass range, the mass-magnitude relations significantly change as a function of the age of the system due to the rapid evolution of A-type stars across the CMD. The age of each system is therefore estimated, based on the position of the primary on the CMD, before a mass for each component is estimated from the mass-magnitude relations. The estimated masses of each component are summed to produce an estimate of the system mass, hereafter called the photometric system mass.

To demonstrate the analysis procedure, a hypothetical binary system of magnitudes

$M_K(\text{A}) = 1.25$, $M_K(\text{B}) = 5.50$ was used to construct the mass-age relation for each component, and their corresponding sum (Figure 8.5). The evolution of the mass-magnitude relation as a function of age can be then visualised as a continuous function for both components within the system. For this example a set of models was used which includes the pre-Main Sequence (PMS) contraction phase of lower-mass stars, as demonstrated by the increase in the derived mass as a function of age for the companion. The two mass-age curves can then be summed to produce a mass-age relation for the system in question. Using the age estimated for the system based upon its position on the CMD, a photometric system mass can be estimated and compared with the dynamical system mass determined from the orbital elements.

Table 8.4: Measured binary position angle and separation for previously re-solved systems

HIP	Comp.	WDS Designation	Discoverer Designation	Previous Orbit	Instrument	Epoch	θ (deg)	ρ (arcsec)	ΔK (mag)
5300	AB	01078-4129	RST3352	Söderhjelm (1999)	NACO	2005.02	15.73±0.76	0.089±0.001	0.507±0.020
9480	A-B	02020+7054	BU 513	Mason et al. (1999)	NACO	2007.72	126.69±0.38	0.114±0.001	*0.573±0.018
					IRCAL	2008.79	293.97±0.75	0.679±0.011	1.110±0.056
					KIR	2009.67	297.36±0.22	0.666±0.002	1.172±0.013
					NIRI	2010.65	302.11±0.29	0.644±0.004	*1.137±0.007
11569	Aa,Ab	02291+6724	CHR 6	Drummond et al. (2003)	IRCAL	2008.79	43.50±0.80	0.575±0.006	*1.906±0.026
					KIR	2010.10	41.52±2.61	0.602±0.023	1.771±0.301
17954	AB	03503+2535	STT 65	Docobo & Ling (2007)	NIRI	2008.87	194.76±0.31	0.200±0.001	*0.232±0.005
28614	AB	06024+0939	A 2715	Muterspaugh et al. (2008)	NIRI	2009.96	21.95±0.29	0.403±0.002	*1.008±0.006
					KIR	2011.31	21.31±1.06	0.397±0.006	0.896±0.120
36850	AB	07346+3153	STF110	Docobo & Costa (1985)	KIR	2010.09	57.46±0.14	4.663±0.013	*0.698±0.050
44127	BC	08592+4803	HU 628	Eggen (1967)	PHARO	2008.28	242.01±1.04	0.433±0.017	*0.005±0.031
					KIR	2010.10	228.98±0.27	0.568±0.003	0.027±0.023
					KIR	2011.30	223.37±0.31	0.656±0.003	-0.011±0.039
47479	AB	09407-5759	B 780	Söderhjelm (1999)	NACO	2008.12	300.22±0.58	0.099±0.001	*0.082±0.017
76952	AB	15427+2618	STF1967	Muterspaugh et al. (2010)	PHARO	2008.28	112.65±1.07	0.683±0.028	-
					KIR	2011.31	111.37±0.33	0.620±0.005	*1.056±0.030
77660	AB	15513-0305	CHR 51	Docobo et al. (2010)	KIR	2001.34	82.72±2.42	0.188±0.018	-
					KIR	2001.34	81.97±1.59	0.197±0.008	-
					KIR	2001.35	83.38±3.67	0.185±0.016	-
					NACO	2004.50	71.87±0.31	0.247±0.001	*1.487±0.006
					NACO	2006.32	69.74±0.42	0.274±0.003	1.472±0.097
					KIR	2010.10	66.69±0.47	0.330±0.004	1.483±0.058
					KIR	2011.30	64.21±2.57	0.340±0.014	1.455±0.194
80628	Ab,Ab	16278-0822	RST3949	-	PHARO	2008.28	22.56±1.05	0.674±0.027	*2.072±0.066
					IRCAL	2008.56	23.53±0.71	0.685±0.009	1.978±0.057
					KIR	2011.31	34.37±0.29	0.771±0.003	2.237±0.038

HIP	Comp.	WDS Designation	Discoverer Designation	Previous Orbit	Instrument	Epoch	θ (deg)	ρ (arcsec)	ΔK (mag)
82321	BC	16492+4559	A 1866	Popovic (1969)	PHARO	2008.53	247.33±1.03	0.286±0.012	-
					KIR	2011.30	260.51±0.53	0.301±0.005	*0.299±0.044
93506	AB	19026-2953	HDO 150	Mason et al. (1999)	KIR	2008.45	31.05±2.31	0.194±0.010	-
					KIR	2011.31	285.59±0.71	0.304±0.004	*0.320±0.043

* - Photometry measurement used to determine the magnitude of each component in Table 8.6.

Table 8.5: Measured binary position angle and separation for potential orbital monitoring targets

HIP	Instrument	Epoch	θ (deg)	ρ (arcsec)	ΔK (mag)	Projected Separation (AU)
128	NIRI	2008.72	80.64±0.29	0.983±0.006	*3.521±0.021	69.59±1.72
	IRCAL	2008.79	80.73±0.52	0.975±0.013	3.355±0.037	68.98±1.90
2381	NACO	2005.93	279.51±0.26	1.765±0.006	*6.206±0.088	93.75±1.48
	NACO	2007.73	279.13±0.22	1.767±0.008	6.229±0.055	93.86±1.51
	NIRI	2008.79	278.54±0.29	1.759±0.013	7.401±0.711	93.39±1.59
2852	NIRI	2008.79	260.55±0.30	0.931±0.006	*5.001±0.056	45.51±0.82
5310	NIRI	2008.79	174.99±0.30	0.357±0.002	*3.719±0.023	16.88±0.62
18217	IRCAL	2008.79	64.78±0.65	1.037±0.012	2.301±0.029	52.37±1.24
	NIRI	2008.87	64.96±0.29	1.033±0.006	*2.41±0.010	52.13±1.12
29852	NACO	2005.85	210.76±0.22	0.218±0.001	*2.003±0.013	13.49±0.21
	NACO	2005.86	210.80±0.21	0.217±0.001	1.983±0.012	13.44±0.21
51384	PHARO	2008.18	212.43±1.05	2.078±0.084	*4.543±0.169	84.44±3.66
65241	NACO	2005.10	196.95±0.62	0.328±0.003	3.061±0.231	21.65±0.50
	NACO	2008.15	212.75±0.57	0.258±0.003	*3.025±0.097	17.01±0.42
66223	PHARO	2008.53	187.71±1.02	1.381±0.056	*5.660±0.105	96.42±4.73
103298	NIRI	2008.69	115.72±0.30	0.220±0.001	*2.962±0.007	13.29±0.25
109667	NIRI	2008.69	285.17±0.30	1.117±0.007	*3.997±0.011	70.88±2.38
	KIR	2009.66	284.66±0.25	1.108±0.006	4.051±0.073	70.28±2.35
	NIRI	2010.48	284.38±0.29	1.101±0.007	4.044±0.103	69.84±2.34
110787	NIRI	2008.71	211.11±0.35	0.291±0.002	*3.891±0.043	18.38±0.29
116611	NIRI	2008.75	173.11±0.32	0.950±0.006	*5.930±0.089	67.78±1.38
	NIRI	2010.48	172.11±0.34	0.943±0.006	5.794±0.076	67.31±1.34

* - Photometry measurement used to determine the magnitude of each component in Table 8.6.

Table 8.6: Derived parameters of individual components

HIP	Comp.	V_T (mag)	K_S (mag)	$V - K$	M_V (mag)	M_K (mag)	Additional Components	SB Type	Reference
5300	A	5.51±0.02	5.28±0.02	0.23±0.03	1.73±0.08	1.50±0.08			
	B	6.85±0.08	5.85±0.02	0.99±0.08	3.07±0.11	2.08±0.08			
9480 [†]	A	4.69±0.01	4.40±0.13	0.29±0.13	1.95±0.03	1.67±0.13			
	B	6.72±0.01	5.54±0.13	1.18±0.13	3.98±0.04	2.80±0.13			
11569 [†]	Aa	4.67±0.01	4.79±0.03	-0.12±0.03	1.62±0.07	1.74±0.08			
	Ab	8.65±0.16	6.71±0.03	1.94±0.16	5.60±0.17	3.66±0.08			
17954	A	5.81±0.04	5.46±0.02	0.35±0.04	2.05±0.08	1.70±0.07			
	B	6.26±0.06	5.69±0.02	0.57±0.06	2.50±0.09	1.93±0.07			
28614	A	4.32±0.01	4.00±0.26	0.33±0.26	0.94±0.07	0.61±0.27	Aa, Ab	SB1	Fekel et al. (2002)
	B	6.22±0.02	5.01±0.26	1.22±0.26	2.84±0.07	1.62±0.27	Ba, Bb	SB2	Fekel et al. (2002)
36850	A	1.98±0.02	1.93±0.03	0.05±0.04	1.02±0.13	0.97±0.13	Aa, Ab	SB1	Vinter Hansen et al. (1940)
	B	2.88±0.03	2.63±0.04	0.25±0.05	1.92±0.13	1.66±0.13	Ba, Bb	SB1	Vinter Hansen et al. (1940)
44127	A	3.16±0.02	2.71±0.03	0.45±0.04	2.35±0.02	1.90±0.03			
	B	10.88±0.11	6.90±0.04	3.98±0.12	10.07±0.11	6.09±0.04			
47479	C	11.08±0.12	6.90±0.04	4.18±0.12	10.27±0.12	6.09±0.04			
	A	5.82±0.01	5.51±0.02	0.31±0.02	1.51±0.07	1.21±0.07			
76952	B	6.45±0.01	5.59±0.02	0.85±0.03	2.14±0.07	1.29±0.07			
	A	4.05±0.01	4.02±0.23	0.03±0.23	0.80±0.05	0.76±0.23			
77660	B	5.60±0.02	5.07±0.23	0.53±0.23	2.35±0.05	1.82±0.23			
	A	5.21±0.01	4.94±0.02	0.26±0.02	1.72±0.04	1.46±0.04			
80628	B	7.82±0.04	6.43±0.02	1.38±0.04	4.33±0.05	2.95±0.04			
	Aa	4.68±0.01	4.32±0.04	0.37±0.04	1.62±0.08	1.25±0.09	Aa1, Aa2	SB2	Gutmann (1965)
82321	Ab	8.80±0.10	6.39±0.07	2.41±0.12	5.74±0.13	3.33±0.11			
	A	4.87±0.01	4.73±0.02	0.14±0.02	1.16±0.04	1.02±0.04			
93506	B	9.19±0.11	7.33±0.03	1.86±0.11	5.47±0.12	3.62±0.05			
	C	9.29±0.11	7.63±0.04	1.66±0.12	5.57±0.12	3.92±0.05			
93506	A	3.27±0.01	2.90±0.23	0.37±0.23	1.11±0.05	0.74±0.24			

HIP	Comp.	V_T (mag)	K_S (mag)	$V - K$	M_V (mag)	M_K (mag)	Additional Components	SB Type	Reference
	B	3.48 ± 0.01	3.22 ± 0.24	0.26 ± 0.24	1.32 ± 0.05	1.06 ± 0.24			
Monitoring Subsample									
128	AB	-	6.06 ± 0.02	-	-	1.81 ± 0.06	A, B	SBI	Carquillat et al. (2003)
	C	-	9.58 ± 0.03	-	-	5.33 ± 0.06			
2381	A	-	4.83 ± 0.02	-	-	1.21 ± 0.04			
	B	-	11.04 ± 0.09	-	-	7.41 ± 0.10			
2852	A	-	5.43 ± 0.02	-	-	1.98 ± 0.04			
	B	-	10.43 ± 0.06	-	-	6.98 ± 0.07			
5310	A	-	5.25 ± 0.02	-	-	1.88 ± 0.08			
	B	-	8.97 ± 0.03	-	-	5.60 ± 0.08			
18217	A	-	5.48 ± 0.02	-	-	1.97 ± 0.05			
	B	-	7.90 ± 0.02	-	-	4.38 ± 0.05			
29852	A	-	5.60 ± 0.02	-	-	1.64 ± 0.04			
	B	-	7.60 ± 0.02	-	-	3.64 ± 0.04			
51384	A	-	4.87 ± 0.02	-	-	1.82 ± 0.04			
	B	-	9.41 ± 0.17	-	-	6.37 ± 0.17			
65241	A	-	5.69 ± 0.02	-	-	1.59 ± 0.05			
	B	-	8.71 ± 0.09	-	-	4.62 ± 0.11			
66223	Aa	-	5.89 ± 0.02	-	-	1.67 ± 0.06			
	Ab	-	11.55 ± 0.11	-	-	7.33 ± 0.12			
103298	Aa	-	5.26 ± 0.02	-	-	1.35 ± 0.04			
	Ab	-	8.22 ± 0.02	-	-	4.31 ± 0.04			
109667	A	-	5.76 ± 0.02	-	-	1.75 ± 0.07			
	B	-	9.76 ± 0.02	-	-	5.75 ± 0.07			
110787	A	-	5.57 ± 0.03	-	-	1.57 ± 0.04			
	B	-	9.46 ± 0.05	-	-	5.46 ± 0.06			
116611	Aa	-	5.42 ± 0.02	-	-	1.16 ± 0.05	Aa1, Aa2	SBI	Rucinski et al. (2005)
	Ab	-	11.35 ± 0.09	-	-	7.09 ± 0.10			

† - The spectroscopic binary reported by Abt (1965) is the system resolved within the AO data.

HIP	Comp.	V_T (mag)	K_S (mag)	$V - K$	M_V (mag)	M_K (mag)	Additional Components	SB Type	Reference
-----	-------	----------------	----------------	---------	----------------	----------------	--------------------------	------------	-----------

† - The individual component magnitudes may be significantly biased due to the presence of additional companions within the resolution limit of the *Tycho2* and *2MASS* observations.

Table 8.7: Visual magnitude differences for a subset of the sample

HIP	ΔV	Reference
5300	$1.34 \pm 0.10^*$	Horch et al. (2001)
9480	2.03 ± 0.01	Fabricius & Makarov (2000)
11569	3.98 ± 0.16	Christou & Drummond (2006)
17954	$0.45 \pm 0.10^*$	Horch et al. (2004)
28614	1.90 ± 0.02	Fabricius & Makarov (2000)
36850	0.90 ± 0.03	Worley (1969)
44127 A,BC	$7.06 \pm 0.10^*$	Baize & Petit (1989)
44127 BC	$0.20 \pm 0.10^*$	Mason et al. (2001)
47479	0.63 ± 0.02	Mason et al. (2001)
76952	1.55 ± 0.02	Fabricius & Makarov (2000)
77660	2.61 ± 0.04	Docobo et al. (2010)
80628	$4.12 \pm 0.10^*$	Mason et al. (2001)
82321 A,BC	$3.61 \pm 0.10^*$	Mason et al. (2001)
83231 BC	$0.10 \pm 0.10^*$	Mason et al. (2001)
93506	0.21 ± 0.02	Fabricius & Makarov (2000)

* - For ΔV measurements without uncertainties, 0.10 is used

8.5 Results

8.5.1 Astrometric results

The astrometry and photometry measurements of the two subsamples are given in Tables 8.4 and 8.5. Both tables contain the *Hipparcos* designation of the primary, the components of the system under investigation, the instrument and epoch of observation, and the measured astrometric values with corresponding uncertainties. For the orbit subsample, the WDS designation and discoverer code are also listed for reference.

Combining the K -band magnitudes of the sample with the ΔK values reported in Tables 8.4 and 8.5, and the *Hipparcos* parallax, allowed for an estimation of the K -band apparent and absolute magnitudes of the resolved components (Table 8.6). For systems with ΔV measurements reported within the literature (Table 8.7), the corresponding estimated V -band apparent and absolute magnitudes, and $V - K$ colours for each resolved component are reported. Seven members of the overall sample are hierarchical systems with at least one of the components resolved within the AO data consisting of multiple sub-components, indicated in Table 8.6. An example of this is HIP128; the AO data are able to resolve a previously-unknown binary companion within this system (HIP128 C at $\sim 1''$), but are of insufficient angular resolution to resolve the previously-known spectroscopic component HIP128 B. Without an estimate of the ΔV or ΔK between HIP128 A and HIP128 B, the individual magnitudes cannot be estimated and therefore only the blended magnitudes of the two components are listed.

8.5.2 Orbital elements and dynamical masses

Table 8.8: Estimated orbital parameters and corresponding 1σ uncertainties

HP	N. Meas.	Period P (yrs)	Semi-major axis a (")	Inclination i ($^\circ$)	Longitude of Node Ω ($^\circ$)	Epoch of Periastron T_0 (yrs)	Eccentricity e	Longitude of Periastron ω ($^\circ$)	System Mass (M_\odot)
5300	19	$28.36^{+0.04}_{-0.04}$	$0.2396^{+0.0005}_{-0.0005}$	$65.3^{+0.3}_{-0.3}$	$142.7^{+0.3}_{-0.3}$	$2007.94^{+0.02}_{-0.02}$	$0.424^{+0.002}_{-0.002}$	$333.9^{+0.4}_{-0.3}$	3.16 ± 0.34
9480	66	$61.14^{+0.05}_{-0.05}$	$0.614^{+0.002}_{-0.002}$	$16.7^{+0.9}_{-0.9}$	$48.2^{+3.3}_{-3.1}$	$1964.35^{+0.09}_{-0.09}$	$0.355^{+0.001}_{-0.001}$	$19.5^{+3.5}_{-3.7}$	2.72 ± 0.13
11569	11	$50.2^{+1.0}_{-1.0}$	$0.429^{+0.007}_{-0.007}$	$149.0^{+1.7}_{-1.6}$	$180.0^{+2.7}_{-2.8}$	$1993.24^{+0.08}_{-0.08}$	$0.642^{+0.009}_{-0.009}$	$331.3^{+2.6}_{-2.7}$	2.12 ± 0.25
17954	44	$61.2^{+0.1}_{-0.1}$	$0.442^{+0.002}_{-0.002}$	$84.7^{+0.1}_{-0.1}$	$26.4^{+0.2}_{-0.2}$	$1998.30^{+0.08}_{-0.08}$	$0.628^{+0.002}_{-0.002}$	$340.3^{+0.7}_{-0.7}$	4.15 ± 0.39
28614	69	$18.641^{+0.008}_{-0.008}$	$0.2741^{+0.0001}_{-0.0001}$	$96.59^{+0.02}_{-0.02}$	$24.76^{+0.02}_{-0.02}$	$2003.742^{+0.004}_{-0.004}$	$0.744^{+0.001}_{-0.001}$	$217.08^{+0.08}_{-0.08}$	6.36 ± 0.62
36850	207	$466.8^{+6.3}_{-6.1}$	$6.78^{+0.05}_{-0.05}$	$113.56^{+0.09}_{-0.09}$	$41.2^{+0.1}_{-0.1}$	$1957.3^{+0.3}_{-0.3}$	$0.333^{+0.007}_{-0.006}$	$249.3^{+0.6}_{-0.5}$	5.42 ± 0.97
44127	9	$39.4^{+0.1}_{-0.1}$	$0.70^{+0.01}_{-0.01}$	$111.6^{+1.1}_{-1.1}$	$24.5^{+1.2}_{-1.3}$	$1999.1^{+0.6}_{-0.7}$	$0.35^{+0.02}_{-0.02}$	$354.2^{+4.4}_{-4.7}$	0.68 ± 0.04
47479	5	$10.74^{+0.04}_{-0.04}$	$0.1207^{+0.0006}_{-0.0006}$	$128.4^{+1.5}_{-1.4}$	$87.4^{+0.5}_{-0.5}$	$2005.89^{+0.03}_{-0.04}$	$0.365^{+0.009}_{-0.009}$	$18.6^{+1.2}_{-1.2}$	5.83 ± 0.53
76952	104	$91.2^{+0.4}_{-0.4}$	$0.729^{+0.006}_{-0.006}$	$94.45^{+0.07}_{-0.07}$	$111.75^{+0.09}_{-0.09}$	$1931.6^{+0.3}_{-0.3}$	$0.48^{+0.01}_{-0.01}$	$103.8^{+0.5}_{-0.5}$	4.19 ± 0.30
80628	8	$82.8^{+1.5}_{-1.3}$	$0.79^{+0.03}_{-0.02}$	$31.2^{+5.4}_{-6.0}$	$86.8^{+8.1}_{-5.6}$	$1994.1^{+0.9}_{-1.1}$	$0.45^{+0.03}_{-0.03}$	$177.9^{+9.8}_{-7.9}$	4.99 ± 0.75
82321	12	$56.4^{+0.3}_{-0.3}$	$0.279^{+0.005}_{-0.005}$	$37.4^{+2.6}_{-2.8}$	$57.5^{+5.9}_{-6.1}$	$1991.2^{+2.3}_{-2.1}$	$0.13^{+0.02}_{-0.02}$	$69.4^{+8.0}_{-7.5}$	1.16 ± 0.09
93506	42	$21.00^{+0.01}_{-0.01}$	$0.489^{+0.001}_{-0.001}$	$111.1^{+0.1}_{-0.1}$	$74.0^{+0.1}_{-0.1}$	$2005.99^{+0.03}_{-0.03}$	$0.211^{+0.001}_{-0.001}$	$7.2^{+0.6}_{-0.6}$	5.26 ± 0.37

Table 8.9: Previous and revised dynamical system masses

HIP	Old Estimate (M_{\odot})	New Estimate (M_{\odot})
5300	3.45	3.16 ± 0.34
9480	2.98 ± 0.39	2.72 ± 0.13
11569	2.12 ± 0.33	2.12 ± 0.25
17954	3.37 ± 0.35	4.15 ± 0.39
28614	6.33 ± 0.62	6.36 ± 0.62
36850	5.51	5.42 ± 0.97
44127	0.61 ± 0.03	0.68 ± 0.04
47479	7.50	5.83 ± 0.53
76952	4.14 ± 0.28	4.19 ± 0.30
80628	-	4.99 ± 0.75
82321	1.00	1.16 ± 0.09
93506	5.20 ± 0.36	5.26 ± 0.37

The orbital parameters for each system with sufficient orbital coverage are listed in Table 8.8, alongside a system mass estimated from Kepler’s Third Law (hereafter the dynamical system mass) and the number of measurements used to fit the orbit. In Figures 8.6, and 8.7, the refined orbital fits incorporating the new data are plotted along with the previously reported orbit (references listed within Table 8.4). The resulting orbits span a range of periods from 10.78 to 467.4 years, and a range of semi-major axes between $0''.12$ to $6''.78$. The relatively short period of each system allows for orbital motion to be resolved over very short baselines, typically on the order of months. The changes to the estimated dynamical system mass between the previously published orbit fit and the refined fit presented within this study are shown in Table 8.9.

8.6 Discussion

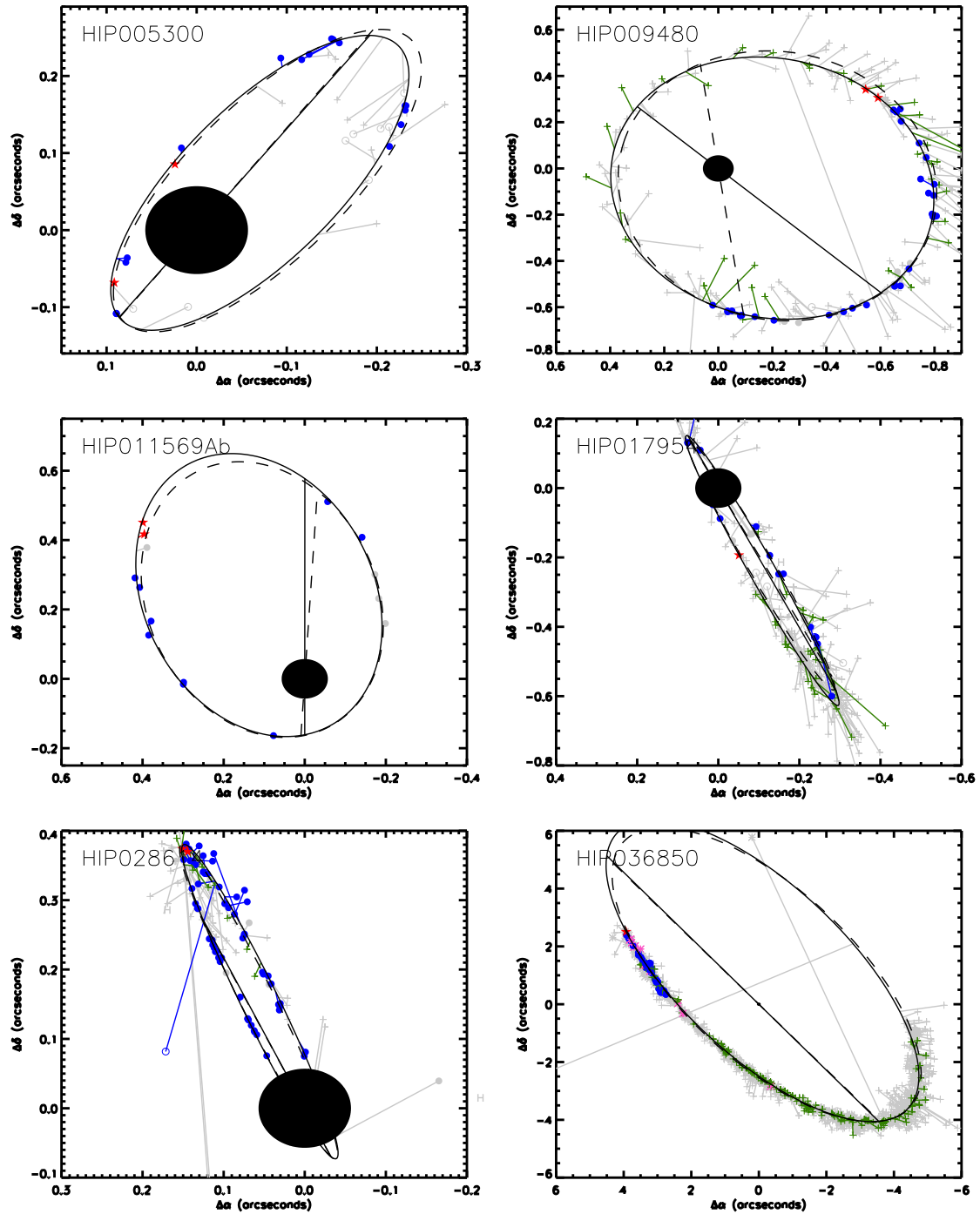


Figure 8.6: Combining the high-resolution observations with historical measurements, refined orbits for 6 binary systems are plotted. The previous orbital fit, obtained from the Sixth Orbit Catalog, is plotted for reference with a dashed line. Each plot uses a similar symbol scheme to the Sixth Orbit Catalog; open blue circles representing eyepiece interferometry, filled blue circles speckle interferometry, green crosses micrometrical observations, and violet asterisks photographic measurements. The high-resolution observations presented within this study are plotted as filled red stars. For each measurement, the corresponding O-C line is plotted, showing the difference between expected and actual position within the orbital path. Symbols in grey represent those measurements presented without formal errors, and are not used while estimating the orbital parameters. Within each plot, the 57mas radius black disc represents the resolution limit for K -band observations at an 8-metre telescope.

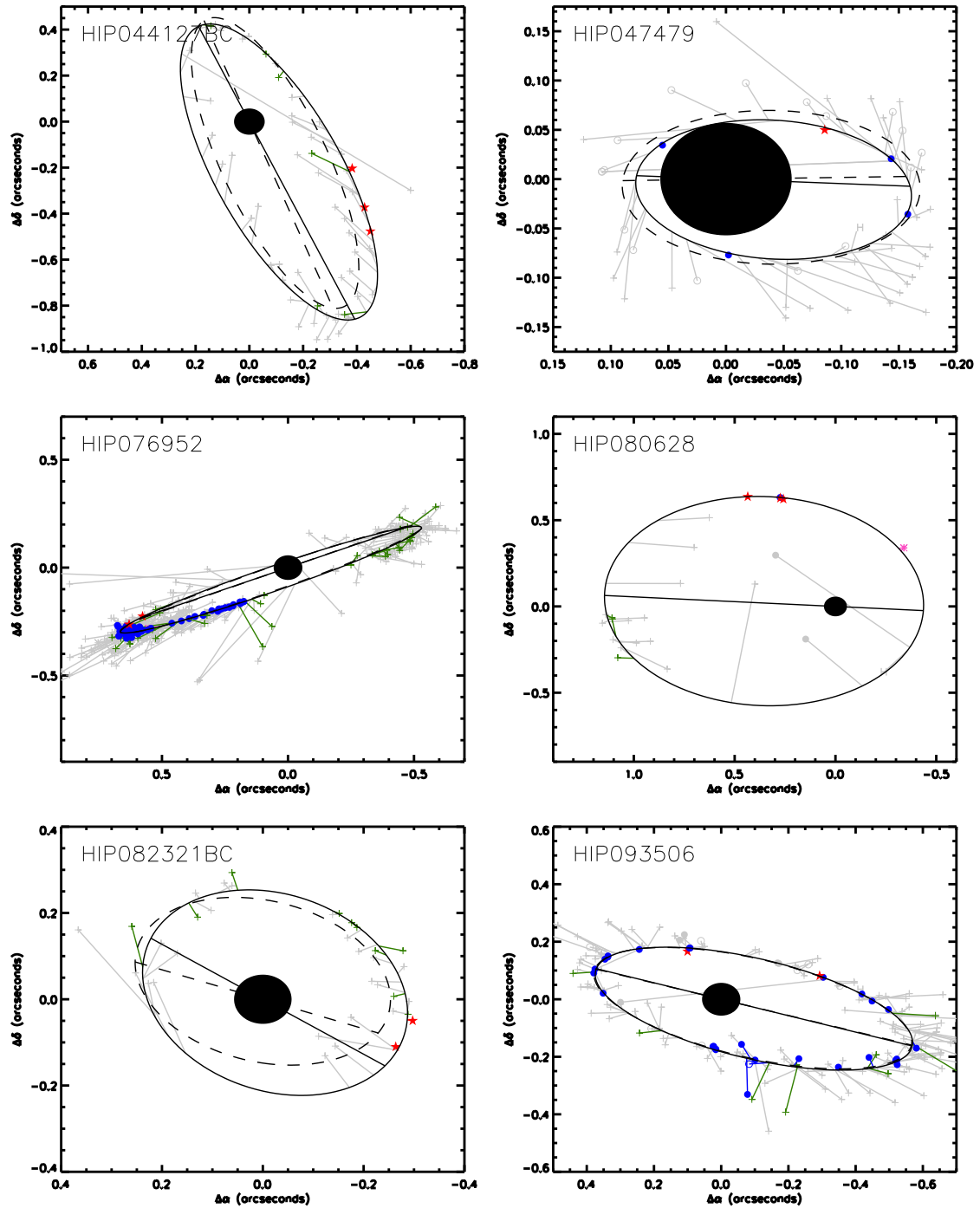


Figure 8.7: Combining the high-resolution observations with historical measurements, refined orbits for 6 binary systems are plotted. The previous orbital fit, obtained from the Sixth Orbit Catalog, is plotted for reference with a dashed line. Each plot uses a similar symbol scheme to the Sixth Orbit Catalog; open blue circles representing eyepiece interferometry, filled blue circles speckle interferometry, green crosses micrometrical observations, and violet asterisks photographic measurements. The high-resolution observations presented within this study are plotted as filled red stars. For each measurement, the corresponding O-C line is plotted, showing the difference between expected and actual position within the orbital path. Symbols in grey represent those measurements presented without formal errors, and are not used while estimating the orbital parameters. Within each plot, the 57mas radius black disc represents the resolution limit for K -band observations at an 8-metre telescope.

Table 8.10: Comparison of dynamical and photometric system masses for each system within the orbit subsample

HIP	Dynamical System		Lejeune & Schaefer		Marigo et al.		Stiess et al.	
	Mass (M_{\odot})	Age (Myr)	Mass (M_{\odot})	Age (Myr)	Mass (M_{\odot})	Age (Myr)	Mass (M_{\odot})	Age (Myr)
Systems identified as doubles								
5300	3.16 ± 0.34	280	3.56 ± 0.13	400	3.47 ± 0.13	355	3.69 ± 0.16	
9480	2.72 ± 0.13	250	3.15 ± 0.20	280	3.12 ± 0.20	160	3.25 ± 0.31	
11569 AaAb [†]	2.12 ± 0.25	100	2.45 ± 0.07	100	2.89 ± 0.15	100	2.97 ± 0.25	
76952	4.19 ± 0.30	315	4.38 ± 0.45	400	4.10 ± 0.40	315	4.38 ± 0.45	
Low-mass binary pair within hierarchical system								
44127 BC	0.68 ± 0.04	-	-	250	0.88 ± 0.01	50	0.83 ± 0.01	
82321 BC	1.16 ± 0.09	400	1.91 ± 0.02	445	1.87 ± 0.02	500	1.90 ± 0.02	
Systems with one unresolved spectroscopic component								
80628	4.99 ± 0.75	630	3.03 ± 0.08	630	3.06 ± 0.18	445	3.15 ± 0.13	
Systems with two unresolved spectroscopic components								
28614	6.36 ± 0.62	630	3.98 ± 0.32	630	3.96 ± 0.28	500	4.18 ± 0.34	
36850	5.42 ± 0.97	280	4.26 ± 0.28	355	4.15 ± 0.24	315	4.34 ± 0.31	
Systems with evidence of unresolved spectroscopic								
17954	4.15 ± 0.39	400	3.49 ± 0.11	400	3.44 ± 0.12	225	3.67 ± 0.16	
47479	5.83 ± 0.53	560	3.99 ± 0.10	560	3.96 ± 0.10	445	4.17 ± 0.14	
93506	5.26 ± 0.37	710	4.11 ± 0.25	710	4.07 ± 0.23	500	4.45 ± 0.36	

[†] - The ages and photometric masses may be significantly biased due to the presence of additional companions within the resolution limit of the *Tycho2* and *2MASS* observations.

High-resolution observations obtained for 26 nearby multiple systems with A-type primaries with projected separations within 100 AU have been presented. The subset of 12 targets with orbit fits have been further divided into four distinct categories primarily based on a comparison between the dynamical mass and the photometric mass estimated from the mass-magnitude relations, as shown in Figure 8.8. The photometric mass estimates for each system using the Lejeune & Schaerer (2001), Marigo et al. (2008), and Siess et al. (2000) grids are shown in Table 8.10. Those systems with only two known components are discussed in §8.6.1, where the importance of metallicity is described. Two hierarchical systems resolved within the AO data are discussed in §8.6.1 and §8.6.1, which allow for a comparison to the models within the K to M-type spectral range. For systems with a dynamical mass excess, significantly higher than the mass predicted from the theoretical mass-magnitude relations, the subset with known spectroscopic components is discussed in §8.6.2, and three systems with evidence suggestive of an additional unresolved component are discussed in §8.6.2. The remaining targets are discussed in the context of continued monitoring of the orbital motion in §8.6.3, of these 11 are newly resolved as a part of the VAST survey, 2 were resolved in recent multiplicity surveys of nearby Southern A-type stars (Ivanov et al. 2006; Ehrenreich et al. 2010), and 1 resolved within a large speckle interferometry survey (McAlister et al. 1987).

8.6.1 Comparison to theoretical models

A-type binaries

Four targets within the orbit subsample are systems where the two known components have been resolved within the high-resolution data; HIPs 5300, 9480, 11569, and 76952. For each of these four targets, the mass-magnitude relations were used to determine how the system mass changes as a function of the estimate of the system age, shown in Figure 8.9. For one system, HIP 76952, the dynamical system mass is consistent with the photometric system mass (Figure 8.9, top panel). The ages of the systems estimated from the position of the primary on the CMD are consistent with their position within the Local Interstellar Bubble (LIB). The minimum age of a star within the LIB, excluding those with relatively high space motions (e.g. the β Pic moving group - Ortega et al. 2002), has been shown to be 160 Myrs (Abt 2011).

The dynamical system masses of the three remaining systems are consistently lower than their photometric system masses. One possible explanation for the apparently low dynamical masses is a non-Solar metallicity. Varying the metallicity has a significant effect on the system age estimate and the mass-magnitude relations. As an example, a $2 M_{\odot}$ star with super-Solar metallicity will be more luminous and have a redder $V - K$ colour index than a similar-mass star of Solar metallicity. A super-Solar metallicity star will appear to be significantly older based on its position on a CMD if Solar metallicity models are used. To explore the effect of the assumption of Solar metallicity for the entire sample, the HIP 5300 system (Figure 8.9, second panel) was studied at varying metallicity values. Using the Solar metallicity models, the dynamical system mass of this system is significantly lower than the photometric system mass (Figure 8.10, top panel). Increasing the metallicity causes the star to appear both younger, and less massive (Figure 8.10, bottom panel). Only eight of the targets included within this study

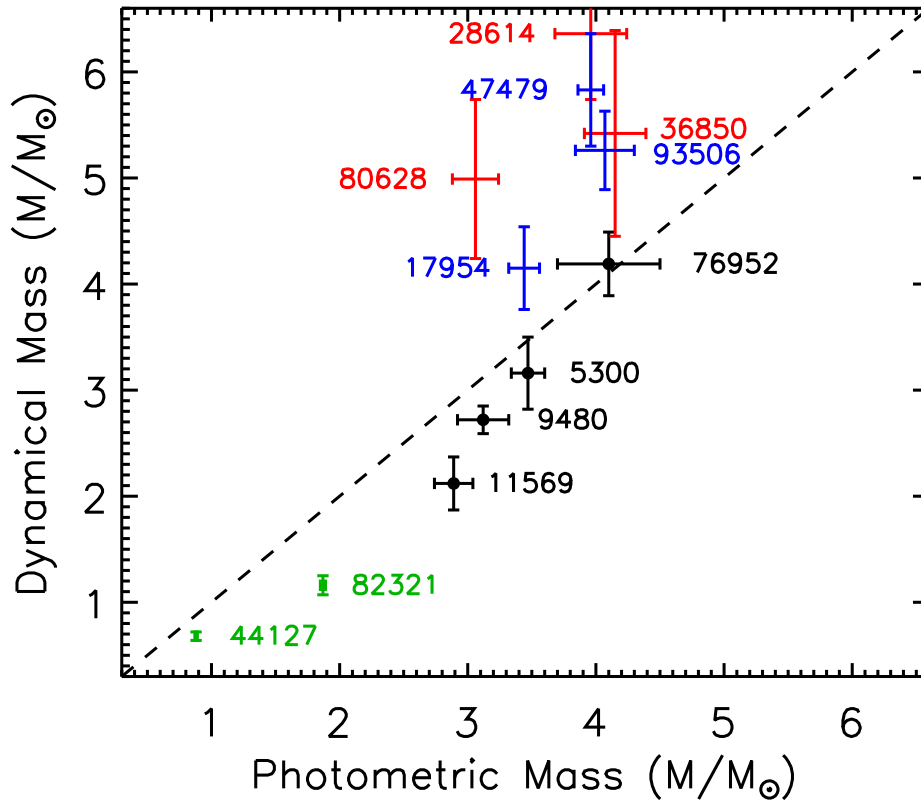


Figure 8.8: Using the method introduced in §4.4, a comparison can be made between the dynamical mass determined from the orbit and the mass estimated from theoretical mass-magnitude relations for the stars within the orbit subsample (the Marigo et al. (2008) models are used for this example). The systems with an A-type star primary which are known to consist only of two components are denoted as black points (§8.6.1). Two hierarchical systems were fully resolved with the AO data, and the lower-mass pair of each system are in green (§8.6.1). The systems which have a significantly discrepant dynamical mass can be explained by the presence of an unresolved companion within the AO data. The targets with known spectroscopic components are plotted in red (§8.6.2), while those systems with evidence suggesting a previously unknown spectroscopic component are plotted in blue (§8.6.2). The dashed line denotes the equivalence between the dynamical and photometric mass.

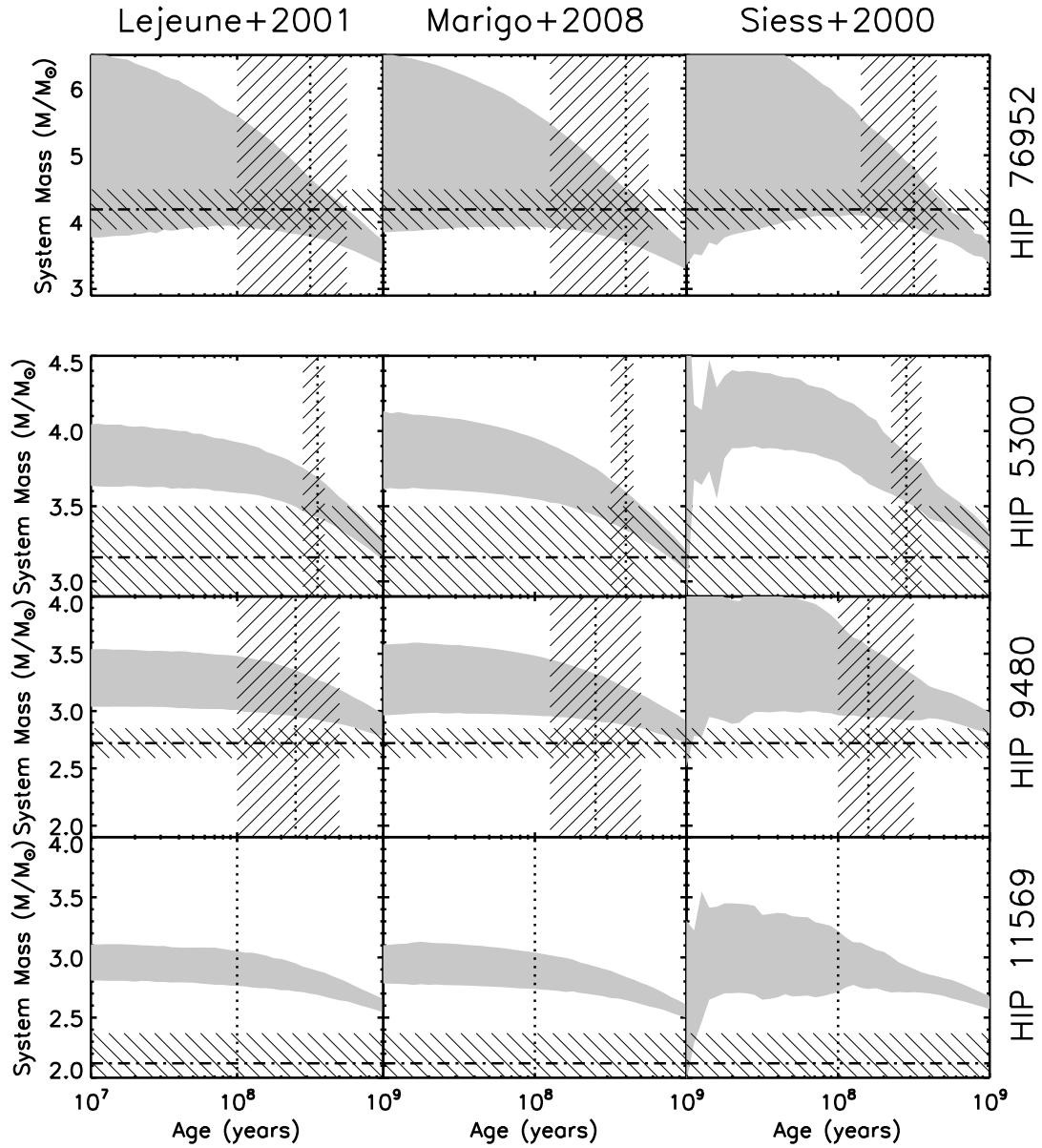


Figure 8.9: The system mass as a function of age based on the mass-magnitude relations derived from three of the model grids. Each panel is similar in nature to Figure 8.5, with the spread in the mass-age relation introduced by uncertainties in both the measured K -band magnitude, and the distance determination. The horizontal dot-dashed line indicates the dynamical mass determined from the system orbit, with the uncertainty denoted by the line-shaded region. The vertical dotted line indicates the age of the system derived from the isochrones, with the line-shaded region denoting the range of ages consistent with the uncertainties in the position of the primary on the CMD. The primary of the HIP 11569 system is significantly bluer than expected for a Main Sequence star, and as such its age has been assigned to 100 Myr, with no corresponding uncertainty. The presence of additional components to the HIP 11569 system, within the resolution limit of both the *Tycho2* and *2MASS* observations, is the likely cause of this bias.

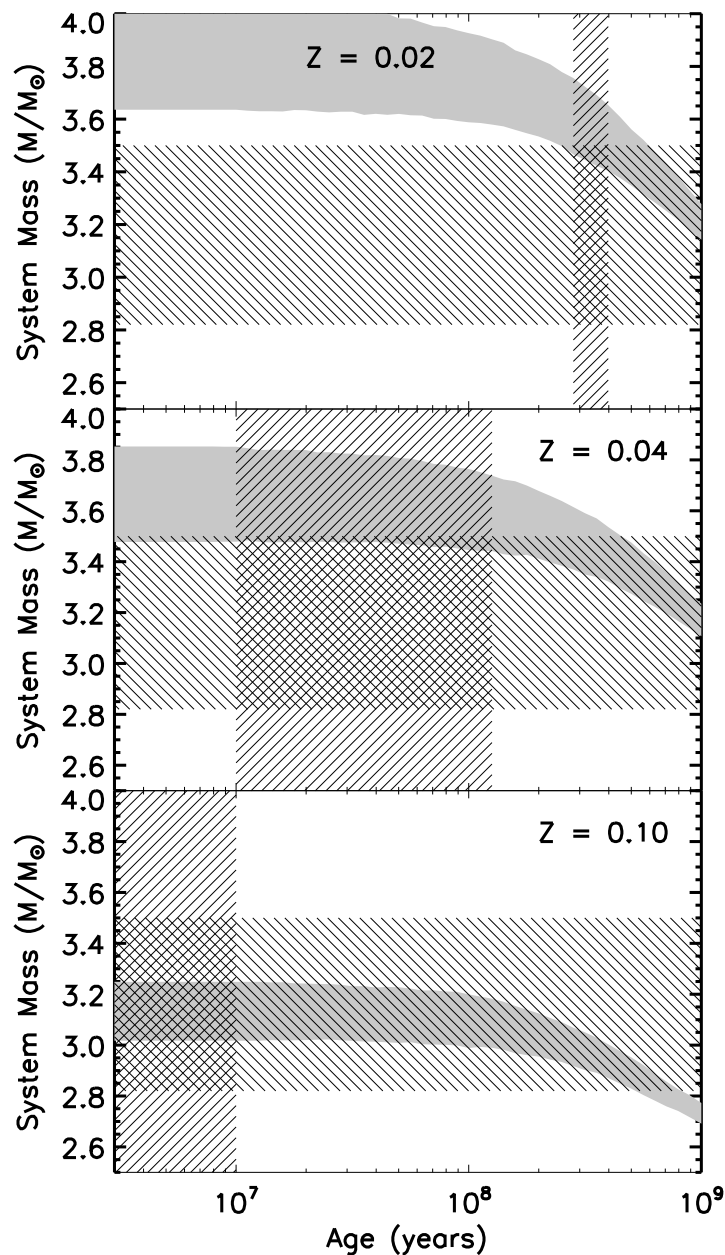


Figure 8.10: (*top panel*): The dynamical mass of the HIP 5300 system (horizontal striped region) is significantly below that of the system mass estimated from mass-magnitude relations calculated from the Solar metallicity models from Lejeune & Schaerer (2001) (shaded region), based on the estimated age of the system (vertical striped region). (*middle panel*): Assuming a higher metallicity ($Z = 0.04$), the position of the components on the colour-magnitude diagram suggests a younger age, and the mass-magnitude relation derived from the metal-enhanced models suggests a systematically lower system mass, although the dynamical mass is still discrepant. (*bottom panel*): With a metallicity of $Z = 0.10$, the age estimate is younger still (<10 Myr), and the discrepancy between the dynamical mass and the mass estimated from the mass-magnitude relation is removed.

have metallicity measurements, either from spectroscopic analysis (e.g. Erspamer & North 2003) or derived from Strömgren photometry (e.g. Song et al. 2001), demonstrating the need for further study in this area.

K- and M-type binaries - HIP 44127

The detection of two hierarchical systems, with pairs of lower-mass companions in a wide orbit around an A-type primary, allows for a comparison of the theoretical models in the low-mass regime where the models differ in the treatment of the contraction phase of these objects (e.g. Figure 8.3). The high-resolution observation of the HIP 44127 system, shown in Figure 8.11, resolves three components to this hierarchical system, with an A-star primary (A) separated by $\sim 4''$ from two fainter, gravitationally bound, companions (BC).

The orbit presented in the Sixth Orbit Catalog of the BC pair around the A-type primary is in disagreement with the recent observations of this system. Although the phase coverage is insufficient for a robust orbital determination, the high proper motion of the primary ($\Delta\alpha = -441.1 \text{ mas yr}^{-1}$, $\Delta\delta = -215.2 \text{ mas yr}^{-1}$) suggests that the BC pair is co-moving. In addition, radial velocity variations detected within the spectra of the primary suggest the presence of a spectroscopic component to this system with a period of ~ 11 years (Abt 1965). The separation of this component was anticipated to be between $0''.2$ and $0''.6$, reaching maximum separation in the middle of 2007 (Docobo & Andrade 2006). No companion consistent with these predictions is resolved within any epoch of the AO data, placing an upper limit to the separation of $0''.08$, $0''.10$, and $0''.10$ in 2008, 2010, and 2011 respectively. The magnitude difference between the primary and the suggested companion, estimated to be $\Delta m = 1.2$, is well within the detection limits of the AO data at the expected separation (Docobo & Andrade 2006).

A refined orbit of HIP 44127 BC is presented in Table 8.8 and Figure 8.7, with an estimated dynamical system mass of $0.68 \pm 0.04 M_{\odot}$. The small magnitude difference between the two components ($\Delta K \sim 0$) suggests a mass ratio close to unity. Assuming individual masses of $\sim 0.34 M_{\odot}$ the components would be of early- to mid-M spectral type (Baraffe & Chabrier 1996), a region of particular disagreement between theoretical models. The Baraffe et al. (1998) and Siess et al. (2000) models both predict that for a binary consisting of two stars of magnitudes equal to the measured magnitudes of the two components ($M_K = 5.87$), the system mass will increase from 0.3 to $0.9 M_{\odot}$ between 10 and 100 Myrs (Figure 8.11), as these models take into account the phase of contraction onto the Main Sequence for lower-mass stars. No such change is predicted by the Marigo et al. (2008) models, with the system mass remaining unchanged between 10 Myrs and 1 Gyr (Figure 8.11). The photometric system masses are only consistent with the dynamical mass at ~ 30 Myrs in the Baraffe et al. (1998) and Siess et al. (2000) models, and are not consistent with any age in the Marigo et al. (2008) models. The metallicity of this system has been measured to be almost Solar (Wu et al. 2010), removing the degeneracy which exists between metallicity and the mass and age of the system.

The position of the primary on the CMD suggests a relatively young age of the system between 50 and 250 Myr. The $V - K$ colours of the BC pair also suggest a young age, between 40 and 100 Myr using the Siess et al. (2000) and Baraffe et al. (1998) models. The inferred

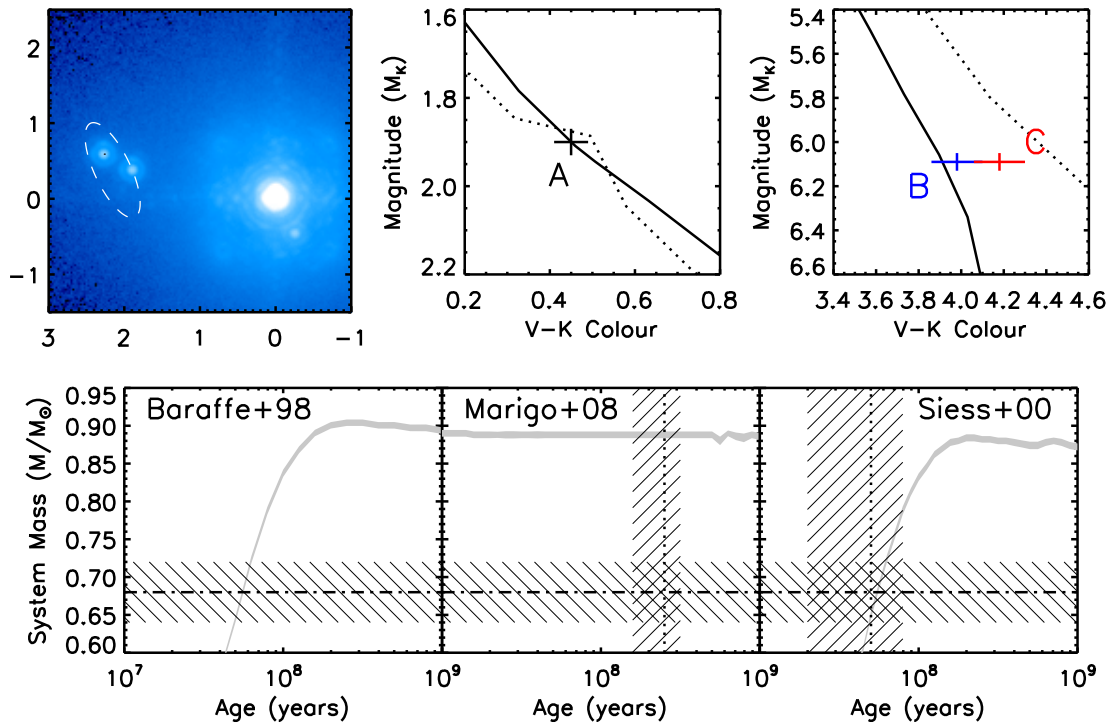


Figure 8.11: *Top row - (left)*: An AO observation of HIP 44127 triple system. The orbit of the lower-mass pair (BC) taken from Table 8.8 is plotted as a solid line for reference. The bright point source to the lower-right of the primary PSF is a known filter ghost. The axis labels are given in arcseconds, with each arcsecond equal to approximately 14.5 AU. *(centre)*: A colour-magnitude diagram highlighting the position of the primary with respect to the theoretical models; Marigo et al. (2008) - solid line, Siess et al. (2000) - dotted line, while the Baraffe et al. (1998) models do not extend to high enough masses. The age of the system was estimated using the isochrone which best fit the position of the primary. *(right)*: A colour-magnitude diagram highlighting the position of the two lower-mass components (B - blue, C - red). The line styles are the same as the centre panel *Bottom row* - The photometric system mass plotted as a function of system age for each of the three models. The vertical dotted line within each panel indicates the age of the system estimated from using each of the models, while the horizontal dot-dashed line indicates the dynamical system mass estimated from the orbital fit. As the Baraffe et al. (1998) models do not extend to the A-type star mass range, an age estimate is not possible.

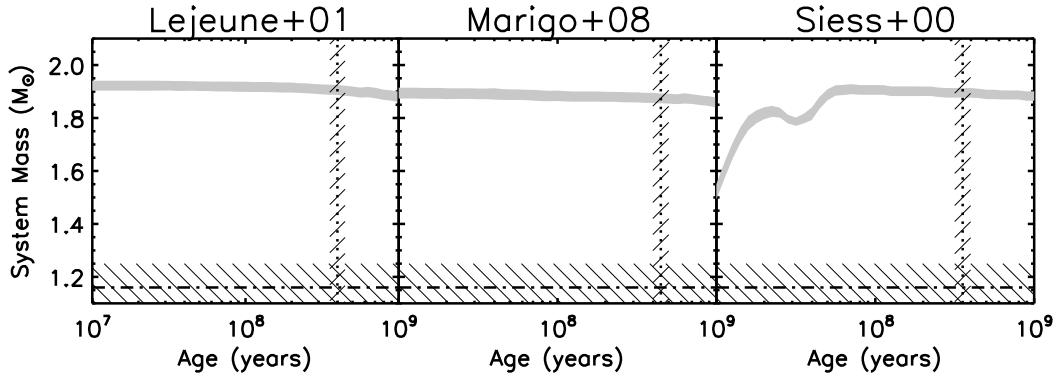


Figure 8.12: The photometric system mass plotted as a function of system age for each of the three models for the HIP 82321 BC system. The vertical dotted line within each panel indicates the age of the system estimated from using each of the models, while the horizontal dot-dashed line indicates the dynamical system mass estimated from the orbital fit. The clear discrepancy between the dynamical and photometric system masses can be explained by the lack of complete coverage of the orbit presented in Figure 8.7. Further high angular resolution observations of this system will allow for an improved determination of the orbital parameters.

young age of the system is not inconsistent with the minimum age of stars found within the LIB (Abt 2011), given the relatively high UVW space velocity of the HIP 44127 system (Palous 1983). The detection of X-ray emission from this system is also of interest. Previous studies have shown that A7 stars such as the primary should not emit X-rays, and that any detection of X-rays from the position of the star can be indicative of a lower-mass companion (e.g. De Rosa et al. 2011). The *ROSAT* source J085913.0+480227 is coincident with the optical position of HIP 44127 (Voges et al. 1999).

This hierarchical triple system warrants further study, primarily in order to refine the orbital fit as the BC pair approaches apastron passage in 2018. This system also makes an ideal candidate for future spectroscopic observations to search for the narrow spectral lines of the two faint companions. With a double-lined spectroscopic orbit fit, model-independent masses can be calculated for the individual components. If the young age suggested by both the position on the CMD and the system mass estimated from the mass-magnitude relations is correct, the BC pair would be an ideal calibrator for the theoretical models in the young, low-mass regime.

K- and M-type binaries - HIP 82321

The hierarchical triple system HIP 82321 was resolved within a single epoch of the AO observations. The A-type primary (A) is $\sim 2''$ from a binary pair of two lower-mass companions (BC) in a wide orbit. The significant proper motion of the primary ($\Delta\alpha = 22.8 \text{ mas yr}^{-1}$, $\Delta\delta = -51.4 \text{ mas yr}^{-1}$), and near constant separation of the three stars, suggest that the lower-mass pair is co-moving with the primary. Spectroscopic measurements of the lower-mass components of this system are possible given the small magnitude difference of the pair with respect to the primary ($\Delta K \sim 2.5$); such spectra would allow for a determination of the individual masses independent of the distance to the system. The *Hipparcos* parallax and *2MASS* K -band mag-

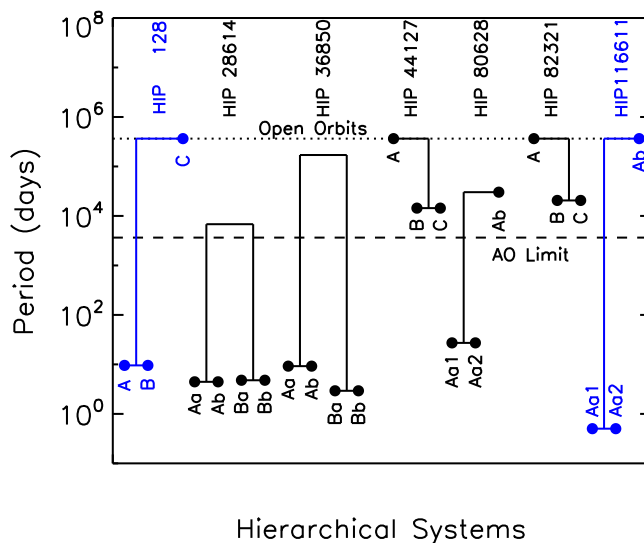


Figure 8.13: A schematic of the 7 hierarchical systems within both subsamples, including only components within a projected separation of 100AU to the A-type primary. The schematic diagram does not include the suspected spectroscopic binaries described in §8.6.2. Those systems which were newly resolved as a part of the VAST survey are highlighted in blue. Each filled circle represents an individual component, with the period of the binary pair denoted by its vertical position. The high-resolution observations are only sensitive to systems with orbital periods greater than ~ 10 years, denoted by the dashed horizontal line. For wide separation systems with indeterminate orbital periods, such as HIP 128 AB-C, the orbital period has been arbitrarily set at 1000 years, denoted by the dotted horizontal line.

nitude measurements of this system allow for a tight constraint of the system age to between 300 and 400 Myrs, based on the position of the primary on the CMD. The primary is also a possible member of the Ursa Major moving group, an association of Solar metallicity stars with an age between 300 Myrs (Soderblom & Mayor 1993) and 500 Myrs (King et al. 2003).

A refined orbit of the BC pair is presented in Table 8.8, with an estimated dynamical system mass of $1.32 \pm 0.05 M_{\odot}$. The photometric system mass, assuming the distance to each component is the same as the primary, is significantly higher at $\sim 2.0 M_{\odot}$ (Figure 8.12). The sparse coverage of the orbit (Figure 8.7) suggests that the orbit fit could be poor, resulting in an incorrect dynamical system mass. The orbit fit would be significantly improved with subsequent observations. An alternative scenario is that the pair are a background binary with a proper motion similar to the primary, which would bring the dynamical and photometrically derived masses into agreement.

8.6.2 Higher-order multiplicity

Known spectroscopic binaries

The presence of an unresolved spectroscopic binary can have a significant impact on the magnitude assigned to each component of the multiple system, increasing the estimated component

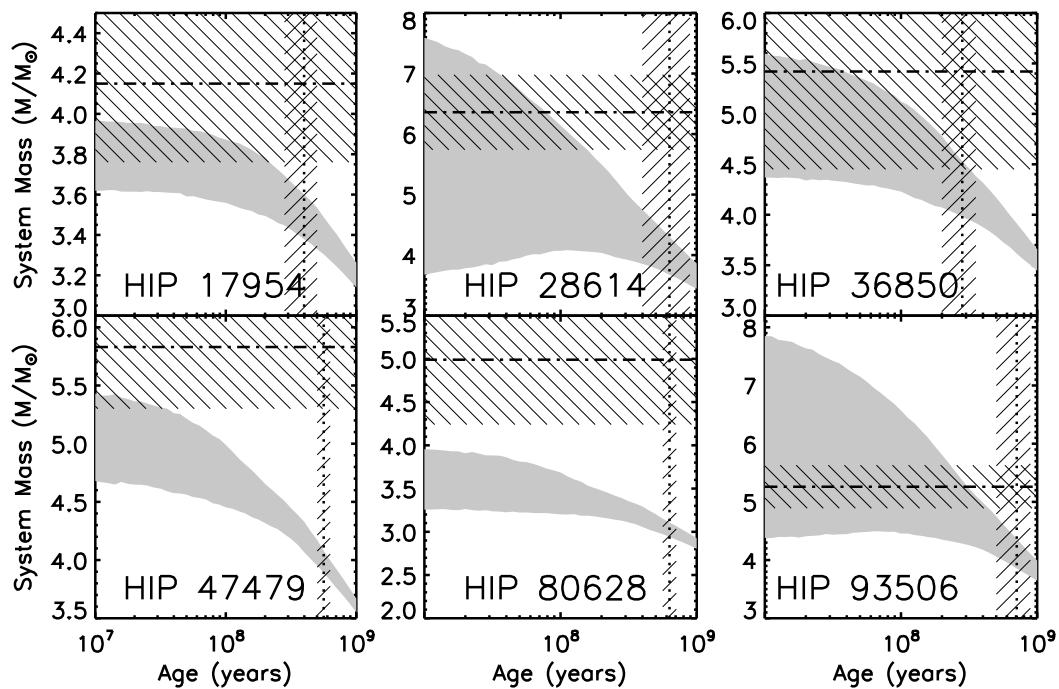


Figure 8.14: The six systems for which spectroscopic components are either known to be present through previous spectroscopic observations (HIPs 28614, 36850, 80628), or thought to exist due to a significant discrepancy between the photometric system mass and the dynamical system mass. For clarity only one model has been used to estimate the photometric system mass (Lejeune & Schaerer 2001). The horizontal displacement between the intersection of the dynamical system mass (dot-dashed line) and the age estimate of the system (dotted), and the photometric system mass curve (grey shaded region), gives an order of magnitude estimate of the mass of the unresolved spectroscopic components.

magnitude by as much as 0.75 mag for an unresolved equal-mass spectroscopic binary. For each target within this study, the literature was searched for references to additional components resolved through spectroscopic or interferometric observation which would influence any comparison made between the dynamical system mass and the photometric system mass (e.g. Figure 8.14). Of the targets within the orbit subsample, three are known to have additional spectroscopic components (HIPs 28614, 36850, 80628). The spectroscopic component to HIP 9480 resolved by Abt (1965) is resolved within the adaptive optics observations. Similarly, for the monitoring subsample, two are known spectroscopic binaries (HIPs 128, 116611). The greater frequency of spectroscopic binaries within the orbit sample, relative to the monitoring sample, can be explained by the narrow spectral lines of the former sample due to their relatively low radial velocities, $\langle v \sin i \rangle = 71 \text{ km s}^{-1}$ compared with $\langle v \sin i \rangle = 115 \text{ km s}^{-1}$ for the latter sample (Abt & Morrell 1995). The magnitudes listed for the resolved components of these systems (Table 8.6) are the blended magnitudes of the listed spectroscopic components. In addition to these known spectroscopic binaries, three members of the orbit subsample are resolved as hierarchical triples within the high-resolution observations (HIPs 11569, 44128, 82321). A schematic representation of the higher-order multiplicity systems is given in Figure 8.13.

For the three systems with known spectroscopic components within the orbit sample, the dynamical system mass includes the mass of each component, regardless of whether it is resolved within the AO data. This causes a significant discrepancy when the dynamical system mass is compared with the photometric system mass (e.g. Figure 8.8), with the dynamical system mass being systematically higher. The discrepancy between the two values cannot be directly converted into a mass for the unresolved components however, as a blended magnitude would have been used when determining the mass from the mass-magnitude relations.

Evidence of spectroscopic components

Systems with significantly higher dynamical masses than photometric masses obtained from mass-magnitude relations are strong candidates for multiple systems with unresolved components which have not been detected in spectroscopic observations. Two such systems are found with the signature of a possible unresolved component: HIP 17954 and HIP 93506 (Figure 8.14), with masses of the order of 0.5 and 1.5 M_{\odot} . Sensitive spectroscopic observations of both systems may lead to the detection of the spectral lines from an unresolved lower-mass component. A similar phenomenon is observed for the HIP 47479 system, although the number of measurements used to determine the orbit is particularly low, making the dynamical mass less certain. The narrow spectral lines of HIP 47479, implied by the low measured stellar rotational velocity (Royer et al. 2007), make it an ideal candidate for spectroscopic follow up. Previous spectroscopic observations of this system reveal $v \sin i$ variations with a magnitude of 40 km s^{-1} (Moore 1932).

From the total sample of 26 systems, and only considering stellar companions within 100 AU, a lower-limit on the higher-order multiplicity of A-type stars can be estimated. Assuming the suspected unresolved companions described earlier in this section are true, there are five double, six triple, and two quadruple systems within the orbit subsample, corresponding to

frequencies of 39, 46, and 15 per cent, respectively. This lower-limit shows an enhancement on the higher-order multiplicity of A-type stars when compared with Solar-type primaries (74 per cent double, 20 per cent triple, and 6 per cent quadruple or higher-order - Raghavan et al. 2010), and is more consistent with the fraction reported for more massive O-type primaries (46 per cent double, and 54 per cent triple or higher-order - Mason et al. 2009).

8.6.3 Continued monitoring targets

Newly-resolved binaries

Thirteen binary systems with projected separations ranging between 13 AU and 96 AU have been identified which would make ideal candidates for future orbital monitoring projects (Table 8.5). The 100 AU projected separation cut-off was applied to select only systems for which orbital motion could be detected with several years of observations. The binaries resolved within the monitoring subsample typically have lower-mass ratios than for the orbit subsample, a demonstration of the effectiveness of AO observations at detecting high-contrast binaries. Based on their position on the CMD, two members of the monitoring subsample (HIP 5310, HIP 18217) appear to lie on the Zero-Age Main Sequence, and the measured magnitude difference between primary and secondary would correspond to a late K or early M-type companion in each case. These companions are of particular interest as they will allow for further tests of the theoretical models within the young, low-mass regime. A gallery of the observations obtained of each target within the monitoring subsample is shown in Figures 8.15, and 8.16.

HIP 77660

An advantage of monitoring binary systems for orbital motion with AO instrumentation over interferometric techniques is the elimination of the quadrant ambiguity. In some cases, the output of the image processing of speckle data results in a 180° ambiguity on the position angle measurement (Bagnuolo et al. 1992). This may lead to a scenario where orbital motion is thought to exist for a binary pair, when in fact this motion is the product of such a quadrant uncertainty combined with the true linear motion of the companion. The ambiguity can be resolved by observing the system using AO imaging, where no reconstruction is required to obtain the final science image.

Based on the AO observations of the binary system HIP 77660, it appears that such a quadrant ambiguity has occurred, making linear motion appear as orbital motion, as shown in Figure 8.17. The significant proper motion of the system ($\Delta\alpha = -91$ mas/yr, $\Delta\delta = -28$ mas/yr), as measured by *Hipparcos*, is inconsistent with a stationary background object. While future measurements of this system will be able to resolve the presence of orbital motion after a sufficient time baseline, spectroscopy or multi-colour photometry will allow for a rapid characterisation of the properties of both components.

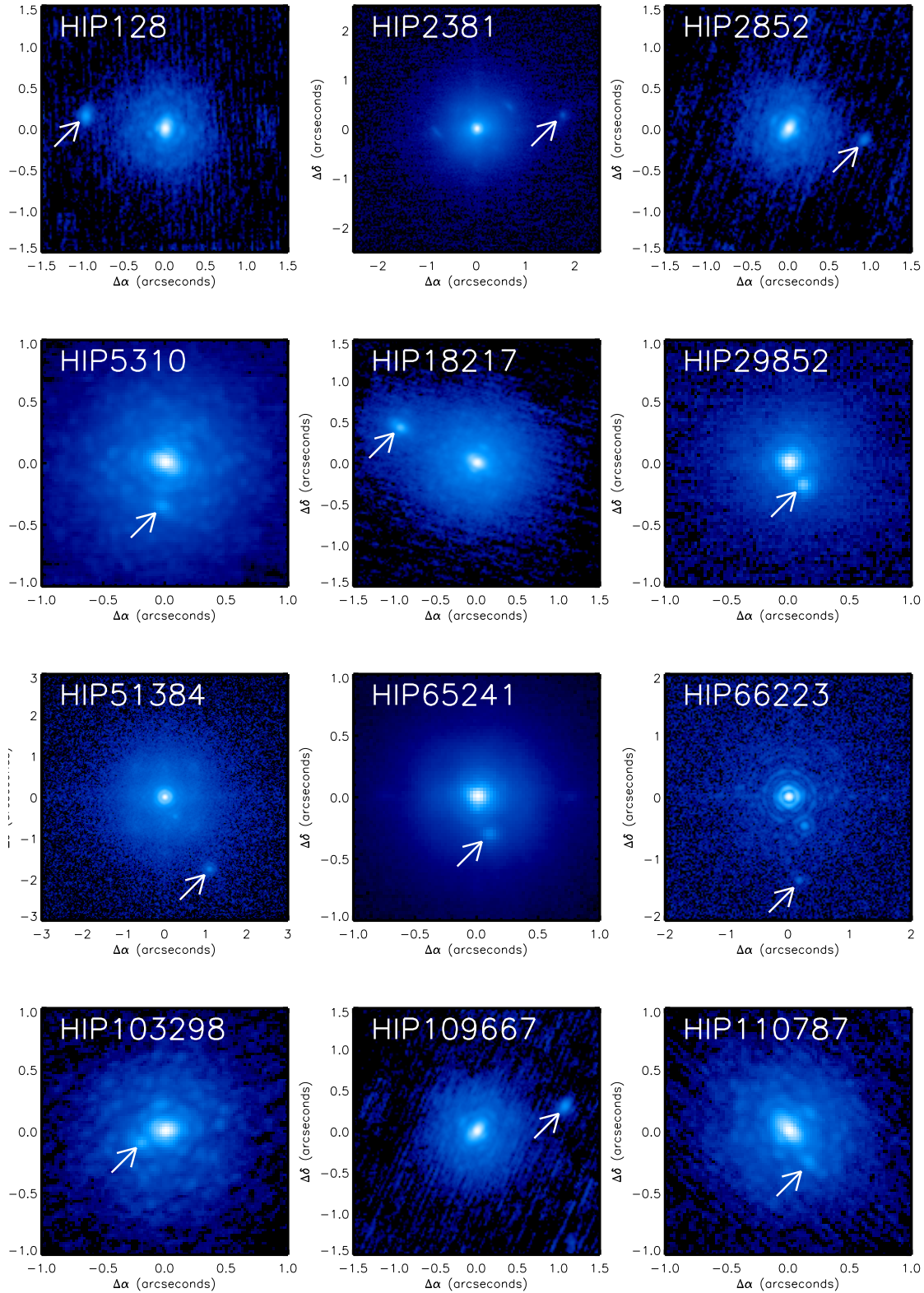


Figure 8.15: Observations of twelve of the thirteen systems with projected separations $< 100\text{AU}$ suggested as future orbital monitoring targets. The companion in each image is highlighted, with a logarithmic image scale between 1 (white) and 10^{-6} (black) relative to the peak intensity of the primary.

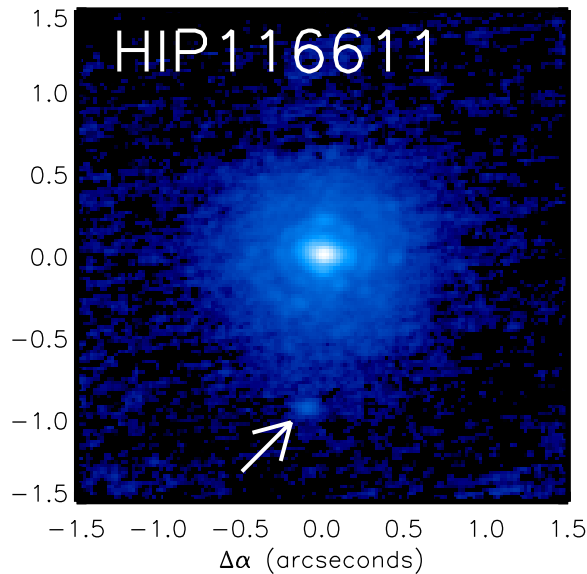


Figure 8.16: (*continued*): An observation of one of the thirteen systems with projected separations < 100 AU suggested as future orbital monitoring targets. The companion in each image is highlighted, with a logarithmic image scale between 1 (white) and 10^{-6} (black) relative to the peak intensity of the primary.

8.7 Summary

High-resolution observations of 26 nearby multiple systems with A-type primaries with projected separations < 100 AU have been presented, 11 of which are binaries newly resolved as a part of the VAST survey. For those systems with sufficient orbital motion coverage, refined orbital parameters were calculated and the estimated dynamical system mass was compared to masses derived from theoretical models. Due to their rapid evolution across the CMD, removing the significant age degeneracy for lower-mass solar-type stars, binaries with A-type components are ideal targets with which to test theoretical models. Four such systems were investigated, with one system having consistent dynamical and photometric system mass estimates. Of the remaining three systems, each had a dynamical mass significantly lower than that predicted from the models. While this discrepancy may be indicative of a true divergence between the models and observations, the lack of metallicity measurements for these systems provide another explanation. Future orbital monitoring observations of A-star binary systems will provide further refinement to the orbital parameters and, combined with refinement of the magnitude, metallicity, and parallax measurements, will improve the analysis performed within this study.

Observations of two hierarchical systems, consisting of an A-type primary and a tight low-mass binary pair in a wide orbit allowed this analysis to be extended to the lower mass regime. The primary of the triple HIP 44127 suggests a young system age (< 100 Myr), making the M-dwarf pair interesting for comparison with evolutionary models. It is also shown that a dynamical system mass significantly higher than the photometric system mass is suggestive

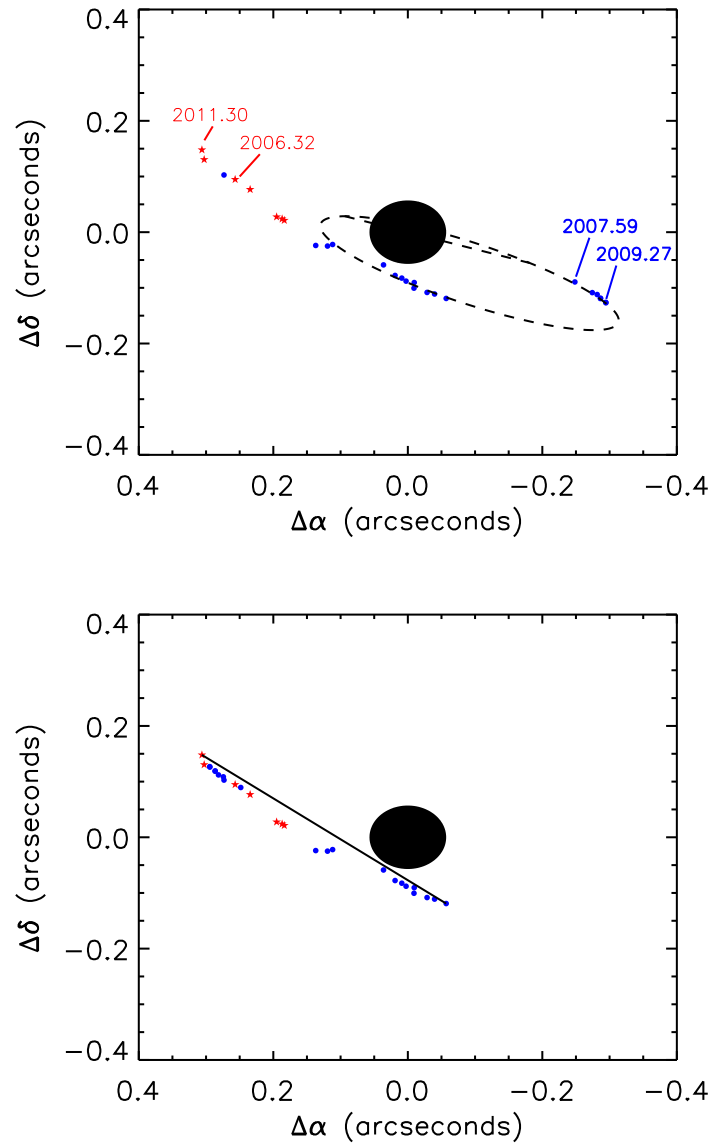


Figure 8.17: (*top panel*): The historical measurement of the system HIP 77660, plotted with the orbital fit estimated by Docobo et al. (2010). This system demonstrates the quadrant ambiguity limitation of the speckle interferometry technique. The binary companion was measured by Tokovinin et al. (2010) using speckle interferometry to be at a position angle of 248.4° to 246.8° between mid-2007 and mid-2009 (blue filled circles, top right). The AO images, which do not suffer from the same quadrant ambiguity, shows the binary at a position angle of 69.7° to 67.3° between mid-2006 and mid-2011 (red filled stars, left). (*bottom panel*): The relative position of the secondary, with 180° added to the four speckle interferometry measurements which were inconsistent with the observations presented within this study. The solid line connects the first and last observations, showing a deviation away from linear motion. Further observations are required to determine if this deviation is indicative of the true orbital path of the secondary about the primary.

of an unresolved spectroscopic component within the system. Demonstrated on several known spectroscopic binaries, systems which exhibit this discrepancy are ideal candidates for future spectroscopic or interferometric observations in an attempt to detect these hypothetical companions. Interferometric observations may be required to resolve these purported companions, as the rotationally broadened spectral lines of the rapidly rotating members of the monitoring sample (Abt & Morrell 1995) may preclude the detection of additional components using spectroscopy. Including the three systems with evidence of an unresolved close companion, a lower-limit on the higher-order multiplicity can be estimated from the 13 systems within the orbit subsample as 39 per cent double, 46 per cent triple, and 15 per cent quadruple. The remaining systems for which an orbit could not be determined are candidates for orbital monitoring projects with ground-based high-resolution observations. A number of these systems are of particular interest, based on age estimates derived from the position of the primary on the CMD, and the magnitude difference between the two components.



Due to the large number of observations obtained as a part of the VAST survey, significant avenues of scientific research relating to A-type stars can be explored, as demonstrated by the investigation of the unexplained X-ray detection of early-type stars described in Chapter 7. In this chapter I will briefly summarise several aspects of the VAST survey that require further development, and go on to consider other areas of research which can make use of the large set of high resolution observations.

9.1 Continued study of A-type binaries

The separation range over which the survey is sensitive to companions is restricted, relative to comparable surveys of Solar-type stars (e.g. Figure 6.8). It is evident that further observations must be obtained to extend the sensitivity of the sample towards both close, and wide binary systems. Prior to the publication of the statistical results of the VAST survey, I intend to use historical direct imaging observations to resolve common proper motion companions to a subset of the members of the VAST sample. With an average of 40 years between observations obtained as a part of the First and Second Digital Sky Survey (DSS1 and DSS2), and due to the relatively high proper motion of the VAST sample members, a common proper motion companion can be readily identified by a rapid blinking of the two observations. Using this method, it should be possible to characterise the wide binary population between 10^3 and 10^4 AU, providing further constraints on the overall shape of the separation distribution. A measurement of the frequency of close binary companions, with separations within 50 AU, will require future dedicated interferometric observations. I intend to pursue this avenue of research with my collaborators at the Naval Prototype Optical Interferometer (NPOI).

Of particular concern is the unknown physical nature of some of the candidate companions detailed in Chapter 5, with over half without previous observations confirming that they are gravitationally bound to the primary around which they were resolved. Due to the large scope of the survey, it was not feasible to obtain follow up observations of each detected

companion candidate. It was therefore decided to use a statistical probability cut-off, based on the local density of *2MASS* point sources, to differentiate between companion candidates and background objects. Although the measured multiplicity fraction and companion mass ratio are consistent with those observed for early-type stars within the Sco OB 2 association (Kouwenhoven et al. 2005), a similar statistical criterion was used to remove contamination from background objects. The results of this work would be significantly strengthened with follow-up observations of the resolved companion candidates, either through an analysis of the proper motion of the companion with respect to the primary, or multi-colour photometry. Such follow-up observations would likely take place after the publication of the initial results.

9.2 Future research areas

In addition to the publication of the results presented within this thesis, I intend to continue my research into the multiplicity of A-type stars. By exploiting the large set of observations that were obtained as a part of the VAST survey, I hope to consider a number of research areas:

- With a correlation between the results of the VAST survey, and mid-infrared photometric measurements obtained from *IRAS*, *Spitzer*, and *WISE*, I will investigate the correlation between the presence of companions and debris disks. The influence of a binary companion on the formation and stability of both circumstellar disks and planetary systems is an ongoing area of research (e.g. Trilling et al. 2007).
- Using a subset of our observations obtained at CFHT and Gemini, I will estimate constraints on the frequency of wide brown dwarf companions to A-type stars. Although notable examples of wide substellar companions to A-type stars exist (Lowrance et al. 2000; Lafrenière et al. 2011), their population is currently unconstrained.
- Explore the possibility of using a high-resolution near-infrared spectrograph to characterise the population of binaries which are not resolvable using either adaptive optics or interferometric observations. Combining these observations with the results of an interferometric study should provide substantial coverage of the binary population within 50 AU, crucial for constraining the overall shape of the separation distribution.
- Using the experience I have gained while conducting this study, extend the work to more massive B-type stars within the Solar neighbourhood. I am already involved in a collaboration which has obtained a significant number of adaptive optics observations of B-type stars within 100 pc. An analysis of the data will provide constraints over a similar range of separations as presented within this study, providing continued encouragement for theoretical predictions regarding the binary properties for higher-mass stars.

- Aarseth, S. J. & Heggie, D. C. 1976, *A&A*, 53, 259
- Abt, H. A. 1965, *ApJS*, 11, 429
- Abt, H. A. 2011, *AJ*, 141, 165
- Abt, H. A. & Levy, S. G. 1976, *ApJS*, 30, 273
- Abt, H. A. & Levy, S. G. 1985, *ApJS*, 59, 229
- Abt, H. A. & Morrell, N. I. 1995, *ApJS*, 99, 135
- Adams, F. C., Ruden, S. P., & Shu, F. H. 1989, *ApJ*, 347, 959
- Agekyan, T. A., Anosova, Z. P., & Bezgubova, V. N. 1969, *Astrophysics*, 5, 329
- Allen, P. R. 2007, *ApJ*, 668, 492
- Allen, P. R., Koerner, D. W., McElwain, M. W., Cruz, K. L., & Reid, I. N. 2007, *AJ*, 133, 971
- Andersen, J., Clausen, J. V., Nordstrom, B., Tomkin, J., & Mayor, M. 1991, *A&A*, 246, 99
- Anderson, E. & Francis, C. 2011, *VizieR Online Data Catalog*, 5137, 0
- Andrews, S. M. & Williams, J. P. 2007, *ApJ*, 659, 705
- Armitage, P. J. & Bonnell, I. A. 2002, *MNRAS*, 330, L11
- Arsenault, R., Salmon, D. A., Kerr, J. M., et al. 1994, *SPIE Conference Series*, 2201, 833
- Bagnuolo, W. G. J., Mason, B. D., Barry, D. J., Hartkopf, W. I., & McAlister, H. A. 1992, *AJ*, 103, 1399
- Baize, P. & Petit, M. 1989, *A&AS*, 77, 497
- Baraffe, I. & Chabrier, G. 1996, *ApJ*, 461, L51
- Baraffe, I., Chabrier, G., Allard, F., & Hauschildt, P. H. 1998, *A&A*, 337, 403

- Basri, G. & Reiners, A. 2006, *AJ*, 132, 663
- Bate, M. R. 2000, *MNRAS*, 314, 33
- Bate, M. R. 2001, *The Formation of Binary Stars*, 200, 429
- Bate, M. R. 2009, *MNRAS*, 392, 590
- Bate, M. R. 2011, *MNRAS*, 417, 2036
- Bate, M. R. 2012, *MNRAS*, 419, 3115
- Bate, M. R. & Bonnell, I. A. 1997, *MNRAS*, 285, 33
- Bate, M. R., Bonnell, I. A., & Bromm, V. 2002, *MNRAS*, 336, 705
- Bate, M. R., Bonnell, I. A., & Bromm, V. 2003, *MNRAS*, 339, 577
- Bate, M. R., Bonnell, I. A., & Price, N. M. 1995, *MNRAS*, 277, 362
- Beardsley, W. K. 1964, *AJ*, 69, 532
- Beckers, J. M. 1993, *ARA&A*, 31, 13
- Becklin, E. E. & Zuckerman, B. 1988, *Nature*, 336, 656
- Bergfors, C., Brandner, W., Janson, M., et al. 2010, *A&A*, 520, A54
- Berghofer, T. W. & Schmitt, J. H. M. M. 1994, *A&A*, 292, L5
- Billères, M., Delfosse, X., Beuzit, J.-L., et al. 2005, *A&A*, 440, L55
- Boesgaard, A. M. & Friel, E. D. 1990, *ApJ*, 351, 467
- Bonnefoy, M., Chauvin, G., Dumas, C., et al. 2009, *A&A*, 506, 799
- Bonnell, I. & Bastien, P. 1992, *ApJ*, 401, 654
- Bonnell, I., Martel, H., Bastien, P., Arcoragi, J.-P., & Benz, W. 1991, *ApJ*, 377, 553
- Bonnell, I. A. 1994a, *MNRAS*, 269, 837
- Bonnell, I. A. 1994b, *ASPC*, 65, 115
- Bonnell, I. A. 2001, *The Formation of Binary Stars*, 200, 23
- Bonnell, I. A. & Bate, M. R. 1994, *MNRAS*, 271, 999
- Bonnell, I. A., Bate, M. R., & Zinnecker, H. 1998, *MNRAS*, 298, 93
- Boss, A. P. 2001, *ApJ*, 563, 367
- Boss, A. P. & Bodenheimer, P. 1979, *ApJ*, 234, 289

- Boss, A. R. 1986, *ApJS*, 62, 519
- Bouvier, J. & Corcoran, P. 2001, *The Formation of Binary Stars*, 200, 155
- Burgasser, A. J., Kirkpatrick, J. D., Brown, M. E., et al. 1999, *ApJ*, 522, L65
- Burgasser, A. J., Kirkpatrick, J. D., Cruz, K. L., et al. 2006, *ApJS*, 166, 585
- Burgasser, A. J., Kirkpatrick, J. D., Reid, I. N., et al. 2003, *ApJ*, 586, 512
- Carpenter, J. M. 2001, *AJ*, 121, 2851
- Carquillat, J.-M., Ginestet, N., Prieur, J. L., & Debernardi, Y. 2003, *MNRAS*, 346, 555
- Cazes, J. E. & Tohline, J. E. 2000, *ApJ*, 532, 1051
- Chabrier, G. & Baraffe, I. 1997, *A&A*, 327, 1039
- Chabrier, G. & Küker, M. 2006, *A&A*, 446, 1027
- Chaname, J. & Gould, A. 2004, *ApJ*, 601, 289
- Chanan, G. A., Troy, M., & Ohara, C. M. 2000, *Society of Photo-Optical Instrumentation Engineers (SPIE) Conference Series*, 4003, 188
- Christou, J. C. & Drummond, J. D. 2006, *AJ*, 131, 3100
- Clarke, C. J. 1996, *MNRAS*, 283, 353
- Clarke, C. J. & Pringle, J. E. 1991, *MNRAS*, 249, 584
- Close, L. M., Siegler, N., Freed, M., & Biller, B. 2003, *ApJ*, 587, 407
- Cowley, A., Jaschek, M., & Jaschek, C. 1970, *AJ*, 75, 941
- Daniel, K. J., Linsky, J. L., & Gagné, M. 2002, *ApJ*, 578, 486
- De-Pontieu, B., McIntosh, S. W., Carlsson, M., et al. 2007, *Science*, 318, 1574
- De Rosa, R. J., Bulger, J., Patience, J., et al. 2011, *MNRAS*, 415, 854
- de Zeeuw, P. T., Hoogerwerf, R., de Bruijne, J. H. J., Brown, A. G. A., & Blaauw, A. 1999, *AJ*, 117, 354
- Debernardi, Y., Mermilliod, J.-C., Carquillat, J.-M., & Ginestet, N. 2000, *A&A*, 354, 881
- Delgado-Donate, E. J., Clarke, C. J., Bate, M. R., & Hodgkin, S. T. 2004, *MNRAS*, 351, 617
- Dent, W. R. F., Torrelles, J. M., Osorio, M., Calvet, N., & Anglada, G. 2006, *MNRAS*, 365, 1283
- Docobo, J. A. & Andrade, M. 2006, *ApJ*, 652, 681
- Docobo, J. A. & Costa, J. M. 1985, *Circ. d'Inf.*, 96

- Docobo, J. A. & Ling, J. F. 2007, *AJ*, 133, 1209
- Docobo, J. A., Tamazian, V. S., Balega, Y. Y., & Melikian, N. D. 2010, *AJ*, 140, 1078
- Dohlen, K. 2006, in *Ground-based and Airborne Instrumentation for Astronomy (SPIE)*, 62690Q-62690Q-12
- Doyon, R., Nadeau, D., Vallee, P., et al. 1998, *SPIE*, 3354, 760
- Drummond, J., Milster, S., Ryan, P., & Roberts Jr, L. C. 2003, *ApJ*, 585, 1007
- Ducati, J. R. 2002, *Stellar Photometry in Johnson's 11-Color System (Strasbourg: CDS)*
- Duchêne, G. 1999, *A&A*, 341, 547
- Duchêne, G., Delgado-Donate, E., Haisch, K. E. J., Loinard, L., & Rodríguez, L. F. 2007, *Protostars and Planets V*, -1, 379
- Dupuy, T. J., Liu, M. C., & Bowler, B. P. 2009, *ApJ*, 706, 328
- Duquennoy, A. & Mayor, M. 1991, *A&A*, 248, 485
- Durisen, R. H., Gingold, R. A., Tohline, J. E., & Boss, A. P. 1986, *ApJ*, 305, 281
- Durisen, R. H., Sterzik, M. F., & Pickett, B. K. 2001, *A&A*, 371, 952
- Eggen, O. J. 1967, *ARA&A*, 5, 105
- Ehrenreich, D., Lagrange, A.-M., Montagnier, G., et al. 2010, *A&A*, 523, 73
- Ersparmer, D. & North, P. 2003, *A&A*, 398, 1121
- ESA. 1997, *The Hipparcos and Tycho Catalogues*, ESA SP-1200
- Fabian, A. C., Pringle, J. E., & Rees, M. J. 1975, *MNRAS*, 172, 15P
- Fabricius, C. & Makarov, V. V. 2000, *A&A*, 356, 141
- Fekel, F. C., Scarfe, C. D., Barlow, D. J., et al. 2002, *AJ*, 123, 1723
- Fekel, F. C. J. 1981, *ApJ*, 246, 879
- Feldmeier, A., Puls, J., & Pauldrach, A. W. A. 1997, *A&A*, 322, 878
- Figueras, F. & Blasi, F. 1998, *A&A*, 329, 957
- Fischer, D. A. & Marcy, G. W. 1992, *ApJ*, 396, 178
- Fisher, R. T. 2004, *ApJ*, 600, 769
- Fregeau, J. M., Ivanova, N., & Rasio, F. A. 2009, *ApJ*, 707, 1533
- Fried, D. L. 1966, *Journal of the Optical Society of America (1917-1983)*, 56, 1372

- Fugate, R. Q., Fried, D. L., Ameer, G. A., et al. 1991, *Nature*, 353, 144
- Fukagawa, M., Tamura, M., Itoh, Y., et al. 2010, *Publications of the Astronomical Society of Japan*, 62, 347
- G del, M. 2004, *A&AR*, 12, 71
- Ghez, A. M., McCarthy, D. W., Patience, J. L., & Beck, T. L. 1997, *ApJ*, 481, 378
- Ghez, A. M., Neugebauer, G., & Matthews, K. 1993, *AJ*, 106, 2005
- Giampapa, M. S., Prosser, C. F., & Fleming, T. A. 1998, *ApJ*, 501, 624
- Goodman, J. & Hut, P. 1993, *ApJ*, 403, 271
- Goodwin, S. P. 2010, *Philosophical Transactions of the Royal Society A: Mathematical, Physical and Engineering Sciences*, 368, 851
- Goodwin, S. P., Whitworth, A. P., & Ward-Thompson, D. 2004a, *A&A*, 414, 633
- Goodwin, S. P., Whitworth, A. P., & Ward-Thompson, D. 2004b, *A&A*, 423, 169
- Gray, D. F. 1992, *Camb. Astrophys. Ser.*, Vol. 20,, -1
- Green, R. M. 1985, Cambridge and New York, Cambridge University Press, 1985, 533 p.
- Gutmann, F. 1965, *Publications of the Dominion Astrophysical Observatory Victoria*, 12, 391
- Habets, G. M. H. J. & Heintze, J. R. W. 1981, *A&AS*, 46, 193
- Hamidouche, M., Looney, L. W., & Mundy, L. G. 2006, *ApJ*, 651, 321
- Hardy, J. W. 1998, *Adaptive Optics for Astronomical Telescopes*
- Hartkopf, W. I., McAlister, H. A., & Franz, O. G. 1989, *AJ*, 98, 1014
- Hayashi, C. & Nakano, T. 1963, *Prog. Theor. Phys.*, 30, 460
- Hayward, T. L., Brandl, B., Pirger, B., et al. 2001, *PASP*, 113, 105
- Heggie, D. C. 1975, *MNRAS*, 173, 729
- Henry, T. J. 1991, Ph.D. Thesis Arizona Univ., Tucson.
- Henry, T. J. & McCarthy, D. W. J. 1990, *ApJ*, 350, 334
- Hernandez, J., Hartmann, L., Megeath, T., et al. 2007, *ApJ*, 662, 1067
- Hilditch, R. W. 2001, *An Introduction to Close Binary Stars*
- Hills, J. G. 1975, *AJ*, 80, 809
- Hills, J. G. 1976, *MNRAS*, 175, 1P

- Hinkley, S., Oppenheimer, B. R., Brenner, D., et al. 2010, *ApJ*, 712, 421
- Hodapp, K. W., Jensen, J. B., Irwin, E. M., et al. 2003, *PASP*, 115, 1388
- Hoffleit, D. 1964, New Haven, Conn.: Yale University Observatory, 1964, 3rd rev.ed., edited by Hoffleit, Dorrit, -1
- Høg, E., Fabricius, C., Makarov, V. V., et al. 2000, *A&A*, 355, L27
- Horch, E., Ninkov, Z., & Franz, O. G. 2001, *AJ*, 121, 1583
- Horch, E. P., Meyer, R. D., & van Altena, W. F. 2004, *AJ*, 127, 1727
- Howell, S. B. 2000, *Handbook of CCD astronomy / Steve B. Howell*. Cambridge, U.K. ; New York : Cambridge University Press, c2000. (Cambridge observing handbooks for research astronomers ; 2), -1
- Hubber, D. A. & Whitworth, A. P. 2005, *A&A*, 437, 113
- Hubrig, S., Le Mignant, D., North, P., & Krautter, J. 2001, *A&A*, 372, 152
- Huélamo, N., Neuhäuser, R., Stelzer, B., Supper, R., & Zinnecker, H. 2000, *A&A*, 359, 227
- Huensch, M., Schmitt, J. H. M. M., & Voges, W. 1998a, *A&AS*, 127, 251
- Huensch, M., Schmitt, J. H. M. M., & Voges, W. 1998b, *A&AS*, 132, 155
- Hummel, C. A., Mozurkewich, D., Armstrong, J. T., et al. 1998, *AJ*, 116, 2536
- Ivanov, V. D., Chauvin, G., Foellmi, C., et al. 2006, *Ap&SS*, 304, 247
- Jeans, J. H. 1919, *MNRAS*, 79, 408
- Jess, D. B., Mathioudakis, M., Erdélyi, R., et al. 2009, *Science*, 323, 1582
- Johnson, J. A., Butler, R. P., Marcy, G. W., et al. 2007, *ApJ*, 670, 833
- Kalas, P., Graham, J. R., Chiang, E., et al. 2008, *Science*, 322, 1345
- King, J. R., Villarreal, A. R., Soderblom, D. R., Gulliver, A. F., & Adelman, S. J. 2003, *AJ*, 125, 1980
- King, R. R., Parker, R. J., Patience, J., & Goodwin, S. P. 2012, *MNRAS*, -1, no
- Kirkpatrick, J. D. 2005, *ARA&A*, 43, 195
- Kirkpatrick, J. D., Reid, I. N., Liebert, J., et al. 1999, *ApJ*, 519, 802
- Kohler, R. & Leinert, C. 1998, *A&A*, 331, 977
- Köhler, R., Petr-Gotzens, M. G., McCaughrean, M. J., et al. 2006, *A&A*, 458, 461
- Köhler, R., Ratzka, T., Herbst, T. M., & Kasper, M. 2008, *A&A*, 482, 929

- Kolmogorov, A. 1941, *Akademiia Nauk SSSR Doklady*, 30, 301
- Kouwenhoven, M. B. N., Brown, A. G. A., Goodwin, S. P., Portegies Zwart, S. F., & Kaper, L. 2009, *A&A*, 493, 979
- Kouwenhoven, M. B. N., Brown, A. G. A., Zinnecker, H., Kaper, L., & Portegies Zwart, S. F. 2005, *A&A*, 430, 137
- Kouwenhoven, M. B. N., Goodwin, S. P., Parker, R. J., et al. 2010, *MNRAS*, 404, 1835
- Kraft, R. P. 1970, *Spectroscopic Astrophysics. An Assessment of the Contributions of Otto Struve*, -1, 385
- Kratter, K. M. 2011, *From Darkness to Light: Origin and Evolution of Young Stellar Clusters*, 447, 47
- Kratter, K. M. & Matzner, C. D. 2006, *MNRAS*, 373, 1563
- Kratter, K. M., Matzner, C. D., Krumholz, M. R., & Klein, R. I. 2010a, *ApJ*, 708, 1585
- Kratter, K. M., Murray-Clay, R. A., & Youdin, A. N. 2010b, *ApJ*, 710, 1375
- Kraus, A. L., Ireland, M. J., Martinache, F., & Hillenbrand, L. A. 2011, *ApJ*, 731, 8
- Krolik, J. H. 1983, *Nature*, 305, 506
- Kroupa, P. 1995, *MNRAS*, 277, 1522
- Kroupa, P. 2001, *MNRAS*, 322, 231
- Lada, C. J. & Lada, E. A. 2003, *ARA&A*, 41, 57
- Lafrenière, D., Doyon, R., Marois, C., et al. 2007a, *ApJ*, 670, 1367
- Lafrenière, D., Jayawardhana, R., Janson, M., et al. 2011, *ApJ*, 730, 42
- Lafrenière, D., Jayawardhana, R., & van Kerkwijk, M. H. 2010, *ApJ*, 719, 497
- Lafrenière, D., Marois, C., Doyon, R., Nadeau, D., & Artigau, É. 2007b, *ApJ*, 660, 770
- Lagrange, A.-M., Gratadour, D., Chauvin, G., et al. 2009, *A&A*, 493, L21
- Larson, R. B. 2001, *The Formation of Binary Stars*, 200, 93
- Latham, D. W., Davis, R. J., Stefanik, R. P., Mazeh, T., & Abt, H. A. 1991, *AJ*, 101, 625
- Lejeune, T. & Schaerer, D. 2001, *A&A*, 366, 538
- Lenzen, R., Hartung, M., Brandner, W., et al. 2003, *SPIE*, 4841, 944
- Liu, M. C., Dupuy, T. J., & Ireland, M. J. 2008, *ApJ*, 689, 436
- Lloyd, J. P., Liu, M. C., Macintosh, B. A., et al. 2000, *SPIE*, 4008, 814

- Lodato, G., Meru, F., Clarke, C. J., & Rice, W. K. M. 2007, *MNRAS*, 374, 590
- Lowrance, P. J., Schneider, G., Kirkpatrick, J. D., et al. 2000, *ApJ*, 541, 390
- Lucy, L. B. & Ricco, E. 1979, *AJ*, 84, 401
- Lucy, L. B. & White, R. L. 1980, *ApJ*, 241, 300
- Luhman, K. L. 2004, *ApJ*, 614, 398
- Macintosh, B. 2006, in *Advances in Adaptive Optics II (SPIE)*, 62720L-62720L-12
- Makarov, V. V. 2007, *ApJS*, 169, 105
- Makarov, V. V., Zacharias, N., & Hennessy, G. S. 2008, *ApJ*, 687, 566
- Mamajek, E. E., Kenworthy, M. A., Hinz, P. M., & Meyer, M. R. 2010, *AJ*, 139, 919
- Mamajek, E. E., Meyer, M. R., & Liebert, J. 2002, *AJ*, 124, 1670
- Marcy, G. W. & Benitz, K. J. 1989, *ApJ*, 344, 441
- Marigo, P., Girardi, L., Bressan, A., et al. 2008, *A&A*, 482, 883
- Marois, C., Macintosh, B., Barman, T., et al. 2008, *Science*, 322, 1348
- Marois, C., Zuckerman, B., Konopacky, Q. M., Macintosh, B., & Barman, T. 2010, *Nature*, 468, 1080
- Mason, B. D., Douglass, G. G., & Hartkopf, W. I. 1999, *AJ*, 117, 1023
- Mason, B. D., Gies, D. R., Hartkopf, W. I., et al. 1998, *AJ*, 115, 821
- Mason, B. D., Hartkopf, W. I., Gies, D. R., Henry, T. J., & Helsel, J. W. 2009, *AJ*, 137, 3358
- Mason, B. D., Wycoff, G. L., Hartkopf, W. I., Douglass, G. G., & Worley, C. E. 2001, *AJ*, 122, 3466
- Mathieu, R. D. 1994, *ARA&A*, 32, 465
- Matzner, C. D. & Levin, Y. 2005, *ApJ*, 628, 817
- Mazeh, T., Goldberg, D., Duquennoy, A., & Mayor, M. 1992, *ApJ*, 401, 265
- Mazeh, T., Simon, M., Prato, L., Markus, B., & Zucker, S. 2003, *ApJ*, 599, 1344
- McAlister, H. A., Hartkopf, W. I., Hutter, D. J., & Franz, O. G. 1987, *AJ*, 93, 688
- McAlister, H. A., Mason, B. D., Hartkopf, W. I., & Shara, M. M. 1993, *AJ*, 106, 1639
- McCaughrean, M. J. & Stauffer, J. R. 1994, *AJ*, 108, 1382
- McDonald, J. M. & Clarke, C. J. 1995, *MNRAS*, 275, 671

- Meru, F. & Bate, M. R. 2010, *MNRAS*, 406, 2279
- Micela, G., Sciortino, S., Harnden, F. R., et al. 1999, *A&A*, 341, 751
- Micela, G., Sciortino, S., Kashyap, V., Harnden, F. R., & Rosner, R. 1996, *ApJS*, 102, 75
- Micela, G., Sciortino, S., Serio, S., et al. 1985, *ApJ*, 292, 172
- Micela, G., Sciortino, S., Vaiana, G. S., et al. 1988, *ApJ*, 325, 798
- Moeckel, N. & Bally, J. 2007, *ApJ*, 656, 275
- Moeckel, N. & Bate, M. R. 2010, *MNRAS*, 404, 721
- Moore, J. H. 1932, *Publications of Lick Observatory*, 18, 1
- Morel, M. & Magnenat, P. 1978, *A&AS*, 34, 477
- Muterspaugh, M. W., Hartkopf, W. I., Lane, B. F., et al. 2010, *AJ*, 140, 1623
- Muterspaugh, M. W., Lane, B. F., Fekel, F. C., et al. 2008, *AJ*, 135, 766
- Nakajima, T., Oppenheimer, B. R., Kulkarni, S. R., et al. 1995, *Nature*, 378, 463
- Offner, S. S. R., Kratter, K. M., Matzner, C. D., Krumholz, M. R., & Klein, R. I. 2010, *ApJ*, 725, 1485
- Ortega, V. G., de la Reza, R., Jilinski, E., & Bazzanella, B. 2002, *ApJ*, 575, L75
- Ortega, V. G., Jilinski, E., de la Reza, R., & Bazzanella, B. 2007, *MNRAS*, 377, 441
- Owocki, S. P., Castor, J. I., & Rybicki, G. B. 1988, *ApJ*, 335, 914
- Palous, J. 1983, *Bulletin of the Astronomical Institutes of Czechoslovakia*, 34, 286
- Pan, X., Shao, M., & Kulkarni, S. R. 2004, *Nature*, 427, 326
- Parker, R. J., Goodwin, S. P., & Allison, R. J. 2011, *MNRAS*, 418, 2565
- Parker, R. J., Goodwin, S. P., Kroupa, P., & Kouwenhoven, M. B. N. 2009, *MNRAS*, 397, 1577
- Patience, J., Ghez, A. M., Reid, I. N., Weinberger, A. J., & Matthews, K. 1998, *AJ*, 115, 1972
- Patience, J., Zavala, R. T., Prato, L., et al. 2008, *ApJ*, 674, L97
- Patterson, J. & Raymond, J. C. 1985, *ApJ*, 292, 535
- Paulson, D. B., Sneden, C., & Cochran, W. D. 2003, *AJ*, 125, 3185
- Petr, M. G., Coudé du Foresto, V., Beckwith, S. V. W., Richichi, A., & McCaughrean, M. J. 1998, *ApJ*, 500, 825
- Pickering, E. C. 1890, *The Observatory*, 13, 80

- Pizzolato, N., Maggio, A., Micela, G., Sciortino, S., & Ventura, P. 2003, *A&A*, 397, 147
- Popovic, G. M. 1969, *Bulletin de l'Observatoire Astronomique de Belgrade*, 27, 33
- Pourbaix, D., Tokovinin, A. A., Batten, A. H., et al. 2004, *A&A*, 424, 727
- Preibisch, T. 1999, *New Astronomy*, 4, 531
- Preibisch, T., Brown, A. G. A., Bridges, T., Guenther, E., & Zinnecker, H. 2002, *AJ*, 124, 404
- Press, W. H., Teukolsky, S. A., Vetterling, W. T., & Flannery, B. P. 1992, Cambridge: University Press, |c1992, 2nd ed.
- Pringle, J. E. 1989, *MNRAS*, 239, 361
- Raghavan, D., McAlister, H. A., Henry, T. J., et al. 2010, *ApJS*, 190, 1
- Randich, S. 2000, *ASPC*, 198, 401
- Reggiani, M. M. & Meyer, M. R. 2011, *ApJ*, 738, 60
- Reid, I. N., Cruz, K. L., Burgasser, A. J., & C Liu, M. 2008, *AJ*, 135, 580
- Reipurth, B. 2000, *AJ*, 120, 3177
- Reipurth, B. & Zinnecker, H. 1993, *A&A*, 278, 81
- Richardson, E. H., Fletcher, J. M., Morbey, C. L., Oschmann, J. M., & Pazder, J. S. 1998, *SPIE Conference Series*, 3353, 600
- Roberts, L. C. & Neyman, C. R. 2002, *PASP*, 114, 1260
- Roddier, F. 1988, *Appl. Opt.*, 27, 1223
- Rousset, G., Lacombe, F., Puget, P., et al. 2003, *SPIE*, 4839, 140
- Roxburgh, I. W. 1966, *ApJ*, 143, 111
- Royer, F., Zorec, J., & Gómez, A. E. 2007, *A&A*, 463, 671
- Rucinski, S. M., Pych, W., Ogłóza, W., et al. 2005, *AJ*, 130, 767
- Sargent, W. L. W. 1964, *ARA&A*, 2, 297
- Schatzman, E. 1949, *AnAp*, 12, 203
- Schmitt, J. H. M. M., Golub, L., Harnden, F. R., et al. 1985, *ApJ*, 290, 307
- Schmitt, J. H. M. M., Micela, G., Sciortino, S., et al. 1990, *ApJ*, 351, 492
- Schmitt, J. H. M. M., Zinnecker, H., Cruddace, R., & Harnden, F. R. 1993, *ApJ*, 402, L13
- Schröder, C. & Schmitt, J. H. M. M. 2007, *A&A*, 475, 677

- Schwarzschild, M. 1948, *ApJ*, 107, 1
- Shapiro, S. L., Lightman, A. P., & Eardley, D. M. 1976, *ApJ*, 204, 187
- Shatsky, N. & Tokovinin, A. 2002, *A&A*, 382, 92
- Siess, L., Dufour, E., & Forestini, M. 2000, *A&A*, 358, 593
- Simon, M., Close, L. M., & Beck, T. L. 1999, *AJ*, 117, 1375
- Simon, M. & Prato, L. 1995, *ApJ*, 450, 824
- Simon, T., Drake, S. A., & Kim, P. D. 1995, *PASP*, 107, 1034
- Skrutskie, M. F., Cutri, R. M., Stiening, R., et al. 2006, *AJ*, 131, 1163
- Skrutskie, M. F., Forrest, W. J., & Shure, M. 1989, *AJ*, 98, 1409
- Smith, B. A. & Terrile, R. J. 1984, *Science*, 226, 1421
- Soderblom, D. R. & Mayor, M. 1993, *AJ*, 105, 226
- Söderhjelm, S. 1999, *A&A*, 341, 121
- Song, I., Caillault, J.-P., Navascues, D. B. y., & Stauffer, J. R. 2001, *ApJ*, 546, 352
- Soubiran, C., Le Campion, J.-F., Cayrel de Strobel, G., & Caillo, A. 2010, *A&A*, 515, 111
- Spiegel, E. A. & Weiss, N. O. 1980, *Nature*, 287, 616
- Stamatellos, D., Hubber, D. A., & Whitworth, A. P. 2007, *MNRAS*, 382, L30
- Stamatellos, D., Maury, A., Whitworth, A., & André, P. 2011, *MNRAS*, 413, 1787
- Stamatellos, D. & Whitworth, A. P. 2009, *MNRAS*, 392, 413
- Stassun, K. G., Mathieu, R. D., Cargile, P. A., et al. 2008, *Nature*, 453, 1079
- Stauffer, J. R., Caillault, J.-P., Gagne, M., Prosser, C. F., & Hartmann, L. W. 1994, *ApJ*, 91, 625
- Stern, R. A., Schmitt, J. H. M. M., & Kahabka, P. T. 1995, *ApJ*, 448, 683
- Sterzik, M. F. & Durisen, R. H. 1998, *A&A*, 339, 95
- Sterzik, M. F. & Durisen, R. H. 2003, *A&A*, 400, 1031
- Sterzik, M. F. & Tokovinin, A. A. 2002, *A&A*, 384, 1030
- Sturrock, P. A. 1999, *ApJ*, 521, 451
- Tatarski, V. I. 1961, *Wave propagation in a turbulent medium* (New York: Dover Publications, Inc.)

- Thomas, S. J., van der Blik, N. S., Rodgers, B., Doppmann, G., & Bouvier, J. 2007, *The Formation of Binary Stars*, 2, 250
- Tohline, J. E. 2002, *ARA&A*, 40, 349
- Tohline, J. E. & Durisen, R. H. 2001, *The Formation of Binary Stars*, 200, 40
- Tokovinin, A. 2008, *MNRAS*, 389, 925
- Tokovinin, A., Mason, B. D., & Hartkopf, W. I. 2010, *AJ*, 139, 743
- Tokovinin, A. A. 2000, *A&A*, 360, 997
- Tokovinin, A. A. & Smekhov, M. G. 2002, *A&A*, 382, 118
- Topka, K., Golub, L., Gorenstein, P., et al. 1982, *ApJ*, 259, 677
- Trilling, D. E., Stansberry, J. A., Stapelfeldt, K. R., et al. 2007, *ApJ*, 658, 1289
- Vaiana, G. S., Cassinelli, J. P., Fabbiano, G., et al. 1981, *ApJ*, 245, 163
- Valtonen, M. J. 1988, *IAU Colloq. 96: The Few Body Problem*, 140
- Valtonen, M. J. 1998, *A&A*, 334, 169
- van den Berk, J., Portegies Zwart, S. F., & McMillan, S. L. W. 2007, *MNRAS*, 379, 111
- van Leeuwen, F. 2007, *A&A*, 474, 653
- Vinter Hansen, J. M., Neubauer, F. J., & Roosen-Raad, D. 1940, *Lick Observatory Bulletin*, 19, 89
- Voges, W., Aschenbach, B., Boller, T., et al. 1999, *A&A*, 349, 389
- Voges, W., Aschenbach, B., Boller, T., et al. 2000, *VizieR On-line Data Catalog*, 9029, 0
- Ward-Thompson, D., André, P., Crutcher, R., et al. 2007, *Protostars and Planets V*, -1, 33
- Whitworth, A., Bate, M. R., Nordlund, Å., Reipurth, B., & Zinnecker, H. 2007, *Protostars and Planets V*, -1, 459
- Whitworth, A. P. & Stamatellos, D. 2006, *A&A*, 458, 817
- Woodward, J. W., Tohline, J. E., & Hachisu, I. 1994, *ApJ*, 420, 247
- Worley, C. E. 1969, *AJ*, 74, 764
- Wu, Y., Singh, H. P., Prugniel, P., Gupta, R., & Koleva, M. 2010, *A&A*, 525, A71
- Zahn, J.-P. 1977, *A&A*, 57, 383
- Zimmerman, N., Oppenheimer, B. R., Hinkley, S., et al. 2010, *ApJ*, 709, 733
- Zuckerman, B. & Song, I. 2004, *ARA&A*, 42, 685